NSTX-U FY2013 Year End Report

J. Menard, M. Ono, and the NSTX-U Research Team

September 13, 2013 – Version 13

Table of contents

- **Summary of FY2013 Notable Outcomes** **2**
- **Facility and Diagnostics** **8**
- **Research Results – FY13 Milestones** **27**
  - R(13-1): Perform integrated physics and optical design of new high-k_θ FIR system 28
  - R(13-2): Investigate the relationship between lithium-conditioned surface composition and plasma behavior 30
  - R(13-3): Perform physics design of ECH and EBW system for plasma start-up and current drive in advanced scenarios 32
  - R(13-4): Identify disruption precursors and disruption mitigation and avoidance techniques for NSTX-U and ITER 38
- **Additional Research Highlights** **47**
  - Boundary Physics 47
  - Materials and PFC Research and Development 65
  - Macroscopic Stability 70
  - Transport and Turbulence 102
  - Energetic Particles 111
  - Wave Heating and Current Drive 116
  - Solenoid-Free Plasma Start-up 126
  - Advanced Scenarios and Control 135
- **NSTX-U FY2013 Publications** **146**
- **NSTX-U FY2013 Presentations** **153**

Summary of FY2013 Notable Outcomes:

<u>Outcome 1.1a</u> *"Support the FES joint research target to explore enhanced confinement regimes without large edge instabilities, but with acceptable edge particle transport and a strong thermal transport barrier and to extrapolate these regimes to ITER."*

NSTX-U strongly supported the FY2013 joint research target by leading and organizing this activity among the 3 participating facilities (DIII-D, NSTX, Alcator C-Mod). Stefan Gerhardt (PPPL) was the leader of the JRT and coordinated many group teleconferences and discussions/meetings between the participating researchers. The NSTX team contributed data from Enhanced Pedestal H-mode (EP H-mode) experiments and developed a better understanding of the range of ion temperature profile shapes in EPH, developed improved correlations between the ion temperature pedestal parameter and the edge rotation shear, and (in Q3) initiated an assessment of turbulence as inferred from the edge reflectometer (UCLA), and examined those results with XGC0 and GS2 modeling. The NSTX contribution complements results from Alcator C-Mod and DIII-D investigation the "I-mode" regime of operation (for which the edge particle transport is L-mode-like but the thermal transport is H-mode like), and also complements studies of the Quiescent H-mode (QH) regime on DIII-D which emphasized studies of the dependence of the edge-harmonic-oscillation (EHO) on density and collisionality.

<u>Outcome 1.2a</u> *"Carry out high impact research relevant to NSTX-U through domestic and international collaborations"*

In continuation of last year's aim of maximizing the productivity of the NSTX research team during the Upgrade outage, NSTX-U researchers collaborated on a range of domestic and international facilities performing research relevant to both future NSTX-U science and operations also to the host facility. More detail on the results of these collaboration activities can be found in the research milestone summaries and research highlights provided in subsequent sections of this report.

In the area of macroscopic stability, NSTX researchers collaborated on the KSTAR facility in South Korea. PPPL and Columbia University researchers participated in the development of improved plasma boundary shape control and improved access to low inductance and high elongation plasma operation. These control and scenario developments enabled access to increased normalized beta and enabled studies of MHD stability near the no-wall stability limit. PPPL researchers also led studies of bounce-harmonic resonance effects in neoclassical toroidal viscosity NTV theory, and such effects were observed in KSTAR for the first time in a tokamak. These results were successfully compared to the IPEC model and published in Physical Review Letters. NSTX researchers from the University of Washington also participated in disruption mitigation experiments studying up/down injection asymmetry effects during massive gas injection (MGI) on DIII-D, and this research is important to ITER and will also inform planned MGI experiments on NSTX-U.

In the area of power exhaust, NSTX-U researchers (PPPL, LLNL) collaborated on DIII-D to implement improved real-time multi-x-point control for the snowflake divertor and also implemented real-time measurements of the divertor plasma temperature and radiation to actively feedback control the divertor detachment. These capabilities are important for advanced divertor control in both NSTX-U and DIII-D. Several PPPL researchers also participated in DIII-D machine operations to maintain these operations skills for the resumption of NSTX-U.

In the area of energetic particle physics, NSTX-U researchers from Florida International University (FIU) and PPPL obtained first data from a DD fusion product/rate detector on MAST, and this novel diagnostic will be used to infer fusion source profiles for testing fast-ion transport models on MAST and NSTX-U. Researchers from PPPL also explored TAE avalanche physics on MAST and DIII-D.

In transport research, as part of a collaborative effort with the MAST tokamak in England, UCLA, and NSTX, a Doppler Backscattering (DBS) was installed during the M9 campaign in 2013. DBS probes intermediate-k density fluctuations ($k_\theta > \sim 3$ cm^{-1}). Dr. Jon Hillesheim of MAST (a recent UCLA graduate) installed the UCLA systems in June 2013, and has since operating them. The system (16 channels, 30 – 75 GHz, cutoffs @ 1 – 7 x 10^{13} cm^{-3} in O-mode) can be configured for DBS or reflectometry. Initial DBS data was obtained during a pedestal scaling experiment led by Dr. Ahmed Diallo from the NSTX-U team. The DBS shows a variation during the ELM cycle in the turbulent spectrum in the pedestal at $k_\theta \approx 7$ cm^{-1}.

Momentum transport studies have also been pursued through collaboration on MAST. Motivated by the difference in predicted ITG/TEM momentum pinch between conventional and spherical tokamaks, and the lack of experimental data in NSTX L-modes, a perturbative momentum transport experiment was proposed to run at MAST in FY13. In a manner following similar NSTX H-mode experiments, edge magnetic field perturbations were used to modify the toroidal flow. Data was obtained in Aug. 2013 in both H-mode (using n=4 perturbations) and L-mode (n=3) at two plasma currents each. Where was a noticeable step/change of the toroidal flow with application of the external coil current (IRMP) and subsequent recovery to the original state, as compared to a shot without the applied perturbation. Although there is uncertainty in the torque due to the applied magnetic field, the recovery of the rotation following removal of the perturbation (and unknown torque) will be used to infer diffusive and convective momentum transport components.

In the area of RF research and solenoid-free start-up, for several years ORNL and PPPL have collaborated with the Culham Centre for Fusion Energy (CCFE) to perform EBW plasma start-up experiments on MAST. EBW start-up experiments were last performed on MAST in 2009, using a 28 GHz gyrotron system provided by ORNL that was capable of generating 100-150 kW of RF power. These experiments used a reflective grooved tile on the center stack. Subsequent improvements to the MAST 28 GHz heating system were made by ORNL and CCFE that substantially increased the power level and pulse length of the gyrotron and increased the transmission line efficiency. In 2013 two one-week experimental campaigns were dedicated to EBW plasma start-up in MAST. These campaigns significantly extended the 2009 results. Plasma currents up to 50 kA were generated non-inductively for up to 200 ms with 80 kW of 28 GHz gyrotron power. Also, by optimizing the vertical field ramp, plasma currents of up to 75kA were achieved with about 80 kW of 28 GHz gyrotron power. These results indicate that experiments on NSTX-U using $\geq$1 MW of 28 GHz power should be able to couple ~ 0.6 MW, allowing the power dependence of the driven plasma current during EBW plasma start-up to be studied to much higher powers than on MAST.

For helicity injection plasma start-up, a collaboration with the QUEST experiment in Kyushu, Japan has been led by researchers from the University of Washington. A goal of this collaboration is design a coaxial helicity injection system for QUEST, and the electrode configuration of this design has recently been decided. QUEST has ECH heating and all metal walls, and is potentially an excellent test-bed to assess ECH/EBW heating of CHI start-up plasmas applicable to NSTX-U.

In materials and PFC research, experiments on lithiated plasma facing component materials have been conducted on the Magnum-PSI linear plasma device located at the Dutch Institute for Fundamental Energy Research (DIFFER). Magnum-PSI is a magnetized, linear plasma device designed for simulating the divertor conditions expected in ITER-class devices. The plasma conditions present at the Magnum-PSI target provide similar density and temperatures as those found in NSTX, for example, during the previous liquid lithium divertor campaign. An NSTX-developed prototype lithium evaporator (the LITER-1C) was installed on the Magnum-PSI experimental device and loaded with lithium. Lithium was then deposited onto a substrate material after calibrating the deposition rate in the Magnum-PSI preparation chamber. High-power discharges were performed which resulted in a temperature ramp of the surface up to 1300C over the course of 7 seconds and the plasma response to this high-temperature surface was examined. During the course of exposures, two regimes were found: (1) an intense cloud of lithium emission was formed directly in front of the target and persisted for 3-4s which then transitioned into (2) a less intense, more diffuse emission pattern. The role of lithium vapor shielding in contributing to power dissipation in such targets is under active investigation.

<u>Outcome 3.1b</u> – "*Develop a prioritized research plan for NSTX-U to provide an assessment, within five years, of the viability of the ST concept as an attractive Fusion Nuclear Science Facility"*

In FY2013 the NSTX Upgrade 5 year plan for FY2014-2018 was written and completed by the NSTX-U research team and successfully reviewed by an FES-appointed peer review panel in May 2013. The review panel found that:

> *"The scientific and technical merit of the proposed NSTX-U research program is very high. The proposed research targets several of the most urgent and significant issues in spherical torus (ST) physics, including*
>
> - *Fully non-inductive startup, ramp-up, and sustained operation,*
> - *Confinement and transport at low collisionality,*
> - *3D field effects for ELM and rotation control, and*
> - *Divertor power and particle control and PFC development.*
>
> *The facility upgrades and diagnostic improvements that are included in the NSTX-U project will significantly enhance capability of the facility. As the most powerful and best diagnosed spherical torus in the world, NSTX-U will be in a good position to address critical issues for extension of the ST concept into the nuclear regime – non-inductive start-up/ramp-up and power handling at large values of power/radius. Furthermore the program is well positioned to explore fundamental physics issues of stability and transport at low aspect ratio."*

To guide the prioritization of research and facility upgrades for the near-term, five high-level goals were established for the NSTX-U five year plan period of 2014-2018:

1. Demonstrate stationary 100% non-inductive operation at performance that extrapolates to ≥ $1MW/m^2$ neutron wall loading in FNSF
2. Access reduced ν* and high-β combined with the ability to vary q and rotation to dramatically extend ST plasma understanding
3. Develop and understand non-inductive start-up and ramp-up to project to ST-FNSF operation with small or no central solenoid
4. Develop and utilize the high-flux-expansion "snowflake" divertor combined with radiative detachment to mitigate very high heat fluxes
5. Begin to assess high-Z PFCs plus liquid lithium to develop high-duty-factor integrated PMI solutions for SS-PMI and/or FNSF facilities, and beyond

These goals represent essential milestones for the assessment of the viability of an ST-based FNSF and also address critical issues for fusion development generally. As is evident from these goals, the highest priorities are to: establish fully non-inductive plasma operation (both ramp-up and sustainment), access and understand transport at low collisionality and high-beta, and to develop power exhaust methods using advanced divertors, radiation, and ultimately liquid metals on high-Z PFC substrates. To place these 5 year plan goals in context, it should be noted that the NSTX-U research team developed a long-range vision and corresponding goals extending through FY2021 to inform the U.S. next-step conceptual design for FNSF including the optimal aspect ratio, divertor, and PFCs. The long-range vision and the associated goals organized by topical science area are shown in Figure 5YP-1.

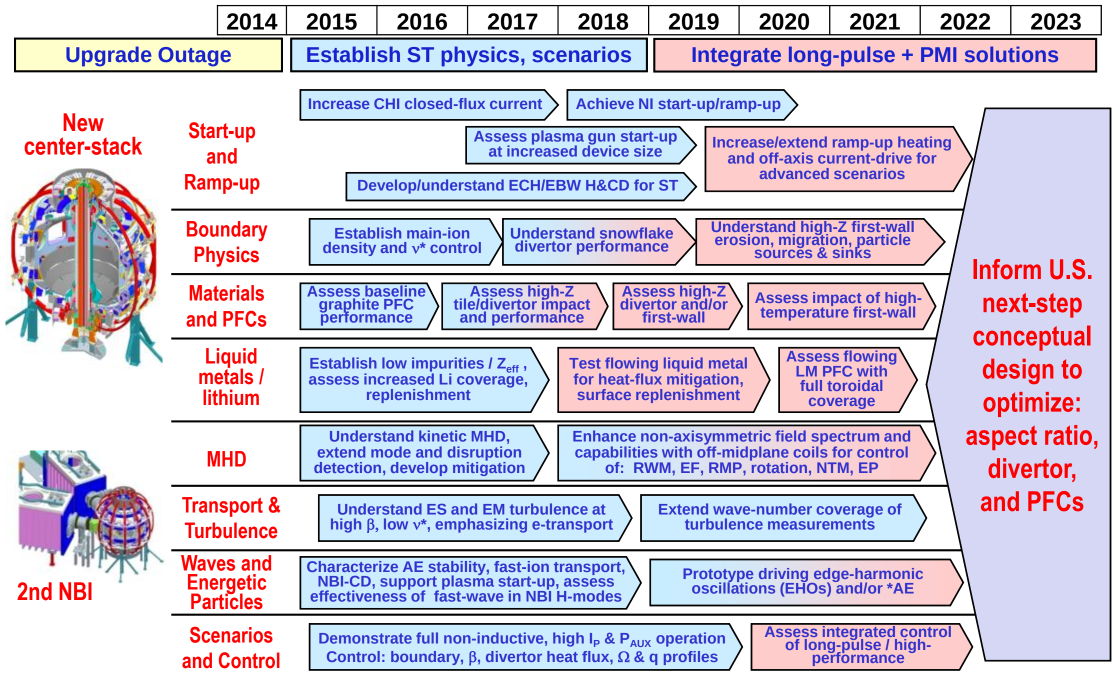

Figure FYP-1: Long-range goals and plans for NSTX-U research in support of FNSF, ITER, PMI research, and DEMO (assumes incremental funding 10% above base funding).

As shown in Figure 5YP-1, near-term research emphasizes establishment of the ST physics basis and operating scenarios (light blue) in support of assessing the viability of an ST-based FNSF (i.e. aspect ratio optimization). In later years, non-inductive sustainment would be integrated with both non-inductive start-up/ramp-up and divertor exhaust solutions, with an ultimate goal of integrating high-performance steady-state ST operation with advanced PMI solutions.

Diagnostic and facility enhancement plans supporting these near-term and long-term research goals have also been developed and are described in the 5 year plan. The highest priority near-term enhancements are show pictorially in Figure 5YP-2 organized by scientific issue to be resolved. These enhancements were chosen and ranked according to programmatic impact, cross-links/multiple use, and cost. Programmatic impact considerations included: importance to next-step ST viability, physics or operational contributions to ITER, and uniqueness for ST or in world program. Based on these criteria, the 3 highest priority facility enhancements (base funding) are:

1. A divertor cryo-pump for density and collisionality control important to all science areas and scenarios, while also enabling comparisons between cryo and lithium coating pumping.
2. A 28GHz, 1MW gyrotron for ECH/EBW heating of helicity-injection start-up plasmas for HHFW and/or NBI ramp-up, and longer-term to assess EBW heating and current-drive.
3. Off-midplane non-axisymmetric control coils (NCC) to provide far greater variation of the poloidal and toroidal 3D field spectrum for control of error fields, resistive wall modes, rotation, and ELMs to ensure access to sustained high beta operation.

With incremental funding, boundary/PMI research would be enhanced by accelerating conversion to high-Z walls, implementation of a flowing liquid Li divertor module, and the installation of divertor Thomson Scattering in support of diagnosing advanced divertor configurations.

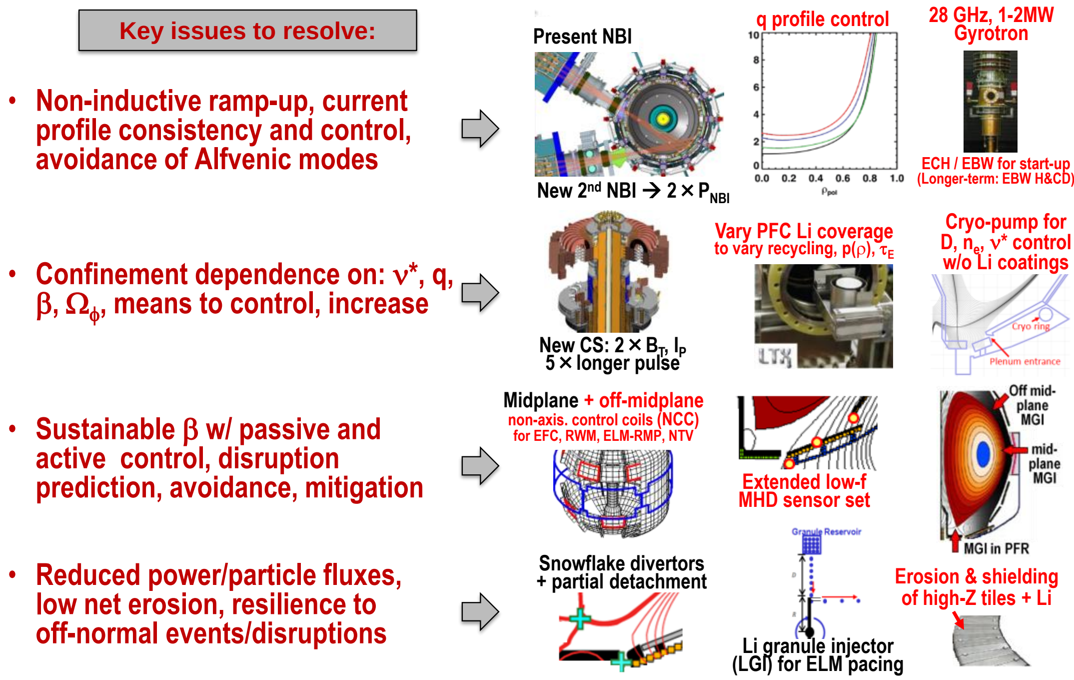

Figure FYP-2 - Key scientific issues to be resolved and proposed high-priority research tools in support of the 5 high-level goals. Existing/early tools are labeled in black, new/additional tools are labeled in red.

If the NSTX-U 5 year plan facility enhancements are implemented and the research goals described above are achieved, the ST will be well-positioned to become a viable candidate for an FNSF, advanced approaches to mitigating FNSF/DEMO-relevant heat fluxes will have been demonstrated (for short durations), and predictive capability for next-step STs, ITER, and DEMO will have been significantly expanded. Further, NSTX-U/PPPL researchers and the wider ST community will be well-positioned to lead or contribute to any future larger-scale FNSF design activities.

NSTX-U FY2013 Year End Report: Facility and Diagnostics

In FY 2013, the NSTX-U team continued to make a rapid progress on the NSTX Upgrade Project during the extended outage as described below. The NSTX-U Facility Operations team maintained the NSTX-U device, auxiliary systems, and site infrastructure to support the planned research efforts when NSTX-U starts plasma operations in FY2015. The team also initiated the preparation for the NSTX-U facility commissioning and subsequent plasma operations. Onsite support for equipment provided by other collaborating institutions was provided through the collaboration diagnostic interface budget. There were a number of important facility operation related enhancements carried out in FY 2013 which are needed to take full advantage of the NSTX-U device capabilities. With the enhanced plasma control requirements for longer duration plasmas expected in NSTX-U, an upgrade to the existing plasma control system is being implemented as part of the base program. In addition due to the aging D-site rectifier infrastructure and greater demands expected for NSTX-U, refurbishments of the TF and PF rectifiers (i.e., firing generators) are being performed by the base program. The TFTR-era motor generator with weld cracks are being repaired and refurbished. The final designs for the modifications to the Multi-Pulse Thomson Scattering (MPTS) diagnostic required for the NSTX Upgrade were completed in FY 2013 as described in Diagnostic Milestone Report D(13-1). Fabrication, assembly and installation of the necessary modifications to the MPTS diagnostic has begun and the completion is scheduled to occur in early FY 2014 to support system start-up in FY 2014. The preparation of the NSTX-U commissioning and plasma operation has begun. To provide capabilities needed to carry out the NSTX-U scientific research, the NSTX Team identified high priority facility and diagnostic enhancements for post upgrade operations as the part of the successful DOE NSTX-U Five Year Plan Review conducted in May 21 – 23, 2013. These included diagnostics and physics capabilities provided by NSTX Research Team members from U.S. laboratories other than PPPL.

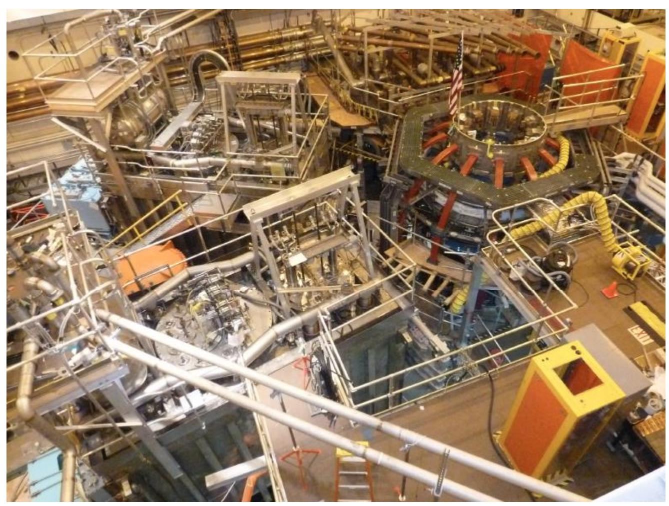

Fig. FD-1. Aerial view of the NSTX-U Test Cell, September 2013.

Facility and Diagnostic Milestones for FY2013

Facility Milestone F(13-1): Complete procurement of components and begin installation of refurbished D-Site Rectifier Firing Generators. (September 2013, completed on September 2013)

Milestone Description: Procurement of all components for the D-site rectifier firing generators will be completed. Firing generator chassis assembly and testing will take place and installation of the refurbished 68 firing generators will begin to support star-up testing in FY 2014.

Milestone F(13-1) Report: The D-site rectifiers (Transrex AC/DC Convertors of the NSTX Field Coil Power conversion System (FCPC)) provide a pulsed power capability of 1800 MVA for 6 seconds every 300 seconds. The modular converter concept of 74 identical, electrically isolated 6-pulse "power supply sections" was originally used on TFTR and then 68 of them were adapted to NSTX-U which has a more complex topology including anti-parallel and three wire configurations. Precise control of thyrister firing angles by the FCPC firing generators (FGs) has always been necessary for NSTX operations, and becomes more critical for the new 8-parallel, 130kA TF system configuration. The new Firing Generator (FG) delivers firing pulses with far greater resolution, precision, and repeatability. In FY 2013, procurement of all components for the D-site rectifier firing generators was completed. The prototype FG has been fully tested in a Transrex rectifier, and production units are being fabricated. Firing generator chassis assembly and testing will take place and installation of the refurbished 68 FG has begun to support star-up testing planned in FY 2014.

Diagnostic Milestone D(13-1): Complete final design of the Multi-Pulse Thomson Scattering (MPTS) diagnostic modifications and begin installation of the modifications (September 2013, completed in September 2013)

Description: To prepare for the post upgrade operation the final design of the MPTS diagnostic will be completed and installation of the necessary modifications to MPTS will begin.

Milestone D(13-1) Report: Modifications to the Multi-Pulse Thomson Scattering (MPTS) diagnostic required for the NSTX Upgrade were designed, and fabrication and installation of the needed components has started. The larger diameter of the center stack in NSTX-U requires re-aiming of the MPTS laser beams to avoid striking the center stack, which would cause damage to it as well as an unacceptable level of scattered laser light in the vacuum vessel. Re-aiming of the laser beams requires several other changes to the MPTS diagnostic configuration: 1) a new laser beam dump is provided on a new vacuum vessel port (located at Bay L) on the opposite side of the vacuum vessel from the laser input port; 2) the laser input port on the vacuum vessel is moved several centimeters on the vacuum vessel and re-aimed to achieve the needed laser beam path; and 3) the MPTS light collection optics are modified and re-aimed to provide high-resolution imaging of the re-aimed laser beam. Design of the reconfigured MPTS system to meet these requirements was completed in FY2013 and three final design reviews were held to validate the design of the ex-vessel components. The new laser exit port and the new laser input port were installed on the vacuum vessel in FY2013. Fabrication and procurement of many of the needed ex-vessel components is underway and fabrication drawings for the remaining ex-vessel components are being prepared. The reconfigured MPTS diagnostic will be installed in FY2014 prior to NSTX-U first plasma and commissioned in early experimental operation following first plasma.

NSTX Upgrade Project Accomplishments

The NSTX Upgrade (NSTX-U) Project which has two major components, new center stack, and 2nd NBI, has made excellent progress in FY 2013. The Upgrade Project activities ramped up rapidly in all areas and are currently on pace to be completed in the fall of 2014 well ahead of the Sept 2015 CD-4 completion target date. The recent NSTX-U Test Cell aerial view taken in September 2013 is shown in Fig. FD-1.

New Center Stack Upgrade

The new center-stack part of the NSTX Upgrade Project has multiple elements including the fabrication of the new center-stack, the structural enhancements to the device for the ~ 4x increased electromagnetic forces, and the associated sub-system enhancements to supported the doubling of the TF current and 5 sec plasma pulse length. The new center-stack is connected to the outer TF through 36 U-shaped TF Flex Buses. A more detailed the center-stack drawing is shown in Fig. FD-2. The NSTX Upgrade Project has begun work on the critical path fabrication of the center-stack (CS) components including friction stir welding of lead extensions to the inner TF conductors.

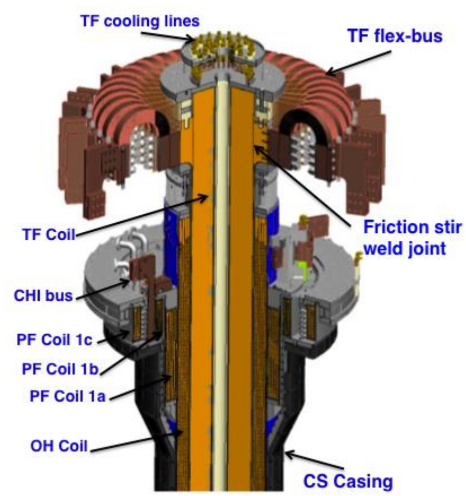

Fig. FD-2. A schematic of the new center-stack and the TF joint area.

The TF flex-bus is an important component to handle the TF current (130 kA) for about 7 sec while the accommodating the vertical growth of inner TF coil conductor of ~ 1cm and the electromagnetic forces. The TF flex-bus was successfully manufactured using EDM process and tested for 200,000 cycles which is more than three times the pulse cycle requirement. All of the TF flex-bus has been procured. In FY 2013, the center-stack TF bundle fabrication has started. NSTX technical staff have also set up in-house manufacturing facilities for soldering the TF cooling tubes and manufacturing of the OH and TF coils. The Inconel Casing was delivered in December 2012. Requisition for the Inner PF coils and structure was placed. The inner TF bundle manufacturing stages are shown in Fig. FD-3. After sandblasted, primed and insulated, the insulated inner TF conductors are installed into the quadrant mold for Vacuum Pressure Impregnation (VPI) with CTD-425 (Cyanide-Ester Blend Hybrid) as shown in Fig. FD-3. The first quadrant was successfully VPI'd in early March 2013 and it passed the electrical test. The individual Quadrants are VPI'd was completed in July 2013 and the full TF bundle VPI is being prepared to be completed in September 2013 as shown in Fig. FD-3 (a) and (b). The winding of the OH coil over the full TF bundle will be performed followed by a VPI of the entire TF-OH center-bundle. In parallel, the Center-Stack Casing with the welding of the 700 inconel studs for mounting the carbon tiles to the walls is being prepared as shown in Fig. FD-3(c). The carbon tiles (PFC) will then be mounted with surface diagnostics to the casing walls. Once the inner poloidal field (PF) coils arrive, they will also be joined to the casing as shown in Fig. FD-2. The completed OH/TF bundle and CS casing will be transported to the NSTX-U for final assembly. Delivery of the completed CS Assembly is scheduled for Spring 2014.

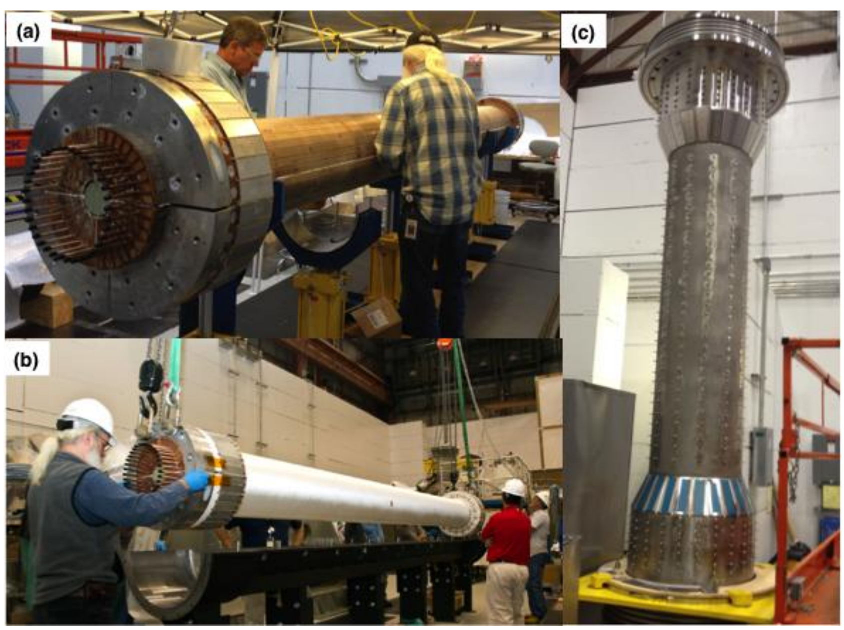

Fig. FD- 3. (a) Inner TF bundle assembled from four quadrant sections. (b) TF bundle with fiberglass ground insulation being lowered into the VPI mold. (c) Center-stack casing with tile studs.

NSTX-U Device Structural Enhancements

In order to handle the anticipated 4x greater electromagnetic forces for NSTX-U, the vacuum vessel and associated magnetic field coil support structures must be enhanced accordingly. During FY 2013, most of the procurements for the component fabrication of the umbrella structure reinforcements, PF 2/3 support upgrade hardware and PF 4/5 support upgrade hardware were completed. Two new outer TF legs were fabricated and installed to replace the ones with the cooling water leak and electrical insulation issues. The outer TF leg support upgrades were also fabricated and being installed. The TF-VV clevises to better support outer TF legs were welded onto the vessel. The new umbrella legs were installed on the machine. The vacuum vessel leg attachment connections were modified to clear the clevises. In addition, since the plasma disruption forces are also expected to increase by a factor of 4, the internal passive plates were reinforced by replacing the stainless steel attachment hardware with Inconel versions. The support structure enhancement activities are nearly complete. Some photos of the support structure enhancements are shown in Fig. FD-4.

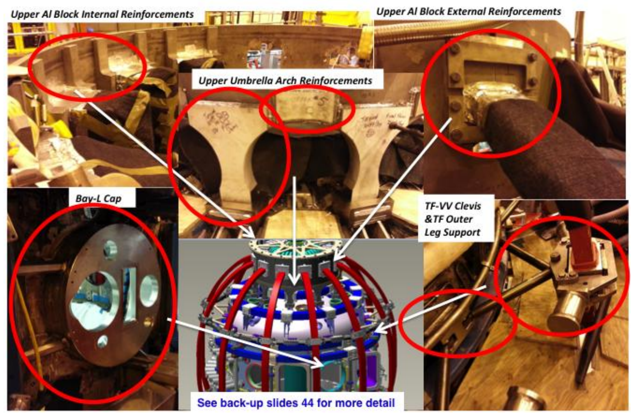

Fig. FD-4. NSTX-U Device Structural Enhancements.

Second Neutral Beam Injection System Upgrade

The 2nd NBI upgrade scope is to add a complete, functional second beam-line (BL) to NSTX-U at aiming tangency radii of 110, 120 and 130 cm compared to 60, 70, 80 cm for the 1st Present NBI. This task largely utilizes the existing TFTR NBI infrastructure. The 2nd NBI tasks include the TFTR NBI BL tritium decontamination, refurbishments, sources, relocation, services, power and controls, and NTC arrangements, as well as Vacuum Vessel modifications, the NBI and TVPS Duct, and NBI armor. After completing the decontamination and component refurbishment, the 2nd NBI BL relocation began in FY 2013.

The BL box and lid were moved into the NTC and reassembled as shown in Fig. FD-5. The installation of the support structure and alignment of the BL has been completed. The refurbished 90 inch flange, ion dump, calorimeter, and bending magnet were installed on the BL. The source platform has been fully decontaminated and installed. The latest 2nd NBI view can be seen in the recent (September 2013) test cell aerial view shown in Fig. FD-1. Relocation also included moving three High Voltage Enclosures (HVEs) from the TTC Basement into the NTC which was completed in the second half of FY 2013.

The BL services include deionized water, vacuum, Liquid Nitrogen (LN) and Liquid Helium (LHe) cryogenics, SF6, feedstock gas, and pneumatics. Progress includes the fabrication and installation and completion of the LN manifolds in the NTC and on the BL, as well as fabrication of LHe lines and valve manifolds in the NBI shops. Penetration drilling and installation of LHe manifold system piping to the test cell is complete. All of the LN and LHe cryogenics piping installations have been completed. Leak checking of cryo lines is in progress with all internal lines completed. The deionized water system installation subcontract was awarded and work has been completed. Final welds and testing is imminent. The deionized water pump subcontract to upgrade the ion source and ion dump water pumps is on order.

Power system progress includes the preparation of specification and purchase of all major cabling required to fully connect the N4ABC power systems from the TFTR area to the NTC location via the TFTR Test Cell Basement. The major high voltage cabling triax has been manufactured, delivered, and successfully tested on site. A power cable and tray procurement package has been prepared and awarded for installation of tray and cable pulls to connect the power supplies. This subcontract will begin installation work on or about October 1, 2013 (FY 2014). The penetrations required in the NTC West wall have been completed for all of the power cabling.

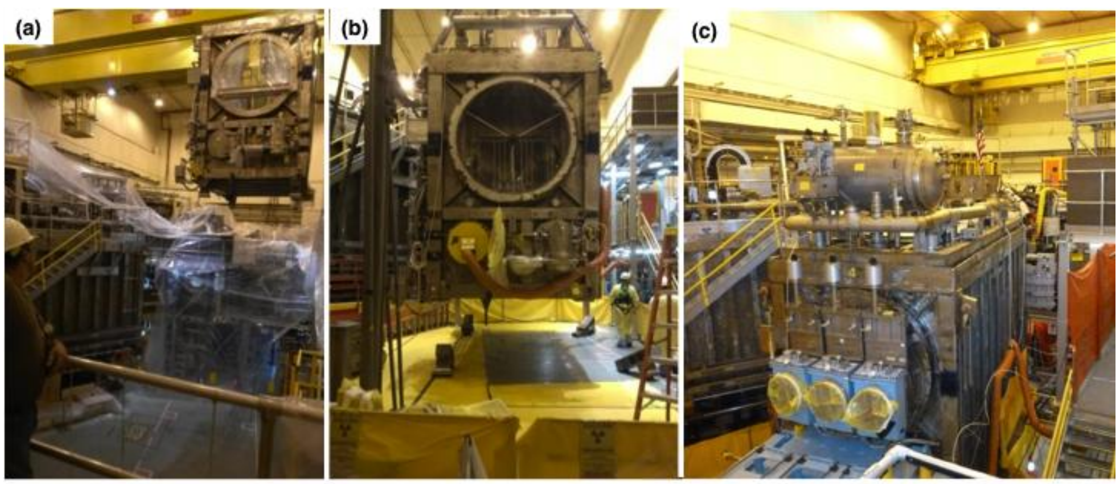

Fig. FD-5. (a) 2nd NBI Beam Box being lifted over NSTX-U (b) Beam Box placed in its final location and aligned (c) Beam Box being populated with components.

Major progress on controls is noted. Racks have been installed in the gallery area and populated with chassis electronics to control both BL1 and BL2. The Local Control Centers for N4ABC have been addressed to add NI electronics and LabView software controls. Power supply controls have been updated in the Switchyard, Surge Rooms, Mod/Regs, and Decels. Three Gradient Grid Dividers have been fabricated for the Mod/Regs and installed. Progress continues on LCCs to modify them for National Instruments interface and LabView control system. LabView programming is in progress.

Fabrication of the NBI armor to be located inside the VV is complete. The carbon tiles have been machined. The backing plates have been fabricated and the assembly and brazing are also

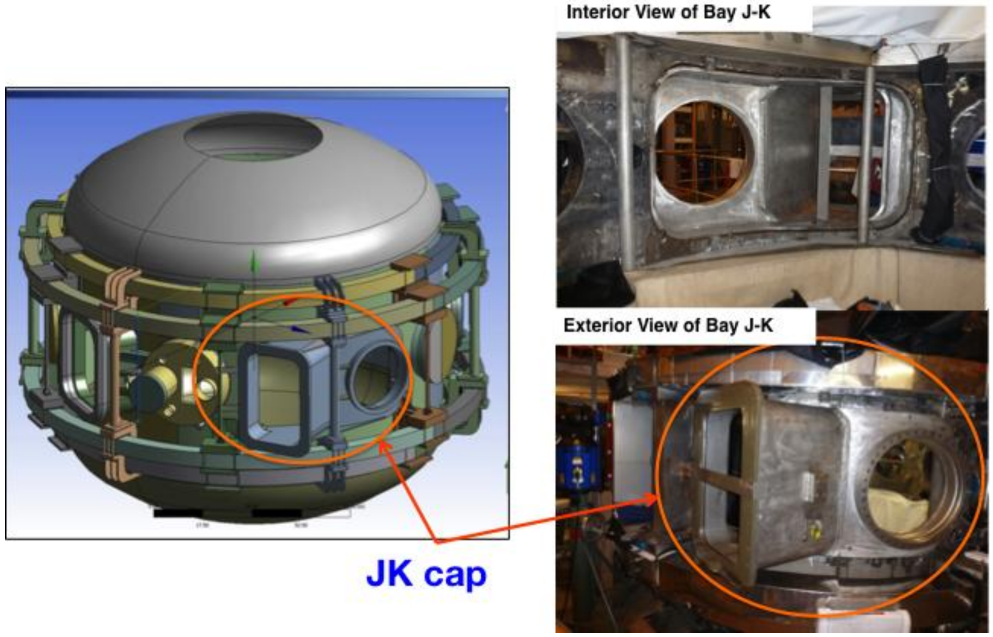

Fig. FD-6. Bay J-K cap for the 2nd NBI tangential injection port schematic and pictures on NSTX-U.

completed. Final structural welding is complete in the VV. Assembly and installation of the NBI armor quadrants is imminent. The Bay H port cover modification for the armor is complete.

The Duct and VV modification at Bay JK has been completed. A new Bay JK "bay window" or cap was required for accommodating the strongly tangential aiming angles. The NBI vacuum vessel modification is shown in Fig. FD-6. The opening for the new caps was cut on the VV and the welding of the new Bay JK and Bay J caps onto the VV has been completed. The JK reinforcement installation in the VV is complete. The sFLIP diagnostic port reinforcement near Bay J has been completed. The rectangular bellows for the NBI duct has been fabricated and leak checked. The major flanges and structures for the duct have been fabricated and welding is complete. Shield installation is in progress. Since the original vacuum vessel duct and the torus vacuum pump system (TVPS) located in Bay L were removed, the TVPS was incorporated into the NBI transition duct for NSTX-U. The Torus Vacuum Pump System (TVPS) ducts have been fabricated. All procurements for the duct and TVPS are delivered. The large circular bellows and the rectangular bellows flange have been procured, manufactured, and received. Leakchecking of the duct components is in progress. Assembly and duct installation is planned first quarter FY2014. The Torus isolation Valve for the BL has been received and installed on the BL. The NTC required extensive rearrangements to create the floor space for the BL. All rearrangements have been completed. New platforms have been installed. The TVPS racks have been moved to the gallery area.

With successful completion of the above tasks, preoperational testing of BL systems and N4ABC power and controls will be required to commission subsystems and confirm readiness for operations. This testing will begin in FY2014 and flow into startup operations based on project baseline schedules and funding profiles. NB Ion Source installation is planned in June 2014 with low level and beam conditioning in July. CD4 operation of beams into armor is expected in August of 2014 but depends on and requires ACC review and test cell access restrictions for beam conditioning.

TF and OH Power Systems for NSTX Upgrade

NSTX Upgrade requires an increase in the TF field. Thus the TF feed was designed to a rating of 1kV, 129.8kA for 7.45 seconds every 2400 seconds. Also the design is such that the pulse period can be reduced to 1200 seconds in the future by providing additional power cabling in the power loop. The NSTX rating was 1kV, 71.2kA for 1.3 seconds every 300 seconds. To meet the upgrade requirements, four additional branches are added to the existing four branches. The existing four TF Safety Disconnect Switches (SDS) will be continued to be used with two parallel branches through each SDS. Extensive power cabling reconfiguration has been undertaken in the TF wing of Field Coil Power Conversion (FCPC) building. Ninety-six (about 6200 feet) TFTR-era cables are being disconnected, removed, and scrapped. Hundred of cables (about 5800 feet) are to be pulled and installed. Also additional cables from the Transition area to the NSTX test cell are to be provided for TF circuit. So far (as of September, 2013), about 90% of the installation work is completed.

New accurate fiber optic DCCTs (+/-150kA) will be provided to measure the TF current. The PF1A circuit is redesigned without the ripple suppression reactors, which were used with the previous PF1A coils. These ripple reduction reactors (the original PLT TF coils) will now be used in the upgraded OH circuit as the branch DC current limiting reactors (CLR) and the power cabling will be modified as needed. The existing OH power supply is designed to have the capability of 6kV, +/-24kA and meets the new requirements based on PSCAD analysis.

Rectifier Control System Upgrades

The D-site rectifiers **(**Transrex AC/DC Convertors of the NSTX Field Coil Power conversion System (FCPC) **)** provide a pulsed power capability of 1800 MVA for 6 seconds every 300 seconds. The modular converter concept of 74 identical, electrically isolated 6-pulse "power supply sections" was originally used on TFTR and 68 of them were then adapted to NSTX-U which has a more complex topology including anti-parallel and three wire configurations. In order to extend the useful operational life of this system, which has remained largely unchanged since 1984, it is necessary to replace key elements of the FCPC controls. The elements to be redesigned are the Firing Generators, the Fault Detectors, the electromagnetic relays which provide the interlock logic in the "Hardwired Control System (HCS)", and the HCS to Fault Detector interface. The rationale for this refurbishment is based on the facts that many parts are nearing end-of-life due to age and wear, replacement parts are rare or unavailable, and that performance can be improved to the NSTX-U requirements using more modern control equipment. Precise control of thyrister firing angles by the FCPC firing generators has always been necessary for NSTX operations, and becomes more critical for the new 8-parallel, 130kA TF system configuration. In addition, the ability to separately control the "A" and "B" sections of each power supply unit allows for more efficient utilization of the available sections. The new Firing Generator (FG) is the highest priority task [see Milestone F(13-1)] and, compared to the original FG, will deliver firing pulses with far greater resolution, precision, and repeatability, and can receive and process separate commands to the A and B sections as noted above. The prototype FG has been fully tested in a Transrex rectifier, and production units are being fabricated. The new Fault Detector (FD) provides the same functionality as the existing FD in terms of faults detected, but includes an improved external interface compatible with the present NSTX data acquisition system. The implementation of the new FD is considered a lower priority than the FG, but testing of the FD prototype has been completed in conjunction with the new FG in a Transrex rectifier. The final design of the new FD will be completed and documented, but a new set of FD's will not be assembled and installed at this time. The electromagnetic relay logic in the Hardwired Control System (HCS-Relays) is being replaced with PLC-based interlock logic. This will provide enhanced reliability via the elimination of old electronic devices, and will provide an interface to the NSTX data acquisition system which will indicate the status of all interlock logic criteria. A further improvement to the system involves the implementation of PLC compatible I/O modules to each Transrex power supply, interfacing the new FD, and connecting to the PLC in the HCS control board (HCS-FD). This feature provides a redundancy to the existing HCS fault logic, and includes the ability to see the status of each individual power supply in the loop.

Progress in the NSTX-U Science Tool Development

HHFW Upgrades - NSTX-U will have roughly twice the current and magnetic fields as NSTX. The forces on the current straps of the HHFW antenna (see Fig. FD-7) will increase by a factor of roughly four, and the reaction forces at the center conductor of the feed-through become unacceptable. Addition of a compliant section into the center conductor allows the end of the current strap to move without imparting a load to the vacuum feedthrough. A compliant center conductor was designed, using results from a finite element analysis of the antenna to define the motion of the end of the strap, electrostatic analysis to minimize the electric field strength at the center conductor, and analyses of mechanical stress and Joule heating. A successful conceptual design review showed that the compliant conductor satisfied all of the design requirements. An evaluation on the RF test stand is necessary to confirm that the voltage standoff will match the analytical predictions. Prototypes of the compliant center conductor were procured [Fig. FD-7], and two antenna boxes were removed from NSTX for installation into a refurbished RF test stand. The modified test

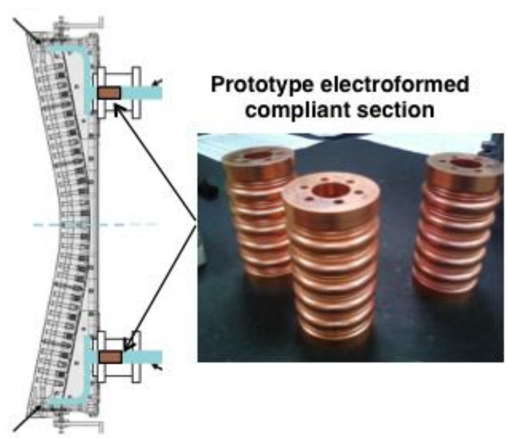

Fig. FD-7. HHFW antenna and the prototype electroformed compliant section.

stand contains two antenna boxes, allowing for effects of mutual inductance to be examined. The straps are a single-feed configuration, which is sufficient for investigating voltage breakdown. Testing on the strap is expected to begin before the end of FY13.

ECH/EBW System Design

The NSTX ECH/EBW System design for NSTX-U has begun to support discharge initiation and current drive during plasma startup. The status of the physics design of the ECH and EBW system for plasma start-up and current drive in advanced scenarios is described in the FY2013 Research Milestone R(13-3) report. Here the attributes of the physical system are outlined. It is planned to be a 28GHz RF system capable of injecting approximately 1.5MW into the plasma via a single antenna installed on NSTX-U. It will be configured around a 2MW gyrotron to be designed by Tsukuba of Japan, with auxiliary components provided by MIT, PPPL and outside vendors. The gyrotron design is an engineering extension of a successful 1 megawatt design produced for Kyushu University. The target installation date for the NSTX-U ECH system is the end of FY16.

Macro-stability Tools

While NSTX-U is a modification of NSTX, changes to the device conducting structure (e.g. new 2nd NBI port structure), mid-plane RWM control coils, and equilibria require re-computation of $n = 1$ active RWM control performance using proportional gain, and RWM state space control. The upgrade also adds new capability, such as independent control of the 6 RWM coils. This new capability, combined with the upgrade of the RWM state space controller will also allow simultaneous $n = 1$ and $n = 2$ active control, along with $n = 3$ dynamic error field correction. Finally, the active control performance of the proposed off-mid-plane non-axisymmetric control coils (NCC) to be evaluated [see the MHD section]. A significant increase in controllable β_N is expected with the RWM state space control in NSTX-U, as was found for NSTX.

Disruption Mitigation Systems

A key issue for ITER, and the tokamak/ST line of fusion devices in general, is the avoidance and mitigation of disruptions. Most of the disruptions are expected to be mitigated by massive gas injection (MGI). In support of the planned Massive Gas Injection Experiments on NSTX-U, the University of Washington has designed, fabricated, and built the proto-type of a new design Electromagnetic Massive Gas Injection Valve for installation on NSTX-U. The valve is similar in design to the MGI valve design that is being considered for ITER. Both off-line tests as well as experiments on NSTX-U using this valve design will help inform the final design of these valves for ITER. The valve is at present undergoing off-line tests at the Univ. of Washington. After these tests are completed later this year, three such valves will be built for installation on NSTX-U. Prior to fabricating the proto-type valve, a design peer review was held at PPPL on 6 March 2013 to ensure all systems associated with this valve are compatible with NSTX-U procedures and policies.

CHI Gap Overhang Tiles

The base line PFCs for the initial NSTX-U operation is graphite tiles. Because of the increased plasma heat loads due to the increased NBI heating power and pulse duration which projects to about 10x divertor heat load, it was decided to enhance the protection of the CHI Gap. "CHI Gap" is the region between the NSTX-U inner and outer vacuum vessels, above or below the CHI insulators. In particular, because of the new PF 1C coil which is placed in the CHI Gap region, an improved protection was deemed necessary. Hence, as shown in Fig. FD-8, the graphite tiles on both the inner and outer divertors will be extended downwards, shielding these components from plasma contact. This narrower and deeper CHI gap will protect the vessel and PF-1C coil from excessive heat flux and protect the plasma from metal contamination, while continuing to provide the capability for CHI operations. The overhung tiles were being fabricated in FY 2013.

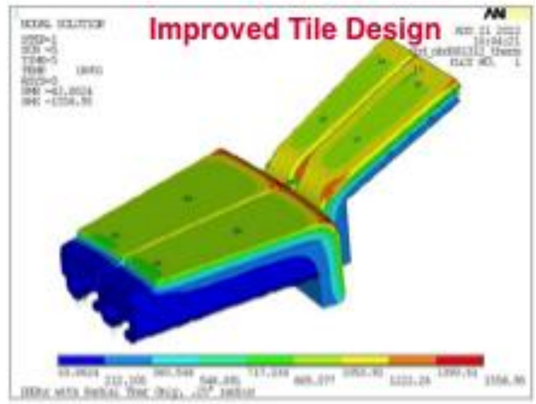

Fig. FD-8. New CHI gap overhung tile design to provide necessary protection from ~ 10x higher divertor heat loads.

Lithium Granule Injector for ELM Control

The lithium granular injector for ELM pacing which was successfully demonstrated on EAST will be available for NSTX-U. The Granular Injector (GI) that has been developed uses a dropper to feed lithium spheres to a rotating impeller that injects the spheres into the edge of a fusion plasma. The use of pre-formed solid lithium pellets however limits their size to one diameter and for a given dropper load and makes us depend on a manufacturer with a proprietary fabrication process. With these concerns in mind, a Liquid Lithium Pellet Dripper (LLPD) is being developed in FY 2013 to address these issues with the goal of using the lithium spheres to trigger small ELM's to control impurity build up in the plasma. The LLPD consists of a reservoir of liquid lithium, T > 181^{o}C that is forced through a small orifice. As the liquid lithium leaves the orifice, the Rayleigh instability allows a finite volume of liquid lithium to be pinched off. Surface tension then pulls the lithium into a sphere. The sphere travels down a guide tube and cools forming a lithium pellet. The greatest advantage of this system is that with careful selection of parameters it should be possible to control the frequency and also the size of the drops. Though lithium is the liquid metal to be used on NSTX-U, initial studies in the lab have been performed with Wood's metal. Using argon gas to drive the liquid metal through the orifice, the drop size and frequency are a function of the gas pressure. Wood's metal measurements were performed at PPPL, while the LLPD was run with lithium at the CPMI labs at the University of Illinois at Urbana-Champaign. The frequency and drop diameter have a strong correlation with the density of the liquid metal as well as the pressure. With pressures up to 1 atmosphere, pellets were produced up to frequencies of 1 kHz in Wood's metal and 2 kHz in lithium. Pellet size also varies with pressure and density. Higher pressures produce smaller pellet sizes down to 0.6 mm diameters. Am electromagnetic (EM) drive is being explored to replace the gas driven system, based on moving the liquid metal via a J×B force. The calculations show that a current of several hundred amps will be needed for a magnetic field of 0.3 T to adequately drive the liquid metal. Modulating the current can control the frequency, and the amplitude determines the size of the pellets being produced.

Lithium Evaporator and Upgraded Lithium Coating Systems

With encouraging results in NSTX, the NSTX lithium evaporator (LITER) system is planned to be available for NSTX-U from Day 1. To complement the LITER system which is designed to coat the lower divertor region with lithium vapor between-shots ("slow" coating), a new Li evaporator design is being developed in FY 2013 for an upper aiming evaporator to cover the upper divertor region. A conceptual design has been developed using electron beam heating to promptly evaporate Li to the upper vessel. This has advantages of requiring no shutters after evaporation. Since the evaporator is outside of the plasma volume, the discharge can commence without retracting the evaporator. This reduces the time between the end of the evaporation and the start of the discharge ensuring minimal passivation of the fresh lithium.

Laboratories for Material Characterization and Surface Chemistry

NSTX-U is collaborating with two new laboratories established at PPPL in collaboration with Princeton University dedicated for materials characterization and surface chemistry experiments. The Surface Science and Technology Laboratory is equipped with three surface analysis systems and an ultrahigh vacuum deposition chamber. Substrates for vapor deposition of metal films can be heated and cooled from 85 – 1500K using liquid nitrogen cooling and resistive and electron-beam heating. These systems have a variety of surface diagnostics, including high resolution electron energy loss spectroscopy (HREELS), which is capable of probing both optical and vibrational excitations over a wide range of 0 - 100 eV with an electron energy resolution of 3 meV, alkali ion-scattering spectroscopy (ALISS), and angle-resolved X-ray photoelectron spectroscopy (XPS). Another instrument has XPS, low energy ion scattering (LEIS), and reflection high-energy electron diffraction (RHEED) capability for thin film growth studies. In this laboratory, the time evolution of the chemical composition of lithium surfaces exposed to typical residual gases found in tokamaks was recently measured. Solid lithium samples and a TZM alloy substrate coated with lithium have been examined using XPS, temperature programmed desorption (TPD), and Auger electron spectroscopy (AES) both in ultrahigh vacuum conditions and after exposure to trace gases. Lithium surfaces near room temperature were oxidized after exposure to 1-2 Langmuirs (1L=1x10-6 torr s) of oxygen or water vapor. The oxidation rate by carbon monoxide was four times less. An important result of the measurements for NSTX-U is that lithiated PFC surfaces in tokamaks were found to be oxidized in about 100 s depending on the tokamak vacuum conditions which is much less than a typical time duration between the tokamak plasma shots. A second laboratory, the Surface Imaging and Microanalysis Laboratory, contains a high-performance field emission Auger and multi-technique surface microanalysis instrument with a field emission electron source and lateral resolution of 30 nm for elemental analysis of surfaces of samples on the micro and nano scale.

CHI upgrades

NSTX-U will have numerous important upgrades for transient CHI that will significantly increase the CHI current start-up magnitude. These upgrades will be implemented over a period of three years. In FY 2014, the Univ. of Washington group has formulated a detailed plan for implementing these systems in a systematic manner that would allow NSTX-U to demonstrate full non-inductive start-up and current ramp-up during the next five years. The group conducted a study of the CHI systems and diagnostics required for CHI start-up on NSTX-U in FY2015, and identified additional CHI-related upgrades to diagnostics that are being installed on NSTX-U. The needs for gas injectors and neutral pressure gauges to support all of NSTX-U plasma operations was examined, as a result of which new ports were installed on the NSTX-U vessel.

NSTX-U Diagnostic System Preparation

The NSTX-U diagnostic planning meeting was held in July 2011 and also in July 2012. Since the 2012-2016 non-laboratory NSTX-U diagnostic grant recipients were decided in FY 2012, they represent a significant fraction of the planned NSTX-U diagnostic capability. The diagnostics which were operational in FY 2011 are generally expected to be available for the NSTX-U operation unless otherwise noted. A major effort to realign the MPTS system is described in the diagnostic milestone report D(13-1). The design work on the new high-Kf FIR scattering system by UC Davis is reported in the FY 2013 research milestone R(13-2) report. A list of the existing diagnostic systems which are expected to be available for NSTX-U within two years of operation is shown in the Table FD-1.

MHD/Magnetics/Reconstruction
- Magnetics for equilibrium reconstruction
- *Halo current detectors*
- *High-n and high-frequency Mirnov arrays*
- Locked-mode detectors
- RWM sensors

Profile Diagnostics
- MPTS (42 ch, 60 Hz)
- T-CHERS: $T_i(R)$, $V_\phi(r)$, $n_C(R)$, $n_{Li}(R)$, (51 ch)
- P-CHERS: $V_\theta(r)$ (71 ch)
- *MSE-CIF (18 ch)*
- *MSE-LIF (20 ch)*
- *ME-SXR (40 ch)*
- Midplane tangential bolometer array (16 ch)

Turbulence/Modes Diagnostics
- *Poloidal Microwave high-k scattering*
- *Beam Emission Spectroscopy (48 ch)*
- Microwave Reflectometer,
- *Microwave Polarimeter*
- Ultra-soft x-ray arrays – multi-color

Energetic Particle Diagnostics
- *Fast Ion D_α profile measurement (perp + tang)*
- Solid-State neutral particle analyzer
- Fast lost-ion probe (energy/pitch angle resolving)
- Neutron measurements

Edge Divertor Physics
- Gas-puff Imaging (500kHz)
- Langmuir probe array
- Edge Rotation Diagnostics (T_i, V_ϕ, V_{pol})
- *1-D CCD H_α cameras (divertor, midplane)*
- *2-D divertor fast visible camera*
- Metal foil divertor bolometer
- AXUV-based Divertor Bolometer
- IR cameras (30Hz) (3)
- *Fast IR camera (two color)*
- Tile temperature thermocouple array
- *Divertor fast eroding thermocouple*
- Dust detector
- Edge Deposition Monitors
- Scrape-off layer reflectometer
- Edge neutral pressure gauges
- *Material Analysis and Particle Probe*
- *Divertor VUV Spectrometer*

Plasma Monitoring
- FIReTIP interferometer
- Fast visible cameras
- Visible bremsstrahlung radiometer
- *Visible and UV survey spectrometers*
- *VUV transmission grating spectrometer*
- *Visible filterscopes (hydrogen & impurity lines)*
- Wall coupon analysis

New capability, Enhanced capability

Table FD-1. Planned NSTX-U Diagnostic Systems within the first two years of operations.

We note that at least half of those diagnostic systems have strong collaboration components. While most of the diagnostic systems are inactive in FY 2013, we shall briefly describe some noteworthy diagnostic activities particularly by the NSTX-U collaborating institutions in FY 2013 in the following sections. The NSTX-U diagnostic installation activities are expected to take place in FY 2014.

Fast Te profiles using the ME-SXR diagnostic

A new software code was developed by the Johns Hopkins Group using neural network processing to reconstruct the electron temperature profile from Multi-energy Soft X-ray (ME-SXR) data as shown in Fig. FD-9. This data will be obtained with a tangentially viewing core ME-SXR system and an edge ME-SXR system, with ~2cm and < 1cm spatial resolution respectively, which will be installed and ready for day-1 operation on NSTX-U. Initially, synthetic X-ray data was used to test the sensitivity of the reconstructions to changes in the plasma electron temperature, density, and impurity content. It was discovered that 2-3 SXR arrays with different filters were sufficient to reconstruct changes in electron temperature for typical NSTX-U plasmas with an rms error of ~5-7%. However, plasmas which exhibit large changes in impurity concentrations, such as the introduction of a high-Z flake, large amounts of dust, or deliberate seeding of high-Z impurities, demonstrated larger rms error (>10%) and may require additional constraining measurement information such as from the spatially resolving JHU Transmission Grating Imaging Spectrometer (TGIS). Inclusion of synthetic TGIS data reduced the rms error of the reconstructed profiles by ~40-50%. Similarly, the addition of other diagnostic measurements relevant to the deconvolution of the Te, ne, and ni contributions to the X-ray emission such as the line-integrated density measurement from FIReTip further reduced the reconstruction uncertainty. One advantage of the neural network algorithm compared to emissivity model-based analysis is the ability to incorporate a wide range of disparate sources of data without requiring precise cross-calibrations.

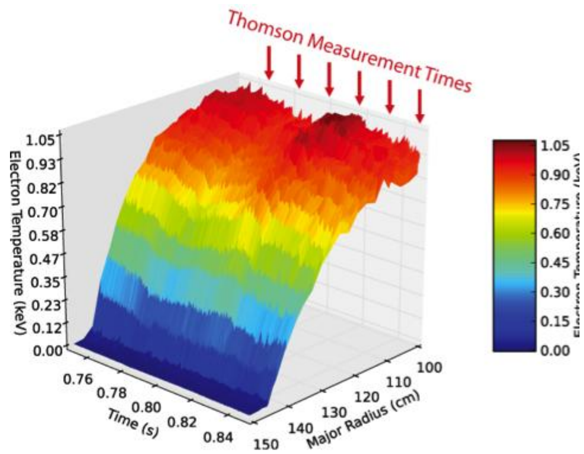

Fig. FD-9. Time-evolving T_e profile found with a neural network applied to optical ME-SXR data. The red arrows indicate when the Thomson scattering diagnostic makes a measurement.

Motional Stark Effect – Collisional Induced Fluorescence

With a doubling of the magnetic field as part of the NSTX upgrade the Motional Stark Effect measurement based on Collisionally Induced Fluorescence (MSE-CIF) collection optics can be optimized to increase the throughput. With the higher field this will change the optimal aperture width and polarization fraction for maximizing the signal-to-noise. We will use our numerical models and optical design code to re-optimize the aperture width. The MSE-CIF system will starts with 18 sightlines but the real-time capability will be also implemented as described. In FY 2013, all the computer hardware for rt-MSE has been tested and working according to plan. Acquisition time is sufficiently fast to meet the real-time requirements. We are in process of testing and optimizing the algorithms for rt-MSE.

Motional Stark Effect – Laser Induced Fluorescence

The Motional Stark Effect measurement based on Laser Induced Fluorescence (MSE-LIF) diagnostic will provide measurements of the field line pitch angle profile without requiring injection of the heating neutral beam needed for the present MSE system on NSTX-U which is based on collisionally induced fluorescence (MSE-CIF). It will therefore provide critical data for measuring RF-driven current in NSTX-U without the competing effect of current driven by the heating neutral beam. Also, direct reconstruction of the total plasma pressure profile should be possible from its capability to make local measurements of the total magnetic field in the plasma. Combining this measurement with the comprehensive thermal profile measurements already available on NSTX-U, the fast-ion pressure profile can be inferred and compared to prediction to determine the influence of Alfvén Eigenmodes and other MHD activity on fast-ion confinement. Furthermore, the data from the two MSE systems, MSE-CIF and MSE-LIF, can be combined to calculate the radial electric field profile, an important element in plasma transport research. In collaboration with researchers from Nova Photonics Inc., the installation and commissioning of the first three channels of the Motional Stark Effect measurement based on Laser Induced Fluorescence (MSE-LIF) was successfully completed in August 2011. For NSTX-U Day-1 operation, 20 sightlines of the MSE-LIF system will be available. In FY 2013, procurement has been focused on adding additional MSE-LIF channels. All the detectors and filters have arrived for half the channels. The new optical fibers have ben ordered and we are expecting the first batch to arrive early FY 2014.

Beam Emission Spectroscopy

The Beam Emission Spectroscopy (BES) diagnostic on NSTX-U, based upon observing the Dα emission of collisionally-excited neutral beam particles, will enable direct spatially-resolved measurements of longer wavelength density fluctuations in the plasma core, providing valuable insights into the suppression of ion turbulence and the attainment of near-neoclassical ion confinement on NSTX-U in collaboration with the University of Washington-Madison. There were two main activities by the UW group. First, BES detectors, data acquisition, and instrument control capabilities will expand from 32 to 48 detection channels. The additional channels will expand the utilization of BES sightlines for experiments and reduce the need to reconfigure delicate fibers. In FY2013, the UW group fabricated 16 new detectors and assembled detector system at UW, delivered the first 8-channel detector system to PPPL, and procured the data acquisition system. In FY14, the UW group will deliver the second 8-channel system and integrate new components in the existing BES infrastructure at PPPL. The second BES upgrade activity is the 2D reconfiguration for boundary measurements. The UW group and PPPL engineers are reconfiguring the outer BES optical assembly for 2D measurements in the NSTX-U boundary region, including pedestal and SOL. The 2D measurements will enable observations of turbulent eddy motion and flow fields for more sophisticated analysis of turbulent dynamics. In FY13, the UW group performed the optical system analysis for BES sightlines in the 2D configuration. In FY14, the UW group and PPPL engineers will fabricate the 2D optical assembly and reconfigure fibers for 2D measurements.

Microwave Polarimeter Magnetic Fluctuation Diagnostic

UCLA has successfully tested the 288 GHz polarimeter for NSTX-U on DIII-D. This was the thesis project for UCLA graduate student J. Zhang. The polarimeter was positioned near the midplane of DIII-D, viewing along the major radial direction, with a tile mounted on the inner wall to reflect the beam. Run time was dedicated to testing the polarimeter over a wide range of conditions. Synthetic diagnostic modeling, which predicts the measured polarimeter phase to vary strongly with vertical position and BT, was used to plan the experiment. Vertical movement of the plasma (+- 20 cm) during each discharge was used to substantially vary the strength of the Faraday Rotation effect due to the horizontal component of B. Plasmas with a wide range of BT (0.75-2.0 T) were created to substantially vary the amount of elliptization resulting from the Cotton-Mouton effect. Calculations with the synthetic diagnostic code using EFIT equilibrium reconstructions of the experimental plasmas, in conjunction with density profiles measured via Thomson scattering, agree with the measured phase over a wide range of BT and plasma height. A discharge with BT = 0.75T (NSTX-U like parameters) is shown in Fig. FD-10, where the polarimeter phase is strongly dominated by the Faraday Rotation effect. A discharge with BT = 2.0 T shown the polarimeter phase is strongly dominated by the Cotton-Mouton effect. These results will be presented in an article recently submitted to Physics of Plasmas.

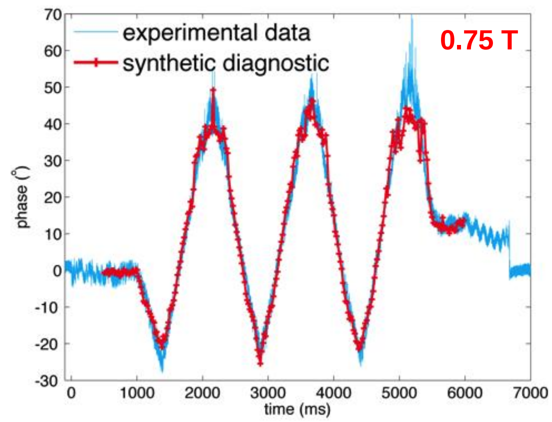

Figure FD-10: Measured polarimeter phase with a synthetic diagnostic calculation during height scan for discharges with B_T = 0.75 T.

Magnetics For Equilibrium Reconstruction, Boundary Control, and RWM Suppression

NSTX had a comprehensive set of magnetic diagnostics, including ~ 45 poloidal flux loops, ~ 60 magnetic field sensors for constraining equilibrium reconstruction codes such as EFIT, and 48 in-vessel sensors for measuring and controlling resistive wall modes. These sensor systems will be retained on NSTX-U, but with some significant improvements. In particular, the density of poloidal magnetic field probes flux loops in the divertor region will be increased, in anticipation of improving the magnetic reconstruction of snowflake divertor configurations. Furthermore, a second vertical array of poloidal field sensors will be installed on the center column, increasing the redundancy of these critical measurements. Finally, the density of poloidal magnetic flux loops in the vicinity of the divertor coil mandrels will be increased, allowing better reconstruction of the eddy currents induced in these support structures.

Boundary Physics Diagnostics

The NSTX/NSTX-U facility has been investing strongly in boundary physics related diagnostics in the past several years. There are over 20 boundary physics diagnostic systems on NSTX-U and additional ones are being readied. They includes Gas-puff Imaging (500kHz), Langmuir probe array, Edge Rotation Diagnostics (Ti, Vf, Vpol), 1-D CCD Ha cameras (divertor, midplane), 2-D fast visible cameras for divertor and overall plasma imaging, Divertor bolometer, IR cameras (30Hz), Fast IR camera (two color), Tile temperature thermocouple array, Divertor fast eroding thermocouple, Dust detector, Quartz Microbalance Deposition Monitors, Scrape-off layer reflectometer, Edge neutral pressure gauges, Material Analysis and Particle Probe, Divertor Imaging Spectrometer, Lyman Alpha (Lya) Diode Array, Visible bremsstrahlung radiometer, Visible and UV survey spectrometers, VUV transmission grating spectrometer, Visible filterscopes (hydrogen & impurity lines), and Wall coupon analysis. The preliminary testing of the MAPP probe in LTX was described as a part of the FY 2013 research milestone R(13-3) report.

Divertor Spectrometers and Two-Color Fast Infrared Camera

The LLNL collaboration in the divertor diagnostics area on NSTX focused on new and improved measurements for plasma-surface interaction studies with lithium-coated graphite and molybdenum plasma-facing component, as well as divertor impurity and plasma diagnostics. New capabilities included a new vacuum-ultraviolet divertor spectrometer (SPRED) that was brought from LLNL to NSTX-U to monitor carbon and molybdenum emission in the divertor for impurity and power balance studies. Another new capability intended to support the NSTX-U lithium program is a new near-infrared spectrometer for divertor molecular and atomic spectroscopy. To provide pilot measurements for radiative divertor control, a new optical Penning discharge chamber is installed in the lower divertor area to provide a way to monitor pressure of deuterium or or gaseous impurities (e.g., argon) that could be injected to increase divertor radiated power. Improvements were also made to other LLNL-supported diagnostics, notably the divertor Lyman-alpha and radiometer array, four one-dimensional filtered CCD arrays, divertor imaging spectrometers, and filterscopes. The goal was to provide routine quantitative emission measurements in the upper and lower divertor areas, as well as the inner outer walls.

Dual-ban high-speed IR Thermography

Another important divertor diagnostic recently developed is a two-color or dual-band device developed for application to high-speed IR thermography by ORNL. Temperature measurement with two-band infrared imaging has the advantage of being mostly independent of surface emissivity, which may vary significantly for an LLD as compared to that of an all-carbon first wall. In order to take advantage of the high-speed capability of the existing IR camera (1.6-6.2 kHz frame rate), a commercial visible-range optical splitter was extensively modified to operate in the medium wavelength (MWIR) and long wavelength IR (LWIR). This two-band IR adapter utilizes a dichroic beamsplitter which reflects 4-6 micron wavelengths and transmits 7-10 micron wavelength radiation, each with > 95% efficiency and projects each IR channel image side-by-side on the camera’s detector. The ORNL boundary physics group has designed and implemented a wide angle, 30 Hz infrared camera system on NSTX in FY 2011. A dual-band adapter was also implemented for variable surface emissivity due to lithium films. This system was designed as part of Princeton University student's first year experimental project. In addition, two eroding thermocouples near the PFC tile surface were installed and instrumented. These thermocouples, which have a design response time ~ 1 ms are intended to be used in the future for feedback control of PFC surface temperature in NSTX-U. Finally a set of 16 new "filterscope" chords were implemented. The gain control and data acquisition is done dynamically via PC. The units are capable of 100 kHz sampling speeds.

Divertor Imaging Radiometer

A Divertor Imaging Radiometer for spectrally resolved measurements of the radiated power by Johns Hokins will extend the multi-energy concept to divertor diagnostic by performing absolute measurements of the radiated power in tens of spectral bins covering the range from several eV to few hundred eV (VUV to XUV). The radiometer will use dual transmission gratings in conjunction with a direct detection CCD camera and will view the divertor from the outboard side, with vertically spaced lines of sight from the X-point region to the strike-point region. The instrument will have ≥2 cm space resolution and ≥10 ms time resolution. The proposed diagnostic will provide, for the first time in a tokamak, measurements of the spectrally resolved radiated power from the divertor and will enable determination of the radiating impurity type and charge state distribution over the range of temperatures expected for the NSTX-U divertor. This in turn will provide information on the radiating efficiency and transport of injected impurities for radiative divertor studies, as well as information on intrinsic impurities and associated radiation. In addition, the proposed diagnostic will be used to calibrate and validate the advanced divertor modeling codes used at NSTX-U. We will also study using the radiometer in conjunction with divertor emission modeling for a spectroscopic diagnostic of the electron temperature and cross-field particle transport in the divertor. Even if approximate, such measurements will be useful for the NSTX-U divertor research.

Energetic Particle Diagnostics

In the energetic particle (EP) research area, in addition to the perpendicular and newly implemented tangential fast ion D-alpha (FIDA) diagnostics, additional SSNPA (Solid-State Neutral Particle Analyzer) channels will be implemented since the scanning NPA was removed. Additional diagnostics for EP studies on NSTX-U include neutron rate counters, a scintillator-based Fast Lost-Ion Probe (sFLIP), installed on the vessel wall, and a new charged fusion product (CFP) profile diagnostic. The 16 channel reflectometry will be also installed for the energetic particle mode measurements.

Energetic Particle Distribution Diagnostics

On NSTX-U the radial fast ion profile is characterized through the FIDA and ssNPA systems. A vertical FIDA system measures fast ions with small pitch, corresponding to trapped or barely passing (co-going) particles. A new tangential FIDA system measures co-passing fast ions with pitch ~0.4 at the magnetic axis up to 1 at the plasma edge. Both FIDA systems have time resolution of 10 ms, spatial resolution ≈5 cm and energy resolution ≈10 keV. An upgraded solid-state Neutral Particle Analyzer (ssNPA) will provide energy-integrated measurement of trapped fast ions, with a lower energy threshold Emin~20 keV, from 5 radii. The ssNPA system will mainly work in current-mode to get fast time response. The sampling rate is ≈ 1 MHz. Two ssNPA channels will also incorporate pulse-counting mode capability to obtain energy spectra with ~10 keV energy resolution and ~10 ms temporal resolution. The fast-ion distribution function F is a complicated function of energy, pitch angle, space, and time. Successful reconstruction of F requires multiple measurements with a variety of techniques. The vertical FIDA system is a working diagnostic that has been producing valuable data for several years. Only minor changes to this diagnostic are proposed. The tangential FIDA system is patterned after the vertical FIDA diagnostic. Although it has not collected data during plasma operations, its installation is essentially complete. The SSNPA diagnostic will be displaced from its present location by the new beam-line. A new SSNPA diagnostic will be designed and installed to measure trapped fast ions at several radial locations.

Additional diagnostics for EP studies on NSTX-U include neutron rate counters, a new charged fusion product (CFP) profile diagnostic and a scintillator-based Fast Lost Ion probe (sFLIP), installed on the vessel wall. Neutron counters are strongly weighted toward the higher-energy portion of the distribution function, with no pitch dependence. For example, an increased count rate during HHFW injection is a straightforward indicator of the formation of tails in the fast ion distribution above the NB injection energy. The neutron diagnostic system is being upgraded to expand the system from two to four fission chambers. This upgrade will extend the dynamic range of the system and increase its fault tolerance. In addition, a new neutron source for absolute neutron rate calibrations is being purchased to replace a legacy TFTR-era source that is now too weak to be useful for in-vessel calibrations. Furthermore, a preliminary plan has been developed for long term stability measurements of the neutron system using a low emissivity neutron source.

Similarly to neutron counters, the CFP diagnostic in collaboration with Florida International University would provide direct measurements of the fusion reactivity. Because both protons and tritons are largely unconfined for NSTX-U parameters, fusion products are eventually detected outside the plasma volume. By knowing the magnetic field geometry, their orbit can be tracked back in the plasma. Such orbits are equivalent to curved sightlines for each detector, so that multiple signals can be inverted to infer a radial profile of the high-energy fast ions. A 4-channel CFP prototype has been tested in FY2013 on the MAST device (see the Energetic Particle Research Section). The 3 MeV protons and 1 MeV tritons produced by DD fusion reactions in MAST have been clearly observed. Given the successful observations on MAST, a proposal for a 16-channel system for NSTX-U is envisioned. A scintillator-based Fast Lost Ion probe (sFLIP) contributes to the NB characterization by providing energy and pitch resolved spectra of lost fast ions, e.g. from prompt losses, as the NB tangency radius is varied. sFLIP is being upgraded with a faster CCD detector capable of frame rates up to 100 kHz [10.46]. A set of photo-multiplier tubes is also being installed on sFLIP for energy and pitch integrated measurements at rates up to 250 kHz from 6-10 sub-regions of the sFLIP scintillator plate. Major modifications to the vacuum vessel and two large diagnostic ports to accommodate the new neutral beam lines for NSTX-U has resulted in displacement of the scintillator Fast Lost Ion Probe (sFLIP) from the port it had used during NSTX operations. A suitable alternate port for this diagnostic was identified, and that port was enlarged and substantially reinforced to accommodate the diagnostic. The diagnostic assembly itself will also be reconfigured to fit in the new location, while at the same time extending its range of pitch angle acceptance.

NSTX-U FY2013 Year End Report: Research Results

In FY2013, the NSTX-U research team contributed experimental data and analysis in support of the 2013 DOE Joint milestone*: "Conduct experiments on major fusion facilities, to evaluate stationary enhanced confinement regimes without large Edge Localized Modes (ELMs), and to improve understanding of the underlying physical mechanisms that allow increased edge particle transport while maintaining a strong thermal transport barrier. Mechanisms to be investigated can include intrinsic continuous edge plasma modes and externally applied 3D fields. Candidate regimes and techniques have been pioneered by each of the three major US facilities (C-Mod, D3D and NSTX). Coordinated experiments, measurements, and analysis will be carried out to assess and understand the operational space for the regimes. Exploiting the complementary parameters and tools of the devices, joint teams will aim to more closely approach key dimensionless parameters of ITER, and to identify correlations between edge fluctuations and transport. The role of rotation will be investigated. The research will strengthen the basis for extrapolation of stationary high confinement regimes to ITER and other future fusion facilities, for which avoidance of large ELMs is a critical issue"*

The NSTX-U contributions to the 2013 Joint Milestone are described in a separate report. Summary descriptions of the results of research milestones are provided below. Descriptions of additional selected research highlights are also provided.

FY2013 Research Milestone R(13-1): Perform integrated physics and optical design of new high-k_θ FIR system (Target - September 2013. Completed – September 2013)

Milestone Description: *Previous high-k scattering measurements in NSTX have identified ETG turbulence as one candidate for the anomalous electron thermal transport for both H and L-mode plasmas. However, a definitive connection between ETG turbulence and electron thermal transport could not be established since the previous high-k_r microwave scattering system was not able to measure the predicted peak power of the wavenumber spectrum of ETG turbulence. In collaboration with UC-Davis, a new high-k_θ FIR scattering system will be designed to make this measurement. Detailed physics and optical design of this scattering system will be performed. In particular, the spatial and spectral resolution and coverage of the scattering system will be optimized by integrating ray tracing, quasi-optical analysis and the launching and receiving optics design, based on predicted NSTX-U equilibrium profiles. The FIR laser for the scattering system will also be designed. Alignment and calibration schemes for both launching and receiving optics will be investigated. The above activities will lay a solid foundation for the implementation of this high-k_θ FIR scattering system on NSTX-U.*

Milestone R(13-1) Report:

The 280 GHz high-k tangential scattering system of NSTX will be replaced by a 604 GHz poloidal scattering system being developed by UC Davis for NSTX-U, thereby considerably enhancing planned turbulence physics studies by providing a measurement of the k_θ-spectrum of both ETG and ITG modes. The probe beam in this case will enter the plasma from a port on Bay G while a tall exit window located on Bay L will be employed to collect the poloidally-scattered beams and image them onto an array of 5-8 waveguide mixers. The reduced wavelength in the poloidal system will result in less refraction and extend the poloidal wavenumber coverage from the current 7 cm^{-1} up to > 40 cm^{-1}. Measuring the k-θ spectrum as well as k-r spectrum is crucial for identifying the source of turbulence since the 2D k-spectra driven by different instabilities have difference anisotropies. More importantly, the peak of the 2D k-spectrum has to be measured so that the turbulence amplitude can be experimentally correlated to observed plasma transport. The unique property of the new high-k scattering system design is that it uses only one microwave launching system but is able to achieve four scattering configurations, which are sensitive to different regions of the turbulence 2D k-spectrum owing to the large magnetic shear in NSTX-U. The probe beam and two scattering beams for the two toroidial scattering schemes are plotted in Fig. R13-1-1(a); here the probe beams are tilted

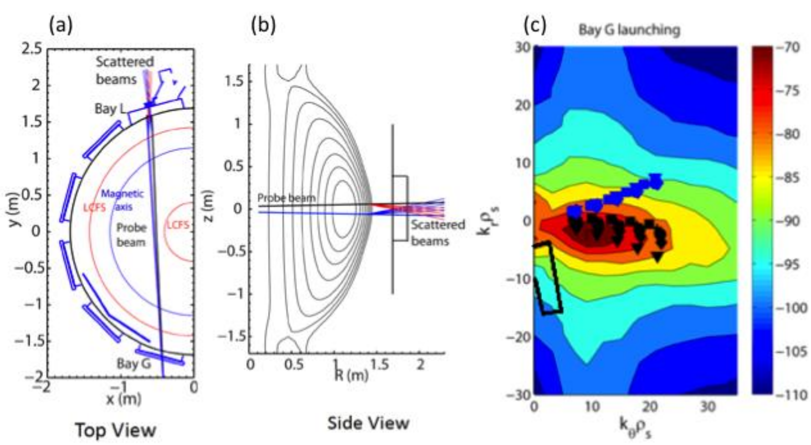

Fig. R13-1-1. High-k scattering system with two scattering schemes. (a) Schematic of the toroidal cross section of the high-k scattering beam geometry. (b) Poloidal cross sectional view of the beam geometry. (c) Regions in 2D k-r and k-θ space covered by two scattering schemes.

toroidally with respect to the scattered beams for +'ve and –'ve radial scattering. In the poloidal scattering arrangement of Fig. R13-1-1(b), the first scheme, plotted in blue, has scattered beams going upward in the positive Z direction (upward scattering) while the other scheme, plotted in red, has scattered beams going downward in the negative Z direction (downward scattering). A total of four scattering schemes is thus possible with different combinations of toroidal and poloidal tilt angles. It is noted that the proposed high-k scattering system mainly relies (as did the previous system) on the large magnetic shear in NSTX-U to provide radial localization. The simulation is performed using predicted profiles for a high-performance NSTX-U H-mode plasma. The anisotropy in the 2D k-spectrum of ETG turbulence, i.e. the existence of ETG streamers, can be determined by comparing the k-spectrum measured by the different schemes. Furthermore, a range of k-θ and k-r can be scanned by varying launching and receiving optics to map a wide range of 2D k-spectrum. An example of the scattering geometries and 2D k-spectrum of turbulence is shown in Fig. R13-1-1(c).

With respect to the laser source and optical hardware, UC-Davis has designed and fabricated a CO2-pumped FIR laser source that delivers >50 mW at 432.5 μm (693 GHz) for use as the initial illumination or launch source for the new high-kθ FIR scattering system on NSTX. On a longer time-scale, UC Davis is collaborating with Lancaster University and Beijing Vacuum Electronic Research Institute (BVERI) to develop a much higher power THz source which would replace the FIR laser. The source (either FIR laser or THz) will be located outside the NSTX test cell, and propagated to the Bay G launcher via low loss corrugated waveguides. Here, UC Davis is in the process of re-machining the previously employed PPPL waveguides for operation at higher frequencies, at a major cost savings to PPPL as compared to fabricating new waveguides. The high-k scattering signals will be collected and imaged through a new receiving window on Bay L by an array of high sensitivity mixers to be fabricated using the UC-Davis nano-CNC machining facilities.

FY2013 Research Milestone (R13-2): Investigate the relationship between lithium-conditioned surface composition and plasma behavior. (Target - September 2013. Completed – September 2013)

Milestone Description: *The plasma facing surfaces in a tokamak have long been known to have a profound influence on plasma behavior. The development of a predictive understanding of this relationship has been impeded by the lack of diagnostics of the morphology and composition of the plasma facing surfaces. Recently, a probe has been used to expose samples to NSTX plasmas and subsequent post-run analysis has linked surface chemistry to deuterium retention. However, with very chemically active elements such as lithium, more prompt surface analysis is likely required to characterize the lithiated surface conditions during a plasma discharge. In support of prompt surface analysis, an in-situ materials analysis particle probe (MAPP) will be used to investigate sample exposure under NSTX-U relevant vacuum conditions. The MAPP will enable the exposure of various samples to plasma followed by ex-vessel but in-vacuo surface analysis within minutes of plasma exposure using state of the art tools. The reactions between evaporated lithium and plasma facing materials and residual gases will be studied. The MAPP will be installed on LTX and the intershot analysis capability will be demonstrated. These inter-shot/time-dependent measurements will provide unique data for benchmarking codes for modeling particle control in NSTX-Upgrade.*

Milestone R(13-2) Report
Progress of MAPP: Materials Analysis Particle Probe

The Materials Analysis Particle Probe (MAPP) [R13-2-1] has been designed to allow the prompt analysis of plasma-facing components exposed to tokamak plasmas. During FY13, MAPP detector and software improvements were made at the Purdue University. The upgraded MAPP (MAPP-U) was returned to PPPL in June of 2013, and attached to a midplane port on the Lithium Tokamak Experiment (LTX) as shown in Fig. R13-2-1a.

Up to four different samples can be exposed to tokamak plasmas and analyzed individually with the MAPP-U diagnostics. In the present study, three samples were stainless steel, which matched the plasma-facing components (PFCs) of LTX, and the fourth was gold to use its well-characterized binding energy spectrum for calibration [R13-2-2]. When inserted into the LTX vessel, the MAPP-U samples were flush with the inner surface of the conducting shell (Fig. 13-2-1b). When the plasma was outboard-limited, MAPP-U samples also served as a limiting surface.

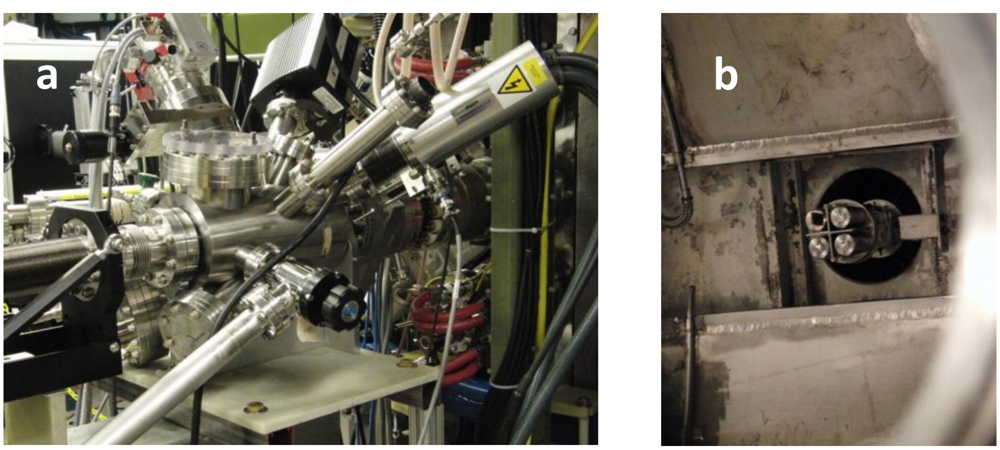

Figure R13-2-1. *(a) MAPP on LTX (b) View of sample holder inside LTX vacuum vessel*

Plasmas in LTX with uncoated stainless steel PFCs lasted around 10 ms and had maximum currents of about 12 kA, even after argon glow discharge cleaning (GDC). Approximately 15 grams of lithium were introduced into the bottom of each shell half, with little effect on the achievable plasma current or pulse duration. Argon GDC was then performed, resulting in a doubling of the plasma current to over 20 kA and the pulse length extending to the 25 – 30 ms range. The need for the GDC may be due to the limited PFC coverage with lithium, since helium GDC had to be performed between shots when lower lithium evaporation rates were used on NSTX [R13-2-3].

X-ray photoelectron spectroscopy (XPS) was used to analyze the samples before and after exposure to LTX plasmas. The improvement in plasma performance correlates with clear changes in the XPS data. Figure R13-2-2a compares XPS measurements before and after the MAPP-U samples were exposed to argon GDC. In the pre-exposure data, there are significant peaks correspond to carbon slightly below 300 eV (C(1s)), and oxygen above 500 eV (O(1s)). The carbon peak in particular is substantially reduced after GDC, but more conspicuously, peaks that are identifiable with the stainless steel (i. e., iron, chromium, and nickel) become observable (Fig. R13-2-2b).

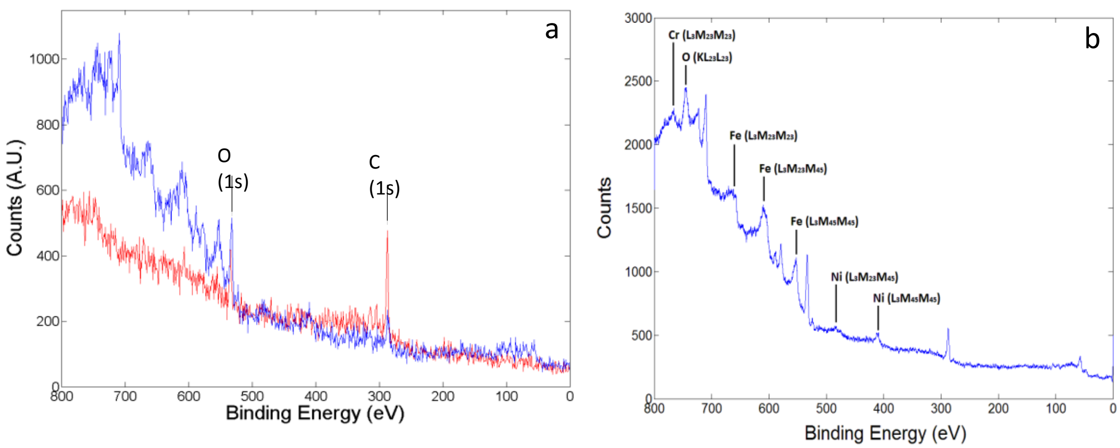

Figure R13-2-2: *(a) XPS spectra before (red) and after (blue) argon GDC. (b) Smoothed XPS spectra after argon GDC with iron, chromium, and nickel peaks identified.*

The MAPP-U data are the first that relate direct PFC measurements with the behavior of tokamak plasmas immediately after surface conditioning techniques are applied. The results are in general agreement with previous *in situ* XPS analysis of GDC on stainless steel [R13-2-4]. The change they suggest for the PFCs as an impurity source is consistent with earlier LTX observations of increased carbon and oxygen influx when plasma conditions degrade [R13-2-5].

References

[R13-2-1] C. N. Taylor et al., Rev. Sci. Instrum. **83**, 10D703 (2012)
[R13-2-2] M. P. Seah, Surf. Interface Anal. **14**, 488 (1989)
[R13-2-3] H. Kugel et al., Phys. Plasmas **15**, 056118 (2008)
[R13-2-4] H. F. Dylla, J. Vac. Sci. Technol. A **6**, 1276 (1988)
[R13-2-5] R. Majeski et al., Phys. Plasmas **20**, 056103 (2013)

FY2013 Research Milestone R(13-3): Perform physics design of ECH and EBW system for plasma start-up and current drive in advanced scenarios (Target - September 2013. Completed – September 2013)

Milestone Description: *For reactor-relevant ST operation it is critical to develop discharge initiation, plasma current ramp-up, and plasma sustainment techniques that do not require a central solenoid. Earlier electron cyclotron heating (ECH) modeling of NSTX CHI startup plasmas with GENRAY and CQL3D predicted 25-30% first pass absorption. In addition, electron Bernstein wave (EBW) startup experiments on MAST in 2009 showed good electron heating when the discharge became overdense. Several hundred kilowatts of coupled ECH/EBWH power in NSTX-U should heat a solenoid-free startup discharge sufficiently to allow coupling of 30 MHz high harmonic fast wave power, that will in turn generate non-inductive plasma current ramp-up. While pressure gradient-driven bootstrap current can provide a large fraction of the plasma current required to non-inductively sustain an ST plasma, an externally driven off-axis current may still be required to provide magnetohydrodynamic stability during the plasma current flat top. EBW current drive (EBWCD) can provide this non-inductive current and thus may play a critical role in enabling high beta, sustained operation of ST plasmas. A 28 GHz ECH and EBWH system is being proposed for NSTX-U. Initially the system will use short, 10-50 ms, 0.5-1 MW pulses to support development of non-inductive startup scenarios. Later the pulse length may be extended to 0.2-0.5 s and the power increased to provide EBWH and EBWCD during the plasma current flat top. EBW startup experiments are being planned on MAST for 2013 to extend the 2009 experiments to higher EBW power. Results from those experiments will support the design for the EBW startup system for NSTX-U. In 2013-2014 GENRAY and CQL3D ECH and EBWH modeling will be performed for NSTX-U plasma startup scenarios and for EBWH and EBWCD during the plasma current flat top for advanced NSTX-U plasma scenarios to support the physics design of the NSTX-U ECH/EBWH system.*

Milestone R(13-3) Report:
Design of the NSTX-U 28 GHz Heating System

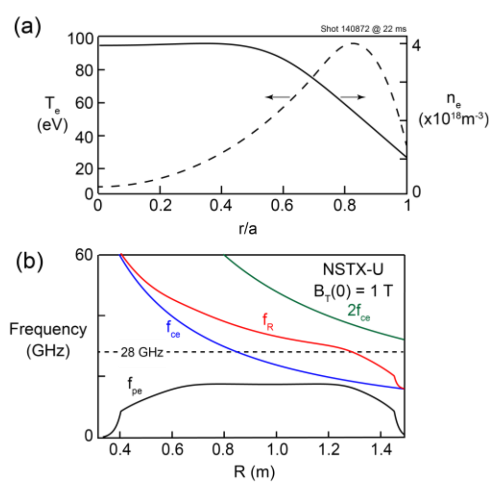

Figure R13-3-1. *(a) Electron density (solid line) and temperature (dashed line) profiles used for GENRAY modeling of a CHI start-up discharge. (b) Electron cyclotron resonances and cutoffs for a NSTX-U $B_T(0)$ = 1 CHI start-up discharge.*

Non-inductive (NI) plasma start-up will be accomplished on NSTX-U through a combination of coaxial helicity injection (CHI) [R13-3-1], outer poloidal field start-up [R13-3-2] and plasma guns [R13-3-3]. The electron temperature (T_e) profiles of CHI discharges are extremely hollow (Fig. R13-3-1(a), dashed line). Fortunately the central electron density of CHI plasmas is low enough, typically ~ 4 x 10^{18} m^{-3} (Fig. R13-3-1(a), solid line) to allow access to ECH at the plasma axis at both $B_T(0)$ = 0.5 T and 1.0 T. At $B_T(0)$ = 1.0 T the electron plasma frequency (f_{pe}) is well below the fundamental cyclotron resonance (f_{ce}) at a major radius, R = 0.9 m (Fig. R13-3-1(b)) where 28 GHz O-mode power is absorbed. Although first-pass damping for fundamental O-mode heating is much weaker than 28 GHz second harmonic X-mode heating at $B_T(0)$ = 0.5 T, wall reflections are expected to significantly enhance the fraction of power absorbed in the plasma. TSC [R13-3-4] simulations predict that the central electron temperature ($T_e(0)$) can be increase from 10 to ~ 100 eV in ~ 20 ms when 0.6 MW of ECH power is coupled into a CHI plasma. This increase in $T_e(0)$ will significantly reduce the plasma current decay rate of CHI plasmas [R13-3-5], and allow coupling of medium to high harmonic fast wave heating and neutral beam injection. The long pulse, megawatt-level gyrotron design being considered for the NSTX-U 28 GHz electron heating system is currently being developed for EC heating on the GAMMA-10 tandem mirror [R13-3-6]. The gyrotron uses a $TE_{8,3}$ cavity mode, will have an output power of ≥ 1 MW, and should be capable of pulse lengths of several seconds. The 28 GHz microwave power will be transmitted to NSTX-U via a low-loss, 50 mm diameter, corrugated $HE_{1,1}$ waveguide. Figure R13-3-2 shows a poloidal cross-section of the NSTX-U vacuum vessel and a $B_T(0)$ = 1 T CHI plasma equilibrium 22 ms after plasma breakdown. This equilibrium was used for GENRAY [R13-3-7] ray tracing simulations. For EC heating of CHI start-up discharges the low-loss waveguide will be connected to a corrugated horn antenna located in vacuum near the midplane of the vacuum vessel. The pulse duration used for heating the CHI start-up plasma will be typically ≤ 50 ms. However, for heating and current drive experiments via O-mode to slow X-mode to EBW (O-X-B) mode conversion [R13-3-8, R13-3-9, R13-3-10] during the I_p flattop the gyrotron pulse length will be increased to several seconds. 28 GHz power will be launched either by a concave steerable mirror launcher or by a phased-array antenna [R13-3-11].

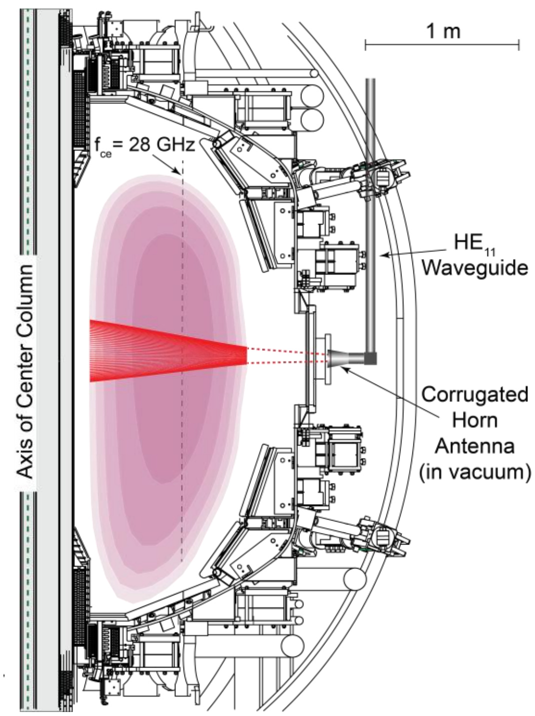

Figure R13-3-2. *Cross section of the NSTX-U vacuum vessel showing the pre-conceptual layout of the 28 GHz waveguide and horn antenna. The axis of the NSTX-U center column is on the far left side of the figure. The plasma equilibrium shown in the vessel is for a $B_T(0)$ = 1 T CHI startup discharge used for GENRAY ray tracing calculations. 100 rays calculated for 28 GHz EC heating are shown in red on the plasma equilibrium (violet shaing).*

Modeling Results for EC Heating During CHI Start-up

28 GHz EC heating of a NSTX $B_T(0) = 1.0$ T CHI start-up discharges has been modeled with the GENRAY ray tracing code. Figure R13-3-3 shows GENRAY ECH modeling results for the kinetic profiles shown in Fig. R13-3-1(a) and the magnetic equilibrium shown in Fig. R13-3-2. 100 rays were used for the ray tracing simulations. The maximum first pass absorption of 5% was obtained with the antenna pointing 1.5 degrees up poloidally and 1.5 degrees toroidally from the normal to the plasma surface (Fig. R13-3-3(a)), so some ability to align the pointing direction of antenna over several degrees is desirable. GENRAY simulations predict an increase in first pass absorption, rising from 5% at $T_e(0) = 10$ eV to over 20% at $T_e(0) = 200$eV (Fig. R13-3-3(b)). Earlier GENRAY simulations of EC heating of $B_T(0) = 0.5$ T NSTX CHI discharges where second harmonic X-mode EC heating was used predicted a much higher first-pass absorption of up to 25% at $T_e(0) = 10$ eV and 80% at $T_e(0) = 200$ eV [R13-3-12].

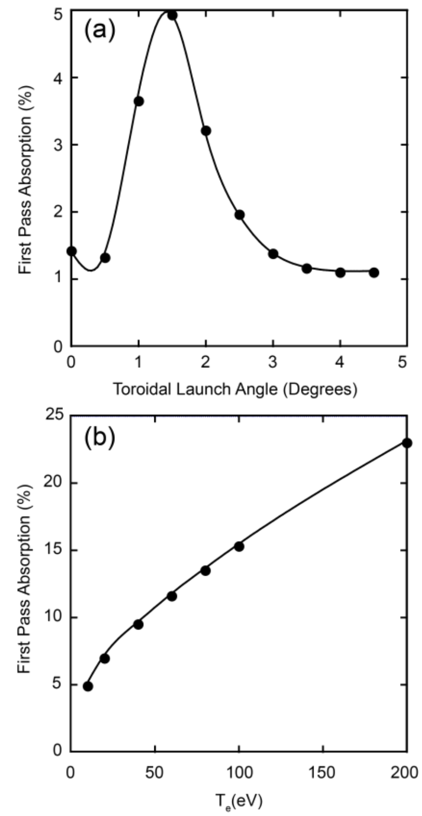

Figure R13-3-3. *GENRAY results for the $B_T(0) = 1$ T CHI discharge. (a) First pass absorption fraction versus the toroidal angle between the antenna axis and the normal to the plasma surface when the antenna is pointing 1.5 degrees up from normal, and (b) the dependence of first pass absorption on T_e when the antenna is pointing 1.5 degrees toroidally and 1.5 degrees up poloidally.*

EBW Plasma Start-up on MAST

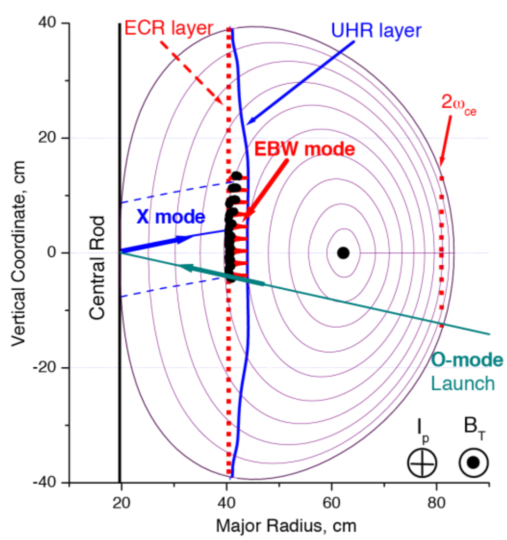

Figure R13-3-4. *Schematic diagram illustrating the technique used for EBW plasma start-up on MAST*

For several years ORNL and PPPL have collaborated with the Culham Centre for Fusion Energy (CCFE) to perform EBW plasma start-up experiments on MAST. EBW start-up experiments were last performed on MAST in 2009, using a 28 GHz gyrotron system provided by ORNL that was capable of generating 100-150 kW of RF power. These experiments used a reflective grooved tile on the center stack. Figure R13-3-4 shows a schematic diagram that illustrates the technique used for the MAST EBW start up experiments. O-mode 28 GHz radiation is launched from the low field side of the plasma, reflects off the grooved tile on the center stack where it is converted to X-mode radiation that then propagates to the upper hybrid resonance (UHR) layer where it efficiently converts to EBWs that once again propagate towards the center stack. But before the EBW power reaches the center stack it is 100% absorbed at the fundamental EC resonance layer that is located on the high field side of the plasma axis in this case.

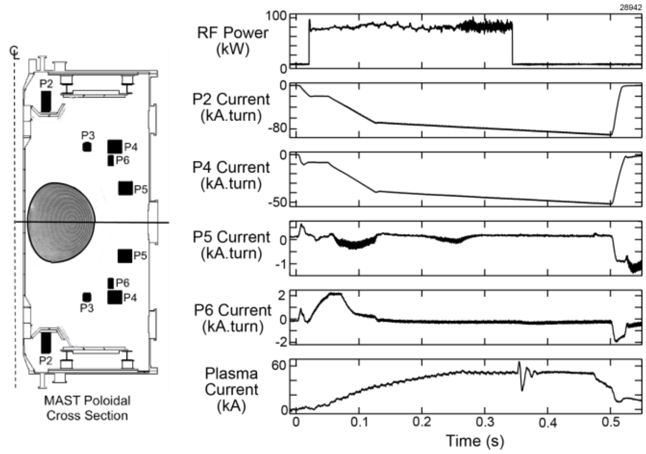

Figure R13-3-5. *28 GHz RF power, poloidal field coil currents and plasma current versus time for the EBW startup plasma that achieved the highest non-inductive, steady state, plasma current in MAST during the 2013 EBW start-up campaign. Poloidal field coil locations on MAST are shown on the left hand side of the figure.*

The 2009 MAST EBW plasma start-up experiments showed that I_p up to 17kA can be generated non-inductively by EBW power and that by optimizing vertical field ramps, I_p up to 33kA could be achieved [R13-3-13]. However, the power and pulse length coupled to MAST during the 2009 EBW start-up experiments was limited by arcing in the transmission line and the general unreliability of the gyrotron system. Subsequent improvements to the MAST 28 GHz heating system were made by ORNL and CCFE that substantially increased the power level and pulse length of the gyrotron and increased the transmission line efficiency. In 2013 two one-week experimental campaigns were dedicated to EBW plasma start-up in MAST. These campaigns significantly extended the 2009 results. Plasma currents up to 50 kA were generated non-inductively for up to 200 ms with 80 kW of 28 GHz gyrotron power [Fig. R13-3-5]. Also, by optimizing the vertical field ramp, plasma currents of up to 75kA were achieved with about 80 kW of 28 GHz gyrotron power [Fig. R13-3-6]. Experiments on NSTX-U using ≥1 MW of 28 GHz power should be able to couple ~ 0.6 MW, allowing the power dependence of the driven plasma current during EBW plasma start-upto be studied to much higher powers than on MAST.

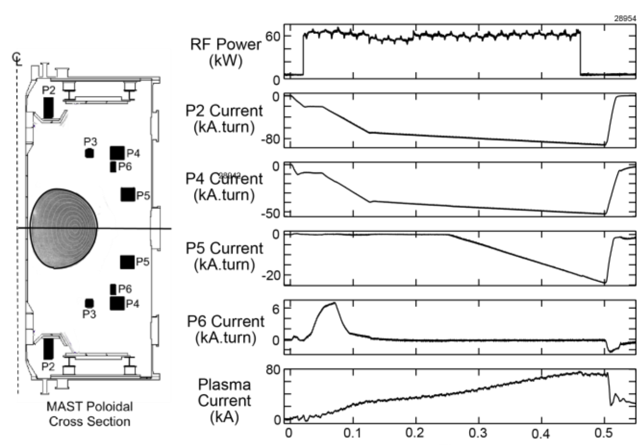

Figure R13-3-6. *28 GHz RF power, poloidal field coil currents and plasma current versus time for the EBW startup plasma that achieved the highest plasma current in MAST during the 2013 EBW start-up campaign by ramping the vertical field (P5 signal). Poloidal field coil locations on MAST are shown on the left hand side of the figure.*

Modeling Results for EBW Current Drive in NSTX-U NBI H-Mode Plasmas

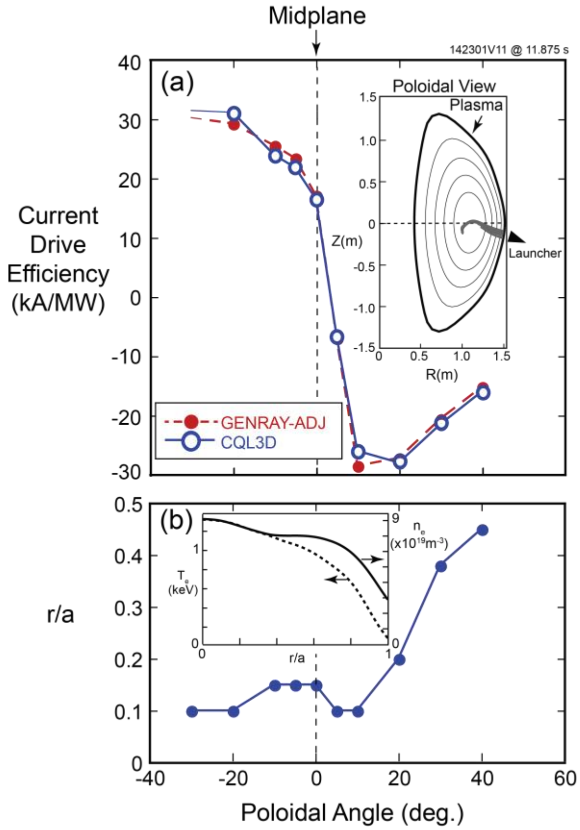

Figure R13-3-8. *(a) EBWCD efficiency versus the poloidal angle (θ) of the launcher location (launcher located at midplane corresponds to $\theta = 0$) for an NSTX-U H-mode plasma. The launcher is oriented to launch $n_{//}$ = - 0.7 to provide efficient O-X-B coupling. Inset shows poloidal cross section with rays calculated by GENRAY when launcher is at $\theta = -20^o$. (b) Location of the peak of the driven current density versus r/a. Shown in the inset are the electron density profile (solid line) and electron temperature profile (dashed line) versus r/a) that were used for the simulations.*

The GENRAY ray tracing code using the ADJ quasi-linear package [R13-3-14] and the CQL3D Fokker-Planck simulation code [R13-3-15] have been used to model EBWH and EBWCD for various H-mode scenarios being considered for NSTX-U [R13-3-16, R13-3-17]. Figure R13-3-8 summarizes EBWCD simulation results obtained for an I_p =1.1 MA, $B_T(0)$ = 1 T NSTX-U H-mode plasma. The density and temperature profiles used for this case are shown in the inset to Fig. R13-3-8(b). The maximum O-X-B mode conversion efficiency was obtained at a parallel launch wavenumber, $n_{//} = \pm 0.7$. The EBW rays were launched at the last closed flux surface and the poloidal angle between the launcher axis and the midplane (θ) was scanned from $\theta = -30^o$ and $\theta = 40^o$ (see inset in Fig. R13-3-8(a)). The maximum EBWCD efficiency of 32 kA/MW was obtained between $\theta = -15^{\,o}$ and -25^o and 28 kA/MW was obtained between $\theta = +10^{\,o}$ and $+20^o$. The peak of the driven current moved from r/a = 0.1 to r/a = 0.45 as θ was changed from = -30^o to $+40^o$ (Fig. R13-3-8(b)). Current densities at the peak of the driven current profile reached 150 kA,m^{-2} [R13-3-12]. There was good agreement between the GENRAY-ADJ and CQL3D simulation results. By adjusting the toroidal magnetic field and/or frequency it is possible to position the peak of the EBW-driven current outside r/a ≥ 0.8 [R13-3-18, R13-3-19].

References

[R13-3-1] R. Raman, et al, Nucl. Fusion **53**, 073017 (2013).
[R13-3-2] W. Choe, et al., Nucl. Fusion **45**, 1463 (2005).
[R13-3-3] D. J. Battaglia, et al., J. Fusion Energy **28**, 140 (2009).
[R13-3-4] S.C. Jardin, et al., J. Comput. Phys. **66**, 481 (1986).
[R13-3-5] R. Raman, et al., Nucl. Fusion **51**, 113018 (2011).
[R13-3-6] A. P. Smirnov and R.W. Harvey, Bull. Am. Phys. Soc. **40**, 1837 (1995).
[R13-3-7] T. Imai, et al., Trans. Fusion Sci. and Tech. **63**, 8 (2013).
[R13-3-8] J. Preinhaelter and V. Kopécky, J. Plasma Phys. **10**, 1 (1973).
[R13-3-9] E. Mjolhus, J. Plasma Phys. **31**, 7 (1984).
[R13-3-10] F. R. Hansen, et al., J. Plasma Phys. **39**, 319 (1988).
[R13-3-11] H. Idei, et al., Proc. 16th Workshop on ECE and ECRH, World Scientific (2011), p. 269.
[R13-3-12] G. Taylor et al., Proc. 17th Workshop on ECE and ECRH, EPJ Web of Conferences **32**, 02014 (2012)
[R13-3-13] V. Shevchenko, et al, Nucl. Fusion **50**, 022004 (2010).
[R13-3-14] A. P. Smirnov, et al., Proc. 15th Workshop on ECE and ECRH, World Scientific (2009), p. 301.
[R13-3-15] R. W. Harvey et al., Proc. 38th EPS Conf. on Plasma Phys. (Strasbourg, France 2011) paper P4.017.
[R13-3-16] S.P. Gerhardt, et al, Nuclear Fusion **52**, 083020 (2012).
[R13-3-17] G. Taylor et al., "*Physics Design of a 28 GHz Electron Heating System for the National Spherical Torus Experiment Upgrade"* Proc. 20th Topical Conference on RF Power in Plasmas, Sorrento, June 2013. (To be published in AIP Conference Proceeding)
[R13-3-18] G. Taylor et al., Phys. Plasmas **11**, 4733 (2004).
[R13-3-19] J. Urban et. al., Nucl. Fusion **51**, 083050 (2011).

FY2013 Research Milestone R(13-4): Identify disruption precursors and disruption mitigation & avoidance techniques for NSTX-U and ITER (Target - September 2013. Completed – September 2013)

Milestone Description: *In order for the tokamak/ST concept to reach its full potential, disruptions must be infrequent, detectable in advance, and amenable to intervention in order to eliminate their consequences. High current disruptions in NSTX-U, for instance, could decondition lithium coated plasma facing components (PFCs) or other lithium conditioning systems, while unmitigated disruptions in ITER have the potential for severe damage to the vessel and PFCs. Indicators of proximity to or the crossing of global, disruptive stability boundaries in NSTX discharges will be developed; these could include MHD signals like resistive wall modes (RWMs), locked modes, rotating MHD modes and/or resonant field amplification, scrape-off-layer current (SOLC), confinement indicators such as the flux consumption and neutron rate, real-time comparison to RWM state-space observer computation, or equilibrium properties such as the pressure peaking and edge safety factor. Strategies for processing and combining the various precursors will be developed, as will requirements for real-time measurements in NSTX-U. A real-time architecture for response to these and other off-normal events will be developed. Potential responses include rapid plasma ramp down, or discharge termination via massive gas injection (MGI). An engineering optimization of the MGI system will be made for NSTX-U, and MGI modeling may be pursued in support of both NSTX-U and ITER. This research will facilitate disruption free operation of present and next-step STs and tokamaks, including ITER.*

Milestone R(13-4) Report:

Disruption warning system development

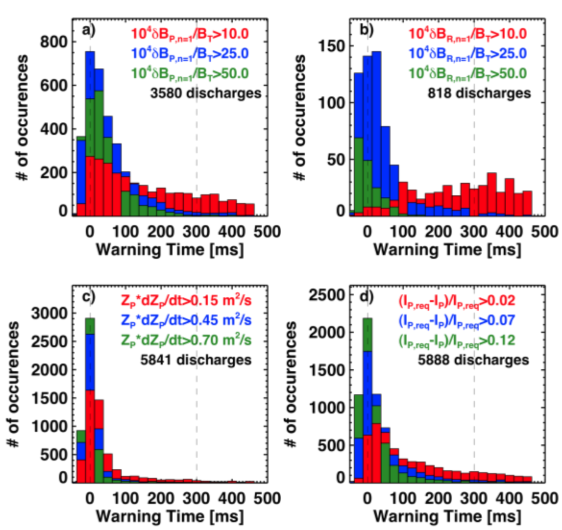

Figure R13-4-1: Histograms of disruption warning times, based on a) the normalized n=1 poloidal field perturbation, b) the normalized quasi-stationary n=1 B_R field perturbation, c) the quantity $Z_P \cdot dZ_P/dt$, and d) the fractional deviation of the plasma current from the requested value.

In order to prepare for NSTX-U operation at higher current and inform the design of the ITER CODAC system, a study of the disruption precursors in NSTX has been undertaken. This study was composed of two parts. First, individual disruption precursors were examined. Second, a method for combining the inputs from multiple diagnostic signals was created, in order to improve the fidelity of the disruption detection. Numerous single diagnostics have been examined to determine if they provide information about imminent disruptions, based on a database of disruptions from the 2006-2011 run campaigns. In particular, threshold levels for each diagnostic test have been assessed, to examine if crossing those thresholds is indicative of the approach to a disruption. Results from these studies are shown in Figs. R13-4-1 and R13-4-2.

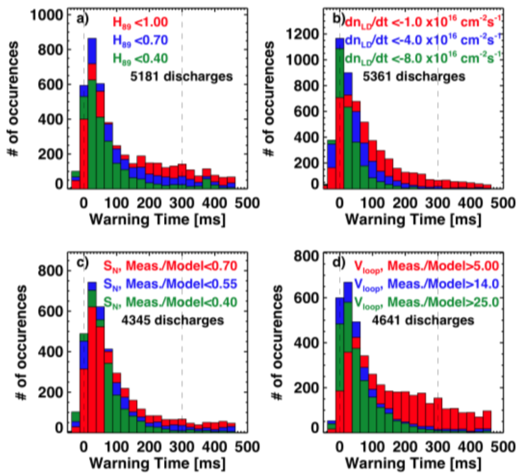

Figure R13-4-2: Histograms of disruption warning times, based on a) the global energy confinement level, b) transients in the line-density evolution, c) the neutron emission, d) the loop voltage.

Figure R13-4-1 shows the results of examining magnetic measurements. In frame a), the n=1 poloidal field perturbation, indicative of locked modes and resistive wall modes is examined. If a disruption is declared when $dB_{P,n=1}/B_T$ exceeds 10^{-3}, a large number of false positives occur. This can be seen in the large number of occurrences with warning times exceeding 300 ms. However, this low threshold also results in a small number of late or missed warnings, as indicated by the very small number of cases with warning times less than zero (negative warning time indicating that the warning was declared after the disruption was initiated). Increasing the threshold to 2.5×10^{-3} and then 5×10^{-3} results in a decrease in the number of false positives, though at the expense of an increase in the late warnings. Similar trends are observed for the n=1 B_R perturbation in frame b).

Frames c) and d) examine other magnetic signals. Frame c) shows examination of the quantity $Z_P \cdot dZ_P/dt$, which has the advantage of being large and positive when the plasma is above the midplane and moving upwards, or below the midplane and moving downwards. It is thus an excellent indicator of the onset of vertical instabilities. The characteristic growth time of these instabilities is ~10s of ms, and so the available warning time is short on the scale of the plot. However, values exceeding 0.45 m^2/s can be used for indicating disruption proximity. Frame d) shows the results of using the deviation of the plasma current from the requested value as an indicator of proximity to disruption. This exercise shows that deviations of ~5-10% are indicative of imminent disruption.

Various confinement signals can be used to indicate proximity to disruption, as shown in Fig. R13-4-2. Frame a) shows that when the global confinement, as captured by the H_{89} parameter, drops beneath 0.7, disruptions become more likely, with a threshold of 0.4 being a good indicator of disruption proximity. Similarly, as shown in frame b) large drops in the line density can be used to assess disruption proximity, as they indicate a substantial reduction in particle confinement.

However, it is often the case that these indicators can be best used to look for disruption proximity if easily evaluated models for the diagnostic signals are available. Examples of this are shown in frames c) and d). In frame c), the ratio is taken between the measured neutron emission and that predicted by a simple, easily evaluated slowing-down model. Here, having this ratio drop beneath ~0.5 is an excellent indicator of disruption proximity, implying that some large perturbation has resulted in a large loss of fast ions. Similarly, in frame d) the measured loop voltage is normalized to that predicted by a simple current drive calculation assuming ITER-

98(y,2) confinement. In this case, increases in the loop voltage can be used to predict that a disruption is imminent.

The discussion of Figs. R13-4-1 and R13-4-2 illustrate that many individual signals can be used to look for disruption precursors. However, no single signal and threshold value can be used find disruptions with simultaneously low rates of false positive and late warnings. The can be seen that in every frame of Figs. R13-4-1 and R13-4-2, for any given threshold value, there are either an unacceptable number of false positives or late warnings; said another way, the thresholds result in a warning system that is either too sensitive, or not sensitive enough. Hence, combining the data from these different diagnostics and tests is necessary.

To define the algorithm, the following two steps are executed.

- A series of ~17 threshold tests such as those described above is defined.
- For each of these tests, a unique "point" value is assigned to each of a set of threshold levels. For instance, for a three-level scheme, corresponding to three threshold levels assigned for each test, a typical point assignment is as given in Table R13-4-1. Up to six-level schemes have been tested, corresponding to six different threshold levels per test and up to 6 points available per test.

test	1 pt (5% FPR)	2 pts (2% FPR)	3 pts (0.5% FPR)
$dB_{P,n=1}/B_T >$	0.0023	0.004	0.0072
$S_N <$, measurement/model	0.49	0.39	0.27
$(I_{P,req}-I_P)/(I_{P,req}) >$	0.08	0.12	0.19
$F_{T,mid-radius}-F_{T,core} <$ [kHz]	1.4	*	*

Table R13-4-1: Subset of the point assignments for a three-level test. The actual test has a total of 17 rows.

Then, at each time step during a discharge, the following steps are executed.

1. Each of the threshold tests is executed, and the number of points for each test is evaluated. For instance, from the first line of Table R13-4-1, a single point would be awarded if $dB_{P,n=1}/B_T$ exceeded 0.0023, two points if it exceeded 0.004, and three points if it exceeded 0.0072.
2. The points from the individual tests are totaled, to form the "aggregate" point total.
3. A disruption warning is declared if the aggregate point total exceeds a pre-defined threshold

The time evolution of this algorithms output is shown in Fig. R13-4-3, for a representative disruption. This disruption is initiated by the locking of an n=1 kink/tearing mode to the wall, as indicated by the abrupt elimination of the black rotating odd-n MHD signature in frame a), followed by the immediate growth of the $dB_{P,n=1}$ locked mode/RWM indicator. Other important signatures include the deviations in the plasma current, the growth of vertical motion, the drop in β_N, the increase in V_{loop} and pressure peaking F_P, and the dropping of the plasma rotation to zero. All of these are captured by the threshold tests and reflected in the evolution of the aggregate point total in Frame d). This value exceeds 30 well before the initiation of the current quench.

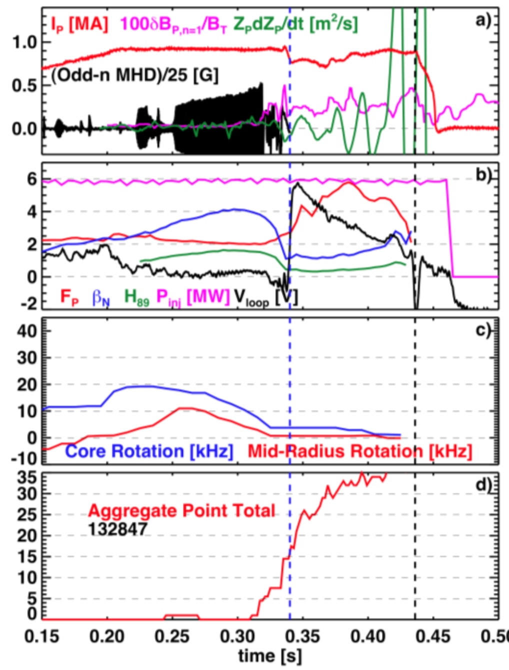

Figure R13-4-3: Example time evolution of disrupting plasma. The first row of each column shows the plasma current, normalized n=1 quasi-stationary B_P perturbation ($dB_{P,n=1}/B_T$), the rotating odd-n B_P perturbation, and vertical motion indicator $Z_P \cdot dZ_P/dt$. The second row of each column illustrates the pressure peaking (F_P), normalized beta (β_N), confinement enhancement relative to ITER-89 scaling (H_{89}), the injected power (P_{inj}), and the loop voltage (V_{loop}). The third row shows the core and mid-radius toroidal rotation frequency, while the bottom row shows the aggregate point total based in the 6-level

The algorithm has been tested against a large database of disruptions, with the results shown in Fig. R13-4-4. Frame a) shows the results from a three level test. If a disruption warning is declared when the aggregate point total exceeds 2 points, then the rate of late or missed disruptions is less than 1%. However, the rate of false positives, defined, as above, when the warning is declared more than 300 ms in advance of the current quench, exceeds 20 %. Note that as per Table R13-4-1, a value of 2 points can easily be achieved by even a single threshold test. However, if the threshold in the aggregate point total is increased to 6 points, requiring at least two tests to register disruptive behavior, the false positive rate drops to 2.5%, while the late/missed warning rate only increases to ~5%. Even better results are achieved for the 6-level scheme in frame b), where the optimal choice of thresholds results in a 3.7% rate of late/missed warnings and only a 2.8% rate of false positives. Further discussion of this algorithm can be found in Ref. [R13-4-1], including a discussion of how the threshold values in Table R13-4-1 were chosen, and a detailed examination false positive and late warning causes.

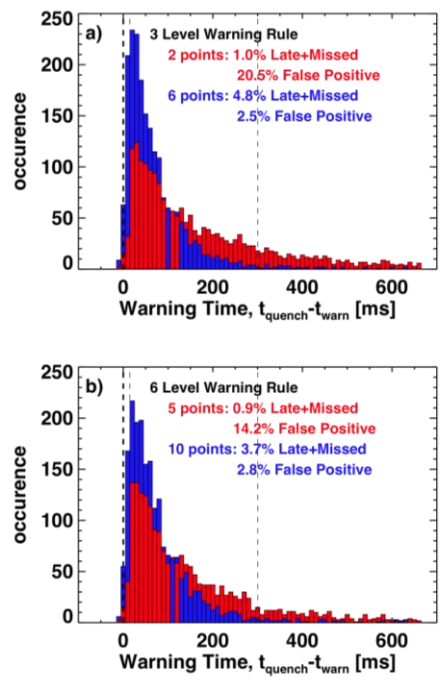

Figure R13-4-4: Histograms of warning times. Frame a) shows the statistical results of the 3 levels tests, while frame b) shows the results of the 6-level test.

Looking forward to future devices, it is planned that some or all of this methodology will be utilized for disruption detection in NSTX-U; this warning will be used to initiate controlled ramp-downs of the plasma energy and current in advance of a disruption, or potentially trigger MGI. For ITER, this result shows that a large range of realtime diagnostics should be used for disruption detection. However, it is not reasonable to assume that the coefficients of this detector (the numerical values in Table R13-4-1) will transfer directly to ITER. Hence a next step will be to implement this scheme on another tokamak, presumably at larger aspect ratio; discussions along these lines have already been initiated with physicists from DIII-D and PSFC. One important means of making the coefficients more general is to interrogate the diagnostics in the context of model plasma behavior, in order to determine from first principles what threshold levels are indicative of instability. A first step in this direction is the use of simple models of the neutron emission and current drive sources in Figs. R13-4-2c) and d) to interpret the measured neutral emission and loop voltage. These models should be extended to include models of the vertical position and n=1 control loops, and more complete models of the current drive sources should be invoked. These will allow a more complete loss of control (LoC) assessment to be made, which can then be used to initiate a fast or slow plasma shut-down.

Disruption warning sensor based on low frequency MHD spectroscopy

Low frequency MHD spectroscopy based on resonant field amplification (RFA) of slowly rotating (10 – 100 Hz) applied n = 1 fields has been used in DIII-D [R13-4-2] and NSTX [R13-4-3] to directly measure the stability of modes that cause disruptions before they become unstable. Typically, the RFA amplitude is correlated with mode stability. However, further analysis of NSTX plasmas is needed to determine the utility of RFA for use as a sensor in a real-time disruption warning algorithm. In particular, the use of such a sensor over the entire NSTX operational space is needed, which goes beyond earlier published NSTX research on RFA, such as in Reference [R13-4-3]. Recent progress in correlating RFA amplitude with mode stability in NSTX is shown in the analysis of dedicated experiments using this technique in the section labeled "*Measured Improvement of Global MHD Mode Stability at High-beta*" in the Macrostability Topical Science Group section of this document [R13-4-4]. As shown in Figure RWM-3 of that section, unstable RWMs correlate with increased n = 1 RFA of the applied n = 1 field, which surprisingly occurs at intermediate (not the highest) values of β_N/l_i. Further detail of the time evolution of the n = 1 RFA amplitude for several of these shots is shown in Figure R13-4-5, now using an algorithm equivalent to that used in reference [R13-4-2] for consistency with past experiments. As has been concluded previously, these plasmas clearly show that β_N and β_N/l_i alone are not good indicators of plasma stability, nor are they adequate when a simple scalar rotation (e.g. a "critical rotation speed") is added to determine stability. These results have recently been analyzed using the MISK code to compare the theoretically computed stability of these plasmas to the RFA amplitude measurements. The MISK results are shown in Figure R13-4-6 for these plasmas using equilibria at the indicated times, and with the plasma rotation profile scanned self-similarly from the profile at these times, to determine the mode stability as a function of rotation.

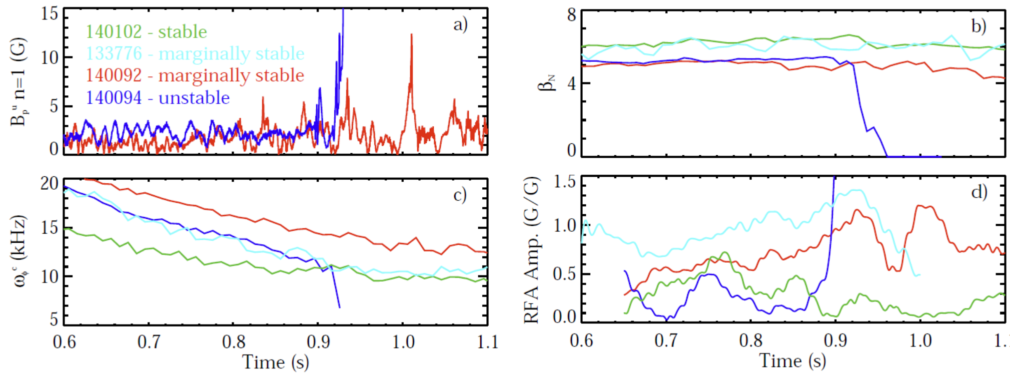

Figure R13-4-5: Time evolution of NSTX plasmas analyzed using low frequency MHD spectroscopy: a) n = 1 decomposition of upper RWM sensor signals, b) normalized beta, c) carbon toroidal rotation near the plasma core, d) n = 1 RFA amplitude.

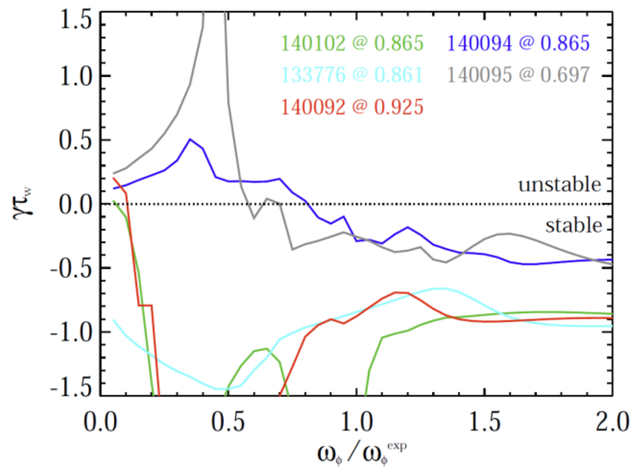

Figure R13-4-6: MISK computed RWM growth rate (normalized to the wall eddy current decay time) vs. scaled experimental rotation for plasmas analyzed using low frequency MHD spectroscopy.

There is good correlation found between experimental mode stability and the MISK analysis (e.g. shot 140094 becomes unstable with about a 20% reduction of the plasma rotation from the equilibrium chosen for analysis, which is what is found in the experiment. However, in certain instances, the RFA amplitude alone appears to be insufficient for use in a real-time instability detection system. For example, again considering the RFA amplitude for shot 140094, the RFA amplitude is relatively low compared to other plasmas that reach RFA amplitudes greater than unity and remain stable. This result shows that additional information will be needed for a reliable real-time stability evaluation. Present analysis continues from this recent conclusion, starting with the examination of the use of the RFA phase in addition to amplitude to more accurately determine plasma stability over the full range of β_N and rotation profiles in NSTX.

Disruption warning sensor – initial physics model

A major goal of disruption avoidance research in NSTX in the upcoming 5 year plan is to determine a relatively simple physics model that can be used in addition to other real-time tools for disruption avoidance. In the context of the present milestone, an initial simple model was targeted, as a starting point for continued evaluation and development in the coming years. Detail on the evaluation of this model is given the section labeled "*Measured Improvement of Global MHD Mode Stability at High-beta*" in the Macrostability Topical Science Group section of this document. Kinetic RWM stabilization theory applied to NSTX high β_N plasmas shows that when the trapped thermal ion's precession motion plus the E×B motion around the torus is near zero in the frame of the slowly rotating mode ($|\omega_E - \omega_D| \approx 0$), energy is most efficiently transferred between the mode and the particles, reducing the free energy that drives mode growth [R13-4-5]. This criteria has been evaluated in a simple manner for the experimental NSTX plasmas described above to determine if the result can be correlated to mode stability in a limited way. The result is shown in the right-hand frame of Figure RWM-3, which shows RFA amplitude plotted against $\langle\omega_E\rangle$, the E×B frequency averaged over a range of normalized poloidal flux extending from $\psi_N = 0.5$ to the top of the density pedestal. Although in the full kinetic treatment the resonance criterion is more complex (ω_D, for example, is dependent on particle pitch angle and energy), since $\omega_D \approx 0$, and ω_E decreases with ψ_N, we can roughly project that a certain finite range of $\langle\omega_E\rangle$ inside the pedestal will provide a stabilizing resonance in the outer surfaces where the RWM eigenfunction is large. This criterion defines an initial simple model that describes a favored operational state for RWM stability. The condition depends on plasma rotation, density, and temperature profiles, which will be available to different degrees in the operation of NSTX-U in the coming years. Near-term analysis will test this simple model, determined from the dedicated RFA experiments, against a wider range of NSTX high beta plasmas.

Disruption warning sensor based on RWM state-space controller

Initial analysis of data from the NSTX RWM state-space controller indicates that the real-time model used to actuate active feedback to counter the $n = 1$ perturbed mode flux can also be used more generally to warn when stability limits are being approached. An advantage of such a model-based controller is that it provides an expectation of how global mode activity will behave in the device as a function of the plasma target parameters. This includes computation of modeled diagnostic measurements in real time. A Kalman filter approach is used to advance the state vector of the RWM state-space controller in the presence of noise $\dot{\vec{x}} = (I_r + B_r K_c)^{-1} A\vec{x} + K_o(\vec{y}_m - \vec{y})$ where $\vec{y}_m$ is the measured magnetic flux in the RWM sensors, $\vec{y} = C\vec{x} + D\vec{I}_f$, is the controller observer computation of the measurements, I_r is the identity matrix, A and B are the plant and control matrices, and the remaining matrices are the computed controller and observer gain

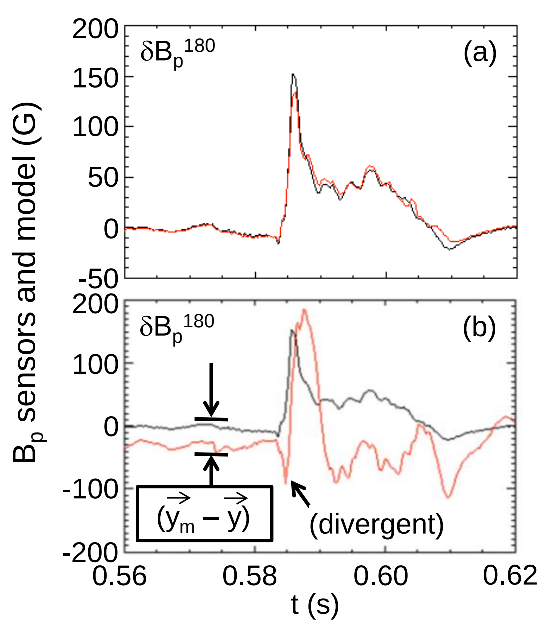

Figure R13-4-7: Open-loop comparison of RWM state-space controller observer model of the field difference measured by diametrically-opposed pair of RWM sensors for (a) a situation that is relatively well-modeled by the observer, and (b) one that is not well-modeled.

matrices determined by the optimal control algorithm. Subscript "*r*" is used to denote the reduced order system matrices. It is clear that the second term represents a correction to the plant matrix evolution of the state vector. While typically used to correct the state in active feedback, it can also be used in real time to determine how incorrect the observer is in reproducing the measurements. Therefore, this difference can be used as a criterion of how incorrect the observer is allowed to be in any given sensor, or collection of sensors, and used as input to a disruption warning system. Such an approach is not possible in more standard control systems that do not have a real-time model of the sensor response. One example of how this system would be implemented is shown in Figure R13-4-7, which compares the measured magnetic field difference in one diametrically-opposed pair of RWM sensors to the real-time controller observer model computation of this flux difference in an open-loop test on a high-β_N NSTX plasma. The upper frame illustrates a situation where the observer model matches the measurements well, which would allow the system to attempt active RWM feedback on the instability.

However, if the real-time model of the sensors cannot match the measured sensors well (here, this is due to the plasma response used being set too large in the model), the large difference between the measurements and model can be used to warn other disruption avoidance systems that RWM active control will not function properly while the plasma is still stable, and use other means to avoid instability. Of particular note is the divergent behavior between measurement and model as the instability onsets, leading to a far greater difference between the real-time model and measurement. This results suggests that two stages of disruption avoidance could be used here – the first being triggered by the difference between model and measurement exceeding a smaller value over a longer time period (which could help guide rotation control, or NBI power or source control), and a second larger value reached in a short time period (here, as the instability onsets) which can be used to trigger a disruption mitigation system. Near-term analysis will examine the database of open-loop observer tests (run for a few hundred NSTX plasmas during the last campaign) to determine the efficacy of this approach for use in NSTX-U.

Disruption mitigation using MGI

The MGI, which is one of the critical protective responses that discharge warning can initiate, has been newly designed and optimized with an improved Electromagnetic MGI valve for installation on NSTX-U. The valve is similar in design planned for ITER, as qualitatively shown in Figure R13-4-8, and is at present undergoing off-line tests at the Univ. of Washington. After off-line tests are completed later this year, three such valves will be built for installation on NSTX-U and would be mounted on an organ pipe in the upper and lower divertor areas and also be installed at the vessel mid-plane. FY2015 NSTX-U MGI experiments would use three such valves at different poloidal locations to initiate studies in support of disruption mitigation physics.

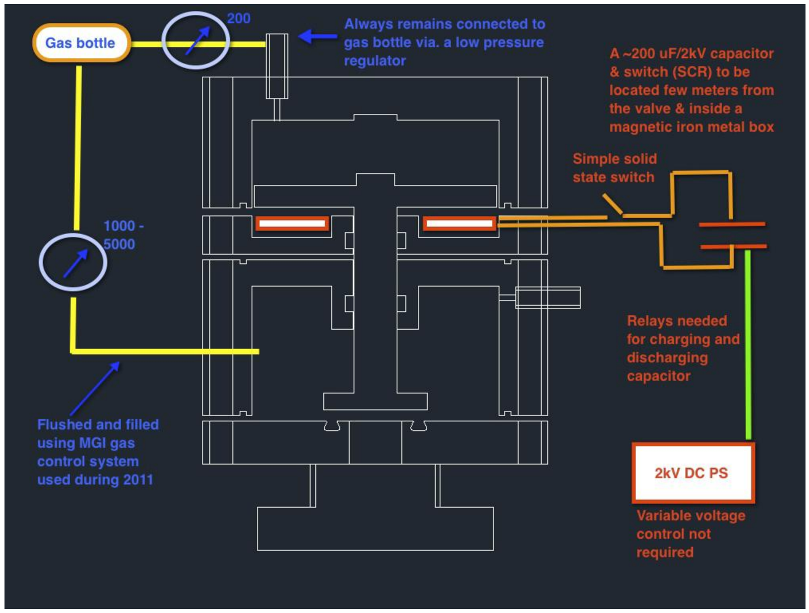

Figure R13-4-8: A 100-200 micro Farad capacitor charged to 2 kV is discharged through the pancake coil to provide discharge current pulse through the coil.

In parallel with experimental preparation, numerical efforts have been initiated with DEGAS-2 Monte-Carlo [R-13-6] code to understand the extent of gas penetration through the SOL region and private flux regions, and to understand the amount of gas the valves must inject to be consistent with the thermal and current quench times scales on ITER [R-13-7]. In addition to supporting NSTX-U needs, this simulation effort focuses on fundamentally studying the edge penetration issues to the separatrix, which is needed for predicting gas penetration efficiencies in ITER. This work complements other 3-D MHD modeling, initiated by the ITER organization, of the gas dissipation inside the separatrix.

References

[R13-4-1] S.P. Gerhardt, et al., Nuclear Fusion **53**, 063021 (2013).

[R13-4-2] H. Reimerdes, M.S. Chu, A. Garofalo, et al., Phys. Rev. Lett. **93**, 135002 (2004).

[R13-4-3] S.A. Sabbagh, A.C. Sontag, J.M. Bialek, et al., Nucl. Fusion **46**, 635 (2006).

[R13-4-4] J.W. Berkery, S.A. Sabbagh, A. Balbaky, et al., "*Measured Improvement of Global MHD Mode Stability at High-beta, and in Reduced Collisionality Spherical Torus Plasmas*" submitted to *Phys. Rev. Lett*. (2013).

[R13-4-5] B. Hu and R. Betti, *Phys. Rev. Lett.* **93**, 105002 (2004)

[R13-4-6] D.P. Stotler and C.F. Karney, "Neutral Gas Transport Modeling with DEGAS 2", Contrib. Plasma Phys. **34** (1994) 392-397

[R13-4-7] T. Abrams, D. P. Stotler, and R. Raman, "Simulation of deuterium and helium massive gas injection for NSTX-U and ITER", Theory and Simulation Workshop, PPPL, 16-18 July, 2013

Additional NSTX-U Research Achievements in FY2013

Beyond the completion of the FY2013 research described above, additional important scientific results were obtained during the FY2013 period and are described below.

Boundary Physics Research Results

Broadly speaking, the boundary physics portion of this report is focused in three sub-topics: pedestal physics, scrape-off layer (SOL) physics, and divertor physics. Thus we first describe pedestal and ELM control research, followed by SOL and divertor research, concluding with a new analysis of lithium evaporation studies in high triangularity discharges in NSTX.

A. Pedestal and ELM Studies

Pedestal Structure Studies in ELMy discharges

Substantial progress has been made in pedestal physics over the last decade, particularly with development of several pedestal structure models. One leading theory on the physics limiting the pressure profile is the EPED model. This model predicts a limit on the pressure gradient in the steep gradient region, and the overall H-mode pedestal pressure height/width. Experimentally model predictions have been correlated with local observed pressure gradients and the maximum pedestal height before peeling-ballooning mode onset. Violation of the peeling-ballooning mode stability criteria is thought to be manifest as large, Type I ELMs.

These two limits have been investigated on NSTX [BP-PED 1], and showed qualitative agreement with the EPED premises. Specifically, the pedestal width scaled nearly linearly with [β_θ^{ped}] in NSTX, as shown in figure Fig. BP-1. The theoretical scaling is associated with a microinstability known as the kinetic ballooning mode (KBM) limiting the pressure gradient. A preliminary KBM calculation for NSTX indicates a width ~ $(\beta_\theta^{ped})^{0.8}$, i.e. the faster than square root scaling at lower R/a. Further research is needed to determine if the NSTX scaling is specific to the device or a general low R/a effect.

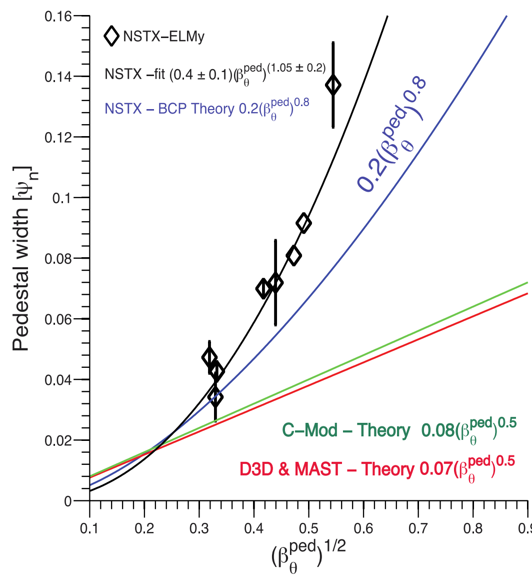

Fig. BP-1. Pedestal width scaling with predicted width scaling.

Pedestal Turbulence in ELM-free and MHD quiescent discharges

It is believed that microinstabilities and the resulting plasma turbulence are responsible for transport in the pedestal region, as is the case in the core plasma. Pedestal turbulence simulations are challenging due to steep pressure gradients, high bootstrap current, and strong E×B shear.

Furthermore, ST edge turbulence simulations are among the most difficult due to high β, large ρ*, strong beam-driven flow, and strong shaping.

NSTX-U collaborators from the University of Wisconsin-Madison (UW) have pursued a systematic comparison between pedestal turbulence measurements from beam emission spectroscopy (BES) and pedestal turbulence simulations from gyrokinetic and fluid codes. In FY12, the UW group tabulated pedestal turbulence parameters from BES measurements (poloidal correlation length, decorrelation time, etc), and then applied machine learning algorithms to identify scalings among turbulence parameters and transport-relevant plasma parameters (see Figure BP-2). The scalings were partially consistent with TEM, KBM, and microtearing turbulence, but notably least consistent with ITG turbulence [BP-PED 2]. In FY13, the analysis expanded to pedestal turbulence fluctuation amplitudes with δn/n≈1-5%. Turbulence amplitude scalings with transport-relevant plasma parameters were consistent with previous results, including the lack of consistency with ITG turbulence [BP-PED 3]. Also in FY13, the UW group obtained gyrokinetic and fluid simulations of NSTX pedestal turbulence to compliment BES measurements. GEM linear gyrokinetic simulations in realistic NSTX pedestal geometry, courtesy of S. Parker at U. of Colorado-Boulder (UC), pointed to a hybrid drift-wave/microtearing instability with collisionality, ∇n, and ∇Ti scalings consistent with BES measurements. The UC group is presently pursuing nonlinear gyrokinetic simulations of NSTX pedestal turbulence. Finally, nonlinear Braginskii fluid simulations (BOUT++) of NSTX pedestal turbulence highlighted the importance of realistic electron dynamics for accurate pedestal turbulence simulations [BP-PED 3].

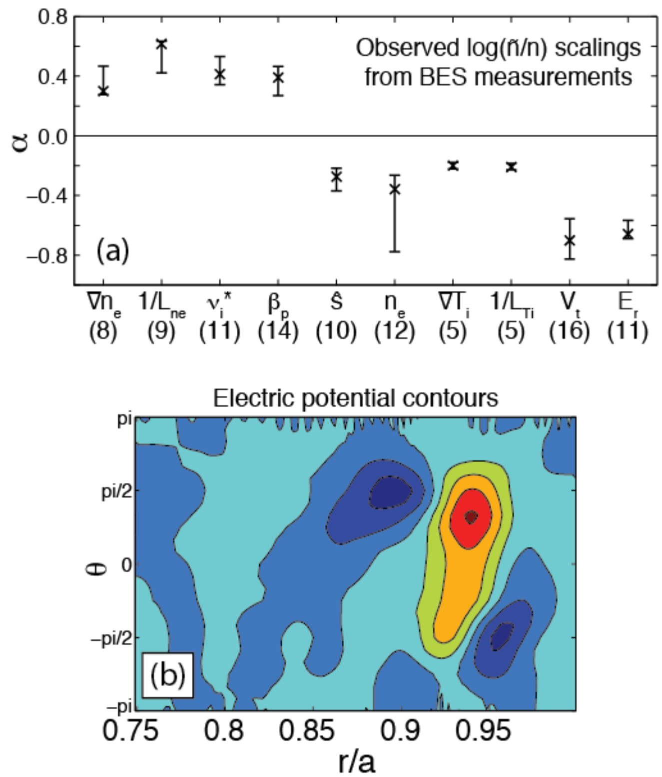

Figure BP-2: (a) Linear scaling coefficients (alpha) between fluctuation amplitudes from BES measurements and transport-relevant plasma parameters and (b) electric potential contours from a linear GEM simulation of pedestal turbulence with realistic NSTX profiles and geometry.

Looking forward to FY14, the UW group will expand the comparison between pedestal turbulence measurements and simulations with more sophisticated plasma models in the BOUT++ code. For instance, Landau fluid and gyrofluid models are expected to be more accurate at intermediate collisionalities in the pedestal. Finally, MHD codes, such as NIMROD and M3D-C1, can simulate the fast nonlinear evolution of ELM bursts, so the UW group plans to initiate a survey of ELM burst evolution in NSTX and DIII-D plasmas by leveraging the fast sampling capabilities of BES measurements.

A number of other gyrokinetic codes have been used to characterize edge microinstability in inter-ELM periods, spanning a broad range in the comprehensiveness of the physics included (i.e, linear vs nonlinear, local vs. global, electrostatic vs. electromagnetic, δf vs. full-f). As another example, a study of the linear gyrokinetic stability of the pedestal was performed using the GS2 code. For a discharge without the application of lithium coating on the plasma-facing components (PFC), these calculations showed that MTM are dominant at the pedestal top (see Fig. BP-3). With lithium applied to the PFCs, the increase in the density gradient in this region stabilized the MTM, and modes with characteristics like those of the TEM becoming dominant with reduced growth rates. In the steep gradient region of the pedestal, ETG modes were found to be unstable both without and with lithium, but with higher growth rates and a lower threshold temperature gradient with lithium, suggesting ETG may have played a role in limiting the electron

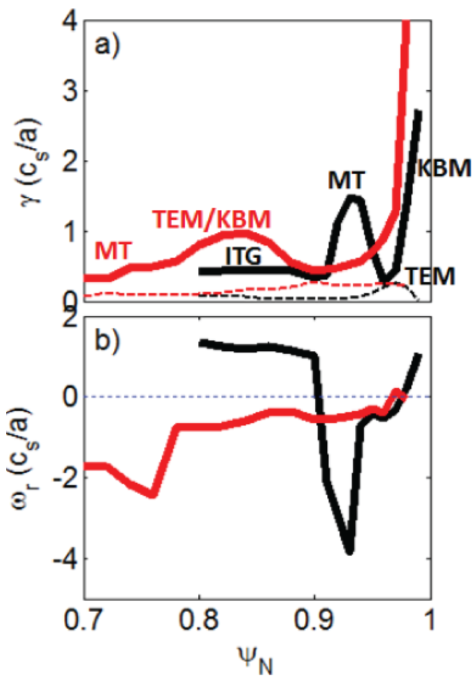

Fig. BP-3:Profiles of a) growth rate (solid) and ExB shear rate (dashed), and b) real frequency of the most unstable mode without (black) and with (red) lithium.

Fig. BP-4: (a) 2D cross-section of the potential fluctuations from XGC1 simulations in the fully nonlinear stage. (b) Zoomed in edge fluctuations indicating the BES and reflectometry measurements region. (c) Evaluations (from simulation) of both radial (4 cm) and poloidal correlation (11 cm) lengths in the edge region showing experimental level radial and poloidal correlation lengths.

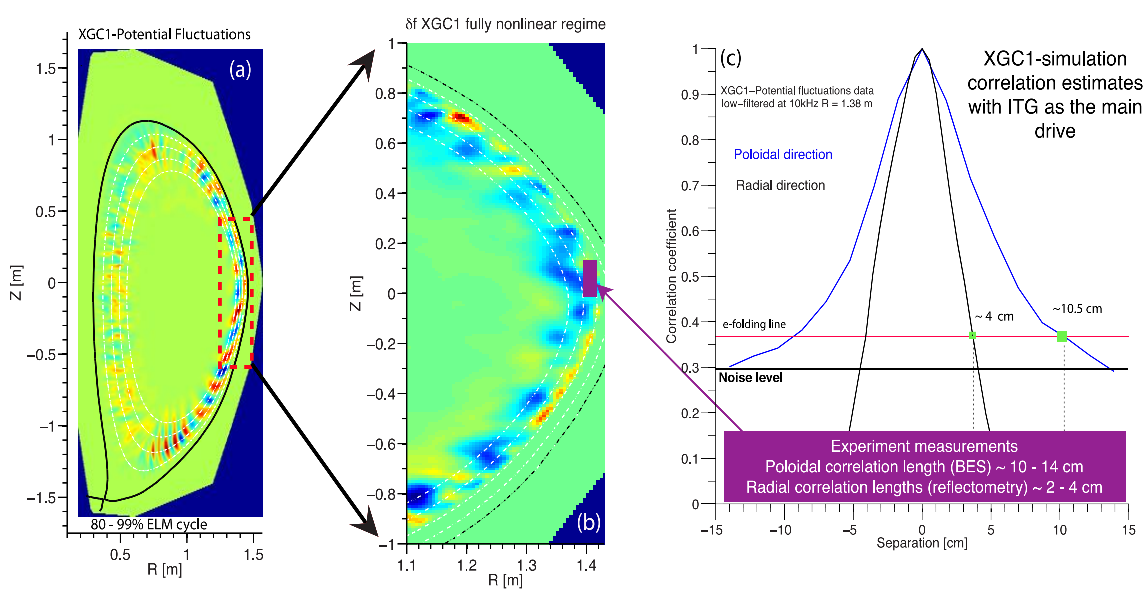

temperature gradient in this region. At mid-pedestal, a hybrid TEM/KBM mode was found to be dominant with and without lithium, with characteristics of both the TEM and KBM [BP-PED 4].

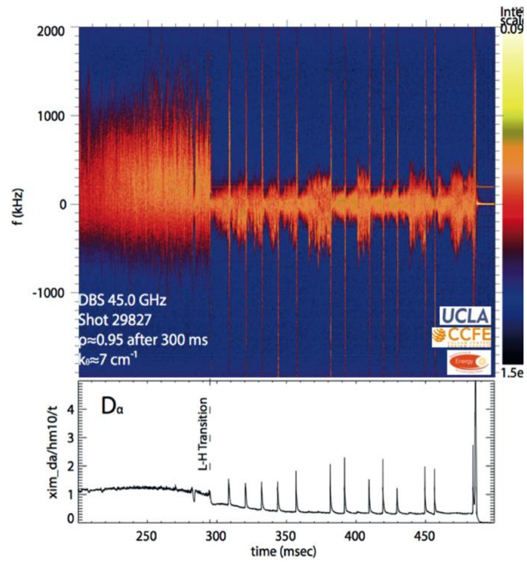

Figure BP-5: MAST shot 29827 – (top) spectrum of backscattered microwave electric field for the 44.5 GHz channel with cutoff in pedestal during H-mode, after t = 300 ms, and (bottom) D_α trace showing L-H transition and ELMs.

Local gyrokinetic linear simulations have also been performed of a separate set of discharges using the GENE code. A hybrid TEM/KBM mode was also identified in the linear GENE simulations during the last 20% of an ELM cycle near the pedestal top, similar to that found within the pedestal using GS2. Global nonlinear simulations using XGC1 have been performed on inter-ELM periods in these discharges as well, allowing the first comparisons of specific turbulent features between experiment and theory. XGC1 nonlinear global gyrokinetic calculations yielded radial and poloidal correlation lengths of potential fluctuations in the pedestal region that were consistent with those from the measurements of density fluctuations discussed above (Fig. BP-4.) [BP-PED 5, 6].

As part of a collaborative effort with the MAST tokamak in England, UCLA, and NSTX a Doppler Backscattering (DBS) was installed during the M9 campaign in 2013. DBS probes intermediate-k density fluctuations (k_θ > ~ 3 cm^{-1}). The system (16 channels, 30 – 75 GHz, cutoffs @ 1 – 7 x 10^{13} cm^{-3} in O-mode) can be configured for DBS or reflectometry. Initial DBS data looks promising. Figure BP-5 shows measurements obtained during a pedestal scaling experiment led by Dr. Ahmed Diallo from the NSTX-U team. The DBS shows a variation during the ELM cycle in the turbulent spectrum in the pedestal at $k_\theta \approx 7$ cm^{-1}.

Pedestal Analysis Software

Several enhancements and updates were made to the H-mode pedestal analysis software, which was installed at NSTX in 2008. An ability to include the fast ion pressure computed with the TRANSP transport code into the MHD equilibrium pressure profile was added which significantly improved the quality of the equilibrium fits. A new model for the bootstrap current based on results from the XGC0 code was added to the equilibrium reconstruction tool. A number of improvements were made to the codes to simplify their application including simplification and consolidation of the code run control tables, improved auto-knotting for the spline fits, and improved documentation. Several improvements in the visualization tools for equilibrium reconstruction and profile analysis were made. An iteration scheme was implemented which remaps the pressure profile in the kinetic EFIT to bring it into agreement with the measured pressure profile. Before this improvement, the pressure profile, which is input to EFIT in poloidal flux space based on a mapping from simple non-kinetic equilibrium, could be distorted by the different flux geometry in the kinetic EFIT. In the new scheme the pressure profile is adjusted for this flux geometry difference and the kinetic EFIT is rerun. A similar iteration scheme was also implemented in the 'VARYPED' EFIT equilibrium generation. The VARYPED EFIT mode is used to create a grid of variations in pedestal current density and pressure keeping the plasma beta fixed for pedestal stability analysis with ELITE. Changes in the flux geometry over the grid previously resulted in the plasma beta not being held fixed and also resulted in coupling between the current density and pressure variation which limited the grid range. In the new iteration scheme the profiles are renormalized to the total stored energy and plasma current based on the flux geometry of the varied equilibrium. This gives a more rectangular variation grid and keeps the overall plasma beta fixed. The rotation profiles were more accurately extrapolated beyond the separatrix to allow better determination of the zero crossing for the radial electric field. A provision was added to allow reconstruction of the impurity density profile from the carbon density rather than the Zeff profile. An overall scale factor for the bootstrap current was added to the kinetic EFIT tool. Failure to include the fast ion pressure and beam driven current in the kinetic EFIT tool was traced to a bug in the TRANSP MDSplus server software.

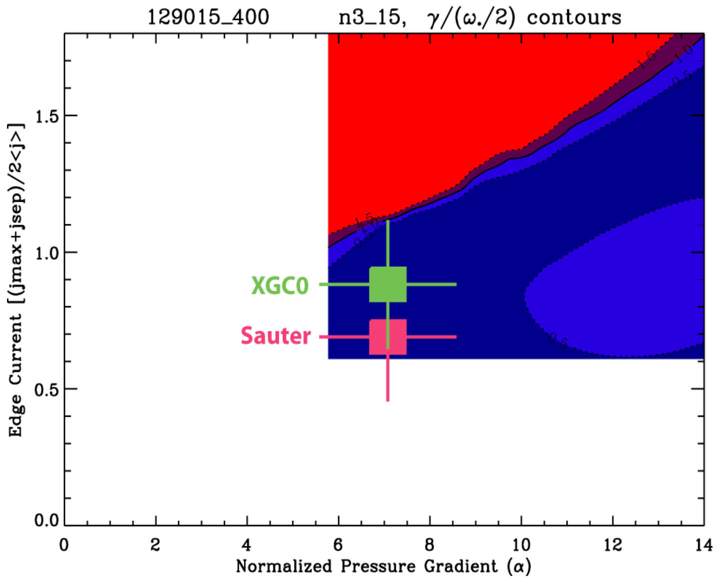

Fig. BP-6. Comparison of peeling-ballooning stability threshold (instability at $\gamma=\omega^*/2$ at boundary between red and blue regions) and pedestal conditions before a Type I ELM with pedestal bootstrap current calculated from XGC0 (green) and Sauter (magenta) models.

Analysis Results

The equilibrium and profile analysis has been applied to the study of ELM suppression in discharges with lithium conditioning leading to a number of publications including [BP-PED-7] and conference contributions. The XGC0 model for bootstrap current [BP-PED-8] predicts an enhancement over the Sauter model [BP-PED-9] by up to 40% for NSTX. ELITE peeling-ballooning stability calculations based on the XGC0 mode indicate a closer agreement between the critical current density for peeling instability and the pedestal conditions just before an ELM (Fig. BP-6).

Plans

A collaborative paper entitled "Independent Control of the Particle Transport Channel as the Critical Ingredient for Avoidance of Deleterious Edge Instabilities in Tokamaks" is in preparation for submission to Nature. The MSE data will be added to the equilibrium reconstruction. We would also like to add the ability to use density profiles from the reflectometer diagnostic as a standard in the profile reconstruction. We will also port IMFIT to NSTX. IMFIT provides a widget-based interface to several high-level analysis codes including EFIT (MHD equilibrium), ELITE (MHD stability), and TRANSP (transport). IMFIT handles construction of input files for these codes and translation of output from one code to input to another.

Projections for active control of ELMs and pedestal on NSTX

In NTSX, in addition to usual active control techniques, the lithium conditioning of the PFC has been observed to provide ELM mitigation and suppression. ELM control will continue to be a high-priority research area in NSTX-U, where the expanded capabilities of the machine will allow several new physics studies. During FY13, the impact of the Non-axisymmetric Control Coil (NCC) on ballooning stability has been investigated in order to assess how the new coil set might be expected to alter the pedestal structure. From the analysis, it was found that the NCC coils might have a strong effect on the KBM stability threshold, which in turn might modify the pedestal structure.

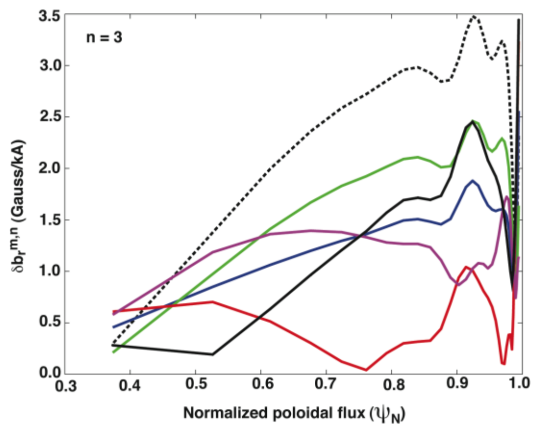

Figure BP-7: Radial profiles of $\delta b_\perp^{m,3}$ versus normalized poloidal magnetic flux for 5 optional NCC configurations as compared to a reference 2x12 primary passive plate coil $\delta b_\perp^{m,3}$ profile given by the black dashed curve with an ESLW = 0.255. Here, the solid green profile is for a 2x6 NCC with even parity and having an ESLW = 0.194, the solid black profile is for a 2x6 NCC with even parity and the lower row shifted by 30º toroidally with respect to the upper row and having an ESLW = 0.170, the solid blue curve is for a 1x12 upper row only and having an ESLW = 0.150, the solid magenta curve profile is for a 2x6 NCC with odd parity and the lower row shifted by 30º toroidally with respect to the upper row and having an ESLW = 0.103 and the solid red curve is for a 2x6 NCC with odd parity and having an ESLW = 0.026.

Non-axisymmetric Control Coil Magnetic Field Modeling

Radial profiles of the flux surface normal vacuum magnetic perturbation field ($\delta b_\perp^{m,n}$) are required to calculate the widths of magnetic islands on each rational surface, with poloidal mode number m and toroidal mode number n, and the plasma response to applied and intrinsic non-axisymmetric magnetic fields. Calculations of $\delta b_\perp^{m,n}$ as a function of normalized poloidal magnetic flux (ψ_N) have been made for various configurations of the primary passive plate NCC as part of a General Atomics collaboration on NSTX-U. Figure 1 shows the magnitude of $\delta b_\perp^{m,n}$ for n=3 perturbations with 1kAt in the NCC. In these configurations, n=3 is the only significant toroidal mode but by varying the coil pattern in the 2x12 configuration from 6 evenly spaced coils toroidally i.e., c,s,c,s,c,s,c,s,c,s,c,s where c=coil and s=space to c,s,c,s,c,c,s,c,s,c,s,s a relatively well balanced n=3 and n=4 spectrum is produced. Other NCC configurations with reduced sets of coils are being studied in order to identify profiles such as the dashed black curve in Figure BP-7 that have large $\delta b_\perp^{m,n}$ components outside ψ_N = 0.85, to produce a broad Edge Stochastic Layer Width (ESLW) while falling off rapidly with ψ_N inside 0.85 to minimize the impact of the non-axisymmetric field on the core plasma.

First observations of ELM triggering by injected lithium granules in EAST

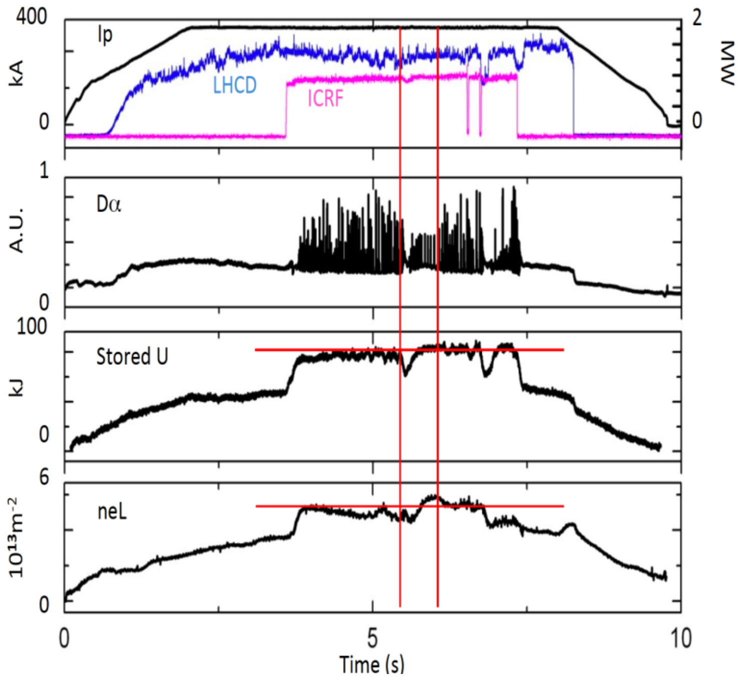

Figure BP-8: H-mode Discharge in EAST (with naturally occurring mixed Type I/Type III ELMs) into which lithium granules were injected for ~ 1 sec. Nearly every granule triggered an ELM, which became locked to the granule injection times.

Large ELMs, would be problematic for ITER, because of the associated large, periodic heat loads on plasma facing components. Two methods to address this issue are elimination of large ELMs altogether with, e.g. 3-D magnetic perturbations, or controlled triggering of rapid, small ELMs for a manageable transient heat load. One proven method for ELM triggering involves injection of periodic, high-speed cryogenic deuterium pellets. The use of fuel pellets, however, introduces the prospect of increased plasma density. The flexibility to use pellet materials other than fuel is desirable.

A granule injector [BP-PED 10] injected lithium spheres at controllable velocities and frequencies was shown to reliably trigger ELMs in H-mode discharges in the EAST device, and these results have been published in FY2013 [BP-PED 11]. Fig. BP-8 shows an ELMy H-mode from EAST; the ELMs between the red vertical lines were all paced by lithium granules. There was only a modest change in density and stored energy. It is planned to use a similar granule injector for ELM pacing studies in NSTX-U.

B. Scrape-off-layer physics

SOL turbulence experiments: Gas-Puffing Imaging Results

In FY2013 an invited paper was presented at the APS-DPP meeting on “Edge sheared flows and the dynamics of blob-filaments” by Jim Myra of Lodestar Research, which featured new data analysis of the 2010 results from the NSTX GPI diagnostic, and detailed comparisons Lodestar’s analytical and numerical edge turbulence models [BP-SOL 1]. The new ‘blob tracking’ data analysis quantified the complex motions and shape distortions of the turbulent blobs seen in the SOL, as illustrated in the small sample of blob tracks in Fig. BP-9. The modeling was able to explain the observed poloidal acceleration and blob distortion in the SOL of a specific low collisionality NSTX shot. This is an important step toward understanding the physics of the turbulent heat and particle transport in the SOL of tokamaks.

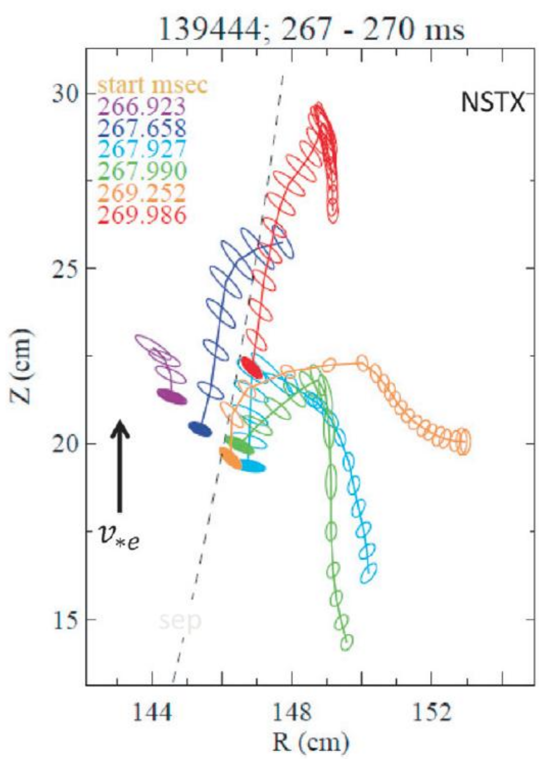

Figure BP-9: Superposition of selected NSTX blob tracks collected in a 3 msec time interval during one shot [1]. All the indicated tracks start in a small region near the filled ellipses. Start times for each track are given in the inset. The electron diamagnetic drift direction is up, and the EFIT separatrix is shown with a dashed line.

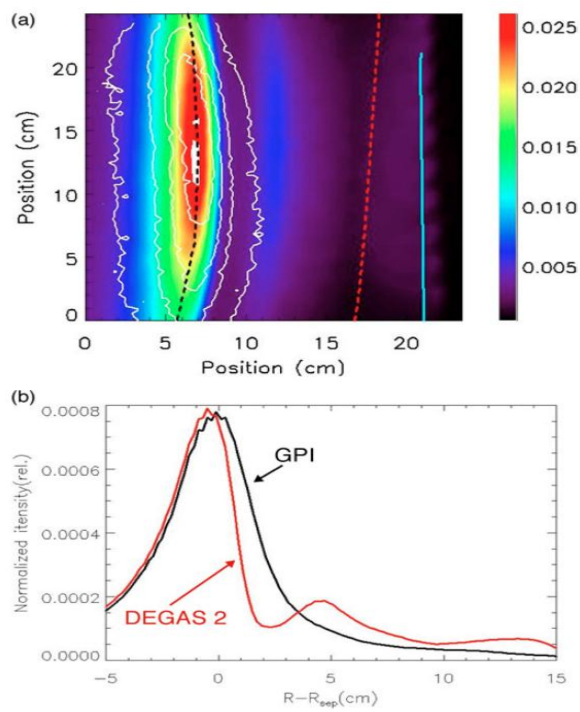

Fig. BP-10: Comparison between the D_α light emission from DEGAS 2 and GPI data for #141324. (a) The color contours are the DEGAS 2 results in units of W / (sr m^2), the equally spaced white contours are the GPI results, the leftmost dashed line is the separatrix, the rightmost dashed line is the limiter shadow, and the nearly vertical line is the gas manifold. (b) The 1-D profiles are obtained by normalizing the 2-D data to the sum over all pixels and then averaging over vertical pixels. The horizontal coordinate is mapped to the outer midplane separatrix.

Also completed and published in FY2013 was a comparison between the GPI gas puff and the DEGAS 2 Monte Carlo neutral transport code [BP-SOL 2], serving as a validation test of DEGAS 2. The radial widths and peak locations of the simulated and measured light emission profiles agreed to within the estimated uncertainties (Fig. BP-10), similar to previous validation efforts. An important new aspect of this validation was a comparison of the absolute magnitude of the light emission. The experimental result for a particular shot was 1/89 +/- 34% photons per atom, while the DEGAS 2 simulation yielded 1/75 +/- 18% photons per atom, again agreeing to within the estimated uncertainties.

A study of the 2-D structure of wave-like ELM precursors [BP-SOL 3] was published, showing the development and ejection of a blob-filament in extraordinary detail, as illustrated in Fig. BP-11. This work was led by graduate student Yancy Sechrest of the University of Colorado. A description of the tools for browsing through large GPI data sets and database techniques for characterizing and visualizing blobs identified in the GPI data was described at an IAEA Technical Meeting in Hefei, China [BP-SOL 4].

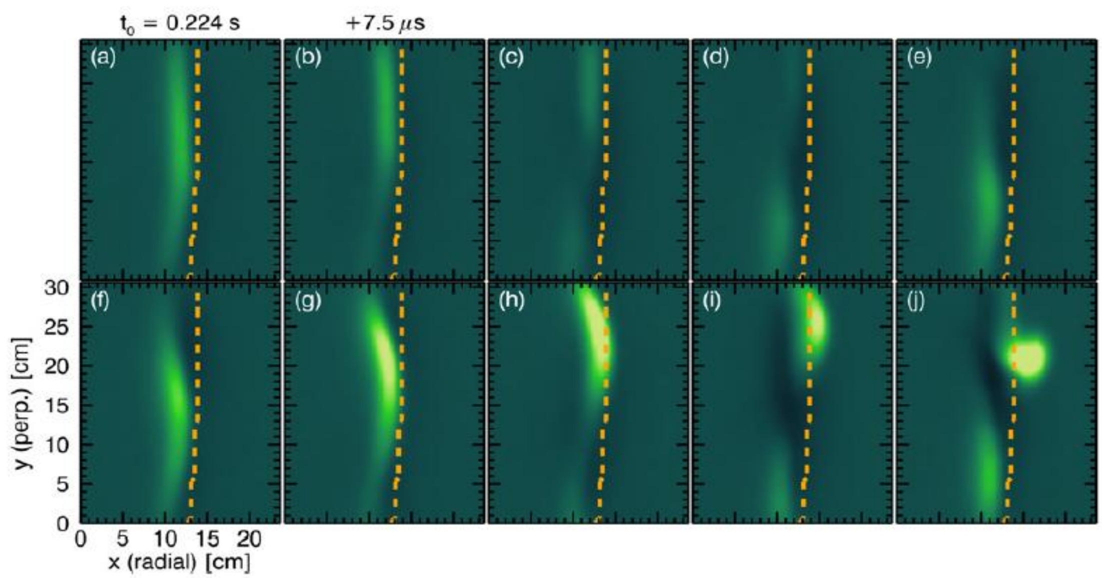

Fig. BP-11: Multiframe image stills of an ELM event with precursor intensity fluctuations from shot 141918. The time between frames is 7.5μs. Distinct mode structure can be seen in precursor oscillations leading to the ejection of the filament in the last two frames. The approximate location of the separatrix is indicated by the dashed line.

New NSTX GPI data analysis work in started in 2013 includes a detailed comparison between edge turbulence data from GPI and beam emission spectroscopy (BES) [BP-SOL 5], and a close examination of the effects of the GPI gas puff on the NSTX edge plasma [BP-SOL 6]. Preliminary results show a high correlation between the turbulence seen in GPI and BES, and a relatively small effect of the GPI puff on the NSTX edge plasma.

Two papers were published in FY2013 from the continuing NSTX collaboration with the EAST tokamak group in China on GPI. The first described the new GPI diagnostic hardware on EAST [BP-SOL 7], and the second described measurements of the turbulence velocity during the dithering L–H transition made using this diagnostic [BP-SOL 8]. Both papers were led by Chinese graduate students at EAST.

SOL turbulence modeling

Lodestar researchers have completed a study of the dynamics of blobs filaments and sheared flows in NSTX edge and SOL plasmas. Previous work [BP-SOL 9] was extended to enable quantitative model comparisons with 2D-spatial, time-resolved GPI data using both seeded blob simulations and quasi-steady turbulence simulations. The exchange of momentum between blobs and flows was evaluated in the model and compared with data using both blob tracks and the observed elliptical deformation of structures related to the Reynolds stress. Mechanisms modeled in the SOLT code were shown to be sufficient to explain the observed Reynolds acceleration. These mechanisms have implications for spontaneous flow generation and symmetry breaking: edge profiles and SOL current flow considerations imply a residual Reynolds stress, i.e. a natural direction for the flows. The work was presented in an invited talk at the APS-DPP meeting [BP-SOL 10] and was recently published [BP-SOL 11].

In separate ongoing work, Lodestar is carrying out SOL turbulence simulations for the heat flux width to assess the effect of lithium coatings [BP-SOL 12]. In the experiment, gradients of plasma energy and particle density as well as density fluctuations are observed to be reduced at the edge in the presence of lithium. This suggests that drift-interchange-driven turbulence plays a role in setting heat flux characteristics in these experiments. To explore this possibility, we have simulated the edge turbulence, in the outboard midplane, driven by edge plasma profiles measured in two NSTX shots, with and without lithium. The study employs the SOLT model code, newly expanded [BP-SOL 13] to include self-consistent ion diamagnetic drift evolution. Initial results show simulated SOL widths within the range of experimental observations and a reduction of edge density fluctuations in the lithium case. Detailed comparisons with shot-specific data and analysis of the underlying simulated turbulence are in progress.

C. Divertor Physics

Snowflake Divertor Projections for NSTX-U

The snowflake (SF) divertor was proposed by Ryutov in 2007 [BP-DIV 1] and many of the predicted magnetic and geometry properties have been confirmed in experiments in TCV, NSTX, and DIII-D. The NSTX experiments, in particular, demonstrated a significant inter-ELM and ELM peak divertor heat flux reduction, reduction of core impurities, and impact on pedestal MHD stability, compatibility with H-mode confinement characterized by acceptable H-mode factors [BP-DIV 2]. The SF divertor configuration is considered a leading heat flux mitigation technique for NSTX-U.

In NSTX-U, two up-down symmetric sets of four divertor coils will be used to test SF divertors for handling the projected steady-state peak divertor heat fluxes of 20-30 MW/m^2 with $I_p \leq 2$ MA, $P_{NBI} \leq$ 12 MW, with pulse length ~ few sec. Magnetic equilibria with SF configurations have been successfully modeled using the ISOLVER Grad-Shafranov equilibrium solver and showed that a robust SF control can be maintained even when time-dependent electromagnetic effects are included.

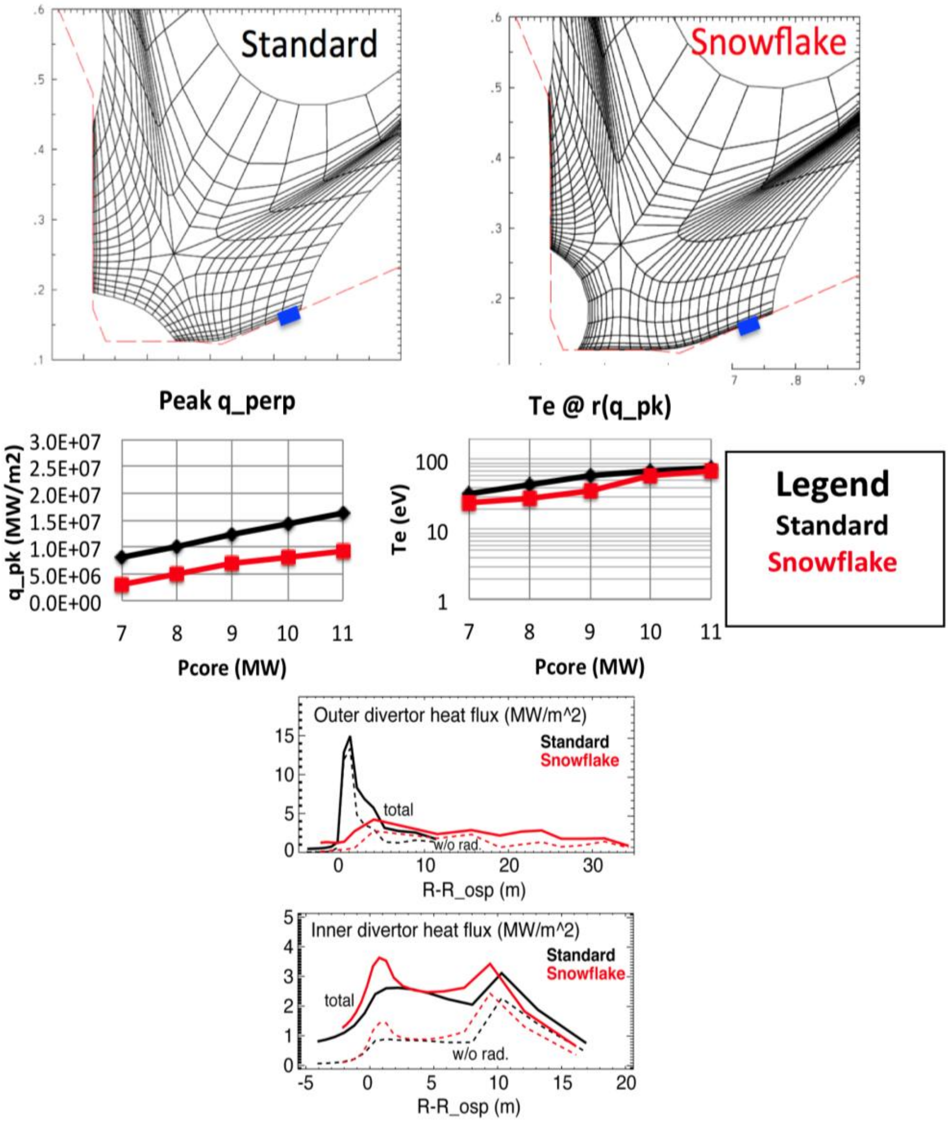

Figure BP-12: Projections of snowflake divertor parameters to NSTX-U from UEDGE modeling: (a – top row) high resolution numerical mesh for standard and snowflake divertors; (b – middle row) peak divertor heat flux and Te as a function of SOL power; (c – bottom two panels): inner and outer divertor heat flux profiles for the 12 MW input power case.

2-D multi-fluid transport models of the SF configuration have been developed for NSTX-U using the UEDGE code. The modeling projections for the NSTX-U SF divertor geometry are favorable and show large reductions in divertor T_e, T_i, as well as peak divertor heat fluxes due to the geometric and radiation effects, both with 4% of carbon impurity and with neon or argon seeding. The modeling results are summarized in Figures BP-12 and BP-13. SF divertor solutions high radiation fraction and P_{SOL} up to 12 MW were obtained, with q_{peak} reduced from ~15 MW/m^2 (standard) to 0.5-3 MW/m^2 (SF). The compatibility of cryopumping and SF power exhaust were also assessed via simulating a reduced neutral albedo at the cryo-pump duct location. It was found that cryopumping would reduce divertor density and radiation, resulting in reduced volumetric power and momentum losses. Nonetheless, the heat flux reduction due to SF geometry would still make the SF an attractive heat flux mitigation scenario.

Radiative divertors use deuterium and/or seeded impurities to reduce divertor particle and heat fluxes through volumetric momentum and energy dissipative processes - the ion-neutral elastic and inelastic collisions, recombination and radiative cooling. In NSTX radiative divertor experiments with D_2 and CD_4 seeding, a significant reduction of divertor heat flux from peak values of 4–10 MW/m^2 to 0.5–2 MW/m^2, simultaneously with good core H-mode confinement, has been demonstrated in 1.0–1.3 s discharges. These experiments demonstrated that partial divertor detachment was obtainable in a compact divertor of a high power density ST even with carbon radiation. It is clear, however, that in order to dissipate SOL powers in excess of 5-10 MW in NSTX-U, higher Z impurities (e.g., nitrogen, neon or argon) will be required. Initial multi-fluid edge transport models have been developed for NSTX-U projections with the UEDGE code. The models showed that peak divertor heat flux reduction via partial detachment can be achieved in both the standard and the SF divertor configurations (easier with the latter) in NSTX-U with neon or argon seeding (e.g. Figure BP-13).

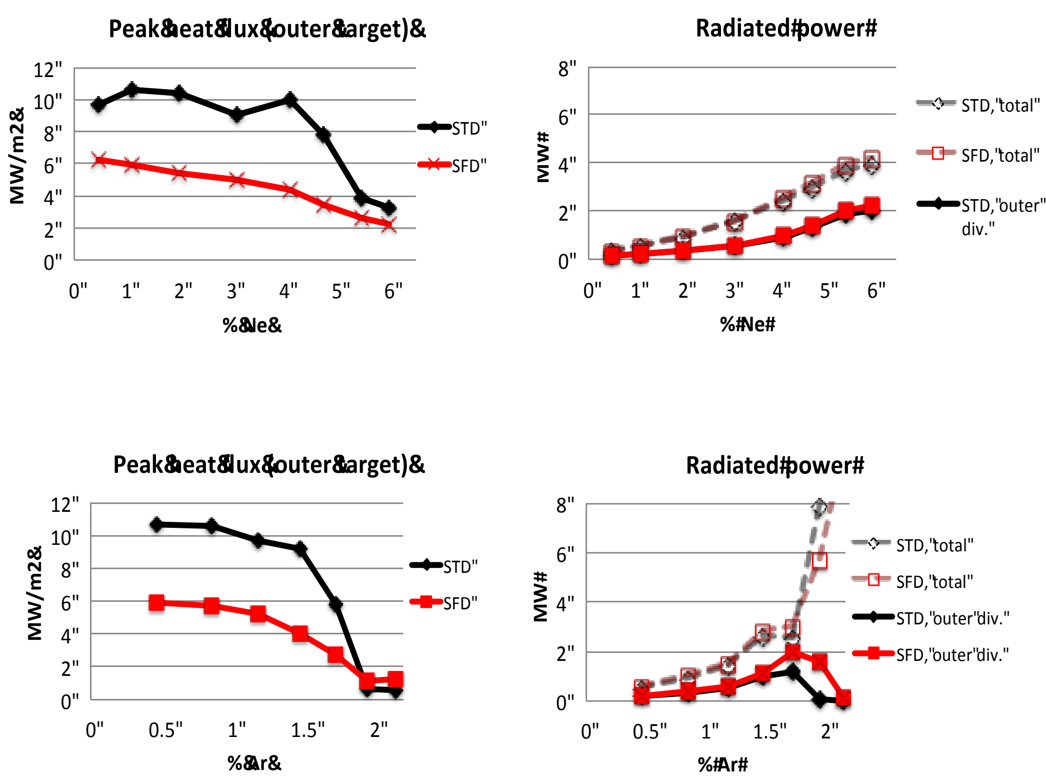

Figure BP-13: Projections of radiative divertor parameters for the standard (STD) and snowflake (SFD) geometries in NSTX-U: Peak heat flux and radiated power with (a – top row) Neon and (b – bottom row) Argon seeding.

Divertor Diagnostics Preparation: Absolutely Calibrated Tangential Imaging

Work is currently underway to upgrade the lower divertor tangential imaging system [BP-DIV 3] of NSTX, adapting it to the NSTX-U device and being able to perform absolutely calibrated measurements. The largest difficulty when performing the calibration for this imaging system resides not on the calibration itself but in maintaining this calibration throughout the several months-long experimental campaign. Coatings inevitably develop through the campaign on the vacuum interface window and other invessel optics such as mirrors. One of the main aspects of the current work is the implementation and use of invessel illumination hardware that will permit the measurement of the optics transmission as the campaign progresses.

Good progress has been made in FY 2013 in the design of the hardware that would result in an absolutely calibrated tangential imaging system for the lower divertor of NSTX-U. A conceptual design review was carried out on Feb. 14, 2013 and final drawings are currently being prepared by engineers at PPPL, namely Bob Ellis. A final design review is expected within the next few weeks (later part of Sept. 2013) to then proceed, if successful, to procurement of parts and fabrication.

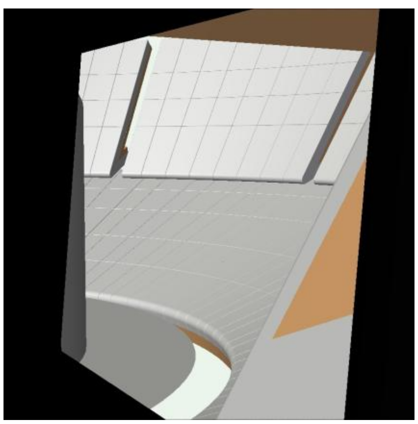

Fig. BP-14 (a) View in NSTX-U through gap on tiles, as reflected on mirror.

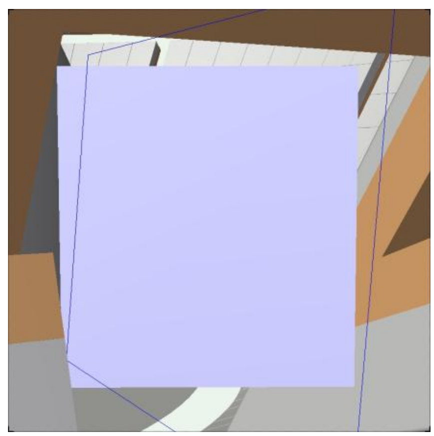

(b)View of diffuse target plate (the edge of the mirror is drawn as reference).

The expected view of the lower divertor of NSTX-U is shown in Figure BP-14(a). The divertor plasma will be observed through a gap on the lower passive plate tiles in Bay F, having the lower passive plate between Bays B and C in the background. The bottom section of the new center stack can be seen on the left within the field of view of the camera. In order to monitor the transmission and reflection of the invessel window and mirror, a target plate made of sand-blasted stainless steel is inserted in field of view (right drawing in figure). This plate acts as a diffuse lambertian source and illumination is provided through a re-entrant set of quartz fibers that are inserted by means of a bellows mechanism.

The absolute calibration is performed while there is manned access to the vessel, before and after the experimental campaign, the measurement of the optics transmission/reflection is done on some days after the day’s experiments have finished.

Divertor diagnostics preparation: Upper Divertor Spectroscopy

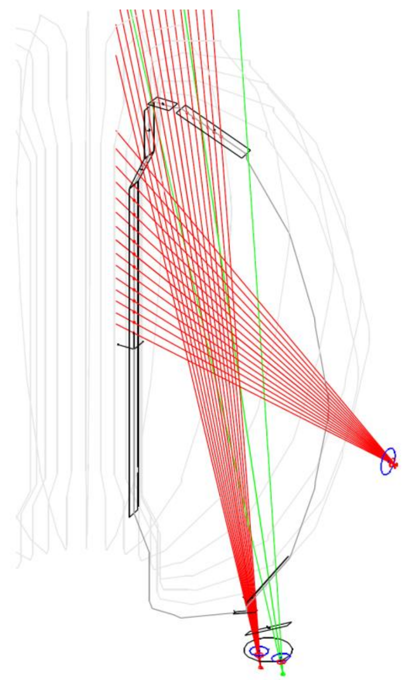

Figure BP-15. Schematic of the diagnostic lines of sight, of the UTK spectroscopic diagnostics. Access from the equatorial plane and machine bottom allow to cover the central column and the upper divertor regions.

Use of lithium wall conditioning has been a key element of the latest NSTX campaigns, with beneficial effects in terms of low recycling, ELM suppression and improved confinement. Lithium coating will be strong part of the experimental program of NSTX-U. Nevertheless, many physics and operational aspects are still to be clarified, especially in view of use of lithium coatings in next step ST devices (FNSF). On one hand, the complex chemistry at play at the wall surface during plasma exposure has still to be understood. This involves complex chemical bounds between D, Li, O, C and elements from refractive substrates, that simulation and experiments have just begun to unravel. On the other hand, the continuous improvement of plasma performance with lithium evaporation remains an open question, intimately related to the issue of material erosion, migration and redeposition. Advancing the understanding of these issues requires accurate characterization of the surface characteristics, especially regarding spatial distribution of lithium layer within the vessel.

To address these issues from an experimental standpoint, a collaboration program with University of Tennessee Knoxville has been established, under FOA collaborative program 2012-2015. The ongoing collaboration supports one postdoctoral scientist on site, and will bring to NSTX-U a set of new diagnostics, whose design, during 2013, has been completed and procurements are ongoing at the time of writing. The key diagnostic comprises two multi-channel spectroscopic view and two infrared views of wall regions previously largely under sampled: the upper divertor and the central stack (Fig. BP-15)

The spectroscopy diagnostic design considers the installation of two collection optics assemblies, each housing an imaging objective lens and a holder for 16 optic fibers heads. The first assembly, equipped with a 105 mm, F/4.2 lens, will be installed at a Bay G bottom port and will provide 16 lines of sights, measuring the upper divertor, from R=0.45 to 0.90 m. The second will be installed at an equatorial Bay J port, with a 60 mm, F/4 lens that provides the larger field of view required to cover the central stack from Z=0 to Z=1.20 m. The optical elements (sapphire vacuum windows, high OH fused silica fibers, and commercial UV graded imaging objectives) are chosen as to ensure transmission in the visible and ultra-violet range of wavelengths (~350-700 nm), to maximize the opportunity of measuring radiation from atomic and molecular impurity species. The spectral analysis of the collected radiation will be performed in the diagnostic acquisition room (DARM) adjacent to the main experimental chamber, where the two bundles of 16 fibers will be connected to a dedicated multi-channel Czerny-Turner spectrometer (320 mm, F/4.6), through a patch panel. These diagnostics will provide spatially and temporally resolved measurement of visible and UV emission from near-wall regions, permitting to characterize the near-wall processes by monitoring the abundance of atomic (e.g. C, Li, O) and molecular species, (Li_2, CD, LiD, Li oxides) within a single plasma discharge and throughout the campaign.

Under the same program, in close collaboration with the ORNL group, the staged installation of two new infrared cameras is included, to extend the pre-existing thermography imaging coverage. The cameras will be installed at Bay G bottom and Bay J equatorial ports to provide measurement to couple with the spectroscopy lines of sights (i.e. upper divertor and central stack). Both cameras will be equipped with a fast-dual-band adapter, for the simultaneous acquisition of imaged in the medium (4-6μm) and long (7-10 μm) infrared, in order to obtain temperature measurement from signal rations, more robust against emissivity and transmission issues. This extended IR imaging capability will enable, not only to study heat flux deposition, but also to measure the tile surface temperature, a key element for modeling of surface evolution, sputtering and erosion rates.

The new diagnostics supported by UTK are intended to complement the existing IR and spectroscopy diagnostics, providing an up/down symmetric coverage of most of the plasma-exposed wall. This capability will be key in NSTX-U, where it is foreseen: (i) to employ double divertor configuration for handling the increased power exhaust; (ii) to introduce Lithium evaporation of upper divertor; (iii) to begin the staged installation of refractory material tiles (Mo).

Parallel SOL transport of intrinsic impurities in NSTX discharges

NSTX H-mode discharges with lithium evaporative coatings are characterized by the suppression of ELMs and a concomitant impurity accumulation with Z_{eff} up to 4 as a result of core carbon buildup [BP-DIV 4]. Although the lithium divertor gross influxes are larger than the carbon ones, lithium does not accumulate in the core and has typical densities of less than 1% of the carbon densities [BP-DIV 5]. Core transport can account only partially (up to a factor of 10) for the difference in the carbon and lithium core inventories. This is a result of the higher neoclassical particle diffusivities for lithium due to the high carbon densities in the NSTX core [BP-DIV 6].

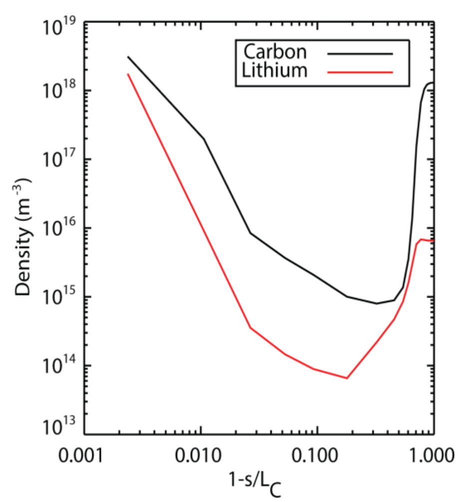

Figure BP-16: Parallel impurity density profiles from a UEDGE simulation in NSTX geometry: carbon in black and lithium in red.

The 2D multi-fluid edge transport code UEDGE [BP-DIV 7] was used to perform simulations in NSTX and slab geometry to understand the differences in parallel transport for carbon and lithium impurities sourced from the NSTX divertor [BP-DIV 7]. In the simulations, charge state resolved carbon and lithium impurities were included. Flux-limited, classical parallel transport was assumed. Midplane kinetic profiles for electron and impurity densities and electron and ion temperatures were used as a constraint for the *ad-hoc* radial particle diffusivities and ion and electron heat conductivities. Divertor heat flux, impurity and deuterium divertor emission were used as a constraint for divertor recycling and impurity sputtering at the target.

Figure BP-16 shows parallel profiles of total carbon (black) and lithium (red) densities along a flux tube in the SOL as a function of the normalized parallel length $1\text{-}s/L_C$, where s is the parallel distance from midplane and L_C is the midplane-to-target connection length (i.e. $1\text{-}s/L_C=0$ represents the target, $1\text{-}s/L_C=1$ represents midplane). The steeper decrease of the lithium density in the near target region ($1\text{-}s/L_C<0.02$) and the weaker pickup upstream ($1\text{-}s/L_C>0.2$) result in upstream lithium densities which are up to 100 times less than carbon densities. In the near target region this is due to the narrower lithium source profile resulting from the shorter lithium ionization mean free path. Upstream, the weaker pickup results from the weaker classical ion temperature gradient force for lithium, due to the lower effective charge with respect to carbon. Differences in parallel transport between carbon and lithium can then potentially contribute to the observed difference in the experimental core impurity inventories.

A scan in the divertor recycling coefficient in UEDGE simulations indicated the worsening of the divertor impurity retention with lower divertor recycling. This suggests that the reduction in divertor carbon influxes observed with lithium conditioning [BP-DIV 7] can be counteracted by the effect of the reduced recycling on the divertor impurity retention. A scan in the lithium sputtering yield (up to a factor of 5 higher than what measured experimentally) indicated that divertor radiation is still dominated by deuterium and carbon while lithium radiation appears to play a small role in the divertor power balance of typical NSTX discharges.

Divertor recycling studies: dependence of H-mode plasma performance on pre-discharge lithium evaporation in high triangularity shapes in NSTX

NSTX used toroidally displaced LiThium EvaporatoRs (LiTERs) to coat divertor plasma-facing components (PFCs) between discharges, initially with carbon PFCs (2009 and earlier) and then with a liquid lithium divertor (LLD) in 2010. Discharges at intermediate triangularity and low elongation with lithium evaporated on graphite PFCs exhibited nearly continuous improvement of edge confinement and stability with increasing pre-discharge evaporation [e.g. BP-DIV 8 and references therein]. A parallel experiment with increasing pre-discharge lithium evaporation in high triangularity, high elongation discharges envisioned for future STs has been analyzed; the trends are similar to those reported for the weakly shaped discharges, demonstrating the benefit to highly shaped discharges. Fig. BP-17(a)-(c) shows that the $D_{\square}$ emission from the lower divertor, center stack, and upper divertor gradually decrease with increasing pre-discharge lithium, reflecting the overall reduction in recycling. Panels BP-17(d)-(e), (g) show that the lower divertor Li-1 light first increases and then saturates, while the line-average density from Thomson Scattering (taken at a fixed time: t=0.325 sec) and mid-plane neutral pressure generally decrease. Panel BP-17(f) shows that the global energy confinement time normalized by the H97L scaling law increases with pre-discharge lithium, albeit with a somewhat weaker dependence than exhibited in the previous dataset [BP-DIV 8]. Thermal confinement analysis also reflects a weaker trend than at lower shaping [BP-DIV 9]. Detailed edge pedestal and stability analysis is commencing, toward determination of the reason for the weaker trend.

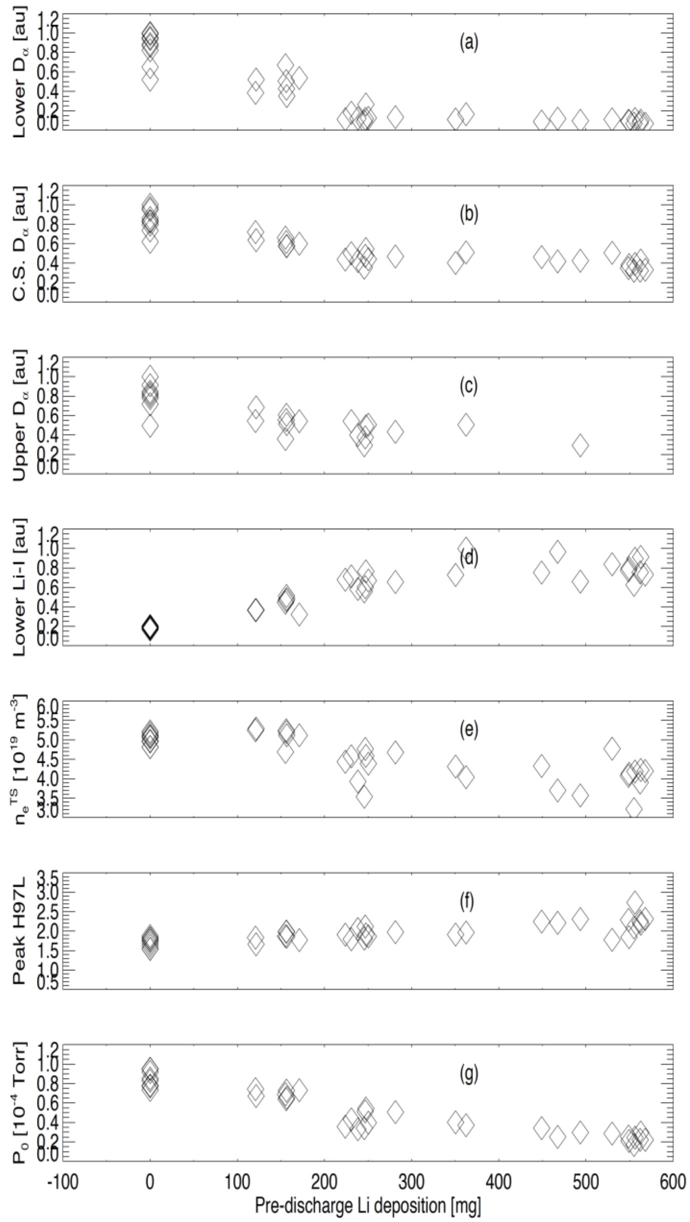

Figure BP-17: dependence of discharge parameters as a function of pre-discharge lithium evaporation: (a) lower divertor D_α, (b) center stack D_α, (c) upper divertor D_α, (d) lower divertor Li-I line emission, (e) line-averaged density form Thomson Scattering at t=0.325 sec, (f) peak energy confinement relative to ITER L-mode 97 scaling,

References

[BP-PED 1] A. Diallo, et al., Nuclear Fusion **51** (2011) 103031.
[BP-PED 2] D.R. Smith, et al., Physics of Plasmas **20** (2013) 055903.
[BP-PED 3] D.R. Smith, et al., submitted to Nucl. Fusion, 2013.
[BP-PED 4] J.M. Canik, et al., Nucl. Fusion at press, 2013.
[BP-PED 5] A. Diallo, et al., Physics of Plasmas **20** (2013) 012505.
[BP-PED 6] A. Diallo, et al., Nucl. Fusion, **53** (2013) 093026
[BP-PED 7] R. Maingi, et al., Nucl. Fusion **52**, 083001 (2012).
[BP-PED 8] S. Koh, et al., Phys. Plasmas **19**, 072505 (2012).
[BP-PED 9] O. Sauter, et al., Phys. Plasmas **6**, 2834 (1999).
[BP-PED 10] D.K. Mansfield, et al., Fusion Eng. Des. **85** (2010) 890
[BP-PED 11] D.K. Mansfield, et al., submitted to Nucl. Fusion, 2013.

[BP-SOL 1] J.R. Myra, et al., Nuclear Fusion **53** (2013) 073013.
[BP-SOL 2] B. Cao, et al., Fusion Science and Technology **64** (2013) 29.
[BP-SOL 3] Y. Sechrest, et al., Nuclear Fusion **52** (2012) 123009.
[BP-SOL 4] W.M. Davis, et al., to be published in Fusion Engineering and Design.
[BP-SOL 5] Y. Sechrest, et. al., "Direct comparison of GPI and BES measurements of edge fluctuations in NSTX", APS DPP abstract, 2013.
[BP-SOL 6] S.J. Zweben et al, "Effects of a GPI deuterium gas puff on the edge plasma in NSTX", APS DPP abstract, 2013.
[BP-SOL 7] S. C. Liu, et al., Rev. Sci. Inst. **83** (2012) 123506.
[BP-SOL 8] L.M. Shao, et al., Plasma Phys. Cont. Fusion **55** (2013) 105006.
[BP-SOL 9] J. R. Myra, et al., 24th IAEA Fusion Energy Conference, San Diego CA, October 8 – 13, 2012, paper 251-TH/P4-23.
[BP-SOL 10] J. R. Myra, et al., Bull. Am. Phys. Soc. **57**, 371 (2012), paper YI3-2.
[BP-SOL 11] J. R. Myra, et. al., Nucl. Fusion **53** (2013) 073013.
[BP-SOL 12] D.A. Russell, et. al., 55th Annual Meeting of the Division of Plasma Physics, November 11-15, 2013 Denver, Colorado.
[BP-SOL 13] D.A. Russell et al., Bull. Am. Phys. Soc. **57**, 67 (2012), paper BP8-159.

[BP-DIV 1] D.D. Ryutov, et. al., Phys. Plasmas **14** (2007) 064502.
[BP-DIV 2] V.A. Soukhanovskii, et. al., Phys. Plasmas **19** (2012) 082504.
[BP-DIV 3] A.L. Roquemore, et. al., Rev. Sci. Instrum. **75** (2004) 4190.
[BP-DIV 4] F. Scotti et al., Nucl. Fusion **53** (2013) 083001.
[BP-DIV 5] M. Podesta et al., Nucl. Fusion **52** (2012) 033008.
[BP-DIV 6] T. Rognlien et al., Contr. Plasma Phys. **38** (1998) 152.
[BP-DIV 7] F. Scotti, invited talk at 2012 American Physical Society – Division of Plasma Physics meeting.
[BP-DIV 8] R. Maingi, et. al., Nuclear Fusion **52** (2012) 083001.
[BP-DIV 9] S.M. Kaye, et. al., Nuclear Fusion **53** (2013) 063005.

Materials and PFC Research for NSTX-U

Magnum-PSI Collaboration Experiments

Experiments on lithiated plasma facing component materials have been conducted on the Magnum-PSI linear plasma device located at the Dutch Institute for Fundamental Energy Research (DIFFER). Magnum-PSI is a magnetized, linear plasma device designed for simulating the divertor conditions expected in ITER-class devices (10^{21} m^{-3}, T_e ~ 1-5eV) [MP-1]. The device currently operates with copper magnetic fields coils with discharge lengths from 5-50s (field dependent) and will soon be upgraded to provide steady-state discharges with a superconducting magnet. The plasma conditions present at the Magnum-PSI target provide similar density and temperatures as those found in NSTX, for example, during the recent liquid lithium divertor campaign [MP-2].

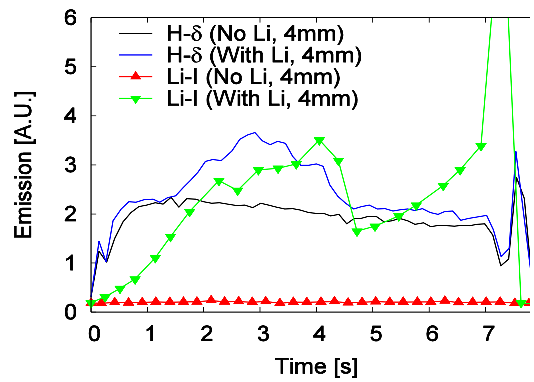

Figure MP-1: *Optical emission from the Magnum-PSI plasma column during high-temperature lithium exposures.*

To support these experiments an NSTX-developed, prototype evaporator (the LITER-1C) was installed on the Magnum-PSI experimental device and loaded with lithium. Lithium was then deposited onto a substrate material after calibrating the deposition rate in the Magnum-PSI preparation chamber. High-power discharges were performed which resulted in a temperature ramp of the surface up to 1300C over the course of 7 seconds and the plasma response to this high-temperature surface was examined with the use of Thomson scattering, optical emission spectroscopy, and heat-flux to the material surface deduced from infrared measurements (both 2D camera and multi-wavelength pyrometry). Filtered fast camera images were taken with a view tangential to the surface of the sample. Exposures were conducted comparing conditions with and without a 1 micrometer-thick lithium layer.

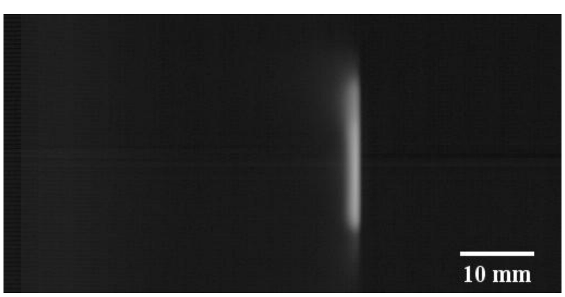

Figure MP-2: *Fast camera image of the lithium emission directly in front of the target (671 nm). The vapor cloud was found to persist 3-4 seconds during plasma bombardment after which time emission transitioned into different regime of erosion.*

During the course of exposures, two regimes were found: (1) an intense cloud of lithium emission was formed directly in front of the target and persisted for 3-4s which then transitioned into (2) a less intense, more diffuse emission pattern. This transition is shown in Figure MP-1 with a chord through the plasma column 4mm in front of the target. An image of the vapor cloud is shown in Figure MP-2. A reduction of current to the target was observed which increased again after the transition in emission. However, power incident on the target was not found to decrease during these discharges. This is a subject of current study but could be reflective of the difference in reflection coefficients between a high-Z (molybdenum) substrate vs. a lithium-coated substrate, and a conversion of the near-surface plasma to a nearly 100% lithium plasma. As Magnum-PSI does not have a significant electron temperature gradient, the plasma is nearly isothermal at 2-4eV for these experiments. These temperatures are unlikely to generate excited states of Li^{1+} and, in fact, no Li-II emission was observed throughout the discharges (548nm emission was monitored). In a tokamak, however, Li-II emission is expected to provide additional power-loss mechanisms and highlights the importance of complementary experiments in NSTX-U.

Erosion and re-deposition of lithium coatings on TZM molybdenum and graphite during high-flux plasma bombardment

Graphite is the planned initial plasma-facing component (PFC) during the first year of operation of the NSTX-Upgrade (NSTX-U) experiment. The installation of a row of TZM molybdenum tiles in the lower outboard divertor is planned after the first run year. Techniques for conditioning the graphite and Mo tiles include the application of evaporative lithium films: these mitigate impurity influx into the core and reduce recycling. Thus it is crucial to plasma performance that the film does not fully erode until a fresh coating is applied. To ensure the efficacy of these films, we need to understand the spatial evolution of the areal density of the coating in the presence of plasma bombardment. Previous experiments [MP-3, MP-4] have measured the gross erosion rate of Li in the presence of D^+ ion bombardment, but these studies were limited to low densities at which minimal Li re-deposition occurs. These studies were also limited to below 500C.

A 3-D semi-analytic erosion/re-deposition model has been developed to simulate the dominant mechanisms of atom loss/gain in thin films. The coating areal density ρ_z is reduced by sputtering, evaporation, and 1-D diffusion into the material. Re-deposition can also increase or reduce the rate of decrease of ρ_z. The model calculates the 3-D ionization rate profile of neutral Li atoms using the ADAS collisional-radiative model [MP-5] as input. It is assumed that all ionized Li re-deposits on the target due to biasing and ion flow. This model predicts near-unity re-deposition fractions for Li-coated TZM Mo targets under bombardment from plasmas of $n_e \sim 10^{20}$ m^{-3} and $T_e \sim 1.5$ eV.

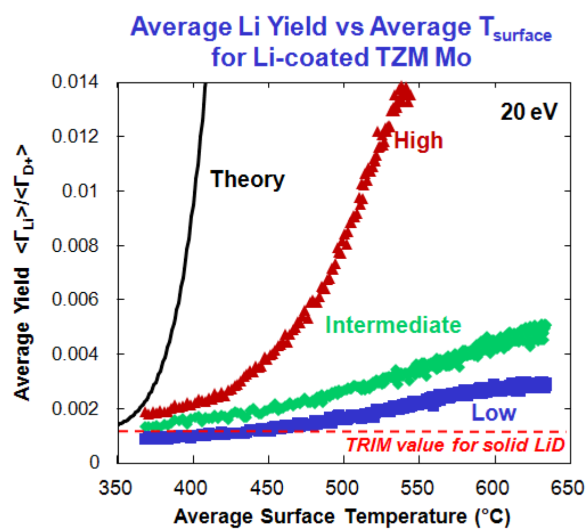

Figure MP-3: *Measured Li yield on Li-coated TZM Mo as a function of sample temperature during each observed "erosion regime." The high-yield regime exhibits an enhancement of approximately a factor of 5 over the intermediate regime. Even the high yield regime lies significantly below the theoretical yield predicted from TRIM and Langmuir evaporation.*

The time evolution of lithium coatings on graphite and TZM Mo were studied in Magnum-PSI [MP-6], a linear plasma device, using ion fluxes up to 10^{24} m^{-2}s^{-1} at electron temperatures < 4 eV. A series of 2-7 s plasma exposures at normal magnetic incidence were run on bare samples of each substrate then repeated after a deposition of 100-1000 nm of Li. Neutral Li density was inferred from fast camera with a Li-I (670.8 nm) filter. Parameter scans were performed in average sample temperature (350 – 650 ˚C). Figure MP-3 portrays three different regimes of Li erosion yield that were observed for Li-coated TZM Mo. The first, "high yield" regime exists while the ratio of integrated D^+ fluence to initial Li areal density is approximately $\Phi_{D+}/\rho_{Li} \leq 250$. An "intermediate" yield regime persists until this ratio reaches $\Phi_{D+}/\rho_{Li} \sim 4000$. Finally, the sample enters a "low yield" regime consistent with evidence of full depletion of Li from the sample. These regimes were similar to those observed during experiments with a 1 micrometer-thick coating described above.

Measured Li coating lifetimes were much shorter on Li-coated graphite. Depletion of the Li coating was observed to begin at $\Phi_{D+}/\rho_{Li} \sim 300$. Even with zero re-deposition, the Li coating was predicted to last until $\Phi_{D+}/\rho_{Li} \sim 5000$ given the measured Li yield. This fast decrease in Li yield on Li-coated graphite is a possible indicator of Li diffusion into the bulk graphite material. The solution of the 1-D diffusion equation for Li in graphite predicts a lifetime < 4s for the 250 nm Li coating using the measured diffusion coefficient D_{Li} in carbon [MP-7] at room temperature. These results suggest the usefulness of high-Z materials as a substrate for Li and B coatings in NSTX-U in order to strongly enhance the film lifetimes.

Whole-machine material migration studies in NSTX discharges

During the last 6 months of FY2013, the Materials and PFCs group has worked to open up a new research effort focusing on long-scale tokamak-induced material migration. The rationale is this: as fusion reactors scale up in size, power, and duty cycle, the quantity of material eroded from the plasma-facing components will rise to levels far above those seen in prior experiments. Changes to PFC composition and topography due to global-scale material migration could have drastic effects on tokamak operation, especially in mixed-material machines such as NSTX-U and ITER. The increased power and small surface area of NSTX-U make it uniquely suited for generating eroded material and studying its transport.

While we have plans to study the erosion and deposition of lithium, molybdenum, and mixed materials, initial analysis has focused on carbon erosion and transport so as to take advantage of NSTX-U's all-carbon initial phase and to establish the physics mechanisms that govern long-range material transport. Computational analysis of poloidally-resolved carbon erosion and deposition patterns in NSTX discharges can now be carried out using the OEDGE (OSM + EIRENE + DIVIMP) code suite.

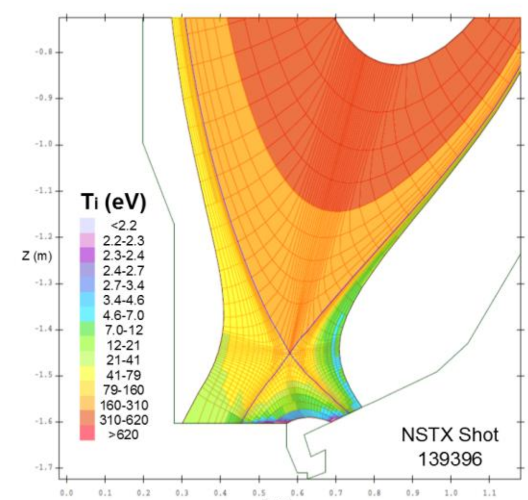

Figure MP-4: *OEDGE-calculated ion temperature contours for an 800kA, 4 MW NBI heated discharge with outer strike point on the LLD. Calculations are based on actual target conditions taken from Langmuir probes on the divertor floor.*

OEDGE uses "onion-skin modeling" to generate a realistic edge plasma background by sequentially solving the plasma fluid equations along magnetic flux tubes, starting from the actual target conditions as determined by Langmuir probe measurements. This calculation is performed iteratively so that it is consistent with the hydrogenic neutral transport calculated by EIRENE. Plasma solutions have been generated in this manner for a well-diagnosed NSTX LLD discharge [MP-2, MP-8], so as to begin to study the sensitivity of erosion patterns to background plasma parameters. Figure MP-4 shows a representative ion temperature contour plot from one such solution, with the computational grid overlaid. Using OEDGE, one can also determine the ionic and neutral particle fluxes striking the walls, as well as their energies. This information is tremendously poloidally non-uniform, as seen in the representative plot of neutral particle flux and energy in Figure MP-5. Estimates of poloidally-resolved physical and chemical sputtering have been obtained using this information, with early results indicating gross erosion rates on the order of 1 μm/s at the strike points. Obviously some fraction of this eroded material will redeposit nearby, so net erosion of divertor components will not be nearly so high. In order to quantify this, the Monte Carlo impurity transport code DIVIMP has been set up in the NSTX geometry to map out the deposition patterns of sputtered neutrals. DIVIMP simulations to determine poloidally-resolved net erosion patterns are ongoing.

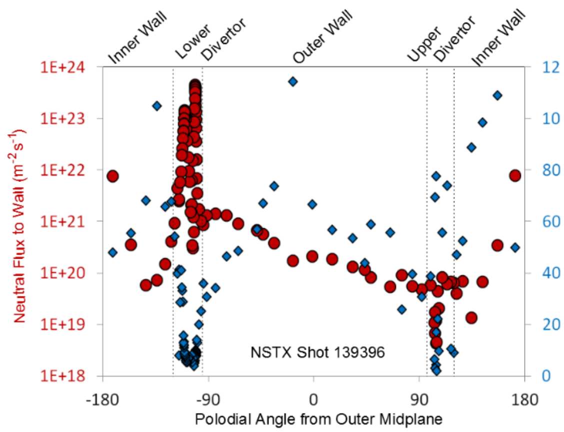

Figure MP-5: *Poloidal spectrum of neutral hydrogenic flux to the wall and average energy of incident neutrals, as derived by OEDGE for the same LLD discharge. Note the large low-energy fluxes to the lower divertor (driving chemical erosion), and the high-energy fluxes striking the main walls (driving physical erosion).*

In parallel with the computational effort, plans have been made for establishing diagnostic support for material migration experiments during the first year of NSTX-U operation. A set of 3 quartz crystal microbalances will be set up in recessed areas along the outer wall, allowing shot-to-shot measurements of erosion and deposition with a sensitivity of 0.7 nm. The MAPP system (described elsewhere) will allow shot-to-shot analysis of the composition of deposited material, in addition to its quantity. An array of witness plate samples will provide wide poloidal coverage of campaign-integrated erosion/deposition at the vacuum vessel wall. Finally, graphite marker tiles (with a silicon marker layer) will be placed in the lower divertor to measure campaign-integrated net erosion in high-flux areas. These marker tiles will be produced in-house, so to that end a magnetron sputter source capable of depositing silicon and graphite has been installed at PPPL. Diagnostic development will continue until the start of plasma operations in 2014.

Liquid lithium loop and PFC development

The Liquid Lithium Test Stand (LLTS), a small experiment currently under construction, is a test bed for development of flowing liquid lithium systems for possible use with plasma-facing components on NSTX-U. LLTS is designed to test operation of liquid lithium under vacuum, including flowing, solidifying (such as would be the case at the end of plasma operations), and re-

Figure MP-6: *Current status of integration of the liquid-lithium test-stand. Reservoirs are shown at upper right and the liquid metal, permanent magnet pump is shown at bottom left.*

melting. Presently, LLTS has an upper reservoir, a lower reservoir, and a pump connected in series. We plan to add another chamber for development of PFCs with a free surface of flowing lithium. There are diagnostics for flow rate, temperature, and pressure in the vacuum system, all logged by LabVIEW. Up to 27 thermocouples will be logging temperature. The current setup is shown in Figure MP-6. Liquid lithium is a hazardous substance: it is hot, corrosive to most materials, and can ignite when exposed to air. Therefore we have had to take special precautions in the design and construction of LLTS. All the lithium-facing surfaces will be made of stainless steel. We use metal-to-metal seals (VCR fittings and Conflat flanges) to join components, substituting a soft steel for copper in gaskets. In order to avoid any moving parts in contact with the lithium for the pump and flow meter, both of these devices use MHD effects. The pump consists of a section of pipe in a solenoid shape with an electric motor's shaft down the axis. Attached to the shaft are six permanent magnets with the poles facing radially in and out. When the shaft rotates, the liquid lithium in the pipe is dragged along by the magnetic field. The flow meter also operates electromagnetically. Permanent magnets create a field across a section of pipe. When the liquid metal flows through the pipe, a voltage (in our case, a few tens of microvolts) is created perpendicular to both the flow and the magnetic field. Although we do not expect any leaks to occur, we have created a leak-detecting circuit that can shut down the heaters and pump in the event of a leak. Surrounding each pipe joint will be a cylinder of copper foil electrically isolated from the pipe. The circuit monitors for continuity between the foil and the pipe. If continuity is detected on any of its 24 channels, a relay will open and shut off the power supply to the heaters and pump. This way the lithium will cool down and solidify, stopping the leak. A front panel display shows which channel registered continuity, and each channel is logged by LabVIEW so that a momentary continuity condition can be recorded. Even if the leak is momentary, the heaters and pump won't turn on again after there is no longer continuity in the circuit: human intervention is needed to push a 'Start' button to re-enable them. As a further precaution, the entire experiment will be housed in a 'shed' with stainless steel sides. Such a structure represents a tertiary level of containment to prevent lithium egress or ingress of other materials in the event that the primary *and* secondary containment systems are compromised.

References

[MP-1] G. De Temmerman, et al., J. Vac. Sci. Technol. A **30** (2012) 041306.

[MP-2] M.A. Jaworski, et al., J. Nucl. Mater. **438** (2013) S384.

[MP-3] R.P. Doerner et al., J. Nuc. Mater., 2001.

[MP-4] J.P. Allain et al., Phys. Rev. B, 2007.

[MP-5] H.P. Summers, "Atomic Data and Analysis Structure User Manual," 2004.

[MP-6] G. De Temmerman et al., Fus. Eng. Des., in press.

[MP-7] N. Itou et al., J. Nuc. Mater. 2001.

[MP-8] M.A. Jaworski, et al., Nucl. Fusion **53** (2013) 083032.

Macroscopic Stability Research

Global and Resistive wall mode stability research (MS-RWM)

Significant progress continues on analysis of the extensive NSTX database including analysis of global mode stability for disruption avoidance (based on both theoretical predictions and direct measurement of mode stability conducted in dedicated experiments utilizing low frequency MHD spectroscopy), active RWM control including design studies for NSTX-U, and neoclassical toroidal viscosity physics related to plasma toroidal rotation control. Attention is being placed on the investigation of the stability dependence of plasma parameter variations to best understand extrapolations to NSTX-U operation. Associated collaborative work also continues on the DIII-D and KSTAR tokamaks. Results have been regularly reported to the ITPA at the bi-annual ITPA MHD Stability group meeting. Of special note in regard to direct request by ITPA leadership is progress on the focused effort on ITPA joint experiment/analysis task MDC-2 conducted by our group to benchmark kinetic RWM stability codes.

Resistive wall mode stability dependence on collisionality

Past NSTX research has established a new understanding of resistive wall mode (RWM) [MS-RWM-1] stability by making quantitative correlation between experiments reaching the mode marginal stability point and kinetic RWM stabilization theory [MS-RWM-2 to 5]. This model has important implications for next-step devices operating at reduced collisionality. Early RWM stabilization models relied solely on plasma collisionality as the stabilizing energy dissipation mechanism, therefore always yielding reduced stability at reduced collisionality – a negative result for future devices. The present kinetic RWM stabilization theory changes this significantly, yielding a more complex stability picture. As before, stabilizing effects of collisional dissipation are reduced at lower ν, but new stabilizing resonant kinetic effects can be enhanced. Generally, stronger resistive wall mode stabilization occurs near broad dissipative kinetic resonances (which depend on the plasma rotation profile – both magnitude and shape) and this stabilization increases with decreasing collisionality. However, in stark contrast, the plasma stability has almost no dependence on collisionality when the plasma is off-resonance (see RWM-1). In this figure, ν and ω_ϕ^{exp} represent NSTX experimental values in high beta plasmas, and kinetic RWM stability calculations producing the mode growth rate are made using the MISK code [MS-RWM-6]. In these calculations both the influence of the bulk plasma on the kinetic effects (e.g. the precession drift resonances, and bounce harmonic resonances [MS-RWM-2]) and the effect of the fast particle population [MS-RWM-7] are included in the computation of the RWM growth rate. These theoretical results can be compared to new analysis of experiments that utilized n = 1 active MHD spectroscopy [MS-RWM-8] diagnosis (which uses n = 1 resonant field amplification (RFA) of a low frequency (40Hz) applied n = 1 tracer field) to directly measure RWM stability [MS-RWM-9].

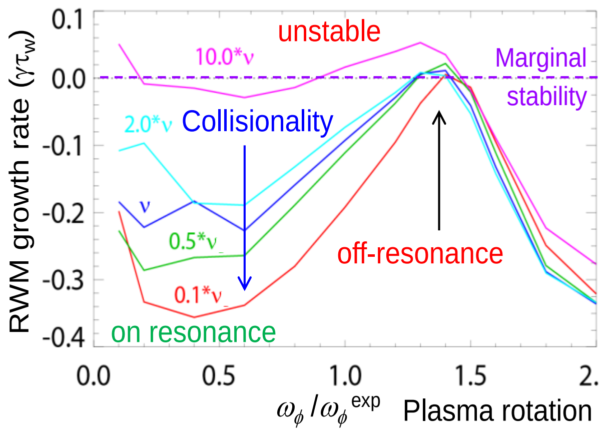

Figure RWM-1: MISK computed kinetic RWM n = 1 stability vs. plasma rotation for varying collisionality.

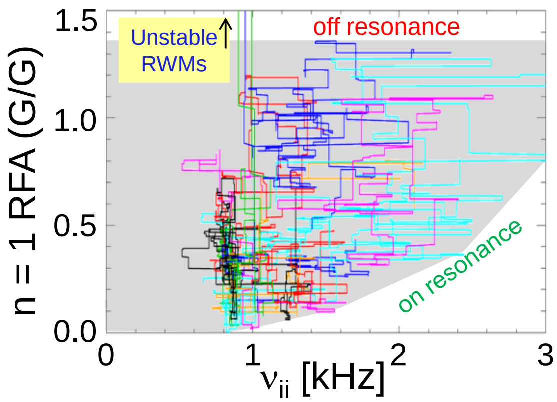

Figure RWM-2: n = 1 RFA amplitude vs. ν_{ii}, showing a relatively large change at low RFA ("on resonance") vs. almost no change at high RFA.

These experiments indicate the expected gradients in RWM stability for plasmas with high $5.5 < \beta_N/l_i < 13.5$ (most are above the $n = 1$ ideal no-wall stability limit) (Figure RWM-2) as a function of ion collisionality. Each trace in the figure shows the variation of the RFA amplitude over each discharge evolution for 20 plasmas shots, over which the ion collisionality, ν_{ii}, is varied by a factor of 5 in the range $0.6 < \nu_{ii}$ (kHz) < 3. The theoretically expected gradients in kinetic RWM stability are generally reproduced by the shape of the upper and lower boundaries of the measured $n = 1$ RFA amplitude. At high $n = 1$ RFA amplitude (the upper boundary), the plasma rotation is further from stabilizing kinetic resonances (off-resonance), and there is almost no change in RWM stability (indicated by the high, and near constant $n = 1$ RFA amplitude) vs. ν_{ii}. This resembles the behaviour shown by theory in Figure RWM-1 labeled "off-resonance" as ν is varied. These plasmas are near marginal stability, and some become experimentally unstable, as labeled in Figure RWM-2. During periods of low $n = 1$ RFA amplitude during the discharge evolution (the lower boundary), the plasma has greater stabilization by kinetic resonances, and there is a clear increase in RWM stability (decrease in $n = 1$ RFA amplitude) as ν_{ii} is decreased. This behaviour is similar to that shown by theory in Figure RWM-1 when the plasma is "on-resonance" and ν is decreased. The definition of RFA used in this analysis is $A_{RFA,s} = B_{p,s}^{plasma}/B_{p,s}^{applied}$, where B_p^{plasma} is the poloidal field generated by the plasma, $B_p^{applied}$ is the applied poloidal field generated by the dominantly $n = 1$ tracer field, and subscript s denotes the values at the location of the RWM sensors. Note that B_p^{plasma} does not contain the applied $n = 1$ field – it is compensated from the sensor measurements. In this analysis, the field, and the applied currents generating them are considered complex variables of the form $|\xi(t)|e^{-in\phi(t)}$, where $|\xi(t)|$ and $\phi(t)$ are the RFA amplitude and phase. This definition is consistent with that used in DIII-D [MS-RWM-8], and other NSTX experiments [MS-RWM-10]. Twelve RWM sensors are used in the RFA analysis. Here, ν_{ii} is averaged over $0.55 < \psi_N < 0.75$ of the profile, inside of the pedestal, and ψ_N is the normalized poloidal flux, $(\psi - \psi_0)/(\psi_a - \psi_0)$, where subscript "$a$" represents the plasma edge, and "0" represents the magnetic axis.

Measured Improvement of Global MHD Mode Stability at High-beta

The dedicated experiments using low frequency active magnetohydrodynamic spectroscopy of applied, rotating n = 1 magnetic fields shown above revealed key dependencies of stability on plasma parameters. Observations from previous NSTX resistive wall mode active control experiments [MS-RWM-11] and the wider NSTX disruption database [MS-RWM-12] indicated that the highest β_N plasmas were surprisingly not the least stable. This is supported by the dedicated RFA experiments, where stability was measured to *increase* at β_N/l_i higher than the point where disruptions were found (Figure RWM-3a). Experimentally, disruptions occurred more frequently at intermediate values of β_N/l_i [MS-RWM-11]. This agrees with the active MHD spectroscopy diagnosis, used to determine the proximity to marginal stability [MS-RWM-9]. The resonant field amplification of the applied 40 Hz co-NBI rotating n =1 seed field shows an increase in RFA to a broad peak near β_N/l_i = 10. This decrease in RWM stability, shown by the increase in RFA, is expected as β_N increases, and has been as reported for DIII-D [MS-RWM-13], JET [MS-RWM-14], and NSTX [MS-RWM-10,15] at lower β_N values. In contrast, and remarkably, RFA is found to *decrease* at higher values of β_N/l_i in NSTX, indicating increased mode stability (Figure RWM-3a). This positive result is presently not thought to be a second stability region for the RWM, but is more likely related to proximity to broad resonances in plasma rotation (e.g. ion precession drift resonance) providing kinetic stabilization of the RWM [MS-RWM-2,4,7]. Note that for the plasmas shown in Figure RWM-3, the RFA shown is an output quantity, and is not limited by plasma energy confinement or other considerations. The figure also illustrates two plasmas (RFA amplitudes increase off-scale in the figure) that become unstable and suffer disruptions at intermediate β_N/l_i. This was not observed at higher β_N/l_i in these experiments. In addition, the plasma boundary configuration is not changed in this database, taken from a dedicated experiment. This favorable behavior is shown to correlate with kinetic stability rotational resonances [MS-RWM-5], and an experimentally determined range of measured *E x B* frequency with improved stability has been initially identified (Figure RWM-3b). This investigation has yielded an initial, highly simplified model for kinetic RWM stability that could be used (as planned) for disruption avoidance by avoiding less stable rotation profiles in NSTX-U.

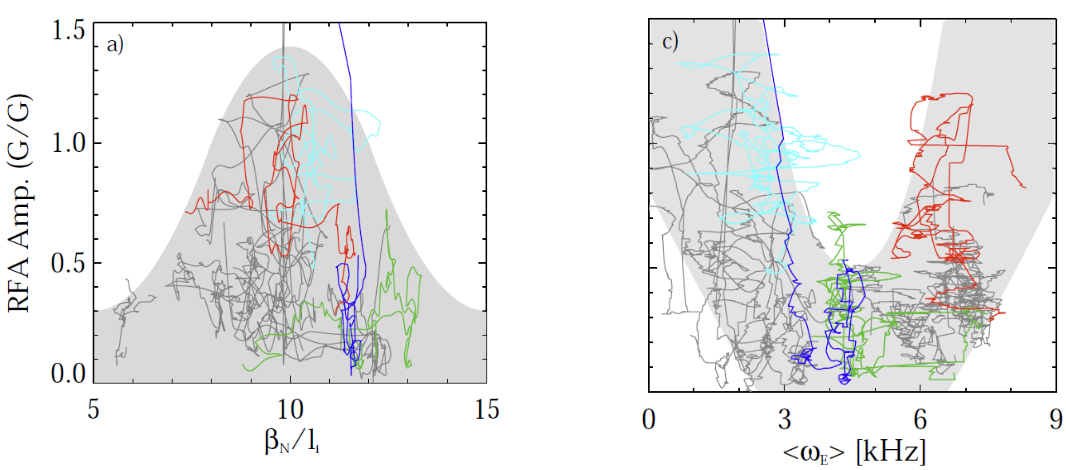

Figure RWM-3: Resonant field amplification (RFA) amplitude vs. a) β_N/l_i, and b) an average E x B frequency, $<\omega_E>$. The grey backgrounds are meant as general guides to the trends in the data and the stability boundaries

RWM active control – sensor/actuator control scoping studies for NSTX-U

The significant RWM amplitude is computed by DCON in the divertor region, found both in single and multi-mode VALEN-3D code studies, motivates the installation of magnetic sensors closer to the divertor region to study the RWM eigenfunction, to compare to expectations of ideal theory, and to directly improve comparisons of the measured mode shape to the real-time NSTX-U RWM state-space controller model. Figure RWM-4 shows the weighted sum of the three primary n = 1 eigenmodes determined using a multi-mode VALEN analysis as well as the proposed locations of the new sensors, indicating that the locations closer to the divertor will improve mode measurement. These sensors are planned for installation in NSTX-U.

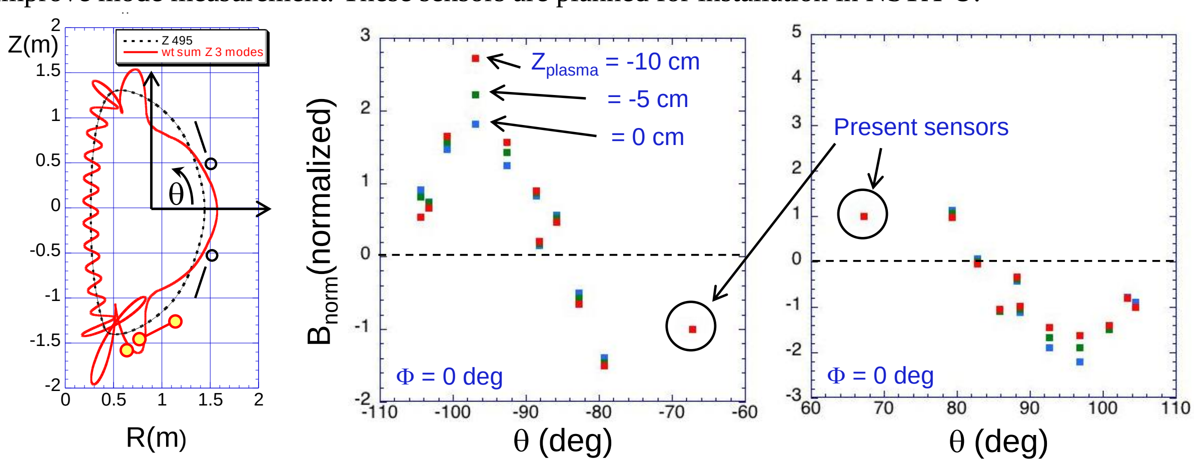

Figure RWM-4: (left) Weighted sum of three-mode amplitude with present magnetics in black and proposed enhanced magnetics in yellow, and the computed normal perturbed field magnitude of the mode at the new sensor locations above (middle frame) and below (right frame) the midplane, normalized to the measurement made at the present sensor locations. Different colored points show the variation caused by shifting the plasma downward by 5 cm (green) and 10 cm (blue).

Figure RWM-5 shows that a significant change to toroidal phase would be measured by the new sensors due to the significant field line pitch in NSTX-U. Note that a relatively long poloidal wavelength still exists (vs. center column region), and the new phase information will help to constrain the active RWM state space controller model.

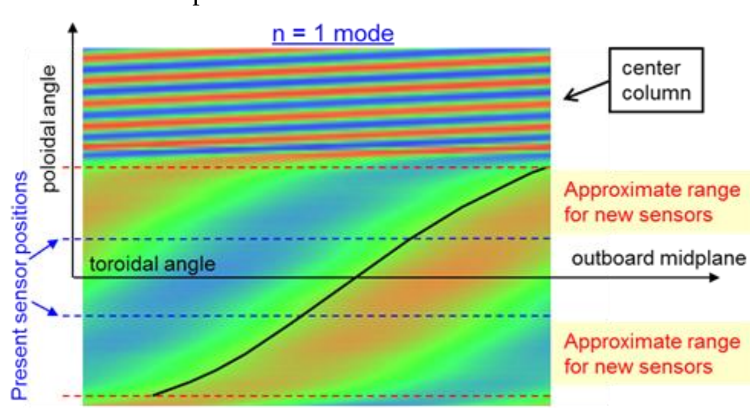

Figure RWM-5: Mode amplitude vs. toroidal and poloidal angle for an n = 1 mode.

Kinetic RWM analysis – ITPA MDC-2 Joint Experiment benchmarking activity

Reliable, validated calculations of resistive wall mode stability, including kinetic effects, are critical for ITER, which cannot tolerate disruptions caused by such instabilities. Benchmarking the calculations of the MISK, MARS-K, and PENT codes for two Solov'ev analytical equilibria has demonstrated good agreement between the codes. The precession drift, bounce, and transit frequencies of particles, which can each cause a stabilizing resonance with the mode, are consistently evaluated between the codes, and are used in the frequency resonance energy integral. Numerical energy integral calculations are consistent between codes as well as with analytical limits. The marginally stable eigenfunctions and fluid growth rates are consistent as well. The most important kinetic effect at low rotation is the resonance between the mode rotation and the trapped thermal particle's precession drift. The codes show good agreement in this term. There exists some differences in the calculations of the bounce and transit resonance terms at higher plasma rotation, stemming from the rational surfaces, but this effect is most prominent at unrealistically high plasma rotation when compared to experiments. All of the codes support the present understanding that RWM stability can be increased by kinetic effects at low rotation through precession drift resonance and at high rotation by bounce and transit resonances, while intermediate rotation can remain susceptible to instability.

KSTAR stability experiments and analysis

Our active collaboration with the National Fusion Research Institute in South Korea, working on the KSTAR superconducting tokamak, reached significant milestones in the past year. In addition to our continued processing of KSTAR equilibrium reconstructions, central to this work, the experiment MP2012-04-23-037 “Long-Pulse Low Rotation Plasma Investigation for ITER Applicability and Instability Characterization in KSTAR High Normalized Beta Plasmas” (S.A. Sabbagh, Y.S. Park, Y.M Jeon, et al.) created plasmas that reached, and surpassed the n = 1 ideal stability limit, demonstrated significant alteration of the plasma rotation profile by non-resonant n = 2 applied field magnetic braking by neoclassical toroidal viscosity, and the demonstration of ELM suppression by the n = 2 field, applied using a midplane-oriented coil, when the applied field reached a sufficiently large magnitude.

A) Operation at, and above the *n* = 1 no-wall limit

Investigation of the stable operating space of KSTAR to ideal MHD modes has been investigated and published in our past work as part of the U.S. International Collaboration with NFRI. The initial theoretical work (Reference [MS-RWM-16]) was supplemented by experiments in the 2010 KSTAR run campaign, which were published in Reference [MS-RWM-17]. These results were supplemented significantly in the 2011 campaign.

A significant milestone was reached during the 2012 KSTAR run campaign when experiment MP2012-04-23-037 created plasmas that reached, and surpassed the n = 1 ideal stability limit, calculated with H-mode pressure profiles (Figure RWM-6). These plasmas had long pulse lengths, on the order of ~ 10s, and were created at reduced toroidal field, with B_T as low as 1.3T.

Rotating MHD modes are found during the H-mode phase of these plasmas, but while they crossed the n = 1 no-wall limit, resistive wall modes (RWM) were not yet found. The discharges were not terminated by disruptions.

It is important to note that (i) the technique of reduced B_T in accessing high β_N ***is not yet saturated***. The highest β_N plasma created were limited by impurity accumulation on the second run day of the experiment, that was attributed to an issue with a component internal to the device. Further improvement of β_N is expected at the lower toroidal field values.

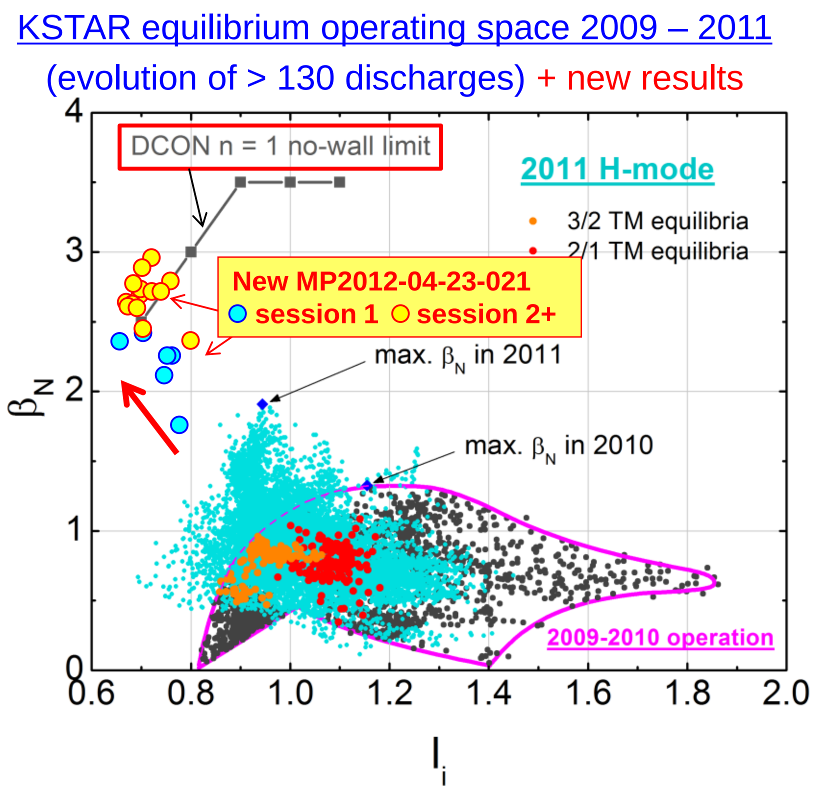

Figure RWM-6: The first operation of KSTAR above the n = 1 ideal no-wall instability limit run in experiment MP2012-04-23-021.

Further techniques will be used to optimize β_N in these plasmas, and plasma collisionality will be altered by the use of supersonic molecular beam injection (SMBI). Another important aspect of the next planned experiment will be to operate at long pulse length at high β_N, establishing a steady-state plasma operating for a duration of a few, to several resistive decay times for further physics studies.

B) Plasma Stability vs. Plasma Rotation and its Shear

Macroscopic MHD stability depends on plasma rotation profile characteristics, including local levels of plasma rotation, and rotation shear. Many studies have been conducted to understand the dependence of plasma rotation and rotation shear on several modes, including the RWM [MS-RWM-5] and NTM [MS-RWM-18]. KSTAR experiments can examine outstanding issues in this area. A connection between tearing mode stability and plasma rotation shear was found in our analysis of KSTAR data (Figure RWM-7), and published by our group along with associated analysis in the 2012 paper “Investigation of MHD instabilities and control in KSTAR preparing for high beta operation”, by Young-Seok Park, et al. Further details can be found in reference [MS-RWM-19].

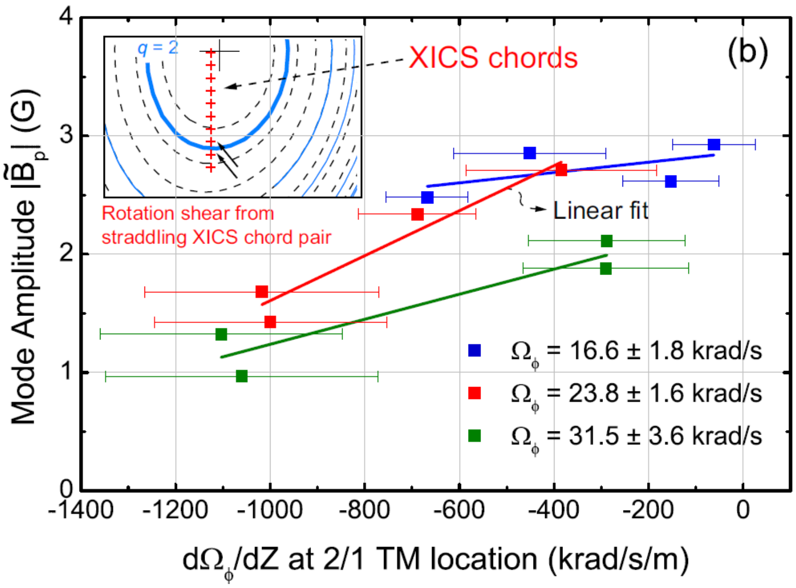

Figure RWM-7: Correlation of 2/1 tearing mode stability with toroidal rotation shear in KSTAR

C) Neoclassical Toroidal Viscosity physics and rotation alteration

Another significant result of KSTAR experiment MP2012-04-23-02 was the clear, reproducible achievement of open-loop plasma rotation control using the inherent 3D effect of non-resonant neoclassical toroidal viscosity, generated by the application of a dominantly n = 2 field using the IVCC. The experiment applied the n = 2 field in steps – both increasing, and decreasing, and showed clear alteration of the plasma rotation profile (Figure MS-RWM-8) with no hysteresis.

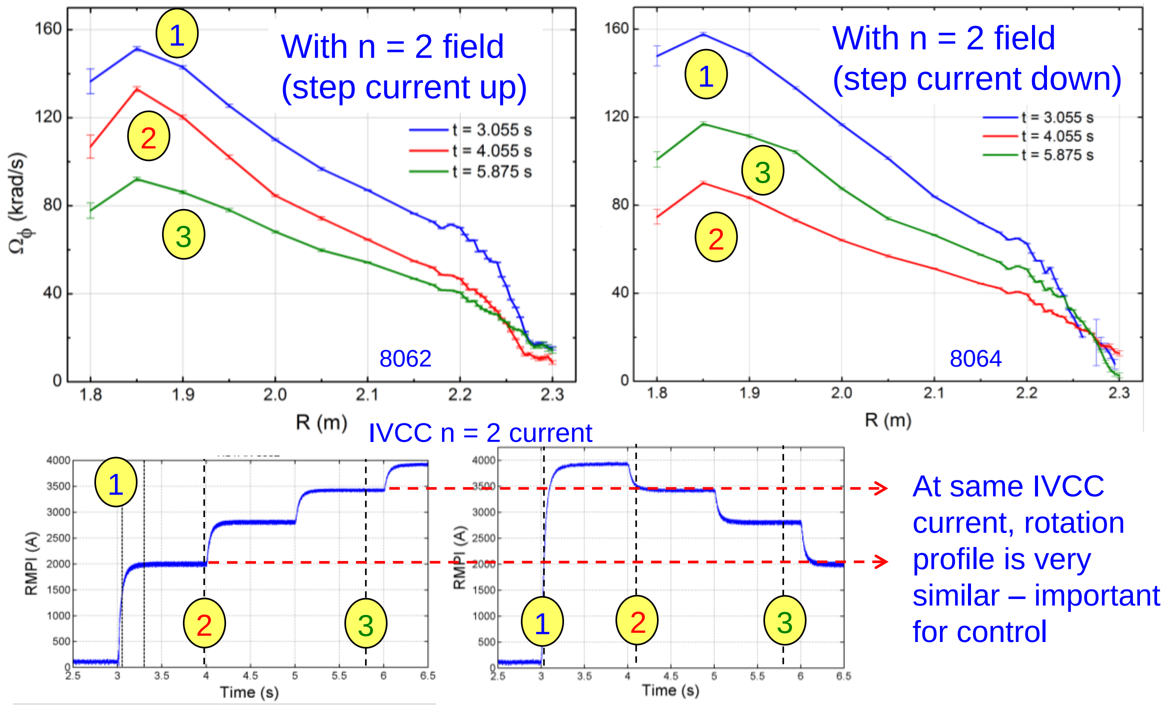

Figure RWM-8: Demonstration of controlled, open-loop plasma rotation profile alteration in KSTAR experiment MP2012-04-23-021 utilizing the IVCC in an n = 2 field configuration.

Three key points of the results shown in Figure RWM-8 are, (i) given sufficient time to evolve and reach a quasi-steady-state (here, 1 second is taken between IVCC currents steps, which is much larger than the momentum diffusion time), the non-resonant n = 2 NTV is sufficiently strong to greatly reduce the plasma rotation, (ii) the rotation profile is not determined by the history of the IVCC current waveform (compare profile "3" in the shot shown on the left in Figure 2, to profile "2" shown on the right), and (iii) the steep rotation gradient in the pedestal region is reduced by the NTV, allowing studies on the effect of reducing this strong rotation pedestal on MHD instabilities. The results above show that both rotation, and rotation shear can be altered in a controlled fashion in future experiments.

NTV is a key tool used in NSTX [MS-RWM-20] and now in KSTAR to allow reduction of plasma rotation (i) without strong resonant damping – as such damping scales inversely with the plasma rotation, $1/\omega_{\phi,}$ and leads to mode locking as the plasma rotation decreases and the rotation drag subsequently increases as ω_ϕ approaches zero, [MS-RWM-21] and (ii) with the ability to make small changes in the plasma rotation. Both of these characteristics are possible through non-resonant NTV due to applied magnetic fields. The KSTAR experiment described used non-resonant n = 2 fields, which also showed strong braking in NSTX) [MS-RWM-3].

An important capability needed in KSTAR for practical use of NTV for rotation braking was the allowance of the IVCC to operate at 4 kA/turn in 2012 – a doubling of the allowed current vs. the 2012 run campaign. But as Figure RWM-8 shows, the maximum allowed IVCC current is still not sufficient to bring the plasma rotation to near zero. Further experimentation aims to reduce the plasma rotation by supplementing the NTV rotation damping with ECH-induced rotation damping (as demonstrated in KSTAR by S.G. Lee, et al. [MS-RWM-22]). The ECH has been shown to reduce the plasma rotation in the core. This is significant, as NTV affects the plasma globally, with maximum local torque occurring closer to the pedestal region. By combining the two techniques, both the plasma rotation level, and the plasma rotation shear can be changed.

D) ELM suppression / mitigation by n = 2 applied fields (midplane actuator coil)

The plasmas in which n = 2 fields were applied, similar to those shown in Figure RWM-8, experienced ELM suppression or mitigation when the current used to generated the field exceeded approximately 3 kA/turn (Figure RWM-9). This result was not found in our experiment of 2011 as an administrative limit of 1.8 kA/turn was imposed at that time. The present experiments are significant as they illustrate that ELM suppression can be obtained using a midplane coil alone. It is important to note that n = 2 fields applied to NSTX plasmas using the midplane RWM coils at constant plasma current did not show ELM suppression. Analysis and comparison of the KSTAR and NSTX results can provide key insight into the mechanism for ELM suppression by the 3D field. A key difference between KSTAR and NSTX in this regard is the device aspect ratio (3.5 vs. 1.3). The larger field line pitch on the outboard side of NSTX plasmas may illustrate the key elements of the relation of the applied 3D field spectrum to the 2D equilibrium field that are responsible for ELM suppression.

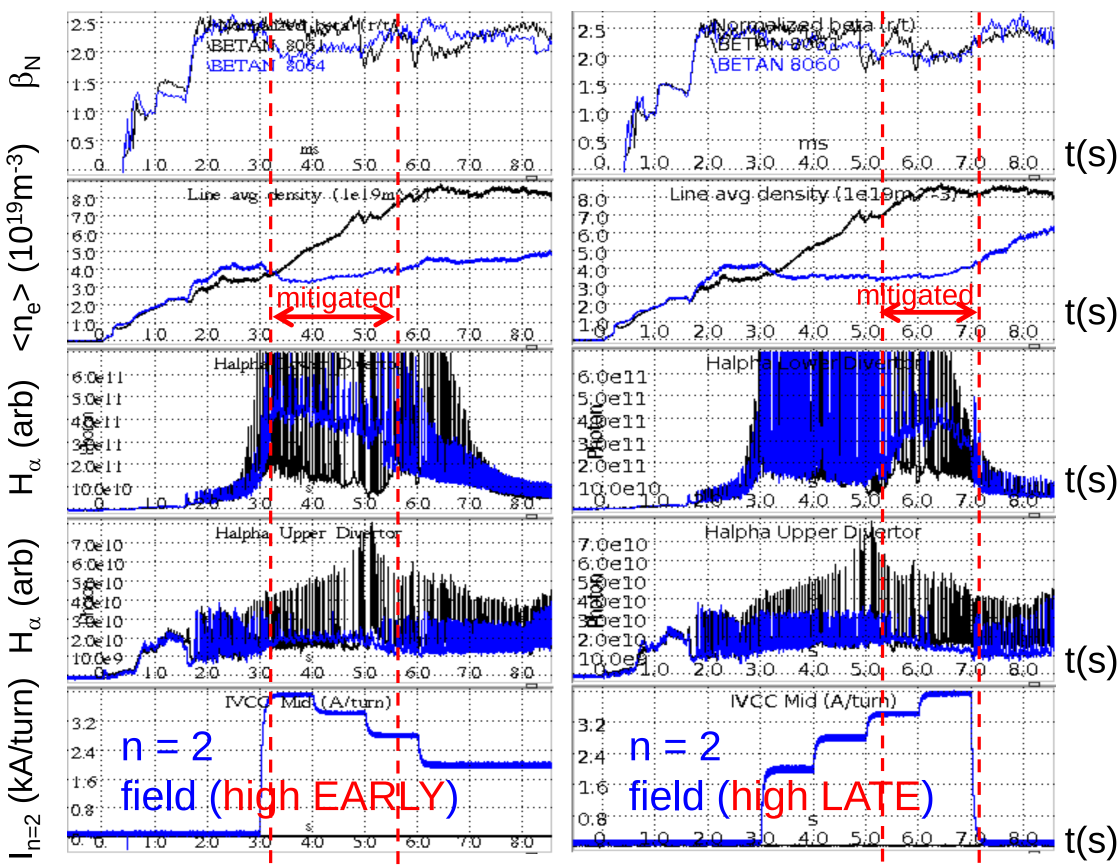

Figure RWM-9: ELM suppression using n = 2 applied fields by a midplane coil alone. The discharge shown in the left column reaches the critical n = 2 current of approximately 3 kA/turn early in the discharge, which the discharge shown in the right column reaches this value later in the discharge.

E) Initial application of M3D-C^1 stability code to KSTAR plasmas

The M3D-C^1 non-linear extended MHD stability code was used for the first time to test the stability of KSTAR equilibria, with H-mode pressure profiles, extrapolated to high β_N values exceeding the n = 1 ideal no-wall limit (β_N = 2.5 in the cases studied) up to the n = 1 ideal with-wall limit (β_N = 5.0 in the cases studied). In these first tests, M3D-C^1 was run in linear mode and the results were compared to those found using the ideal stability code DCON. Using equivalent wall configurations, both codes find the n = 1 MHD with-wall limit at β_N = 5. Figure RWM-10 compares n = 1 eigenmode characteristics as computed by the two codes. The comparison of the perturbed magnetic field is similar between the codes, but not exact – which is expected, as the M3D-C^1 code incorporates a more complete MHD model. Examining the differences found between the codes should give addition insight as to the importance of these differences in actual experiments. These results also provide important preparation for the use of future expansion of the physics model presently ongoing in M3D-C^1 development, which include a resistive wall (for RWM studies) and kinetic effects (for comparison to MISK stability codes studies) [MS-RWM-23].

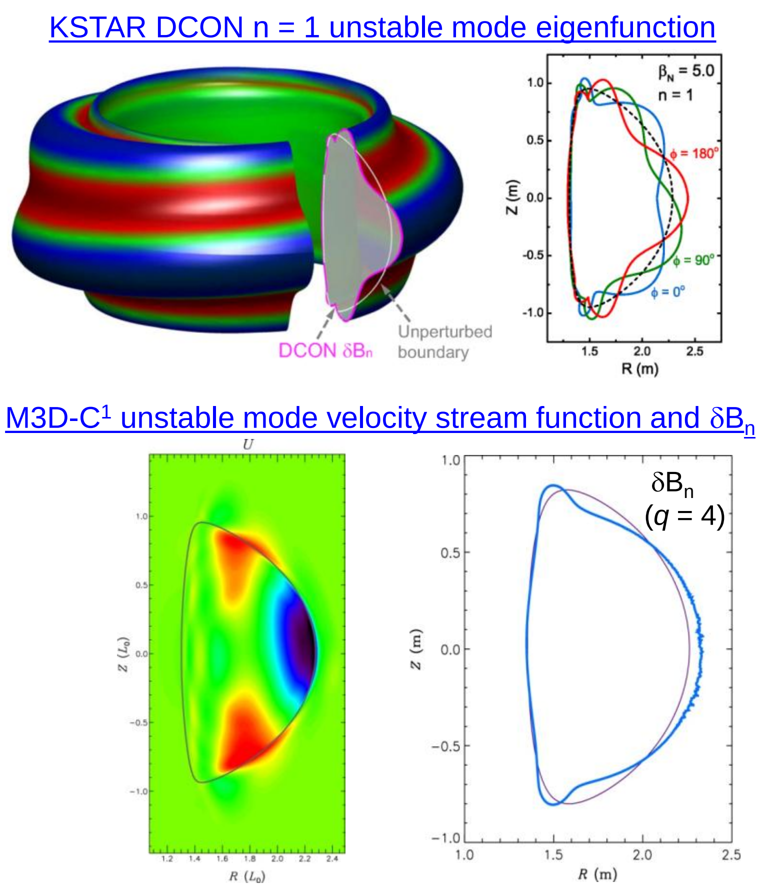

Figure RWM-10: (top) three dimensional illustration of n = 1 ideal MHD linear eigenmode for extrapolated KSTAR H-mode equilibrium with normalized beta near the with-wall limit (the right-hand frame illustrating different toroidal phases of the mode in a typical 2D illustration), (bottom) (left) velocity stream function and magnetic field perturbation of the unstable mode found by the M3D-C^1 code.

F) KSTAR RWM active control design including 3D device model and sensors

In preparation for power supply procurement on KSTAR for RWM control, a design study was conducted to determine the capabilities of the present KSTAR low frequency MHD sensors for use in n = 1 RWM control on the device. It has already been determined that sensors are needed at more toroidal locations than available at present to track toroidally rotating RWMs, so the present design study focused on the ability of the present device sensors to control a non-rotating RWM in the present KSTAR 3D device geometry. Three primary sensor options were tested (i) existing locked mode (LM) sensors (located on the outboard midplane of the device, mounted to the inner vacuum vessel), (ii) existing partial saddle loops (SL) (located near the upper/lower divertor regions, and (iii) a proposed coil set resembling the present coils used for RWM control on NSTX. These sensors, along with the KSTAR 3D conducting structure model are shown in Figure RWM-11.

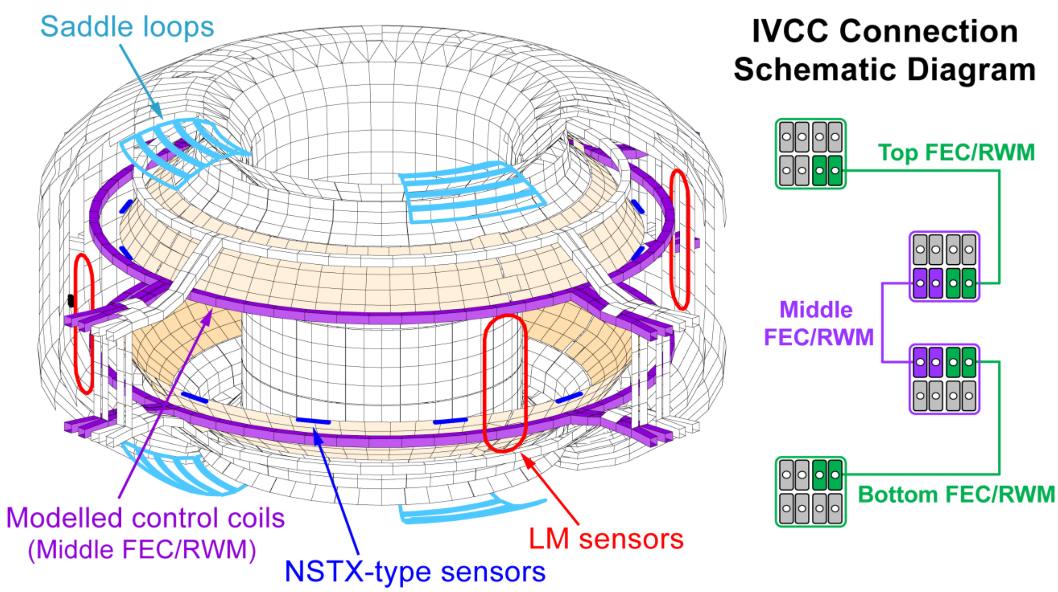

Figure RWM-11: KSTAR 3D conducting structure model used in the VALEN-3D code for the n = 1 RWM control design study utilizing three types of sensors: (i) locked mode (LM), (ii) saddle loop (SL), and (iii) proposed NSTX-type sensors, located as illustrated.

The VALEN-3D code was used to compute the n = 1 RWM stability for these different sensor configurations, and the physics limiting the performance of each configuration was identified. The LM sensors performance (Figure RWM-12) was the lowest performance of the three sensors types. The control performance was shown to be limited by significant eddy currents that flow around the large ports in the vacuum vessel (around which the sensors are mounted). Use of LM sensors without compensation of the applied n = 1 field used for the RWM control produce the lowest performance (maximum β_N ~ 3), which is improved with applied field compensation (maximum β_N ~ 3.5), but still modest (Figure RWM-12). The figure also shows that if the effect of the eddy currents in the vacuum vessel could be eliminated (generally not possible), control with be near ideal. Similar RWM control performance curves are shown in Figure RWM-13 for the partial saddle loop sensors. Here, it is shown that the up/down saddle loop pairs that are located at larger major radial positions shown significantly better performance, which is associated with the sensor having a stronger mutual coupling to the eigenfunction. The best performance for SL sensors with the applied field compensated is β_N ~ 4.6. However, a set of sensors designed and placed in a fashion similar to the NSTX RWM sensors show the best performance, even without applied field compensation (β_N ~ 4.8), and with compensation can reach the with-wall limit of β_N = 5 (Figure RWM-14).

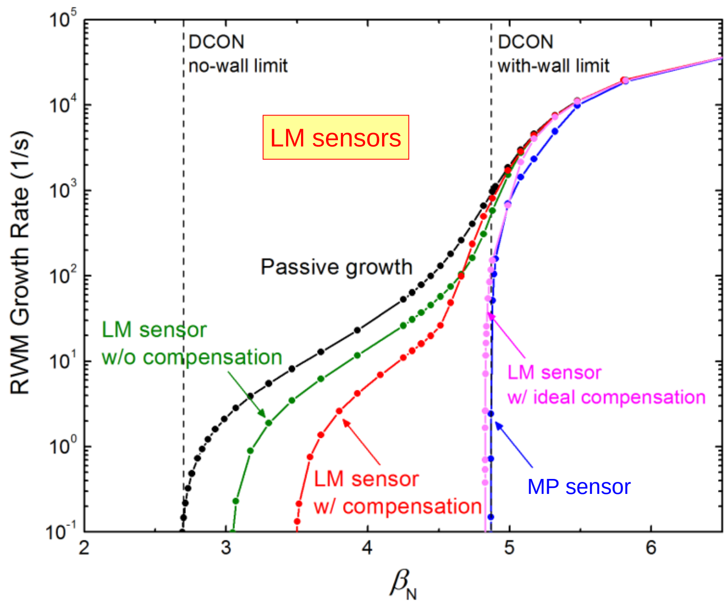

Figure RWM-12: RWM growth rate vs. normalized beta using KSTAR locked mode sensors

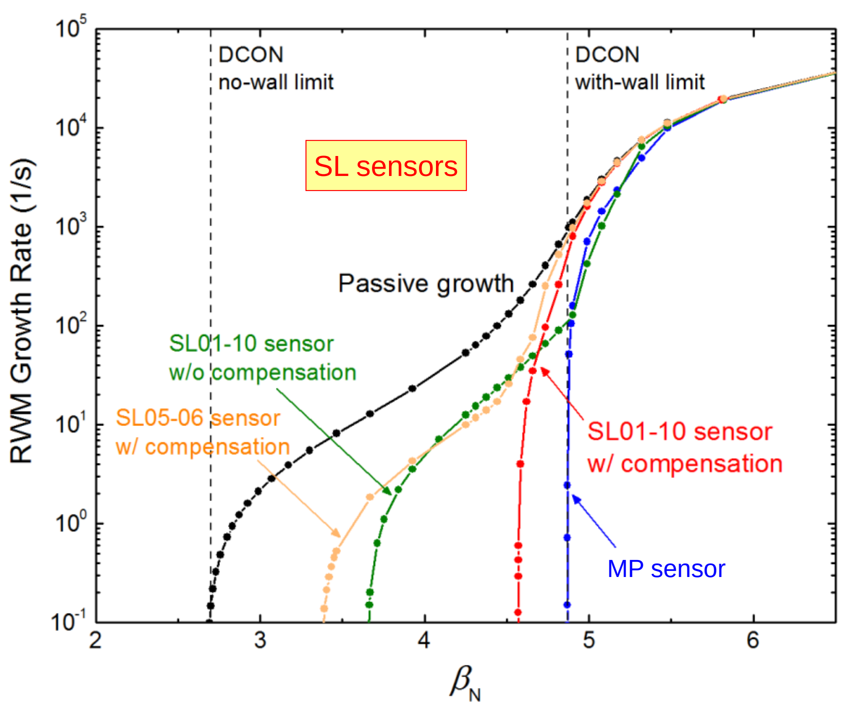

Figure RWM-13: RWM growth rate vs. normalized beta using KSTAR saddle loop sensors

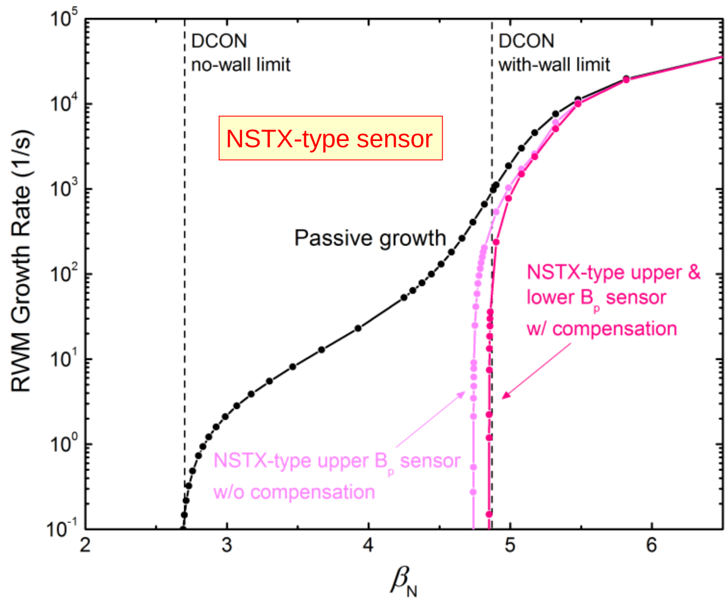

Figure RWM-14: RWM growth rate vs. normalized beta using NSTX-type RWM sensors

References

[MS-RWM-1] A. Bondeson, A. and D. Ward, D., Phys. Rev. Lett. **72**, 2709 (1994).
[MS-RWM-2] B. Hu and R. Betti, Phys. Rev. Lett. **93**, 105002 (2004).
[MS-RWM-3] S.A. Sabbagh, J.W. Berkery, R.E. Bell, et al., Nucl. Fusion **50**, 025020 (2010).
[MS-RWM-4] Y. Liu, M.S. Chu, I.T. Chapman, et al., Phys. Plasmas **15** (2008) 112503.
[MS-RWM-5] J.W. Berkery, S.A. Sabbagh, R. Betti, et al., Phys. Rev. Lett. **104**, 035003 (2010).
[MS-RWM-6] J.W. Berkery, S.A. Sabbagh, R. Betti, et al., Phys. Rev. Lett. **106** (2011) 075004.
[MS-RWM-7] J.W. Berkery, et al., Phys. Plasmas **17** (2010) 082504.
[MS-RWM-8] H. Reimerdes, M.S. Chu, A. Garofalo, et al., Phys. Rev. Lett. **93** (2004) 135002.
[MS-RWM-9] J.W. Berkery, S.A. Sabbagh, A. Balbaky, et al., in Fusion Energy 2012 (Proc. 24th Int. Conf. San Diego, 2012) (Vienna: IAEA) paper EX/P8-07 (http://www-naweb.iaea.org/napc/physics/FEC/FEC2012/index.htm).
[MS-RWM-10] A.C. Sontag, S.A. Sabbagh, W. Zhu, Nucl. Fusion **47** (2007) 1005.
[MS-RWM-11] S.A. Sabbagh, et al., accepted for publication in Nucl. Fusion (2013).
[MS-RWM-12] S.P. Gerhardt, et al., Nucl. Fusion **53**, 043020 (2013).
[MS-RWM-13] H. Reimerdes, J.M. Bialek, M.C. Chance, et al., Nucl. Fusion **45** (2005) 368.
[MS-RWM-14] M.P. Gryaznevich, Y.Q. Liu, T.C. Hender, et al., Nucl. Fusion **52** (2012) 083018.
[MS-RWM-15] S.A. Sabbagh, A.C. Sontag, J.M. Bialek, et al., Nucl. Fusion **46** (2006) 635.
[MS-RWM-16] O. Katsuro-Hopkins, et al., Nucl. Fusion **50**, 025019 (2010).
[MS-RWM-17] Y.S. Park, S.A. Sabbagh, J.W. Berkery, et al., Nucl. Fusion **51**, 053001 (2011).
[MS-RWM-18] S.P. Gerhardt, D.P. Brennan, R. Buttery, et al., Nucl. Fusion **49**, 032003 (2009).
[MS-RWM-19] Y.S. Park, S.A. Sabbagh, J.M. Bialek, et al., Nucl. Fusion **53**, 083029 (2013).
[MS-RWM-20] W. Zhu, S.A. Sabbagh, R.E. Bell, et al., Phys. Rev. Lett. **96**, 225002 (2006).
[MS-RWM-21] R. Fitzpatrick, Nucl. Fusion **33**, 1049 (1993).
[MS-RWM-22] S.G. Lee, J.G. Bak, U.W. Nam, et al, Rev. Sci. Instrum. **81**, 10E506 (2010).
[MS-RWM-23] Y.S. Park, S.A. Sabbagh, J.W. Berkery, et al., Nucl. Fusion **51**, 053001 (2011).

3D field physics research (3D)

Study on 3D field effects on magnetic islands (with LHD collaboration)

3D resonant error fields can produce static magnetic islands until locked to the error field frame, as called locking in tokamaks. Although substantial improvement has been made on parametric scaling on error field threshold to avoid locking [MS-3D-1~3], magnetic island dynamics in the presence of 3D fields needs to be much better understood. For instance, 3D error fields and islands are intrinsic in a helical device and it has been found that these magnetic islands can be suppressed by plasmas, as called healing in LHD, indicating the complexity of island dynamics depending on magnetic field configurations and plasma profiles. Thus a combined effort has been started between PPPL and NIFS to develop consistent understanding and island modeling for both locking in tokamaks and healing in LHD this year.

The intrinsic error field in LHD was identified by electron gun experiments, and it was shown that the error field can be compensated by RMP coils, with currents -120A/T, in 7-O configuration [MS-3D-4]. However, this identification and compensation, made in vacuum, are not consistent with recent RMP experiments and their implications [MS-3D-5]. That is, (1) plasma response was observed very differently in two toroidal (opposite) phases even if RMP currents were same and much higher than 120A/T, (2) magnetic islands are enhanced even if RMP field was opposed to vacuum error field and rather healed when RMP field was aligned with error field. This inconsistency observed by plasma response compared to vacuum prediction is in fact well-known in tokamaks, since perturbed plasma currents are often more influential over external coil currents [3D-1]. In LHD plasma experiments, it is found that healing data with different RMP currents indicate that healing boundary can be consistently combined with two parameters, normalized β_T to applied field, $\beta_T/[(\delta B-\delta B_{err})/B]$, and collisionality ν^* [3D-6]. Here an offset δB_{err} by intrinsic error field is necessary, unless RMP field $\delta B>>\delta B_{err}$. Figure 3D-1 shows the combined healing data with three different RMP currents, 400A/T, 600A/T, 1440A/T, and with δB_{err} /B=-4.0×10-4, where one can see healed and unhealed cases can be well separated.

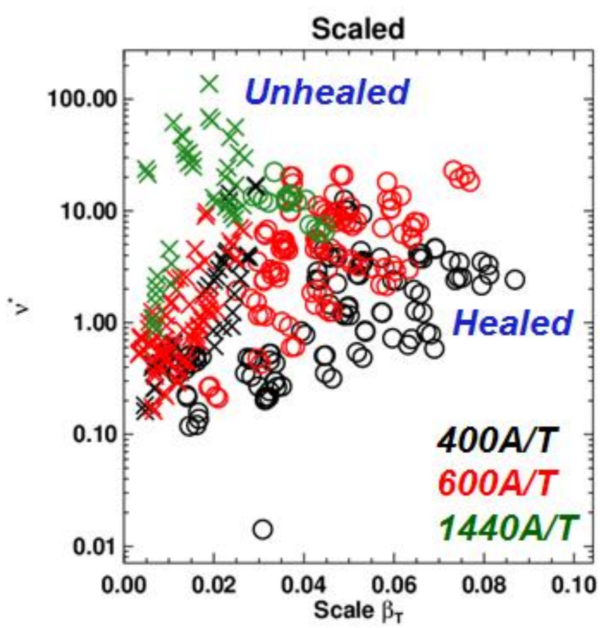

Figure 3D-1. Combined healed (O) and unhealed (×) data with three different field strength (Ampere/Tesla) as functions of scaled β_T and collisionality.

The offset amplitude implied by healing data corresponds to -371A/T, which is much higher than and has an opposite direction to vacuum compensation, -120A/T, since it means +371/A/T would be needed for compensation. This is in fact consistent with recent RMP experiments, and indicates it will be necessary to revise error field compensation, in the presence of plasma. A compass scan is well-known for this purpose in tokamaks, but if difficult in LHD, at least a finer scan of RMP currents from -1.0kA/T to 1.0kAt, in 6-O configuration, will be proposed in the next campaign.

The LHD results also imply self-healing threshold can be well represented by two physical parameters, β_T and ν^*. This motivated the investigation of locking error field scaling by physical parameters, Equation 3D-1, rather than engineering parameters, Equation 3D-2, that have been popular in tokamaks.

$$\delta B/B_T \propto \beta^{0.9\pm0.16}\,\nu^{*0.4\pm0.05}\rho^{*-0.2\pm0.28} \qquad \text{(3D-1)}$$

$$\delta B/B_T \propto n^{1.3\pm0.09}B_T^{-1..7\pm0.12}R^{0.60\pm0.15} \qquad \text{(3D-2)}$$

where ρ^* is the normalized ion sound Larmor radius, n is the density, R is the major radius of the plasma. However, still one can see original scaling in Equation 3D-2 is better with smaller deviations, although engineering parameters such as density is found irrelevant in LHD healing threshold.

The two different representations in scaling between tokamak locking and LHD healing are perhaps manifest by obviously different nature of island dynamics in two cases. That is, tokamak locking is governed by small islands in the presence of substantial inertia whereas LHD healing occurs from large islands without strong rotation. One of outstanding theories for tokamak locking has been recently proposed by R. Fitzpatrick. By taking into account 1/ν-regime flow damping and ion polarization effects for small islands, the linear density correlation in tokamak locking threshold has been successfully reproduced [MS-3D-7]. For LHD, on the other hand, C. Hegna applied the Rutherford equation to describe non-linearly saturated islands, and thereby linear β scaling in LHD healing threshold has also been successfully reproduced [MS-3D-8]. These two theoretical progresses imply that 3D error field physics can be well explained if appropriate neoclassical flow damping model and island dynamics are applied, and that advanced neoclassical calculations such as FORTEC-3D [MS-3D-9] can be used to improve understanding of error field effects and their predictability.

Numerical verification of 3D neoclassical transport

The 3D fields established by externally applied 3D field as well as internally driven 3D fields by perturbed plasma currents can modify fundamental neoclassical transport. This is in generally called non-ambipolar transport [MS-3D-10], and also popularly neoclassical toroidal viscosity (NTV) transport [MS-3D-11,12] when toroidal momentum part of transport is considered. As particle orbits can be significantly modified by and importantly resonated with 3D fields while colliding, precession and collisional rates are main parameters to change NTV transport, often up to several orders of magnitude. In NTV analysis, semi-analytic methods have been very popular.

Either by simplifying precession or collisional rates, the drift kinetic equations can be reduced to be an analytically tractable form with bounce-averaging techniques. Since each of these methods are complicated enough to produce very different predictions if not properly treated or normalized, large efforts have been made on numerical benchmarking to confidently perform NTV analysis in strongly shaped plasmas such as present NSTX and future NSTX-U.

It has been shown that the same principle is in fact used for kinetic RWM stability analysis, and that [MS-3D-13] $T_{\varphi}=2in\delta W_k$, (3D-3)

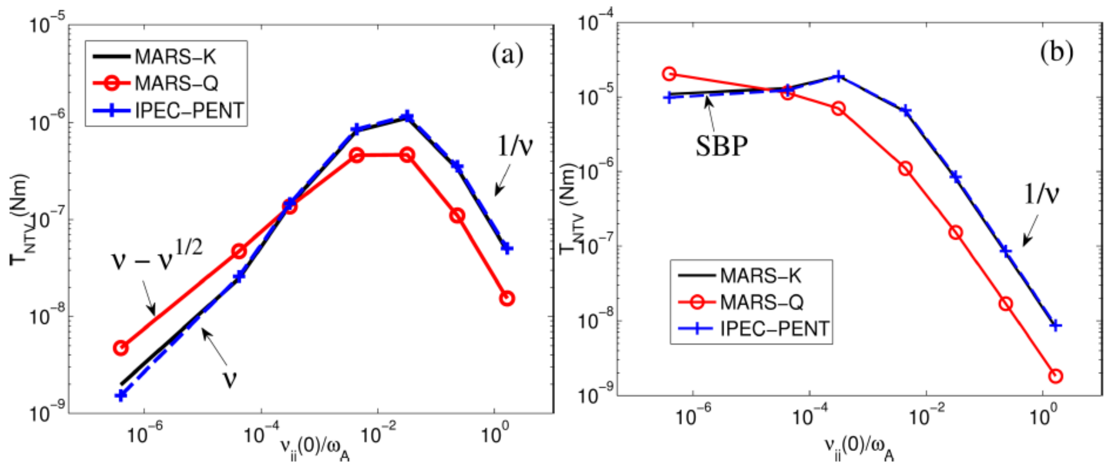

Figure 3D-2: Comparison of the collisionality dependence of NTV torque with (a) $\omega_E=0.1\omega_A$ and (b) $\omega_E=10^{-3}\omega_A$. $\nu_{ii}(0)$ is the ion effective collision frequency at plasma center. For this test, a simple plasma with R/a=10 and circular cross-section is used and perturbed dominantly by (m,n)=(3,1).

which means that the imaginary term of the kinetic potential energy is equivalent to NTV torque within a simple constant factor. This new derivation and theoretical understanding on both kinetic stability and NTV physics led to a unified effort in MS group and extensive benchmarking efforts between MISK [MS-3D-14], MARS-K [MS-3D-15], MARS-Q [MS-3D-16], and IPEC-PENT [MS-3D-17] codes. MISK and MARS-K are δW_k codes, and MARS-K has been recently upgraded to preform NTV analysis by simply accounting the theory equivalence but implementing external 3D boundary conditions. IPEC-PENT is based on Park's formulation of NTV [MS-3D-10], but without geometric simplification that was adopted in previous IPEC-RLAR version of the code. Note IPEC-RLAR has been extensively used in many applications including NSTX, DIII-D, NSTX-U with NCC, and KSTAR up to this year, but the code is being replaced by IPEC-PENT for numerous applications in the future. In results, MISK, MARS-K, and IPEC-PENT codes have exactly the same semi-analytic methods, based on Krook collisional operator but consistent regime combination and without geometric simplification. MARS-Q is developed based on K. C. Shaing's formula with pitch-angle collisional operator but approximated combination across regimes (Pade approximation) and with large aspect ratio expansion [MS-3D-18~21]. The benchmarking between MISK, MARS-K, and IPEC-PENT is an official task agreement with ITER I/O. On the other hand, it is important to check one of three codes to MARS-Q, to verify consistency lying in different formulations, i. e., Shaing's formulation vs. Porcellis' [MS-3D-22] or Park's [MS-3D-10] (PP) formulation.

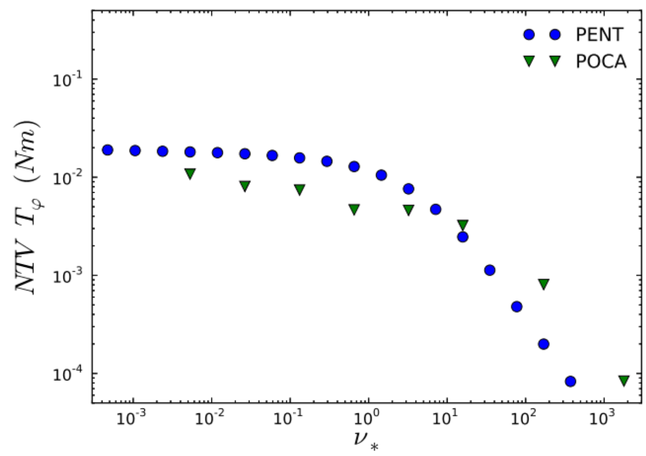

Figure 3D-3: Comparison between POCA and PENT for NTV torque vs. collisionality , for ω_E=0. A simple soloviev equilibrium and a perturbation (m,n)=(3,1) are again used but with some toroidicity such as R/a=2.5.

Figure 3D-2 shows the comparison between MARS-Q and MARS-K depending on the collisionality. IPEC-PENT is shown in addition, but just to indicate numerical verification as MARS-K and IPEC-PENT are based on PP's formulation. One can see the classical 1/ν, ν, and SBP regimes are well reproduced with similar trends, indicating Shaing's and PP's formulation can agree within an order of magnitude. However, the quantitative difference exists with several factors up to 5. In order to clarify this difference, particle simulations by POCA code [MS-3D-23] have been also performed. POCA has the least approximation on 3D neoclassical transport and thus is believed most precise if sufficient number of particles is simulated and followed on exact orbits.

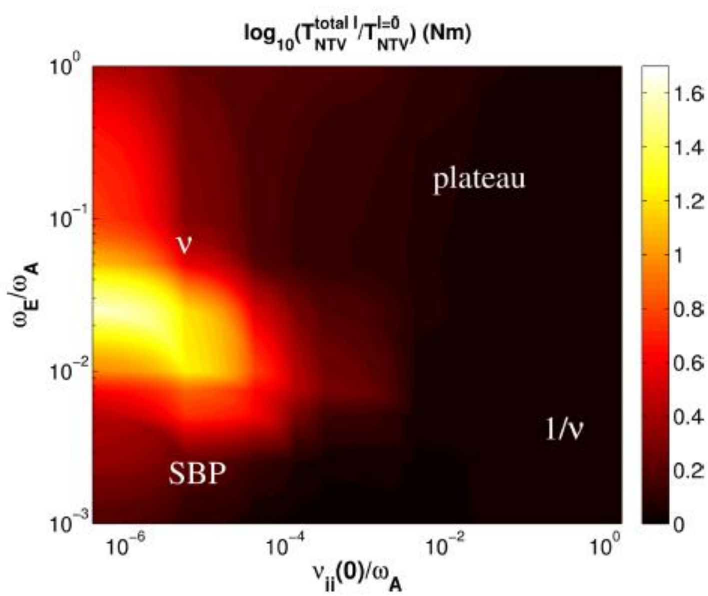

Figure 3D-4: The ratio of the total torque to torque with bounce-harmonic resonances as the function of precession and collisionality. The same target for Figure 3D-2 is used, and IPEC-PENT and MARS-K both agree with this results.

Figure 3D-3 shows the total torque comparison without precession between IPEC-PENT and POCA codes, depending on the collisionality. One can conclude from Figure 3D-2 and 3D-3 that POCA gives the least NTV in SBP regime and IPEC-PENT and MARS-K gives closer answer within a factor of 2~3, while MARS-Q gives overestimation of NTV compared to other codes.

This is due to the geometric simplification used in Shaing's formulation (not by collisional operator as Shaing's SBP also used Krook operator) as explained in details by Reference [MS-3D-17].

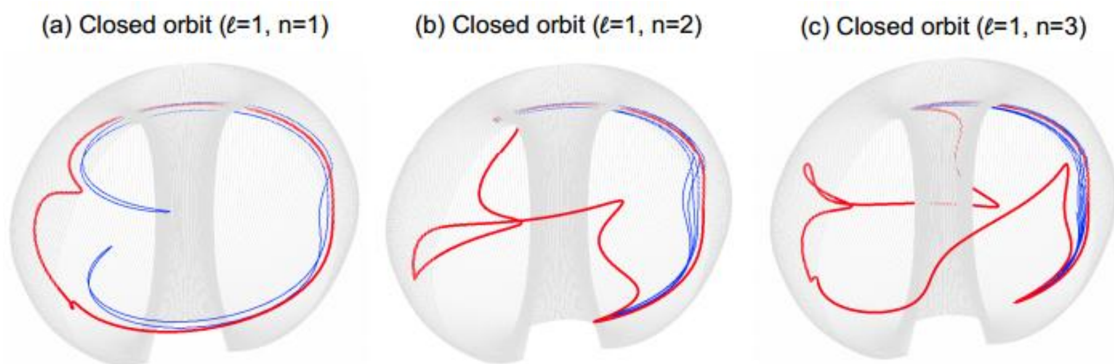

Figure 3D-5: Examples of orbit trajectories of trapped particles subjected into bounce-harmonic resonances in NSTX. Compared to ordinary banana motion (Blue), orbits (Red) are largely modified by precession but still closed by synchronized frequency between parallel motion and perpendicular precession motion.

Another key point that must be emphasized jere is that this comparison is made by only considering precession resonance and by ignoring bounce-harmonic resonances, as Shaing's formulation has not yet combine bounce-harmonic resonances. The importance of bounce-harmonic resonances in general is illustrated by Figure 3D-4. This contour shows total NTV divided by NTV without bounce-harmonic resonances vs. rotation and collisionality, and one can see bounce-harmonic resonances can increase NTV easily more than by an order of magnitude in low collisionality, which is mostly interested in present and future tokamaks. Based on our benchmark and by the reasons discussed so far, MARS-K, MISK, and IPEC-PENT can give better prediction than MARS-Q, if compared with POCA.

POCA can provide the best numerical prediction with the least approximation, and also can illuminate physics mechanism more clearly by resolving detailed particle orbits. One important example is the resonance in particle orbits and applied 3D fields, associated with transport enhancement. Figure 3D-5 shows closed particle orbits in NSTX when the orbit is subjected into bounce-harmonic resonance (Red), compared to ordinary banana orbits when precession motion is ignored. These orbits are closed since the period of perpendicular motion is synchronized with parallel bouncing motion, i. e., $l\omega_b \sim n\omega_P$. When orbits are nearly closed, transport can be largely enhanced as phase-mixing effects suppressing unidirectional transport become ineffective, as illustrated in Figure 3D-6. Note especially radial transport can be strong if field patterns are resonating with the orbit patterns, i.e., $m-nq-l=0$, and but this field resonance should be distinguished from rotational orbit resonance in Figure 3D-6. These resonant effects were predicted by theory, and have been verified by POCA particle simulation this year [MS-3D-24].

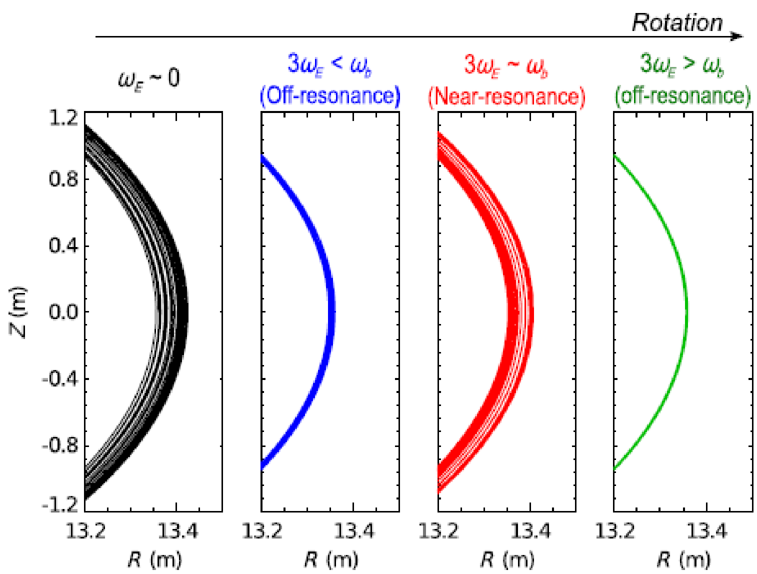

Figure 3D-6: Illustration of transport enhancement of banana orbits by rotational resonances (Black: SBP, Red: BH).

Experimental validation of NTV (with NSTX and also KSTAR collaboration)

In parallel with numerical verification, efforts have been made to validate these calculations in experiments. This is a more complicated issue as (1) it is always difficult to isolate NTV torque in experiments, (2) and also calculations of perturbed equilibrium and the 3D variation in the field strength may be not fully self-consistent. Previously IPEC-RLAR (now updated to IPEC-PENT without geometric simplification) were applied to NSTX but did not find quantitative agreement with experimentally measured torque profiles. Generally NSTX cases serve extreme examples by high-β and strongest shaping in ST geometry, and thus need more precise methods in calculations. One example is shown in Figure 3D-7, where IPEC-RLAR and POCA results are compared with experimental torque density profiles.

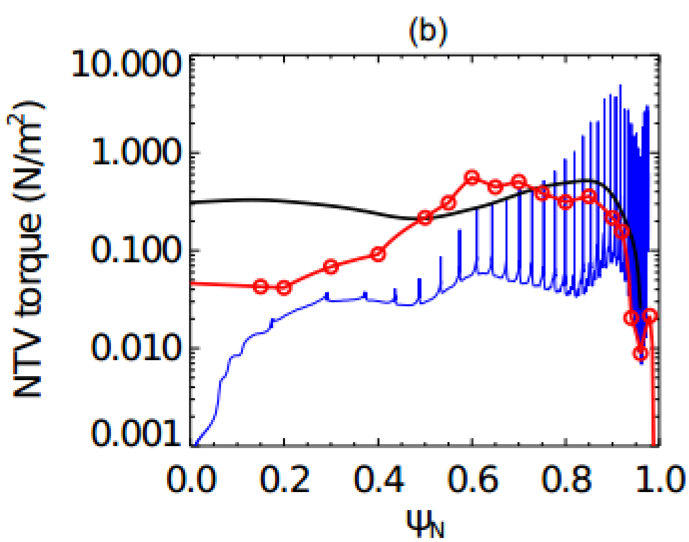

Figure 3D-7: Comparison of torque profiles among experiment (Black), IPEC-RLAR (Blue), and POCA (Red), for NSTX #124439@t=0.5s.

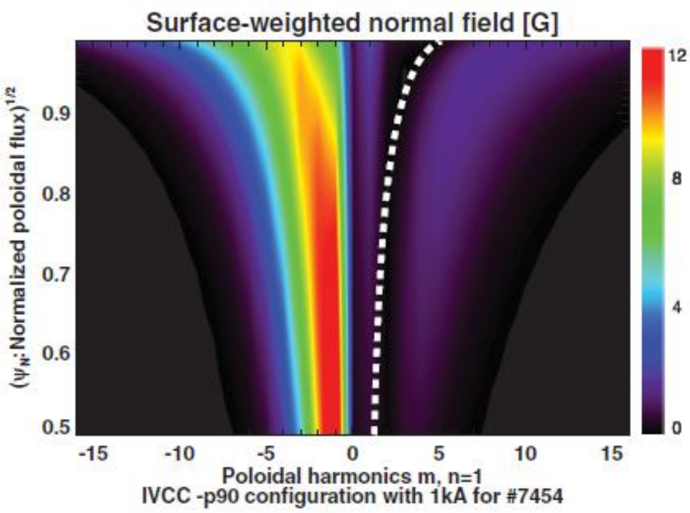

Figure 3D-8: The spectrum contour of the applied field as a function of poloidal modes m and plasma radius. The while dot line is the locus of the resonant mode m~nq, and its location on the other side of the spectral peak indicates highly nonresonant characteristics of the applied field.

As one can see, IPEC-RLAR based on IPEC 3D equilibrium provides reasonably qualitative explanation without free parameters including plasma responses for observed torque density profiles, but only within an order of magnitude. POCA calculations clearly improved agreement especially in the edge, indicating its superior precision as expected. There is still a significant difference, especially in the core, which may indicate the need of fully self-consistent 3D equilibrium including neoclassical friction forces or better isolation or interpretation of experimental torques in the future. Note that POCA prediction for the total torque ~ 2.7Nm is indeed close to experimental value ~3.5Nm, but prediction for torque density profile requires deeper and more details of NTV physics.

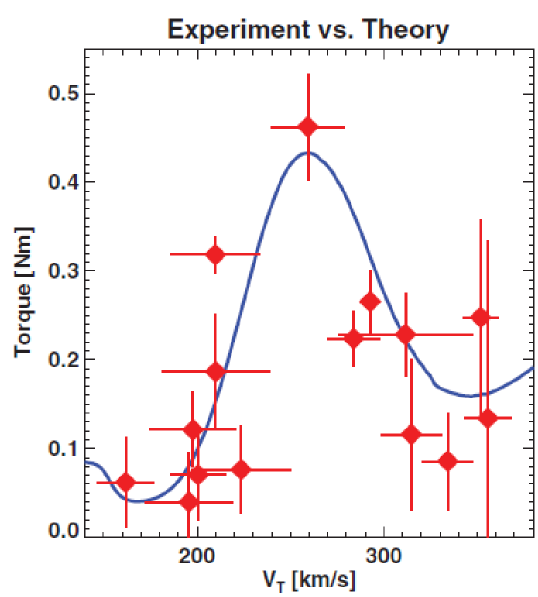

Figure 3D-9: The comparison between theory and experiment for the NTV braking torque as a function of toroidal rotation. Both agree on the resonant rotation and the torque peak values.

Another experimental study is carried out in KSTAR, by utilizing its unique capabilities of three rows of internal 3D coils. Specifically the focus was made upon observation of bounce-harmonic resonance, since a highly non-resonant n=1 can best separate each bounce-harmonic resonances while minimizing the strong n=1 resonant effects and KSTAR 3D coil set is almost unique to produce the highly non-resonant n=1. Using three rows of coils, the field pattern can be adjusted to be orthogonal to the field line pitches in most of outboard section, resulting in spectrum contour shown in Figure 3D-8 and the spectral peak on the other side of m=0 compared to the field line pitches. Indeed this field modified only toroidal rotation without any perturbation or resonant effects in other parameters. This rotational braking was tested with different injection torques and thus initial rotation level, and the test showed that the braking can be strong in a particular level of rotation. This is precisely predicted by theory and the rotational resonance is identified by the 1st bounce-harmonic resonance by calculations. Figure 3D-9 shows the comparison and agreement between theory and experiment for the total torque. Although theoretical calculations are conducted by IPEC-RLAR, this approximation is valid for KSTAR target cases which are all in low-beta and relatively weak shaping. Indeed, IPEC-PENT prediction is very similar to IPEC-RLAR for these KSTAR cases. This is the first successful experimental observation of bounce-harmonic resonance that has been predicted by theory and verified by POCA simulation.

References

[MS-3D-1] J.-K. Park et al., Phys. Rev. Lett. **99** (2007) 195003
[MS-3D-2] J.-K. Park et al., Nucl. Fusion **51** (2011) 023003
[MS-3D-3] J.-K. Park et al., Nucl. Fusion **52** (2012) 023004
[MS-3D-4] T. Morisaki et al., Fusion Sci. and Technol. **58** (2010) 469.
[MS-3D-5] M. Jakubowski, Private communication.
[MS-3D-6] Y. Narushima et al., Nucl. Fusion **48** (2008) 075010
[MS-3D-7] R. Fitzpatrick, Plasma Phys. Contol. Fusion **54** (2012) 094002
[MS-3D-8] C. Hegna, Phys. Plasmas **19** (2012) 056101
[MS-3D-9] S. Satake, J.-K. Park et al., Phys. Rev. Lett. **107** (2011) 055001
[MS-3D-10] J.-K. Park et al., Phys. Rev. Lett. **102** (2009) 065002
[MS-3D-11] W. Zhu, S. A. Sabbagh et al., Phys. Rev. Lett. **96** (2006) 225002
[MS-3D-12] K. C. Shaing, J. D. Callen, Phys. Fluids **26** (1983) 3315
[MS-3D-13] J.-K. Park, Phys. Plasmas **18** (2011) 110702
[MS-3D-14] J. W. Berkery et al., Phys. Rev. Lett. **97** (2006) 045004
[MS-3D-15] Y. Q. Liu et al., Plasma Phys. Control. Fusion **52** (2010) 104002
[MS-3D-16] Y. Sun, Y. Liang, K. C. Shaing et al., Nucl. Fusion **51** (2011) 053015
[MS-3D-17] N. Logan, J.-K. Park et al., in preparation to submission (2013)
[MS-3D-18] K. C. Shaing, Phys. Plasmas 10 (2003) 1443
[MS-3D-19] K. C. Shaing et al., Phys. Plasmas 15 (2008) 082506
[MS-3D-20] K. C. Shaing, S. A. Sabbagh et al., Plasma Phys. Control. Fusion **51** (2009) 035009
[MS-3D-21] K. C. Shaing, S. A. Sabbagh et al., Nucl. Fusion **50** (2010) 025002
[MS-3D-22] F. Porcelli et al., Phys. Plasmas **1**, (1994) 470
[MS-3D-23] K. Kim, J.-K. Park et al., Phys. Plasmas **19** (2012) 082503
[MS-3D-24] K. Kim, J.-K. Park et al., Phys. Rev. Lett. **110** (2013) 185004

Non-axisymmetric control coil applications in NSTX-U (NCC)

NSTX research in the past has made a new understanding of plasma response to non-axisymmetric (3D) magnetic field in ST and generally tokamaks. As 3D magnetic field applications are recognized essential to mitigate instabilities such as locking, braking, or generally control global and edge instabilities such as RWMs and ELMs in the next step devices such as ITER, and thus a new non-axisymmetric control coil (NCC) set has been proposed for NSTX-U to study physics advantages associated with various 3D magnetic field. Assuming staged NCC implementation, mainly two partial NCC and full NCC configurations have been considered as shown in Figure NCC-1, and physics capabilities on active RWM control, error field correction, rotation control with NTV braking, and ELM stability control, have been compared with existing midplane coils in NSTX.

Active RWM control

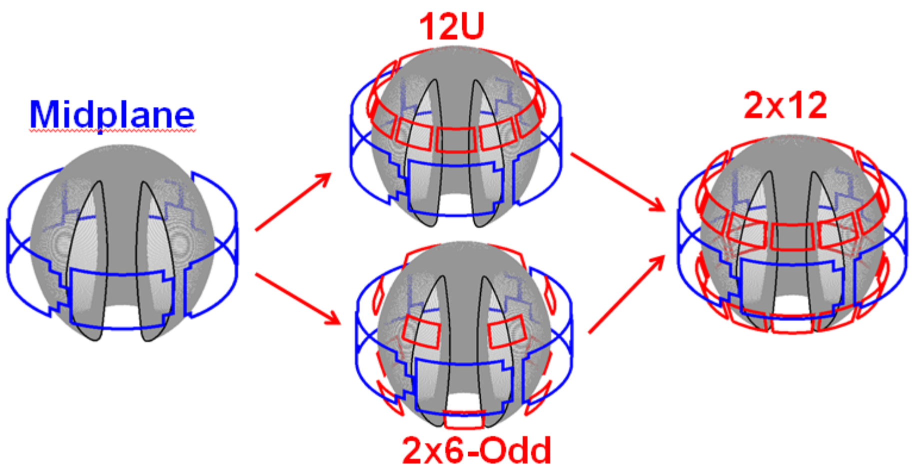

Figure NCC-1: Present partial NCCs (12U and 2x6-Odd) and full NCC (2x12), compared to the existing midplane coils. The partial NCC options have been compared for a staged installation before the full NCC

Performance improvement by NCC is apparent in active RWM control. A series of NSTX-U theoretical equilibria were created with varying normalized beta and used in the VALEN-3D code to evaluate the $n = 1$ RWM control performance for different possible incarnations of the NCC as one of several physics analyses conducted to determine a superior coil design. RWM growth rate curves for several of the coil configurations tested are shown in Figure NCC-2. In each case shown, the full 3D conducting structure of NSTX-U is included and the action of the NCC coil set and the existing midplane RWM coil set are both included in the RWM control performance evaluation.

While the results in Figure NCC-2 show a clear trend of improved performance from top left to bottom right, it is important to note that the results shown utilize ideal sensors – not the existing sensors on the NSTX device. When the realistic sensors are used, they are significantly influenced by the action of eddy current in the copper passive plates generated by the NCC that are mounted on them in these designs. This important result (and minor issue) will be addressed in the continued design of the NCC for RWM control system including the NCC in NSTX-U.

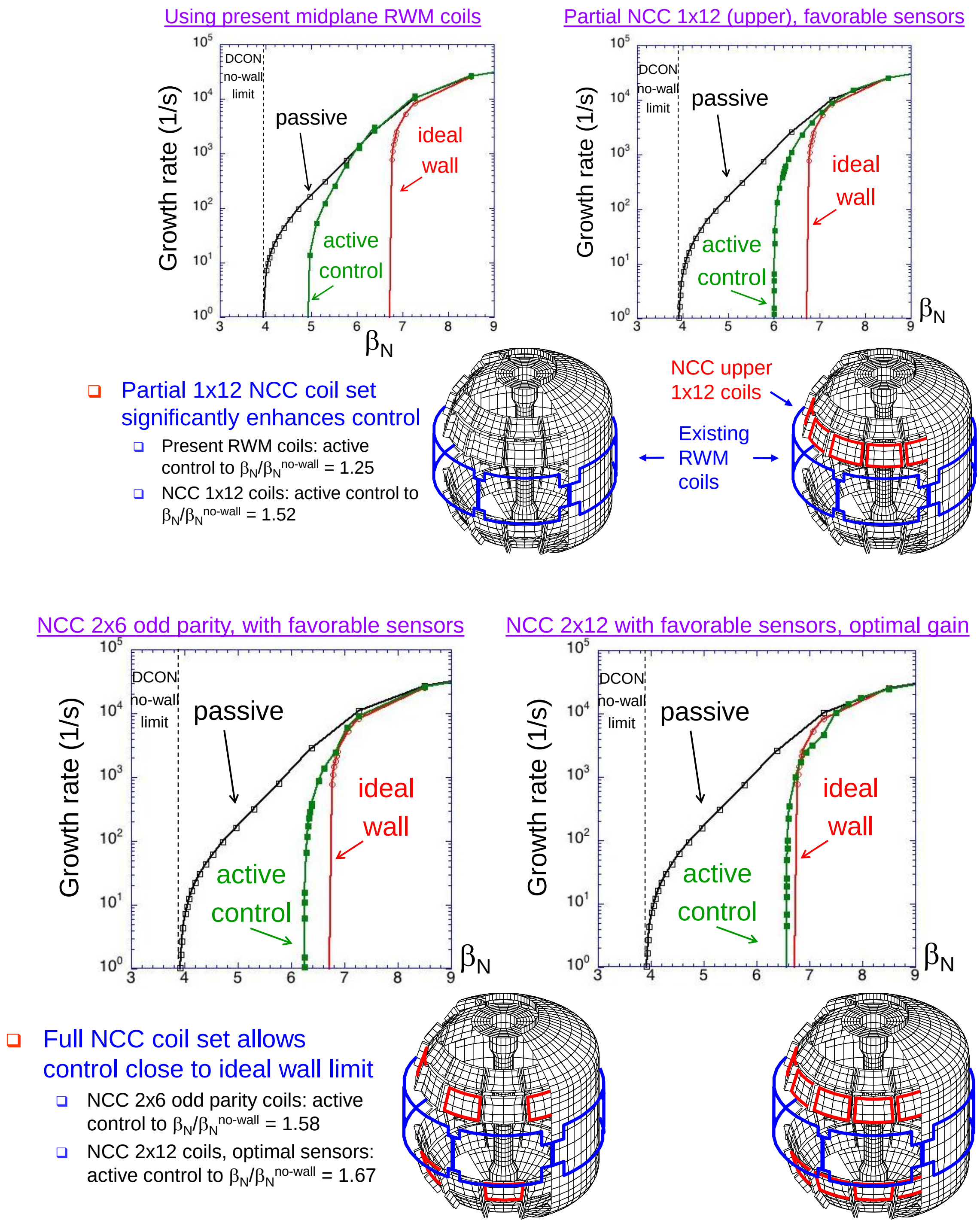

Figure NCC-2: Design study for NSTX-U NCC options considering n = 1 RWM active mode control with 3D conducting structure (stabilizing plates and vessel), and combined action of NCC options (red) and existing RWM coil (blue).

Error field control

Larger sets of coil arrays imply greater flexibility of field spectrum in applications. One of important applications with extended spectral flexibility is to separate non-resonant magnetic field from resonant magnetic field, which often dominates physics driven by non-resonant field effects such as NTV. IPEC-RLAR analysis [MS-NCC-2], Figure NCC-3, shows that NCC, either by partial 2×6-Odd set or full set, can suppress resonant field while producing strong n=1 non-resonant field and NTV by shifting toroidal phase between upper and lower coil arrays. This means n=1 can be highly non-resonant and free from locking or tearing. On the other hand, study shows that NCC can also produce highly pure resonant field if optimized and mixed even with midplane coils, which will be also important to isolate resonant locking effects from NTV and to establish the basis for ITER error field correction criteria.

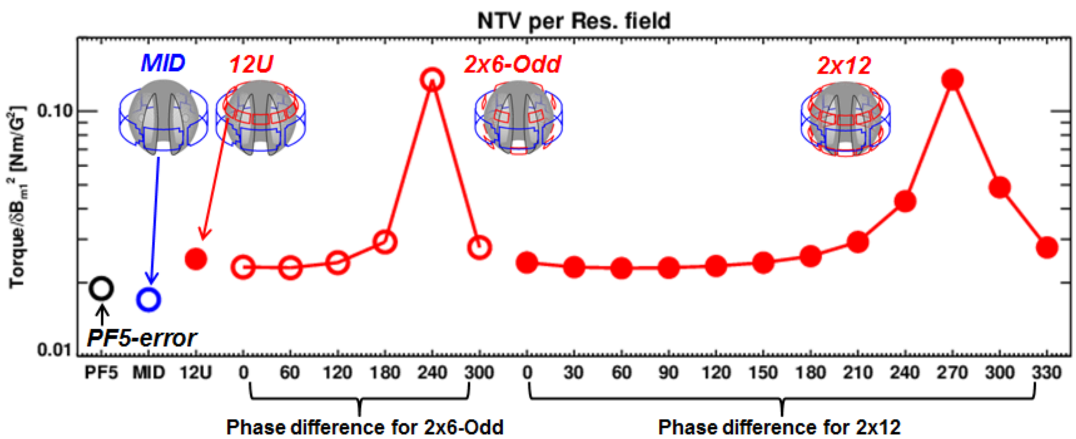

Figure NCC-3: The NTV per resonant fields that are produced by partial and full NCC coils with 1kAt; 12U, 2x6-Odd with 6 different phases (Open red circles), and 2x12 with 12 different phases (Filled red circles), compared to the present midplane coils (Blue). The case by PF5 coils with 20kA is also shown (Black).

Rotation control with NTV

Rotation control by 3D magnetic field has numerous application areas, as most of macroscopic instabilities such as LM, TM, RWM, and also microscopic instabilities such as ITG, TEM, ETG, can be strongly modified by rotation or rotational shear profiles. Thus it is important to investigate and predict a 3D field and coil set that can produce localized NTV braking or a number of different NTV braking profiles combined with injecting torques such as NBI. The study shows that partial NCC can generate different core braking compared to edge braking by an order of magnitude and that full NCC by another order of magnitude if high n=4~6 is utilized, as summarized in Figure NCC-4. This is promising as it implies NCC can produce strong rotational shear. Here it should be emphasized that present NTV analysis tools are not fully established yet. Extensive benchmarking efforts indicate that the IPEC and combined NTV calculations are qualitatively valid in many cases but can be not so precise in high-beta and strongly shaped plasmas such as NSTX and NSTX-U, and thus these NTV calculations will be revised with full geometric calculations and particle simulations. This will be described in details by section for NTV theory and computation.

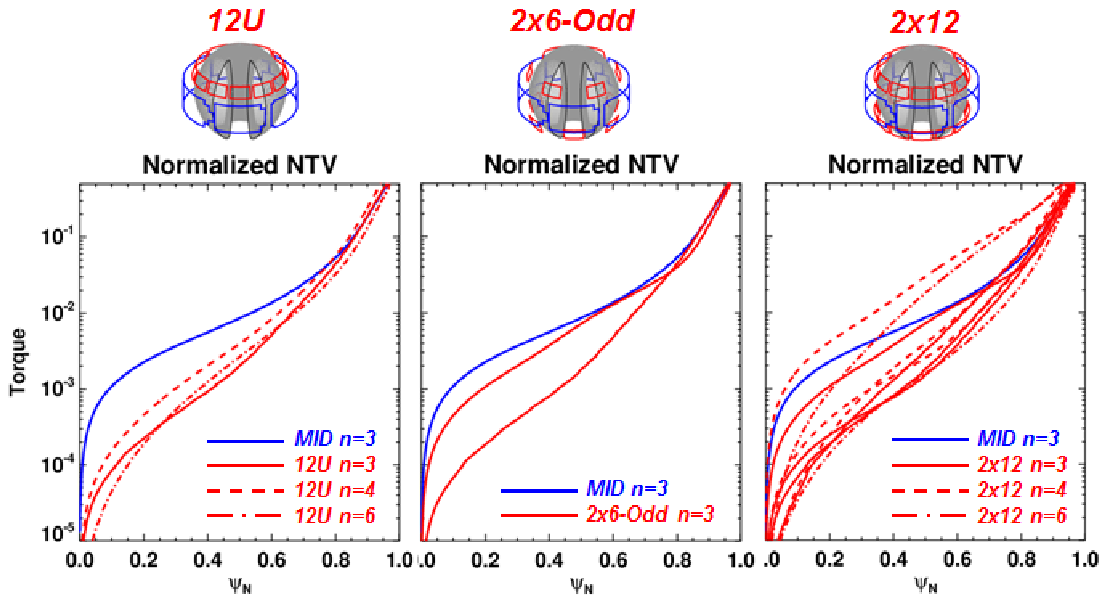

Figure NCC-4: The torque profiles integrated from the core, for the partial 12U, 2x6-Odd and full 2x12 NCC. One can see that the torque values can be changed in the core by an order of magnitude with the partial NCCs, and by another order of magnitude with the full NCC using high n perturbations.

3D Field characteristics for ELM control

Another important issue is whether or not NCC can provide better particle control and also ELM control. The 3D field effects on ELMs are not yet fully understood, although various experimental demonstrations have been achieved in different devices. One of the well-known empirical criteria for ELM suppression is the vacuum Chirikov overlap condition for resonant magnetic perturbation (RMP) [MS-NCC-3], which partially represents the resonant coupling between 3D fields and rational surfaces in the edge. Another condition is the pitch-alignment condition, and this represents the minimized non-resonant field components other than the edge-resonant components. However, the pitch-alignment condition is qualitative, and a more quantitative condition is needed for actual assessment. A figure-of-merit (FOM) parameter for RMP ELM control in the study is defined as the vacuum Chirikov overlap parameter [MS-NCC-4] (with fourth-power to make this parameter independent of field strength), divided by NTV that is representing the non-resonant field components, similarly to the pitch-alignment condition. From Figure [NCC-5] one can see that the FOM can be increased by an order of magnitude with the partial NCC, and even another order of magnitude when the high n = 4 or 6 is utilized with the full NCC. Although no single criterion, including this FOM parameter, has been found to explain RMP ELM control, this analysis indicates that the NCC will enable significantly expanded testing of RMP ELM control over wide ranges of field spectra to improve the physics understanding of ELM mitigation physics.

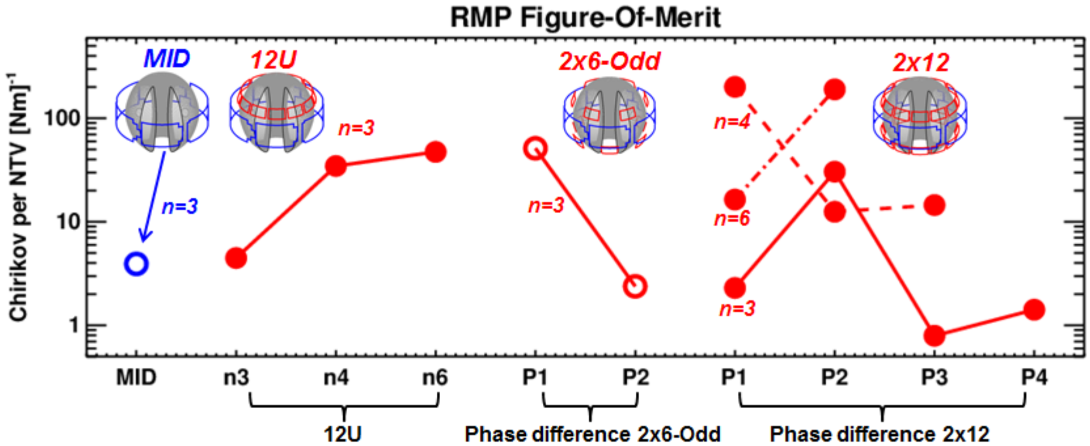

Figure NCC-5: Comparison for figure of merit parameter for ELM control, among existing midplane coils, the two partial NCCs, and the full NCC.

ELM stability changes by 3D fields

An open question on 3D field applications on ELMs is whether the 3D fields directly impact ELM stability such as ballooning stability. For this, a 3D equilibrium is directly generated by running VMEC [MS-NCC-5] with NSTX-U and NCC fields and the infinite n ballooning stability of the 3D equilibrium is then analyzed using the COBRA code [MS-NCC-6]. With the n=3, up-down symmetric and full NCC field applied, the VMEC and COBRA calculations indicate a broad region of ballooning instability with 30% of the outer poloidal flux showing positive growth rates compared the axisymmetric case without the NCC. For comparison, a case

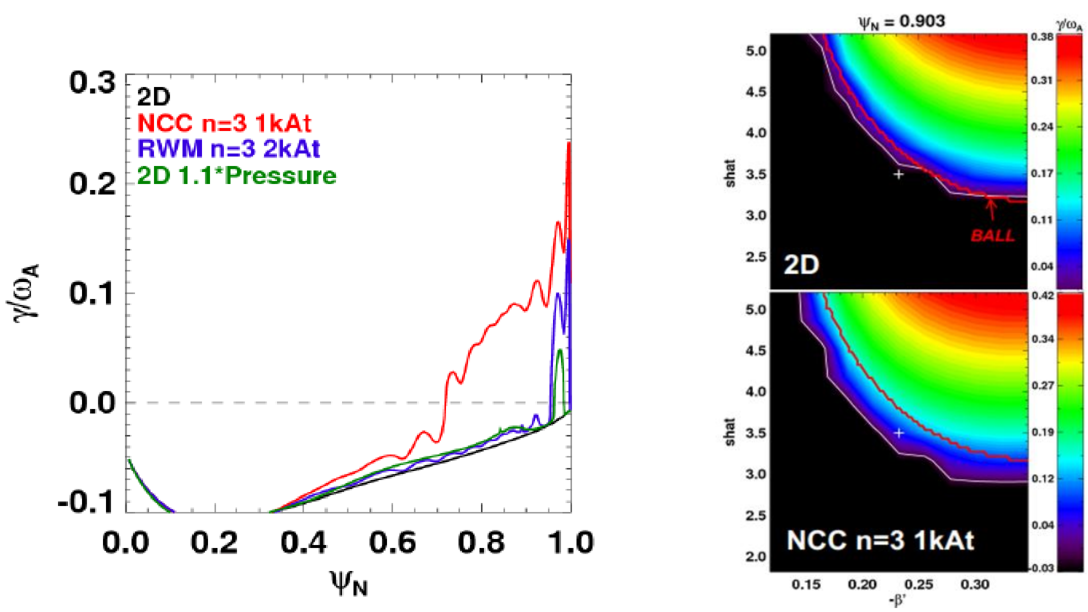

Figure NCC-6: (a) Ballooning growth rates for nominal axisymmetric case (black), with NCC fields applied (red), with RWM fields (blue), and axisymmetric with 10% pressure increase (green). (b) Ballooning growth rates as a function of pressure gradient and magnetic shear (shat) for axisymmetric case and with NCC applied. Red curve indicates axisymmetric BALL calculation of stability boundary.

with the midplane coils energized in an n=3 configuration shows only a narrow edge region that is unstable as shown in Figure NCC-6a. This is consistent with the weak impact of the midplane coil set on ballooning stability in Reference [MS-NCC-7]. Similarly a new axisymmetric ase, with no 3D fields applied but with the plasma pressure increased by 10%, showed only a small unstable region. To more thoroughly determine the changes to the ballooning stability limits caused by the NCC, large sets of VMEC equilibria were generated with the safety factor and pressure profiles slightly modified near a radius of psiN~0.9. Figure NCC-6b shows that the NCC can indeed modify ELM stability boundaries by up to 30% compared to the non-axisymmetric cases in various profiles. Note results by 2D BALL code analysis is also shown to indicate COBRA code can fairly well reproduce stability boundaries in the axisymmetric case. Performed analysis indicates that the NCC can be more effective for ELM triggering and pacing [MS-NCC-8,9], which will be an important area for a test in NSTX-U.

References

[MS-NCC-1] J. Bialek, A. H. Boozer et al., Phys. Plasmas **8** (2001) 2170
[MS-NCC-2] J.-K. Park et al., Phys. Rev. Lett. **102** (2009) 065002
[MS-NCC-3] T. E. Evans et al., Phys. Rev. Lett. **92** (2004) 235003
[MS-NCC-4] M. E. Fenstermacher et al., Phys. Plasmas **15** (2008) 056122
[MS-NCC-5] S. P. Hirshman et al., Comput. Phys. Commun. **43** (1986) 143
[MS-NCC-6] R. Sanchez et al., Comput. Phys. Commun. **135** (2001) 82
[MS-NCC-7] J. M. Canik et al., Nucl. Fusion **52** (2012) 054004
[MS-NCC-8] J. M. Canik et al., Phys. Rev. Lett. **104** (2010) 045001
[MS-NCC-9] J. M. Canik et al., Nucl. Fusion **50** (2010) 034012

Disruption studies

Disruption Mitigation

Experimental results from DIII-D and C-MOD, and NIMROD simulations show that the cold front from the edge, which has been cooled by the massive gas injection pulse, needs to reach the q=2 surface for the onset of rapid core cooling to occur. On ITER, because of the large minor radius of the device and the long transit times for the slow-moving neutral gas, additional results are needed from NSTX and other tokamaks to improve out understanding of MGI physics.

During the past year we accomplished the following tasks.

1. Designed, fabricated, and built the proto-type of a new design Electromagnetic Massive Gas Injection Valve for installation on NSTX-U. The valve is at present undergoing off-line tests at the Univ. of Washington. After off-line tests are completed later this year, three such valves will be built for installation on NSTX-U. Prior to fabricating the proto-type valve, a design peer review was held at PPPL on 6 March 2013 to ensure all systems associated with this valve are compatible with NSTX-U procedures and policies.

2. With the help of Dr. Daren Stotler and Mr. Tyler Abrams of PPPL, we continued work on DEGAS-2 modeling to study gas penetration physics through the edge SOL plasma region to support NSTX-U MGI experiments.

3. As a result of better appreciation of the challenges for safely terminating discharges in ITER and the limitations of the proposed MGI systems for ITER, in 2012 we developed a new concept for a possible future disruption mitigation system. This concept known as "Electromagnetic Particle Injector" (EPI) involves injecting particulate matter of varying sizes and composition using a coaxial projectile accelerated in a coaxial rail run. Off-line experimental testing of a simplified version of this concept will begin after the MGI valve tests are completed [MS-DIS-1,2].

MGI System:
The original NSTX MGI installation used multiple valves in parallel and relied on valves that were used for initiating CHI discharges on NSTX. We have now designed and built an improved design valve, similar in design to the valve that is being planned for ITER. An earlier version of this valve is shown in Figure DIS-1. Figure DIS-2 qualitatively shows the NSTX-U MGI valve operating components and Figure DIS-3 is an engineering drawing showing the valve as it would be mounted on the lower dome organ pipe on NSTX-U. A similar such valve would be mounted on an organ pipe in the upper divertor area and a third valve would be installed at the vessel mid-plane. FY2015 NSTX-U MGI experiments would use three such valves at different poloidal locations to initiate studies in support of Disruption Mitigation physics.

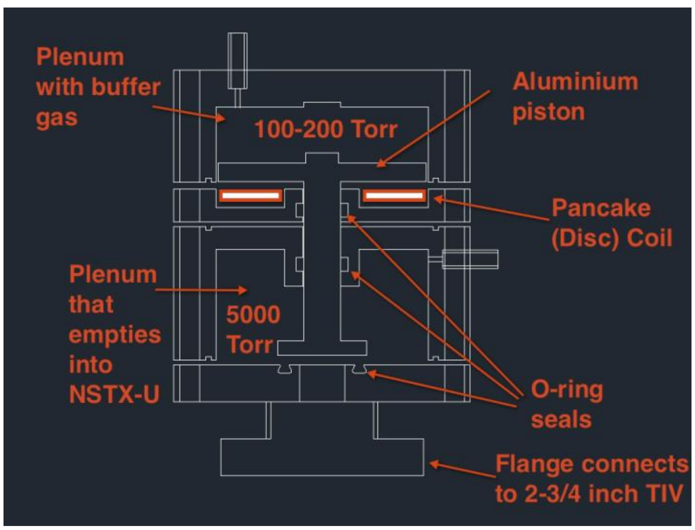

Figure DIS-1: Key components of the Electromagnetic MGI valve. A rapid current pulse in the pancake disc coil induces currents in the aluminum piston, which is repelled from the pancake coil. This causes the O-ring seal in the lower part of the valve to be broken, causing the plenum to empty into the vessel on the 1-2 ms time scale. The operating principle is similar to the valves that were used reliably on a Compact Toroid (CT) injector for fuelling studies on the TdeV tokamak. The CT injector used 10 valves in parallel, all of which were built by our local machine shop.

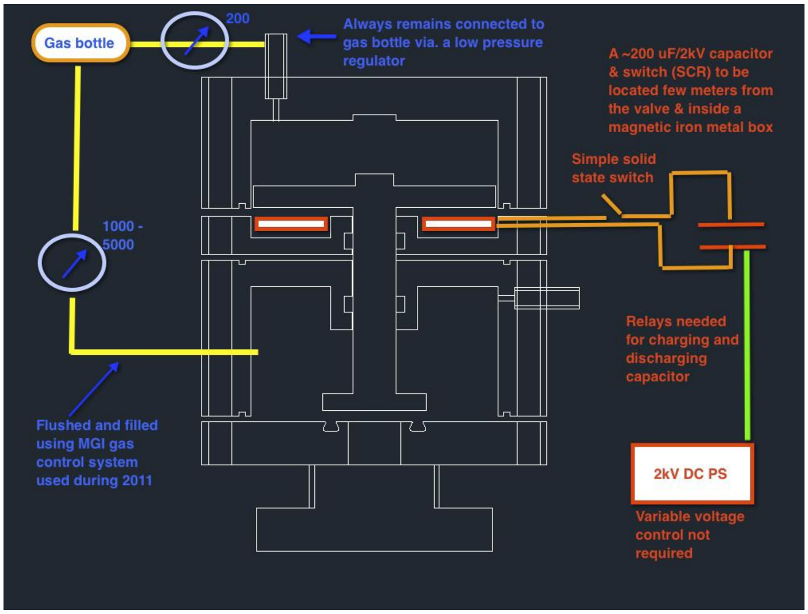

Figure DIS-2: A 100-200 micro Farad capacitor charged to 2 kV is discharged through the pancake coil to provide discharge current pulse through the coil.

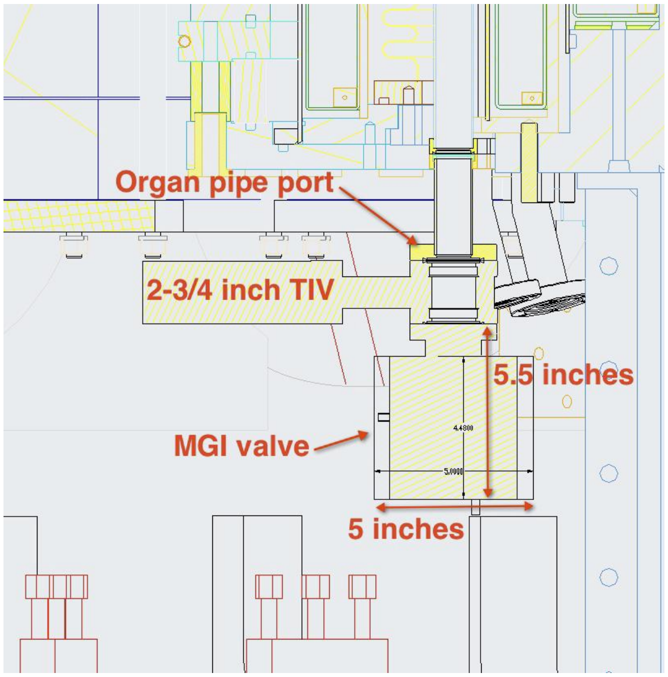

Figure DIS-3: Drawing showing location of the new design MGI valve on a lower organ pipe on NSTX-U. Two additional valves would also be installed at other poloidal locations on NSTX-U for a direct comparison of injection from different poloidal locations, as well as simultaneous injection from all three locations.

DEGAS-2 Modeling

The amount of gas injected in MGI experiments in present tokamaks varies from 100 Pa.m3 to over 2000 Pa.m3, considerably less than the projections for ITER. The fraction of this gas that penetrates the separatrix also varies widely, with penetration efficiencies of over 20% being reported for cases that have a short MGI pulse [MS-DIS-3,4]. To better quantify the amount of gas required in a MGI pulse we have initiated a DEGAS-2 Monte-Carlo [MS-DIS-5] code simulation effort to understand the extent of gas penetration through the SOL region and private flux regions. In addition to supporting NSTX-U needs, this simulation effort focuses on fundamentally studying the edge penetration issues to the separatrix, which is needed for predicting gas penetration efficiencies in ITER. This work complements other 3-D MHD modeling, initiated by the ITER organization, of the gas dissipation inside the separatrix. The results presented here are preliminary. The code employed is not yet capable of simulating energetic SOL flows and so does not yet correctly reflect edge conditions that would exist in a high power discharge. A more energetic plasma in the SOL would increase the gas ionization rate in this region and reduce gas penetration.

In these simulations, a 3-D planar simulation geometry has been developed in which D_2 or He gas is injected from the center of 1 m x 1 m wall. A vacuum region 20 cm wide separates the gas injection source from the edge of the plasma. A parameter sweep was performed in SOL/PFR width (0.2 – 5.0 cm), electron temperature (1 – 100 eV) and density (10^{18}– $2x10^{20}$ m^{-3}). This parameter range includes expected conditions in the SOL and PFR of both NSTX-U and ITER. Simulations indicate the penetration fraction of gas through the NSTX-U SOL will be 0.2-0.6 for D_2 and 0.7-0.9 for He. For injection into the NSTX-U PFR, on the other hand, the penetration fractions increase to 0.4-0.9 for D_2. Actual penetration fractions may be even higher, as gas injected into the PFR need not transit a 20 cm wide vacuum region. However, the penetration fractions strongly depend on the closeness of the divertor X-point to the injection location and on the temperature of the plasma in this region. Note that the effects of the gas puff on the plasma are not accounted for in these simulations. Cooling of the plasma would increase penetration, but the increased density would reduce it. Simulations at the higher electron temperature of 100 eV, corresponding to the ITER SOL conditions, suggest a reduction of at least a factor of two in the penetration fraction. These results imply that the gas penetration fraction strongly depends on both the edge plasma parameters and the injection location, and warrant further studies using a more detailed model. Figures DIS-4 and DIS-5 show some of the results from these simulations.

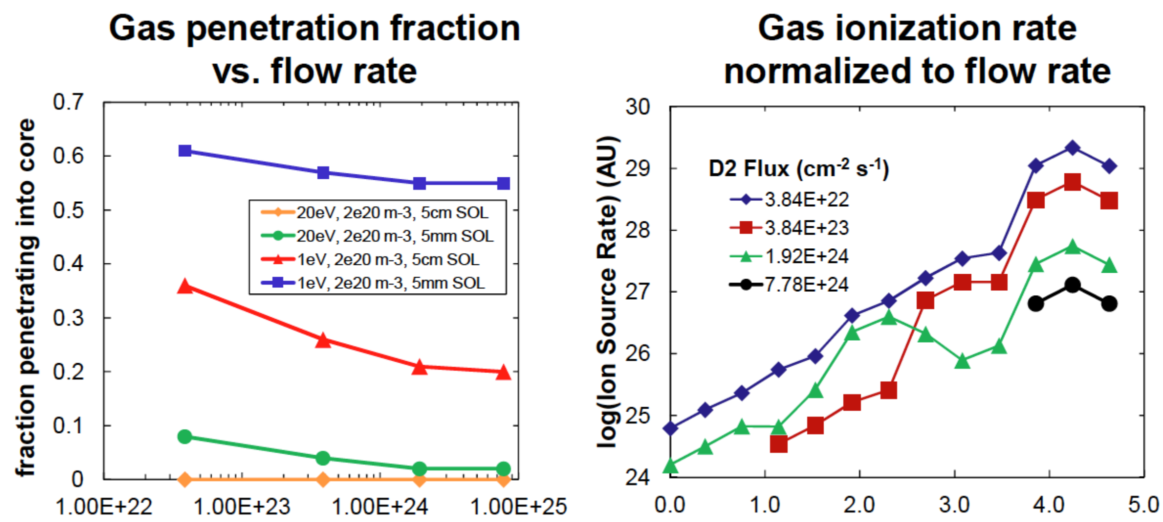

Figure DIS-4: Gas penetration version flow rate shows a decrease of the penetration fraction due to more spreading of the injected gas. The 1eV and 20eV cases are for assumed SOL/pedestal widths of 0.5mm and 5cm cases. Right: Plot of gas ionization rate versus distance from the separatrix. For reference, the private flux region in ITER is predicted to have an electron temperature of less than 2eV and an electron density of below $2x10^{20}$ m^{-3} [MS-DIS-6]. Representative values for these two parameters for detached DIII-D plasmas are an electron temperature of less than 1eV and electron density less than $5x10^{19}m^{-3}$ [MS-DIS-7]. The relatively low electron temperature in the private flux region in both ITER and DIII-D is due to active gas puffing in the divertor region to obtain a detached divertor configuration, which is necessary to reduce divertor heat loads. The electron temperature and electron density in the SOL at the mid-plane region of ITER is predicted to be about 100eV and $2x10^{19}m^{-3}$ [MS-DIS-8]. The corresponding values for DIII-D are an electron temperature less than 20eV and an electron density less than $3x10^{18}$ m^{-3} [MS-DIS-9]. The parameters for the NSTX-U could be expected to similar to those for DIII-D.

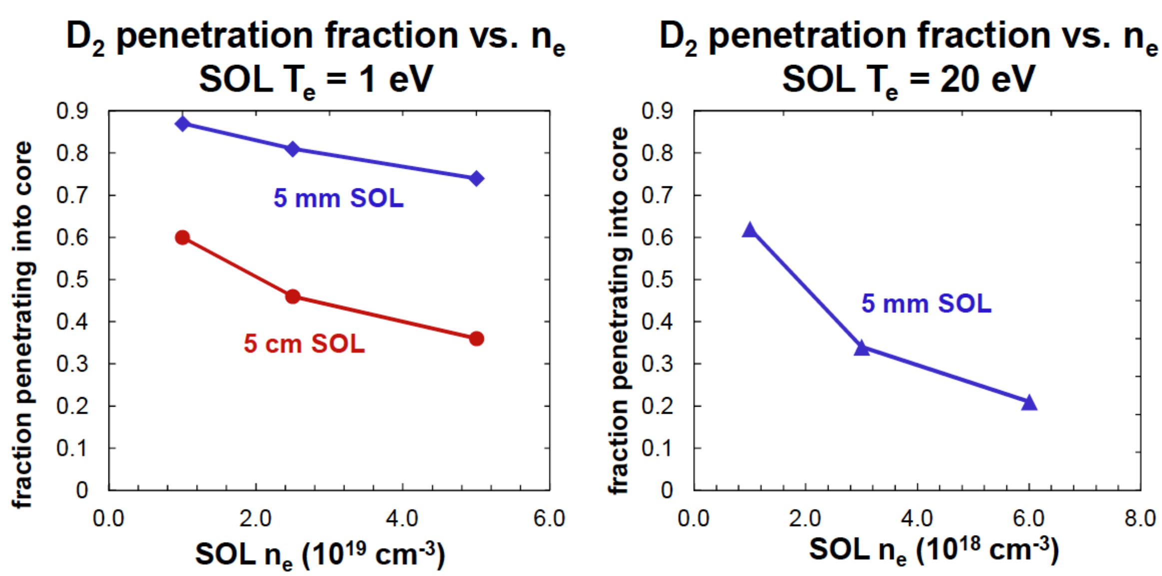

Figure DIS-5: Deuterium penetration fraction versus SOL density for 1eV and 20eV SOL temperature cases

Theory of Halo currents

Stefan Gerhardt's analysis of halo currents during NSTX disruptions [MS-DIS-10] showed four features that have motivated theoretical analyses:

1. Rotating halo currents were observed to have jumps in phase. A theoretical explanation [MS-DIS-10] of the rotation involves the large radial electric field that naturally arises across the open magnetic field lines of the plasma edge. Jumps in the rotation phase occurs [MS-DIS-11] when the impedance of the wall to halo currents depends on the toroidal angle.
2. The halo currents were observed to flow into and out of the wall in only about a third of its toroidal circumference.
3. The n=0 and the n=1 Fourier components of the halo current were observed to have a comparable amplitude when the halo current was observable but before the magnetic axis contacted the wall.
4. Halo currents were found to either flow into or out of a particular wall tile with the sign determined by the poloidal position of the tile.

These last three features can be explained [MS-DIS-12] when the width of the channel in which the halo current flows around the plasma is narrow compared to the amplitude of the plasma kinking. Two discordant constraints are central to the theory: (1) Halo currents must produce the magnetic field distribution required to maintain plasma force balance--a distribution that depends on the two angular coordinates of a torus. (2) Halo currents must flow along the magnetic field lines in the plasma, which implies a dependence on a linear combination of the two angular coordinates - only one angular coordinate is free. These two constraints are sufficiently limiting that many features of halo currents can be understood using results from existing codes.

References

[MS-DIS-1] R. Raman, "Disruption mitigation plans on NSTX," US Disruption Mitigation Workshop, General Atomics, San Diego, March 12-13, 2103
[MS-DIS-2] R. Raman, "Electromagnetic particle injector for NSTX-U," 17th MHD Control Workshop, Columbia University, New York City, November 5-7, 2012
[MS-DIS-3] R. Raman, et al., IEEJ Transc. on Fund. and Materials 132 (2012) 468
[MS-DIS-4] T. Abrams, et al., "Simulations of deuterium and helium massive gas injection for NSTX-U and ITER," Theory and Simulation Workshop, PPPL, 16-18 July, 2013
[MS-DIS-5] D.P. Stotler and C.F. Karney, "Neutral Gas Transport Modeling with DEGAS 2", Contrib. Plasma Phys. 34 (1994) 392-397
[MS-DIS-6] V. Kotov, et al., "Numerical study of the ITER divertor plasma with the B2-EIRENE code package," Bericht des Forschungszentrums Julich, Jul-4257, November (2007)
[MS-DIS-7] S.L. Allen, Rev. Scientific Instrum. 68 (1997) 1261
[MS-DIS-8] A.S. Kukushkin, et al., Nuclear Fusion, 47 (2007) 698
[MS-DIS-9] D.L. Rudakov, et al., Nuclear Fusion, 45 (2005) 1589
[MS-DIS-10] S. P. Gerhardt, Nucl. Fusion 53 (2013) 023005
[MS-DIS-11] A. H. Boozer, Phys. Plasmas 19 (2012) 052508
[MS-DIS-12] A. H. Boozer, Phys. Plasmas 20 (2013) 082510

Transport and Turbulence Physics Research

NSTX transport and turbulence studies in FY2013, in the absence of operation, have focused on analyzing existing data and performing experiment-theory comparisons.

Collisionality dependence of H-mode confinement and transport

A global energy confinement scaling with strong inverse dependence on collisionality has been established for STs [TT-1,2,3]: $B\tau_E \sim \nu_{*e}^{-0.8}$ (see Fig. TT-1(a)), while the ITER scaling on collisionality is much weaker: $B\tau_E \sim \nu_{*e}^{-0.01}$ [TT-4]. The ST confinement scaling leads to an order magnitude of improvement in projected performance of ST-FNSF in contrast to that from the ITER scaling. As seen in Fig. TT-1, this ST global energy confinement scaling is independent of wall conditioning, either using Helium Glow Discharge Cleaning plus occasional boronization for wall conditioning (HeGDC+B) or between-shot lithium conditioning of the vessel walls through evaporation from two LITERs (LIThium EvapoRators) mounted at the top of the NSTX vessel [TT-5,TT-6]. This collisionality dependence also unifies the different engineering scaling observed with different wall condition: $\tau_{E,th} \sim Ip^{0.37}B_T^{1.01}$ for HeGDC+B wall conditioning and $\tau_{E,th} \sim Ip^{0.79}B_T^{-0.15}$ for lithium wall conditioning with the latter scaling similar to those in conventional aspect ratio tokamaks, as embodied in the ITER98y,$_2$ scaling with a strong I_p dependence and a weak B_T dependence. This unification implies that collisionality is more fundamental in determining energy confinement and the difference in engineering scalings comes from what engineering parameter collisionality is correlated with. Indeed, it is found that with HeGDC+B wall conditioning, reduction in collisionality is mostly correlated with the increase in B_T and on the other hand, when lithium is used for wall conditioning, reduction in collisionality is correlated well with increase in amount of lithium deposition.

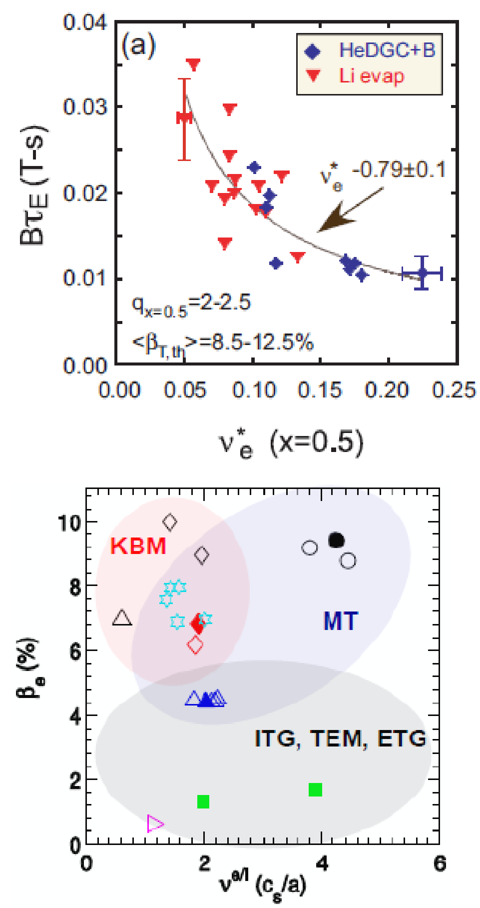

Fig. TT-1: (a) Normalized confinment time as a function of collisionality at ρ=0.5 (b) Local (r/a=0.6-0.7) electron beta and normalized collision frequency for various NSTX-H modes. Shaded regions indicate where in parameter space particular micro-instabilities are predicted to occur based on linear gyrokinetic simulations.

To understand the scaling in core confinement, linear gyrokinetic simulations have been run for many NSTX discharges [TT-7,TT-8]. Linear analysis of the NSTX high beta H-mode discharges (such as those in Fig. TT-1(a)) show that microtearing (MT) modes at ion gyroradius scale lengths ($k_\theta\rho_s$<1) are often unstable and are driven by the electron temperature gradient at sufficiently large electron beta (Fig. TT-1(b)). Microtearing also tends to be stronger at higher electron-ion collision frequency when found in the core, although there are additional dependencies with safety factor (q), magnetic shear (s) and density gradient [TT-9]. For lower beta H-mode discharges, microtearing modes are stable, and instead traditional electrostatic ITG and TEM instabilities are predicted.

For some of the high beta discharges a hybrid trapped electron mode/kinetic ballooning mode (TEM/KBM) instability [TT-8] is also predicted, but generally only for smaller electron collision frequencies. While KBM is hypothesized to be a possible mechanism for constraining the maximum H-mode pedestal pressure gradient, the locations investigated here are in the core confining region, not in the sharp gradient region of the pedestal, suggesting that KBM turbulence could be an additional mechanism controlling core confinement in NSTX at lower collisionality. A transition in dominant regimes from MT to KBM would presumably influence the overall energy confinement scaling and its dependence on collisionality (as shown in Fig. TT-1(a)) [TT-6]. The fact that the ion thermal transport and impurity carbon transport become more anomalous at lower collisionality [TT-6,TT-10] is consistent with the fact that microtearing modes (at high collisionality) transport only electron heat, while the hybrid-KBM ballooning modes (at low collisionality) are effective at transporting heat, particles and momentum [TT-8]. Understanding this dependence is of high priority for NSTX-Upgrade.

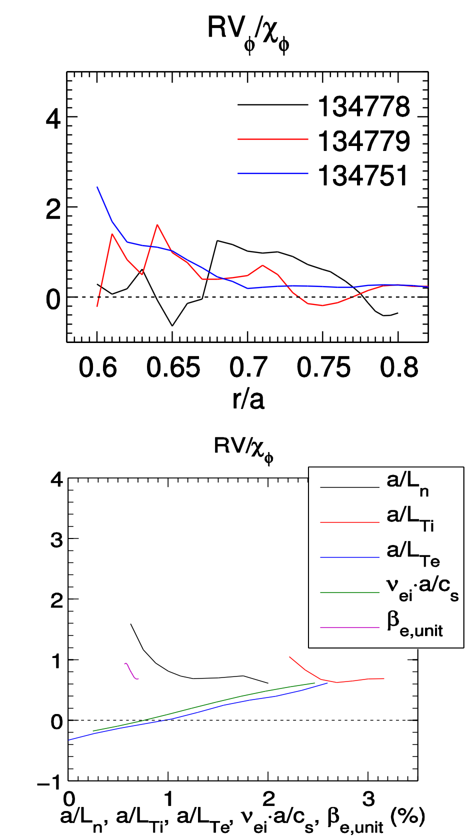

Fig. TT-2: Quasilinear KBM momentum pinch from linear GYRO simulations. (top) Radial profile for three NSTX H-mode discharges. (bottom) Predicted variation with density and temperature gradients, electron collisionality and beta.

Momentum transport

a. NSTX H-modes

Previous perturbative momentum transport experiments in NSTX H-modes have found that a momentum pinch exists, similar to conventional tokamaks, with values of the pinch parameter RV_φ/χ_φ=(-6) to (-1). [TT-11,12,13,14]. In conventional tokamaks this pinch is reasonably well described by the Coriolis pinch for ITG turbulence [TT-15]. In the NSTX H-mode discharges, microtearing modes dominate the unstable linear spectra, although there are sub-dominant ballooning modes that behave like hybrid-KBM instabilities. Quasi-linear fluxes from these high-beta KBM modes predict a weak outward momentum pinch (RV_φ/χ_φ)=0-1 over the experimental measurement region (Fig. TT-2, top) that are inconsistent with the experimental values. Additional parameter scans (Fig. TT-2, bottom) show this predicted KBM momentum convection is relatively insensitive to variations in density and temperature gradients, electron collisionality or beta. Unlike conventional tokamaks, local quasi-linear calculations are unable to describe the observed momentum pinch. In FY14, nonlinear simulations will be run to investigate the importance of nonlinear effects, perpendicular E×B shear, and possibly global effects on the predicted momentum pinch. In addition, in FY13 a collaboration with Bayreuth University in Germany (A. Peeters, W. Hornsby, R. Buchholz) was initiated to investigate the importance of centrifugal effects on momentum and impurity transport using the GKW code [TT-16], and this effort is ongoing.

b. NSTX L-modes

The appearance of electromagnetic microtearing and hybrid-KBM modes in high beta H-mode discharges complicates the theoretical analysis. To simplify experiment/theory comparison and to enable more direct comparison with conventional tokamaks at lower beta, similar analysis was performed for a low beta L-mode plasma unstable to electrostatic ion temperature gradient/trapped electron mode (ITG/TEM) instabilities. Perturbative momentum experiments are not available for NSTX L-mode plasmas. However, the local, quasilinear GYRO calculations do predict effective Prandt numbers ($Pr=\chi_\varphi/\chi_i$, ignoring possible convective contributions) that are in agreement with the experimental Prandtl numbers (Fig. TT-3, top). A local, nonlinear simulation at one radii [TT-17,TT-18] provides an additional prediction of an effective Pr number that also falls within the uncertainty estimate of the measurement. In this case one sees the nonlinearly predict Pr is ~60% of the quasi-linear value, indicating the importance of pursuing nonlinear predictions in the high beta H-mode cases discussed above.

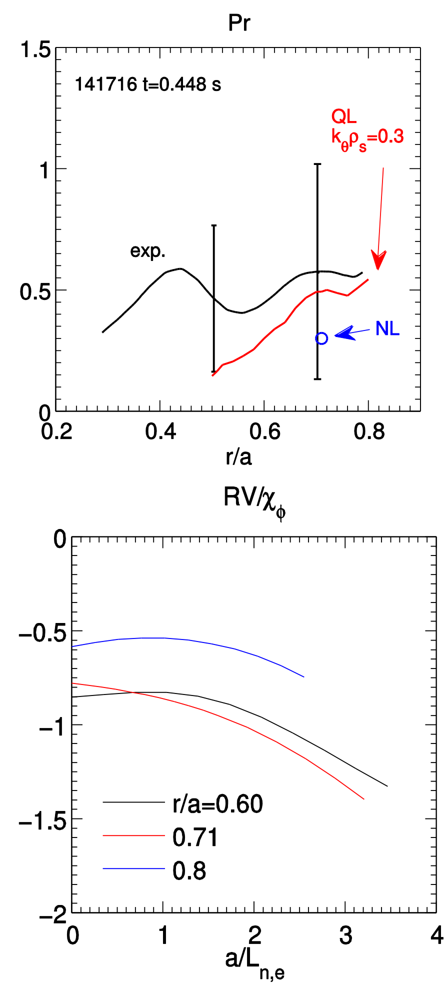

Fig. TT-3: (top) Effective Pr number from experiment (black), quasi-linear gyrokinetics (red) and nonlinear gyrokinetics (blue circle). (Bottom) Predicted quasilinear ITG/TEM pinch parameter dependence vs. density gradient at three radii.

The predicted quasi-linear momentum pinch from ITG/TEM modes for the L-mode plasma are directed inward as typically found in conventional tokamaks. However, they are still relatively small (~-1) and largely insensitive to variations in many parameters investigated, including density and temperature gradient, collisionality, beta, safety factor, and magnetic shear. In particular, the weak dependence on density gradient (Fig. TT-3, bottom) is inconsistent with the expression derived from ITG theory for conventional tokamaks, $RV_\varphi/\chi_\varphi=-4-R/L_n$, suggesting a difference due to the lower aspect ratio of spherical tokamaks.

c. Collaborative MAST experiments on momentum transport

Motivated by the difference in predicted ITG/TEM momentum pinch between conventional and spherical tokamaks, and the lack of experimental data in NSTX L-modes, a perturbative momentum transport experiment was proposed to run at MAST in FY13. In a manner following the NSTX H-mode experiments, edge magnetic field perturbations are used to modify the toroidal flow. Data was obtained in Aug. 2013 in both H-mode (using n=4 perturbations) and L-mode (n=3) at two plasma currents each (400 & 600 kA). Fig. TT-4 shows an example of measured rotation at different tangency radii from 400 kA L-mode discharges. (Note, each toroidal velocity is plotted with a different zero-offset). In particular, there is a noticeable kick of the toroidal flow with application of the external coil current (I_{RMP}) and subsequent recovery to the original state, as compared to a shot without the applied perturbation. Although there is uncertainty in the torque due to the applied magnetic field, the recovery of the rotation following removal of the perturbation (and unknown torque) will be used to infer diffusive and convective momentum transport components.

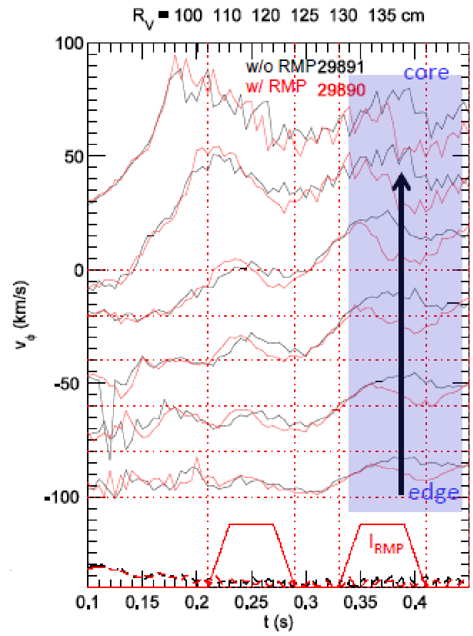

Fig. TT-4: Response of toroidal rotation velocity at different radii (plotted with different zero-offset) due to short n=3 magnetic perturbations (I_{RMP}), compared to a shot without magnetic perturbations.

To provide additional constraint on the inferred momentum transport, additional MAST discharges have been allocated (to run in Sept. 2013) that will use NBI pulses to modify the plasma rotation. In this case the uncertainty in applied torque is removed, as NBI torque can be calculated using the NUBEAM module in TRANSP.

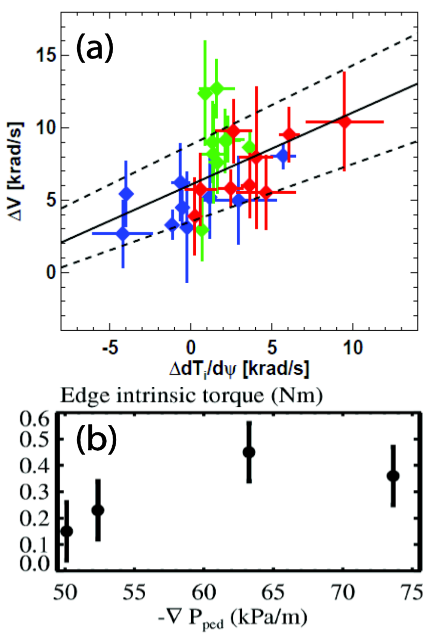

Fig. TT-5: (a) Change in intrinsic rotation vs. change in ion temperature gradient measured through Ohmic L-H transition. (b) Edge intrinsic torque as a function of pedestal pressure gradient in NSTX H-mode plasmas.

d. Intrinsic rotation

Intrinsic rotation generation was studied through the L-H transition in NSTX Ohmic plasmas, taking advantage of the zero momentum input and the long momentum transport time scale (~100 ms) compared to L-H transition time (~ 10 ms) [TT-19]. The inferred intrinsic torque was found to correlate best with ion temperature gradient (Fig. TT-5(a)), consistent with a theoretical prediction of residual stress driven by low-k turbulence [TT-20]. Intrinsic torque is also measured in NSTX NBI-heated H-mode plasmas by using NBI torque steps and is found to have some correlations with pedestal pressure gradient (Fig. TT-5(b)). This result is qualitatively similar to the dependence on pedestal pressure gradient in DIII-D.

e. NSTX-U DBS diagnostic implementation on MAST

UCLA (US) and CCFE (UK) are collaborating to implement Doppler Backscattering (DBS) on MAST during the M9 campaign in 2013. DBS measures plasma flow via the Doppler shift of microwaves backscattered from intermediate scale turbulence (k_θ > ~3 cm^{-1}). Dr. Jon Hillesheim of CCFE (a recent UCLA graduate) installed the UCLA systems in June 2013 and has been operating them since. The system (16 channels, 30 – 75 GHz, cutoffs @ 1 – 7 x 10^{13} cm^{-3} in O-mode) can be configured for DBS or reflectometry. Initial DBS data looks promising. Figure TT-6 show the spectrum of the backscattered microwave electric field for the 44.5 GHz channel which reaches cutoff in the core in an Ohmic discharge. The transition from a negative- to a positive-frequency-peaked spectrum at t ~ 300 ms indicates a change in core rotation speed of the order of ~ 10 km/s and a reversal of the core intrinsic rotation. This occurs with a ~20 % change in plasma density. This type of shift has previously been observed in TCV [TT-21] and Alcator C-mod [TT-22]. This is the first observation in low aspect ratio tokamaks. The shift is thought to be related to the collisionality dependence of turbulent momentum transport [e.g. TT-23].

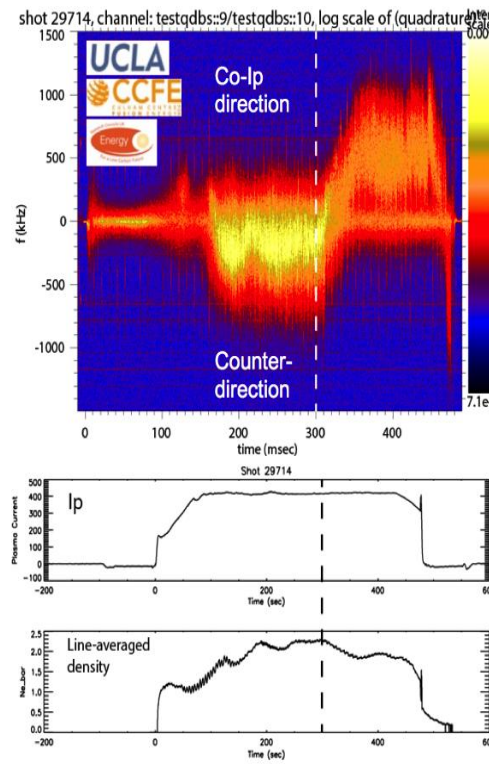

TT-6: MAST shot 29714; (top) spectrum of backscattered microwave electric field for the 44.5 GHz channel which reaches cutoff in the core in Ohmic discharge*; (middle) plasma current and (bottom) line average density for same discharge.*

Non-local transport

Nonlocal thermal transport has been observed on tokamaks and stellarators. For example, recent electron cyclotron heating (ECH) modulation experiments on LHD stellarator have shown that electron heat flux is not correlated with local equilibrium electron temperature gradient but with local turbulence power [TT-24]. Here, we present the first evidence of nonlocal thermal transport in NSTX. The observations were made around RF terminations in a set of NSTX RF-heated L-mode plasmas with toroidal field of 5.5 kG, plasma current of 300 kA. Local electron-scale turbulence was measured with a 280 GHz microwave scattering system (the high-k scattering system) with a fine radial localization of ±2 cm [TT-25], and the scattering system was configured to measure electron-scale turbulence for a $k_\perp\rho_s$ range of 2 to about 10 at about R≈133 to 137 cm (r/a≈0.57-0.63).

From Fig. TT-7(a), it can be seen that the peak injected RF power is about 1 MW and RF heating is terminated at t=479.6 ms (denoted by the vertical solid line). Fig. TT-7(b) plots maximum T_e measured by a Thomson scattering system, and it is clearly seen that the maximum T_e response to RF heating, e.g. $T_{e,max}$ drops after the RF power is terminated. Spectragrams of channel 2 and 3 of the scattering system are shown in Fig. TT-7(c) and (d), respectively. Scattering signals, i.e. the spectral peaks at f<0 shown in Fig. 1(c) and (d), can be distinguished easily from stray radiation, i.e. the central peak at f=0, from about t=300 ms to 550 ms, and we can see that there is a sudden drop in scattering signal power at almost the same time as the RF termination at t=479.6 ms. A closer examination shows that this sudden drop in the turbulence spectral power and the termination of RF heating are not exactly synchronized: the drop in the spectral power happens approximately 1-2 ms after the RF termination and the drop happens in about 0.5-1 ms. This sudden drop in electron-scale turbulence can be clearly seen in Fig. TT-8, where the wavenumber spectral power drops up to a factor of 7 from immediately before (t=479 ms) to after (t=484 ms) RF termination. After this is there is a much slower reduction, with minimal change in spectral power between t=484 and 492 ms.

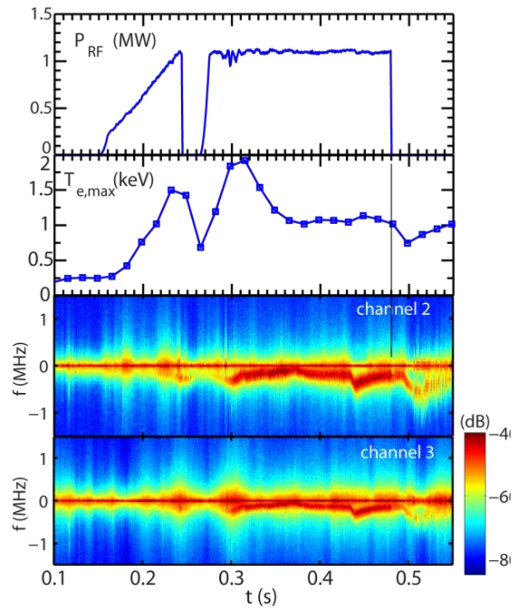

Fig. TT-7: The time traces of (a) injected RF power and (b) maximum T_e; Spectrograms of signals measured by channel 2 (c) and channel 3 (d) of the high-k scattering system. A black vertical solid line extends from (b) to (c) denotes the time at which the RF heating is terminated, i.e. t=479.6 ms.

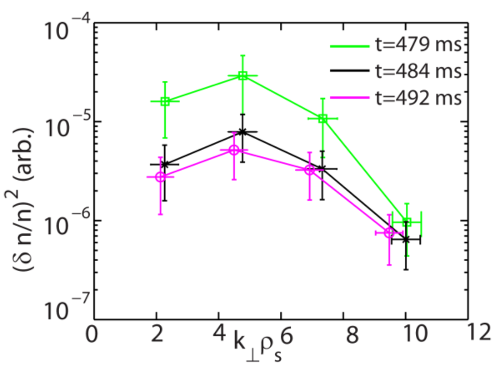

Fig. TT-8: The local k spectra at t=479 ms (before RF termination), 484 and 492 ms (after RF termination) measured by the scattering system (R≈133 to 137 cm, r/a≈0.57-0.63).

Such a sudden drop in turbulence spectral power is found to be independent of local equilibrium gradients, which change less than 15% across the RF termination (t=465-498 ms). Corresponding linear stability analyses show the profiles are not close to marginal stability, so *local* turbulence drive is not expected to change much. However, analysis using the transport code TRANSP coupled with TORIC shows that the electron thermal diffusivity decreases a factor of two across a wide portion of the radial profile immediately after RF termination. Such a drop in χ_e is clearly correlated with the sudden drop in electron-scale turbulence spectral power shown in Fig. TT-8 but not correlated with the variation in the local equilibrium gradients, demonstrating the nonlocal nature of the observed turbulence and electron thermal transport.

Collaborative MAST experiment on particle transport

Impurity transport in NSTX is often found to be described by neoclassical theory [TT-10, TT-26,27]. However, main ion particle transport has not been measured in NSTX. Following NSTX steady state analysis in JRT 2012, a perturbative particle transport experiment was proposed to run in MAST in FY13, using modulated gas puff fueling in conjunction with the high resolution, fast Thomson Scattering diagnostic. First discharges have been obtained (July, Aug. 2013) where density modulation was successfully demonstrated for B_T=5.8 kG and I_p=400 kA. Additional discharges are planned (scheduled for Sept. 2013) to obtain longer duration in higher I_p plasmas, required for achieving good density modulations at different operating conditions. Future analysis will focus on inferring the particle diffusivity and convection from the modulation experiments.

Global GTS simulations and L-mode shortfall

Understanding the possible transport shortfall in L-mode discharges, an issued raised by comparisons of gyrokinetic simulations with DIII-D data, is an important issue for validation. Nonlinear global gyrokinetic simulations using the updated GTS code have been applied to an NSTX L-mode discharge. The GTS simulations include kinetic electrons and cover a range of minor radii from r/a=0.4 to 0.8. Strong E×B flow shear is shown to wipe out most of low-k instabilities (ITG/TEM dominated) in a wide range of minor radii except in the region of largest ion temperature gradient (r/a~0.7) where the instability growth rate is also largely reduced by a factor of 3-5 (Fig. TT-9). The residual fluctuations in the region produce ion transport χ_i~1 m^2/s relevant to experimental level and smaller electron transport. The initial results do not indicate a transport shortfall in the outer core region for NSTX plasmas, consistent with local simulations over the same region [TT-18].

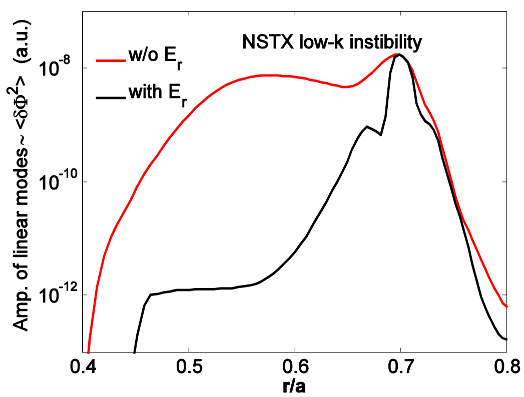

Fig. TT-9: Amplitude profile from global linear ITG/TEM simulations both with and without E×B shear.

Collaboration on DIII-D QH-mode transport analysis

Recent DIII-D experiments and analyses by C. Holland (UCSD) have found that the ion thermal and momentum transport in high density QH-mode plasmas is reproduced by neoclassical transport only [TT-28]. Analysis with the gyro-fluid TGLF turbulence transport model [TT-29] shows the profiles are largely stable to ITG/TEM modes, a situation common to NSTX H-modes. Linear gyrokinetic analysis was performed to determine what other instabilities could provide a possible explanation for the anomalous electron thermal transport. Over the radii investigated (r/a=0.5-0.8) the electromagnetic microtearing (MT) instability was unstable at very low wavenumbers, albeit with rather small growth rates. However, the calculated linear threshold for

MT is very close to the experimental values, suggesting it may provide the limit to the electron temperature gradient (Fig. TT-10). The electron temperature gradient (ETG) instability at small scales ($k_\theta \rho_s \sim 1$) could also be excited, but only with ~40% increase in electron temperature gradient. These conditions provide a very interesting companion to NSTX high beta H-modes that are found to be dominated by linearly unstable microtearing modes [TT-9]. Nonlinear simulations have been initiated, and will continue into FY14, to predict the characteristics of MT turbulence in DIII-D and compare with NSTX predictions [TT-30,31].

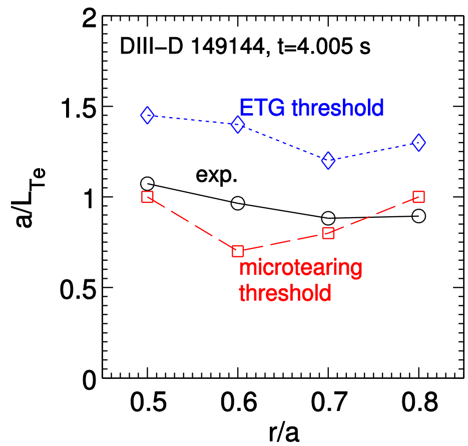

Fig. TT-10: *Normalized electron temperature gradient from DIII-D high density QH-mode, compared with linear thresholds for microtearing and ETG instability (calculated by GYRO).*

BES upgrades for NSTX-U (UW-Madison): detector system expansion and 2D reconfiguration for boundary measurements

NSTX-U collaborators from the University of Wisconsin-Madison (UW) are moving forward with two BES [TT-32] upgrade activities. First, BES detectors, data acquisition, and instrument control capabilities will expand from 32 to 48 detection channels. The additional channels will expand the utilization of BES sightlines for experiments and reduce the need to reconfigure delicate fibers. In FY13, the UW group fabricated 16 new detectors and assembled detector system at UW, delivered the first 8-channel detector system to PPPL, and procured the data acquisition system. In FY14, the UW group will deliver the second 8-channel system and integrate new components in the existing BES infrastructure at PPPL.

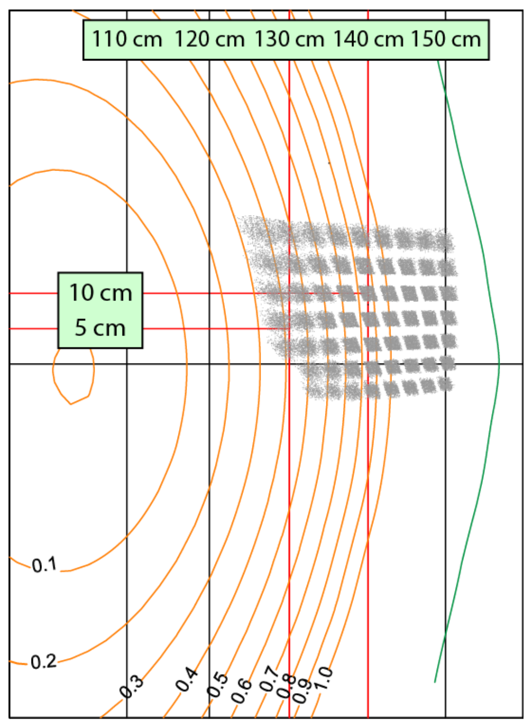

Figure TT-11: Proposed BES sightlines for 2D reconfiguration in pedestal and SOL regions.

The second BES upgrade activity is the 2D reconfiguration for boundary measurements. The UW group and PPPL engineers are reconfiguring the outer BES optical assembly ("R140") for 2D measurements in the NSTX-U boundary region, including pedestal and SOL. The 2D measurements will enable observations of turbulent eddy motion and flow fields for more sophisticated analysis of turbulent dynamics. In FY13, the UW group performed the optical system analysis for BES sightlines in the 2D configuration. In FY14, the UW group and PPPL engineers will fabricate the 2D optical assembly and reconfigure fibers for 2D measurements.

References

[TT-1] S. M. Kaye et al., Nucl. Fusion **47**, 499 (2007).
[TT-2] S.M. Kaye et al., Phys. Rev. Lett **98**, 175002 (2007).
[TT-3] M. Valovič et al., Nucl. Fusion **51**, 073045 (2011).
[TT-4] ITER Physics Basis, Nucl. Fusion **39**, 2178 (1999).
[TT-5] S.M. Kaye, et al., IAEA FEC EX/7-1 (2012).
[TT-6] S.M. Kaye, et al., Nucl. Fusion **53**, 063005 (2013).
[TT-7] W. Guttenfelder et al., IAEA FEC TH/6-1(2012).
[TT-8] W. Guttenfelder et al., Nucl. Fusion **53**, 093022 (2013).
[TT-9] W. Guttenfelder et al., Phys. Plasmas **19**, 022506 (2012).
[TT-10] F. Scotti et al., Nucl. Fusion **53**, 083001 (2013).
[TT-11] S.M. Kaye et al., Nucl. Fusion **49**, 045010 (2009).
[TT-12] W.M. Solomon et al., Phys. Rev. Lett. **101**, 065004 (2009).
[TT-13] T. Tala et al., IAEA FEC ITR/P1-19 (2012).
[TT-14] M. Yoshida et al., Nucl. Fusion **52**, 123005 (2012).
[TT-15] A.G. Peeters et al., Phys. Rev. Lett. **98**, 265003 (2007).
[TT-16] A.G. Peeters et al., Comp. Phys. Comm. **180**, 2650 (2009).
[TT-17] Y. Ren et al., IAEA FEC EX/P7-02 (2012).
[TT-18] Y. Ren et al., Nucl. Fusion **53**, 083007 (2013).
[TT-19] J.K. Park et al., Nucl. Fusion **53**, 063012 (2013).
[TT-20] Y. Kosuga et al., Phys. Plasmas **17**, 102313 (2010).
[TT-21] A. Bortolon et al. Phys. Rev. Lett. **97**, 235003 (2006).
[TT-22] J. Rice et al., Phys. Rev. Lett. **106**, 215001 (2011).
[TT-23] M. Barnes et al., Phys. Rev. Lett. **111**, 055005 (2013).
[TT-24] K.Ida, private communication (2013).
[TT-25] D. R. Smith et al., Rev. Sci. Instrum. **79**, 123501 (2008).
[TT-26] L. Delgado-Aparicio, Nucl. Fusion **47**, 085028 (2009).
[TT-27] L. Delgado-Aparicio, et al., Nucl. Fusion **51**, 083047 (2011).
[TT-28] C. Holland et al., US-TTF, Santa Rosa, CA (2013).
[TT-29] G. Staebler et al., Phys. Plasmas **12**, 102508 (2005).
[TT-30] W. Guttenfelder et al., Phys. Plasmas **19**, 056119 (2012).
[TT-31] W. Guttenfelder et al., Phys. Rev. Lett. **106**, 155004 (2011).
[TT-32] D. Smith et al., Rev. Sci. Instrum. **83**, 10D502 (2012).

Energetic Particle Research

Previous work in the Energetic Particle Research area has been considerably expanded during FY-2013 with respect to three main themes: (i) stability of high-frequency Global and Compressional Alfvén Eigenmodes (GAE/CAE), (ii) modeling of Toroidicity-Induced AEs and of other MHD instabilities such as Energetic Particle Modes and kink modes, and (iii) development of reduced models to interpret and predict AE-induced fast ion loss and redistribution. Results from NSTX have been complemented by experiments conducted in collaboration with the DIII-D and MAST devices.

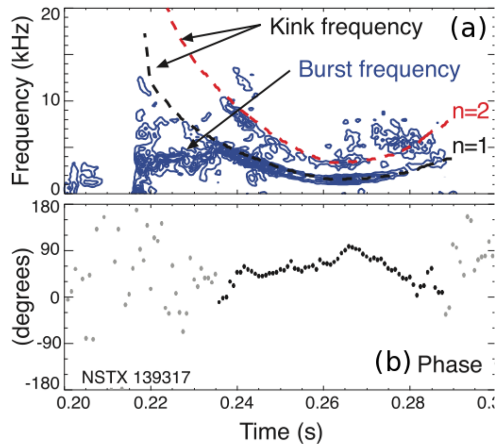

Figure EP-1: *Modification of GAE dynamic on NSTX resulting from coupling with kinks. (Adapted from Ref. [EP-1]). (a) Frequency of kink harmonics (dashed lines) and burst frequency of CAEs (contours). (b) Relative phase between kink and bursts of CAE, showing locking after 240 ms.*

Experimentally, it is found that CAE and GAE modes can exhibit a complex, non-linear behavior when either natural plasma modes (such as kinks) or externally-induced perturbations occur in the plasma. For example, the burst frequency of CAEs is observed to lock on the frequency of unstable kinks (Fig. EP-1), which can be explained by a predator-prey type of model [EP-1]. On the other hand, high frequency energetic particle modes have been observed to respond to static perturbations induced through the external RWM coils [EP-2]. In NSTX H-mode plasmas, robust chirping and bursting activity in the range of frequency 400-600 kHz, attributed to GAE, is strongly modified by when pulsed of n=3 static magnetic perturbation are applied (Fig. EP-2): the mode amplitude is reduced, the bursting frequency is increased, and frequency chirp range is smaller. Calculations of the perturbed fast-ion distribution function indicate that the 3D perturbation can modify the orbits of fast ions that resonate with the bursting modes, affecting directly the mode drive. Both these findings are highly relevant to develop AE control schemes through external perturbation, which is of clear interest for future burning plasmas in ITER and FNSF.

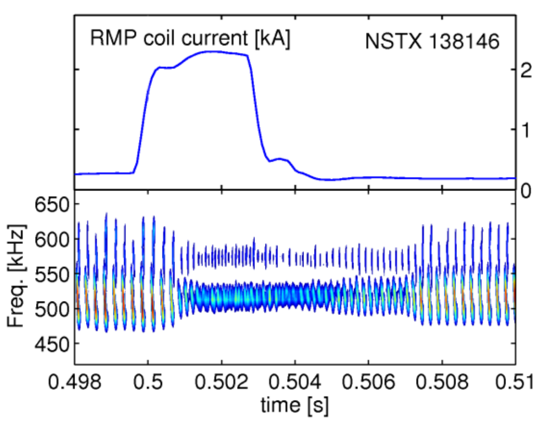

Figure EP-2: *Modification of GAE dynamic (bottom) on NSTX through pulses of Magnetic Perturbations with n=3 (top). (Adapted from Ref. [EP-2]).*

Besides their temporal dynamic, analysis technique for experimentally identifying CAEs and GAEs using local dispersion relations and mode structure measurements have undergone further development [EP-3].

Improved measurements through a reflectometer array [EP-3] and magnetic pick-up coils enabled an improved comparison with predictions from the hybrid-MHD non-linear code HYM [EP-4] in FY13. Excitation of GAE modes and co-rotating CAE modes has been studied for H-mode NSTX discharge #141398 using the HYM code (Fig. EP-3). Co-rotating CAE modes have been found unstable for low toroidal mode numbers (n=4) and for high-n (n=8,9). The co-propagating CAE modes with large toroidal mode numbers n≥8 and frequency range $f>0.4f_{ci}$ are consistent with experimental observations. It was discovered that unstable CAE modes can be strongly coupled with kinetic Alfvén waves (KAW) on the high-field-side. The resonance with KAW is located at the edge of the CAE potential well just inside beam ion density profile (Fig. EP-3). Radial width of KAW is comparable to beam ion Larmor radius. Quasilinear energy flux is directed away from the magnetic axis toward the resonance location, i.e. from the CAE to the KAW. This suggests that dissipation at the resonant location can have direct effect on the electron temperature profile. Two groups of resonant particles, corresponding to regular and anomalous Doppler-shifted cyclotron resonances are found for high-n co-rotating CAEs.

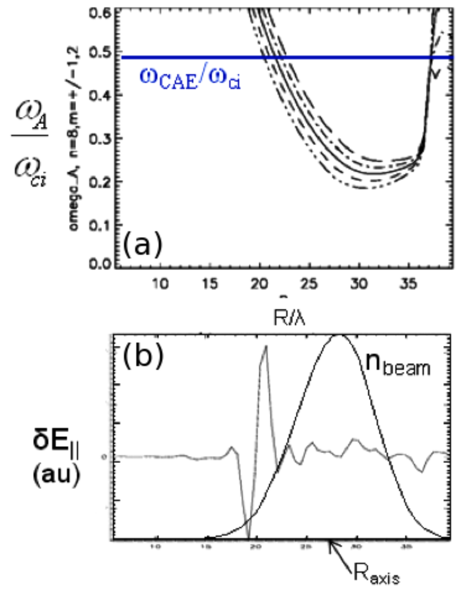

Figure EP-3: *(a) Profiles of Alfvén continuum and $\delta E_{||}$ vs major radius (normalized to ion skin depth) from HYM simulations of a n=8 co-rotating CAE coupled to KAW on NSTX. (b) Radial width of KAW is comparable to the beam ion Larmor radius.*

Numerical diagnostics have been developed in the HYM code to study location of resonant particles in phase-space, which is used to selectively drive CAE mode and suppress the GAE mode, in cases when the GAE is the most unstable mode. This procedure enables the computation of mode structure and frequency of both GAE and CAE modes with same toroidal mode number, which will eventually improve the comparison with experiments.

At frequencies comparable to the plasma rotation frequency, f<30 kHz, the dependence of non-resonant kinks as a function of plasma rotation has been investigated [EP-5]. Although modifications from the zero-rotation case are small for the initial, linear mode growth, rotation can significantly influence the nonlinear dynamics of the (1, 1) mode and the induced (2,1) magnetic island. Simulation results show that a rotating helical equilibrium is formed and maintained in the nonlinear phase at finite plasma rotation. Furthermore, the effects of rotation are found to greatly suppress the (2, 1) magnetic island even at a low level.

Results from NSTX plasmas are forming the basis for projections of AEs and associated fast ion loss/redistribution to NSTX-U scenarios. The linear MHD code NOVA-K has been utilized to assess the effects of different NB injection geometries on TAE stability on NSTX-U, including the effects of the new (more tangential) NB sources [EP-6]. The analysis indicates that TAEs are potentially unstable on NSTX-U, especially when the more tangential NB sources (which results in a strongly peaked fast ion profile) are utilized.

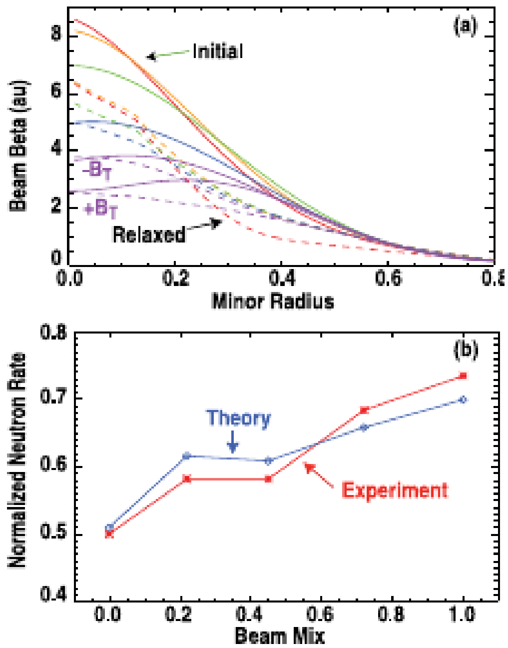

Figure EP-4: *(a) Initial NB ion beta profiles from TRANSP and final (or relaxed) profiles from the 1.5D-QL model. (b) Comparison between experimental and reconstructed neutron rate.*

In parallel with the improvement of existing first-principle numerical codes such as HYM and M3D-K, so-called "reduced" models are also being developed for NSTX and NSTX-U. A *1.5D quasi-linear model* (or *critical gradient model*, CGM) [EP-7] based on computing the critical fast ion profile gradient in the presence of unstable AEs [EP-8] has been developed. After the initial, successful tests on DIII-D and further benchmarking against existing NSTX data, the model will be applied to NSTX-U scenarios. Originally the idea was to use analytic growth and damping rates for TAEs [EP-8]. This allows the computation of the critical fast ion beta gradient profile under the assumption that the quasi-linear diffusion from overlapping resonances is applicable to the case(s) of interest. The applicability of the 1.5D-QL model requires a large number of such modes with no or minor bursting/chirping at saturation. Similar conditions can be envisioned in ITER-like burning plasmas in a variety of plasma scenarios. In practice, the fast ion profile is first computed via TRANSP. If the profile gradient predicted by TRANSP is larger than the computed critical value, the profile is relaxed through the 1.5D-QL model to the critical value, thus providing a prediction of the final gradient profile. The resulting beta gradient is used for subsequent computations of the fast ion beta profile given either the zero boundary condition or maintaining the number of particles constant for the relaxed pressure profile. Comparing the relaxed beta profile with the initial one enables to evaluate EP losses as well as other quantities. The CGM was further validated against experimental data from DIII-D (Fig. EP-4) and surprisingly good agreement was reported [EP-9]. This benchmarking activity lends further support to the CGM and motivates its application on NSTX and projected NSTX-U data.

Another complementary reduced model is being developed to contribute, along with the *1.5D-QL model*, to the NSTX-U milestone FY14-2 on "Development of reduced models for AE-induced fast ion transport". The model is based on a *transport probability function*, which can be derived by either numerical codes (e.g. ORBIT, SPIRAL, HYM) or theory, to evolve fast ion parameters in phase space. Its implementation in NUBEAM/TRANSP and its verification and validation are foreseen for FY14.

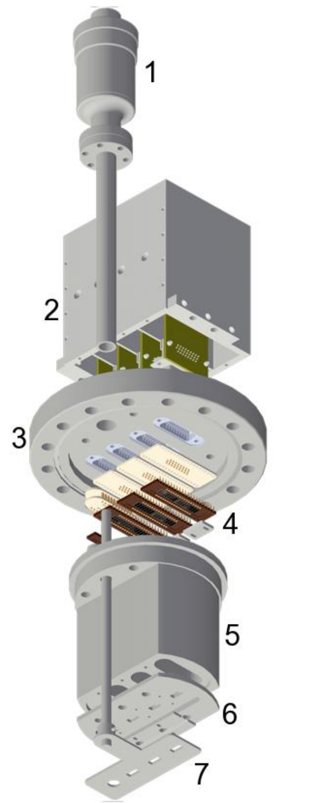

Figure EP-5: *Rendering of the upgraded ssNPA, showing (1) shutter motor, (2) pre-amplifier box, (3) vacuum flange, (4) sensors, (5) collimator unit, (6) entrance slits and (7) shutter blade.*

Preparation for NSTX-U operations is proceeding. The design and construction of an upgraded solid-state Neutral Particle Analyzer (ssNPA) diagnostic is underway (Fig. EP-5). The target design consists of three subsystems at different toroidal locations. Two arrays have 10 radial viewing lines and the other one has 10 tangential viewing lines to complement the existing fast ion diagnostics. The upgraded ssNPA will distinguish the response of passing and trapped fast ions. Signal bandwidth is up to 100kHz, with spatial resolution of ~6cm and four energy bands. The ssNPA system will be used to study fast ion redistribution and loss induced by Alfvén eigenmodes and other MHD instabilities, and acceleration of fast ions by HHFW heating.

A prototype 4-channel charged fusion product detection system for NSTX-U [EP-10] has been tested on MAST. The 3 MeV protons and 1 MeV tritons produced by DD fusion reactions in MAST have been clearly observed. This system is intended to measure the radial profile of the fusion reaction rate. Comparison of profiles from this instrument will be made with those from the MAST neutron camera, which measures the neutron source rate profile. Given the successful observations on MAST, a proposal for a 16-channel system for NSTX-U is envisioned. This instrument has been developed under collaboration with the Florida International University Physics Department. A collaboration with MAST on FIDA diagnostics was also successfully completed [EP-11]. Progress was also made on developing tools to infer the distribution function from FIDA measurements [EP-12].

NSTX-U collaborators from UCLA and MAST have implemented Doppler Backscattering (DBS) on MAST during the M9 campaign in 2013. The system will be installed on NSTX-U after the completion of the MAST experimental campaign in FY13. DBS measures plasma flow, yielding the fluctuating E_r component. The UCLA system has been installed on MAST on June 2013 and has been operating them since. The system (16 channels, 30 – 75 GHz, cutoffs @ 1 – 7 x 10^{13} cm^{-3} in O-mode) can be configured for DBS or reflectometry. Initial DBS data looks promising. TAEs have been observed via DBS reflectometry. Figure EP-6 shows an example. The top panel shows the spectrum of the backscattered microwave electric field for the 42.5 GHz channel in MAST shot 29387. The spectrum shows a substantial Doppler shift to positive frequencies during t = 200 - 300 ms due to rotation of the plasma. The bottom panel shows a spectrum of the time derivative of the phase of the backscattered electric field. Strong fluctuations in the frequency range 100 – 150 kHz are caused by modulation of the Doppler shift of the backscattered microwaves by TAEs, possibly due to a fluctuating ExB flow associated with the TAE electric field perturbation.

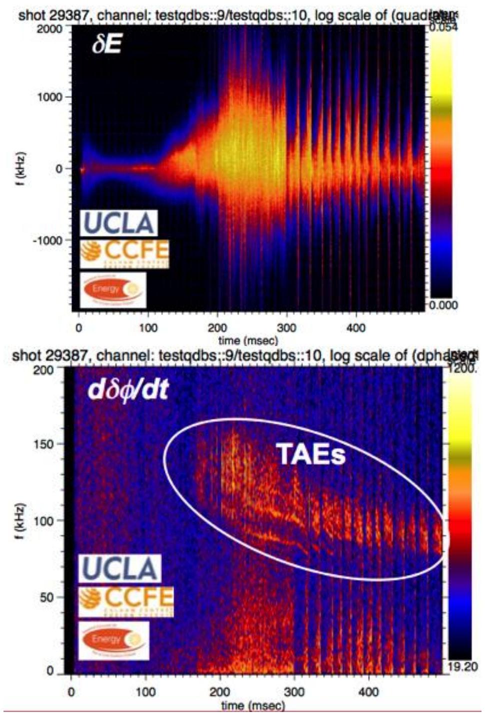

Figure EP-6: *(top) spectrum of backscattered microwave electric field for the 42.5 GHz channel in MAST shot 29387; (bottom) time derivative of the phase of the backscattered electric field.*

Besides diagnostic development, a collaboration with MAST during FY13 has targeted the study of fast ion redistribution caused by TAE avalanches to extend previous studies on NSTX [EP-13][EP-14]. The standard MAST shot appears to have combined TAE/EPM bursts, which may be avalanches. However, a condition was identified where EPMs were relatively weak, leaving just the TAE bursts. A shot was taken in this condition with slightly higher beam power and TAE avalanche-like events were observed. The neutron drops were not clearly visible on the neutron detectors, but D-alpha emission was found to be a sensitive detector of fast ion losses.

Characterization of chirping/bursting AEs in NSTX plasmas was complemented by experiments conducted in collaboration with DIII-D. Bursting modes where reproduced on DIII-D and data analysis is presently ongoing. The goal is to compile a database encompassing a broad range of experimental conditions from both conventional (DIII-D) and low aspect ratio (NSTX, MAST) devices to unfold the underlying physics of bursting AEs and induced fast ion transport. Another set of experiments was performed on DIII-D to explore the use of external fields to affect the dynamics of TAE modes. Good progress was made in identifying a suitable target scenario, thus enabling possible further studies in the coming year.

References

[EP-1] E. D. Fredrickson et al, Phys. Plasmas **20**, 042112 (2013)
[EP-2] A. Bortolon et al, Phys. Rev. Lett. **110**, 265008 (2013)
[EP-3] N. A. Crocker et al, Nucl. Fusion **53**, 043017 (2013)
[EP-4] E. V. Belova et al, Proceedings of the 24th IAEA-FEC Meeting, paper TH/P6-16 (San Diego, CA 2012)
[EP-5] F. Wang et al, Phys. Plasmas **20**, 072506 (2013)
[EP-6] M. Podestà et al, Phys. Plasmas **20**, 082502 (2013)
[EP-7] K. Ghantous et al, Phys. Plasmas **19**, 092511 (2012)
[EP-8] N. N. Gorelenkov et al, Nucl. Fusion **45**, 226 (2005)
[EP-9] W.W. Heidbrink et al., Nucl. Fusion **53**, 093006 (2013)
[EP-10] W. U. Boeglin et al, Rev. Sci. Instrum. **81**, 10D301 (2010)
[EP-11] C.A. Michael et al., Plasma Phys. Cont. Fusion **55**, 095007 (2013)
[EP-12] M. Salewski et al., Nucl. Fusion **53**, 063019 (2013)
[EP-13] E. D. Fredrickson et al, Nucl. Fusion **53**, 013006 (2013)
[EP-14] D. S. Darrow et al, Nucl. Fusion **53**, 013009 (2013)

Wave Heating and Current Drive

Ion-cyclotron range of frequency (ICRF) heating and current drive is an important tool for burning-plasma science. In particular, the potential current-drive capability of a high-harmonic fast-wave (HHFW) system can, in principle, non-inductively ramp-up the plasma current through bulk plasma heating and bootstrap-current enhancement in an FNSF ST device, which will not have a central solenoid for current drive. This is especially important at low plasma currents where neutral beam current drive is ineffective due to poor fast-ion confinement. HHFW power is also a good candidate for on-axis non-inductive current generation in future fusion reactors. Furthermore, the general study of ICRF heating is important for burning plasma, as second-harmonic and minority heating schemes can directly heat ions to improve fusion yields. Indeed, twenty megawatts of ICRF heating are currently planned for ITER.

HHFW SOL/Divertor Interactions in NSTX

HHFW heating and current-drive efficiencies on NSTX can be significantly lowered by interactions of the HHFW with the scrape-off layer (SOL) plasma [RF-1-5], with HHFW power being deposited on both the lower and upper divertor regions in bright and hot spiral patterns, as shown in Fig. RF-1. It is hypothesized that surface waves are being excited just beyond onset density for perpendicular fast-wave propagation [RF-1, 2], but the exact mechanism(s) by which the HHFW power is converted into a heat flux on the divertor regions is not yet identified and is a major subject of investigation. Fully understanding the underlying mechanisms behind this loss mechanism is critical for optimizing HHFW performance and fast wave performance in general, especially for high-power long-pulse ICRF heating in ITER.

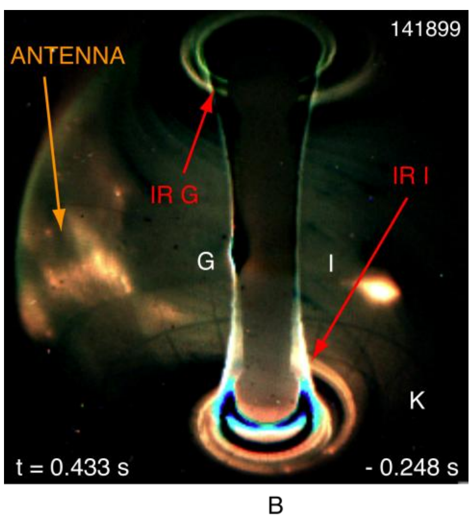

FIGURE RF-1: *Camera view of "hot" RF produced spiral for shot 141899 with an edge magnetic pitch of ~ 40°. Conditions are D_2, B_T = 4.5 kG, I_P = 1 MA, P_{RF} = 1.4 MW, Antenna k_ϕ = -8 m^{-1}, P_{NB} = 2 MW, H-mode with $n_e(0) \sim 5 \times 10^{19}$ m^{-3}, antenna-LCFS gap ~ 6.7 cm. Locations for antenna, ports B, G, I, K, and IR camera views are noted.*

As shown last year, the location and shape of the spirals in the divertor regions is consistent with HHFW power flows through the SOL to the divertor regions along magnetic field lines that pass in front of the antenna [RF-6,7]. This year, additional analysis of infrared (IR) camera data from the divertor regions shows that the different peaks of deposited heat correspond to the different passes of the spiral. This is especially apparent in a magnetic-pitch (q_{95}) scan, as shown in Fig. RF-2, since the radial location of the heat peaks agrees with the results of field-line mapping [RF-8,9]. Since the HHFW power is transported from the antenna region to the divertor region along field lines, the IR data at the divertor can be mapped back to the midplane, giving a radial profile of lost HHFW power flux lost along field lines. As Fig. RF-3 shows, the loss amplitude is large close to the antenna but also close to the separatrix and is small in between. This loss profile is suspected to result from fast-wave-propagation properties across the SOL, but modeling will be needed to determine this definitely.

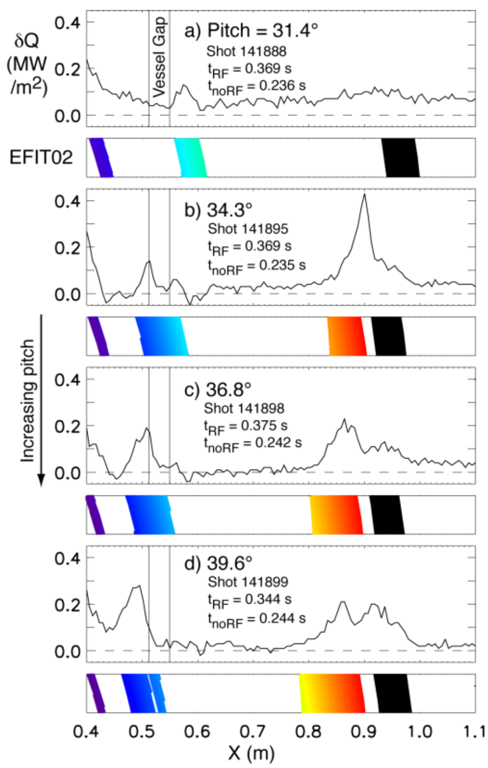

FIGURE RF-2. *(a-d) IR data from Bay I plotted against X, the distance along the sight line, and SPIRAL strike points from the midplane (colored) and from the edge of the bottom antenna plate (black) for shots in a pitch scan. EFIT02 equilibrium fits are taken at 355 ms. IR data taken at times indicated; δQ obtained by subtracting a heat profile from a pre-RF time.*

Figure RF-2 also shows strike points (shown in black) of field lines connecting to the bottom plate of the antenna. These strike-point locations agree with an outer heat-flux peak, implying part of the losses occurs along field lines connecting the lower divertor to the bottom of the antenna box [RF-10].

These experimental observations must be reproduced by any RF model that attempts to include the SOL and associated damping mechanisms. In particular, the AORSA code has been extended to include the SOL [RF-11], where significant electric field amplitudes are observed [RF-12]. However, without including the proper edge damping mechanism in the code, the SOL has no effective sinks for the HHFW power, and the field amplitude must build up to the point where the Poynting flux into the core balance the antenna power. The proper loss mechanism(s) must be identified and included before AORSA can successfully predict the amount of fast-wave power lost to the SOL relative to the power delivered to the core.

Finally, an estimate of the total power dissipated within the spirals was made by using the red light emission of a visible camera as a proxy for the heat flux [RF-10]. This proxy is needed because the IR data is obtained only at a single toroidal location and does not capture the strong variation of the heat flux along the spiral. The estimate shows that approximately half of the HHFW heating power missing from the core is accounted for in the spiral. This means that, within the accuracy of this crude estimate, there may be other loss mechanisms at play. The roughness of this estimate highlights the need for improved IR camera coverage in NSTX-U.

Cylindrical Cold-Plasma Model

The main hypothesis for explaining the HHFW field-aligned losses is fast-wave propagation in the SOL. This hypothesis is motivated by the strong correlation of heating efficiency with the location of the onset density for perpendicular fast-wave propagation. Below this density, the perpendicular wavenumber is imaginary, and the wave fields may evanesce substantially before reaching the core plasma, resulting in poor antenna loading. However, on NSTX, moving this cutoff density too close to the antenna significantly lowered heating efficiencies, perhaps by promoting significant wave propagation in the SOL. Wave propagation in the SOL might explain why the losses occur across the width of the SOL, and the radial profile of lost HHFW power

(Fig. 3(d)) could be indicative of a radial standing-wave pattern in a cavity due to partial reflections of the waves off the steep pedestal gradient.

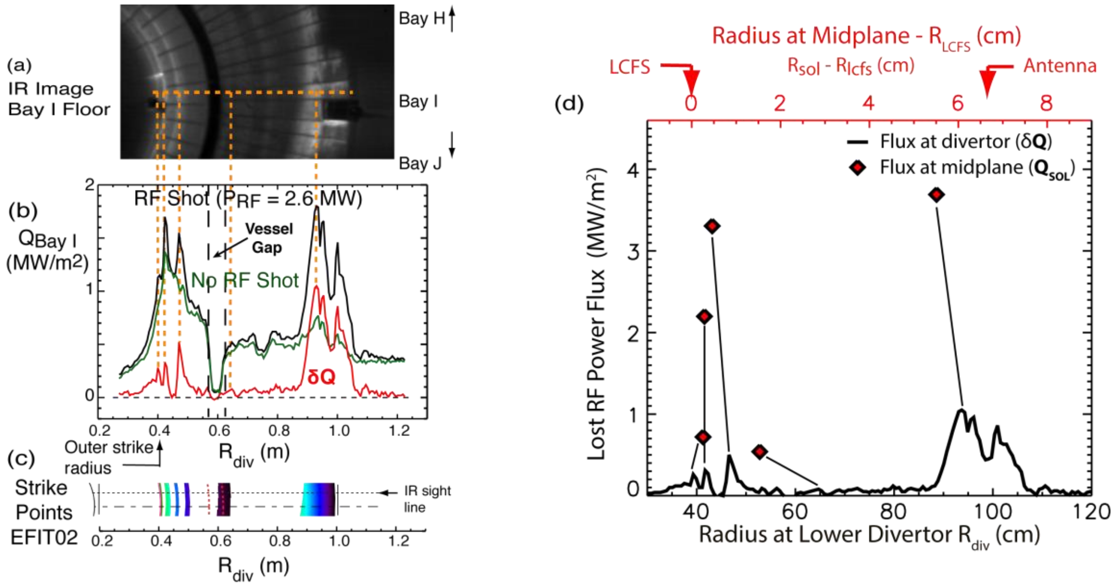

FIGURE RF-3. *IR camera data show that RF heat peaks agree with field-line strike points for an ELMy H-mode plasma (shot 135333, no RF shot 135334). (a) Heat-flux image in which multiple passes of the spiral are identifiable. (b) A radial profile of heat flux plotted against divertor radius (R_{div}). (c) Computed strike points at Bay I [ϕ_{ANT} = -90°, P_{NB} = 2 MW, I_P = 0.8 MA, B_{tor} = 0.45 T]. (d) Calculated values of the power lost at the SOL midplane, Q_{sol}, are shown for the peaks of the measured IR profile for the ELMy H-mode plasma (shot 135333). The power lost in the SOL midplane peaks inboard of the antenna and again outboard of the LCFS. (R_{lcfs} = 1.508 m).*

In order to test this hypothesis, a cylindrical cold-plasma model is being developed. It will include a relatively high-density core plasma surrounded by a relatively low-density annulus to model the SOL. This model will determine the conditions, if any, for significant fast-wave power to propagate in the SOL and what role the onset density plays. As of this past year, the m=0 solution was derived and implemented in a code. Future work will extend the solution to all m and include finite antenna geometry. This will not only determine how much power propagates in the SOL but will also show how closely this power stays aligned with the magnetic field as it propagates away from the antenna. This work will complement modeling efforts using the AORSA RF code because the simplified geometry and physics model will allow rapid exploration of the parameter space.

Non-Maxwellian Ion Plasma Dielectric Contributions in the HHFW version of TORIC

As demonstrated by FIDA measurements in the NSTX and DIII-D experiments, interactions between the HHFW's and fast ions from co-resonant neutral beam injection (NBI) can be strong enough to modify the fast ion distribution functions, thereby affecting the evolution of the plasma discharge. Therefore it is crucial to include non-Maxwellian effects in the ion contribution for the evaluation of the dielectric tensor in the full wave code TORIC-HHFW, which is utilized within the TRANSP code for time-dependent analysis of various NSTX discharges. Such work started in 2011, during which a modified plasma dielectric tensor module for a numerically specified Maxwellian distribution function was developed that accurately reproduced the response obtained previously for an analytic Maxwellian distribution [RF-13: N. Bertelli et. al., 2011]. In 2012 this module was implemented in TORIC-HHFW and initial tests indicated that it was working well. However, several tests in early FY2013 found some discrepancies that were eventually traced to the interpolation routines needed to generate the local susceptibility for the TORIC field calculations. Since the susceptibility is evaluated numerous times in the construction of the matrix representation of the wave equation, numerical efficiency is achieved by pre-computing the dielectric tensor on a four dimensional uniform grid in poloidal angle, the radial flux coordinate, parallel phase velocity, $v_{//}$ (for the required velocity space integrations), and $k_\perp^2$. Without the efficient interpolation algorithm, run times would be unacceptably long since each tensor element is a sum (over dozens of cyclotron harmonics) of singular two-dimensional velocity space integrals. Previously, the interpolation routine used a uniform grid in $k_\perp$. However in small parts of the solution domain $k_\perp^2$ can become negative, which led to errors in the evaluation of the dielectric tensor in those regions. By splitting the interpolation grid into one for positive $k_\perp^2$ and one for negative $k_\perp^2$, and by fixing a normalization error in B/B_{min} along a flux surface, exact agreement is now found between a numerically specified Maxwellian and the equivalent analytic Maxwellian ion distribution. Further tests of the extended code with a slowing down analytical distribution are underway and work is proceeding on a new module to import the NUBEAM distribution functions into this extended TORIC-HHFW code.

Continuing Studies of the Short Wavelength Slow Mode Identified in High Resolution Simulations of the HHFW and ICRF Wave fields in NSTX and C-Mod

Previous AORSA and TORIC-HHFW simulations of HHFW wave heating and current drive in NSTX and C-Mod have found that mode conversion to a slow wave structure is present if enough expansion elements are retained to resolve small-scale spatial structures. Theoretical analysis indicates that the origin of the propagating slow mode can be attributed to warm electron effects, $w < k_{//}v_{te}$, which allow the propagation of the additional wave. Studies undertaken, in close collaboration with ORNL and the PSFC-MIT, verified that the dependence of this mode on finite electron temperature and $k_{//}$ upshift, due in particular to the poloidal magnetic field, and the appearance of localized electron damping, as well as kinetic flux, associated with the new mode, is consistent with the theoretical model. However, convergence problems were found when more expansion modes were added to the solution domain and, in addition, the model predicts a smaller wavelength for the mode than was found in the simulations. Over the past year, we have found evidence that such a slow wave structure persists in NSTX-U simulations with both AORSA and TORIC-HHFW, though agreement with the predicted mode wavelengths has improved in some regimes. Furthermore, the convergence problems in the TORIC simulations are ameliorated if energetic ions are not included in the plasma parameters. As discussed elsewhere in the section entitled “NSTX-U HHFW Simulations”, differences between the predicted ion and electron power partitioning from the AORSA, TORIC-HHFW and GENRAY codes were found when the assumed ion temperatures were large. The code convergence issues may be related to this problem. Studies are now underway to resolve this discrepancy between the codes.

In order to gain some understanding of cause of these convergence problems, simulations of slow modes at lower frequencies ($\omega<<\Omega_{c,i}$) [Stix 1992], where the mode conversion process is better defined, have been examined. It is in this frequency regime that CAE's and TAE's have been observed experimentally. In the low frequency

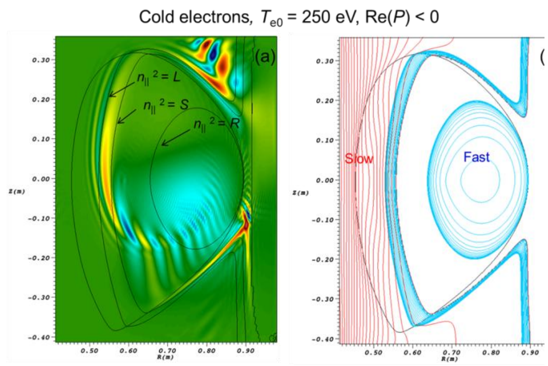

Figure RF-4: *The Alfven resonance in 2D for C-Mod parameters with cold electrons. (a) The slow wave is a surface wave propagating to the left of the Alfven resonance in the mid-plane. (b) The corresponding dispersion solution shows propagation regions for the slow wave in red and the fast wave in blue.*

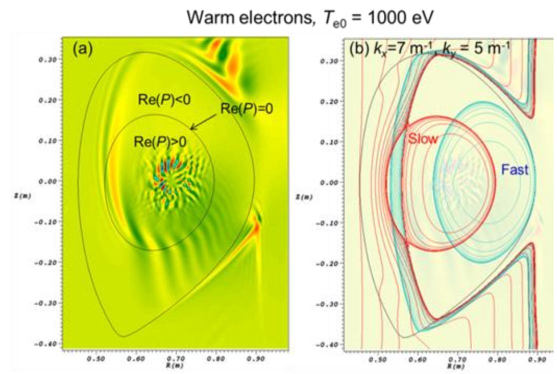

Figure RF-5: *(a) For warm electrons, Re (P) changes sign, and a new wave appears where Re (P) > 0. (b) The corresponding dispersion solution for k_x=7 m^{-1}, k_y = 5 m^{-1} shows a region where both fast (blue) and slow (red) modes propagate simultaneously.*

regime, slow waves can be generated by mode conversion at the Alfven resonance ($n_{\|}^2 = S$). In Fig. RF-4, this process is simulated with AORSA in two dimensions (2D) for Alcator C-Mod parameters: f = 30 MHz, B_0 = 5.29 T, R_0=0.688 m, n_φ = 12, cold ions, and a resolution of 200 × 200. For cold electrons (T_{e0} = 250 eV), the real part of the parallel conductivity Re (P) is negative everywhere, and the slow wave propagates to the left of the Alfven resonance in the mid-plane. Above and below the mid-plane, the poloidal magnetic field is in the direction of wave propagation, so there should not be an exact correspondence with the 1D dispersion relation results. The dispersion solution in Fig. RF-4(b) shows propagating regions for the fast (blue) and slow (red) branches ($k_\infty^2 > 0$). For cold plasma, this dispersion solution is independent of the perpendicular wave number. The slow wave propagates on the high field (left) edge, and does not extend into the core plasma. The only overlap between the fast and slow roots occurs near the Alfven resonance.

For warm electrons in 2D, the situation changes dramatically (see Fig. RF-5). Now there is a region near the magnetic axis where the parallel conductivity changes sign, and a new wave appears where Re (P) > 0. For warm electrons, the dispersion solution depends on the perpendicular mode number through the finite temperature parallel conductivity $P(k_{\|})$, so in Fig. RF-5(b) a mode spectrum (k_x=7 m^{-1}, k_y = 5 m^{-1}) is used. This results in a region of overlap near the magnetic axis where both fast and slow waves propagate simultaneously, and it is in this overlapping region where the new wave appears. The AORSA calculations do not converge in the sense that adding more modes to the spectrum only makes the amplitude of the new wave larger. The appearance of the new wave in Fig. RF-5 appears to require two simultaneous conditions: (1) the presence of a slow wave branch that excites high mode numbers in the solution ($\omega^2/k_{\|}^2 < kT_e/m_e$), and (2) the downshift of $k_{\|}$ for these high mode numbers to very small values. This downshift is easily provided by the poloidal magnetic field. When $k_{\|}$ for a particular mode is downshifted to near zero, that mode becomes un-damped and can grow to very large amplitude. It is possible that the very small values of $k_{||}$ along these lines cause the wave structure observed near the magnetic axis in Fig. RF-5, and this possibility is the focus of some ongoing studies. However, it remains to be seen if this downshift in $k_{//}$ causes the convergence issues observed with both the AORSA and TORIC codes in the higher frequency regimes in C-Mod and NSTX. Studies are now underway to assess the validity of the underlying up/down shift model used in both AORSA and, for noncircular flux surfaces, in TORIC.

NSTX-U HHFW Simulations

NSTX-U, which is presently scheduled to be completed in 2014, will operate with toroidal magnetic fields (B_T) up to 1 T, nearly twice the value used in the experiments on NSTX, and the available NBI power will be doubled. The doubling of B_T while retaining the 30 MHz RF source frequency moves the heating regime from the high harmonic fast wave (HHFW) regime used in NSTX to the mid harmonic fast wave (MHFW) regime. In particular, for deuterium majority ion and $B_T(R_0)$ = 0.55 T (as in NSTX) the harmonic resonances inside of the last closed flux surface range from the 2nd/3rd to the 11th whereas, for $B_T(R0)$ = 1 T, the harmonic resonances inside of the last closed flux surface range from the 2nd to the 5th. To understand possible difference between HHFW heating in NSTX and the corresponding HHFW/MHFW heating in NSTX-U, a series of simulations using the AORSA code has begun [RF-14: C.K. Phillips et al., 2012; RF-12: N. Bertelli et al., 2013].

An H-mode scenario being considered for NSTX-U obtained by using the free-boundary TRANSP code [RF-15: Gerhardt et. al., 2012] was considered, with a magnetic field of $B_T(R0)$=1 T, and the plasma current of I_p =1.1MA. Temperature and density profiles of electrons and main ion species (deuterium) are shown in Figure RF-6(a) and RF-6(b), respectively. The central electron and ion temperatures are given by $Te(0)$ = 1.22 keV and $Ti(0)$ = 2.86 keV, respectively. The central electron density is $n_e(0) = 1.1\times10^{20}$ m$-^3$, and the NBI power is P_{NBI} = 6.3 MW. In this analysis the same temperature profile was assumed for the thermal ion species (including impurities), while for the beam ions temperature (T_{bi}) an effective temperature, given by T_{bi} =(2/3)En_{fast}, was adopted, where E and n_{fast} are the total energy density profile and the density of the beams ions, respectively. The TRANSP simulation provides both of these quantities. The beam ion concentration (100 × n_{fast}/n_e) is about 2% in this specific case. In Figure 3(c), the electron density profile used in these numerical simulations is shown as a function of the major radius (R) in the edge of the plasma.

Figure RF-7 shows the absorption (in percentage) of electrons, thermal deuterium (D), and beam ions (D_{beam}) as a function of the toroidal component of the wave vector, $k_\phi = n_\phi /R$ (where n_ϕ and R are the toroidal mode number and the major radius, respectively) obtained from AORSA. Three different cases have been examined that correspond to three different antenna phases: $|k_\phi|$ = 3, 8, and 13 m^{-1} [RF-1: Hosea et al. 2008; RF-4: Taylor et al., 2010]. Figure RF-7(a) shows the electron and ion absorption predicted by using the electron and ion temperature profiles shown in Figure RF-6(b) (i.e., $T_i(0)$ = 2.86 keV and $T_e(0)$ = 1.22 keV), while in Figure RF-7(b) the ion temperature is lowered by 50% and the electron temperature is unchanged (i.e., $T_i(0)$ = 1.43 keV and $T_e(0)$ = 1.22 keV). In Figure RF-5(c), the ion temperature is again decreased by 50% but the electron temperature is doubled (i.e., $T_i(0)$ = 1.43 keV and $T_e(0)$ = 2.44 keV). In Figure RF-7(a), when $|k_\phi|$ increases, the electron absorption increases while the ion absorption decreases, in agreement with previous works on HHFW (see, for instance, [RF-16: C. N. Lashmore-Davies et al., 2008; RF-17: J. Menard et al., 1999]. More specifically, relatively stronger absorption by thermal deuterium and beam ions is found predominantly at lower $|k_\phi|$. One possible explanation of such strong ion absorption is that the lower electron beta due to the higher magnetic field in NSTX-U might

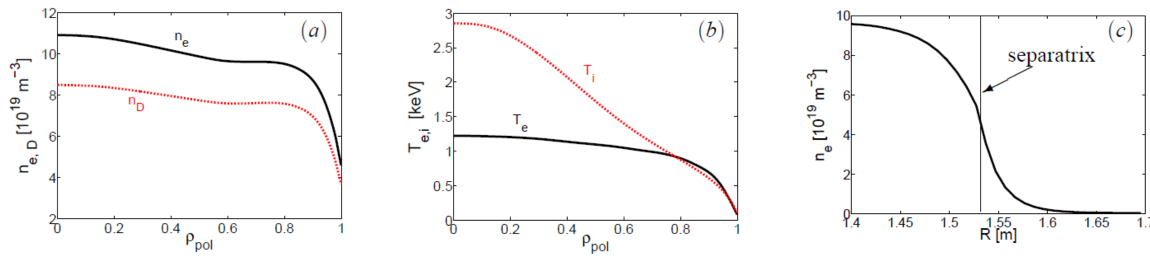

FIGURE RF-6. *Density (Figure (a)) and temperature (Figure (b)) profiles of electron (black line) and the thermal deuterium (redline) as a function of the square root of the normalized poloidal flux, ρ_{pol}. Figure (c) shows the electron density profile in the edge of the plasma as a function of the major radius (R).*

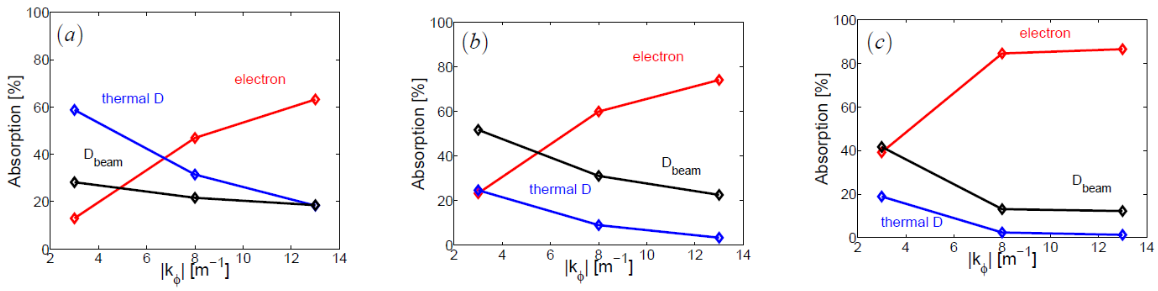

FIGURE RF-7. *Absorption of electrons, thermal deuterium (D), and fast ions (D_{beam}) as a function of the toroidal component of the wave vector (k_ϕ) for a H-mode scenario considered for NSTX-U [RF-12] obtained from AORSA simulations including the scrape-off layer. Figure (a): using electron and ion temperatures shown in Figure 3(b); Figure (b): decreasing T_i by 50% ($T_i(0)$ = 1.43 keV) but T_e the same as in Figure 3(b) ($T_e(0)$ = 1.22 keV); Figure(c): decreasing T_i by 50% ($T_i(0)$ = 1.43 keV) and doubling T_e relative to that used in (a) and (b) ($T_e(0)$ = 2.44 keV).*

result in less direct electron absorption. Another possible reason is that the high value of the ion temperature with respect to the electron temperature (Figure RF-6(b)) can lead to higher ion absorption. From Figures 4(b) and 4(c), the electron absorption increases significantly when the T_i/T_e ratio is decreased, in particular, for $|k_\phi| = 8\ \mathrm{m}^{-1}$. This behavior is more evident in Figure RF-7(c) where T_e is much larger that T_i. At the same time, again more clearly seen in Figure RF-7(c), one sees a strong reduction of thermal deuterium and beam ion absorption (for $|k_\phi| = 8\ \mathrm{m}^{-1}$). The antenna phase corresponding to $|k_\phi| = 3\ \mathrm{m}^{-1}$ seems to be more unfavorable for heating electrons, compared to $|k_\phi|$ = 8 and 13 m^{-1}, for all three ratios of T_i/T_e analyzed.

Figures RF-8(a), and RF-8(b) show the contour plot of the electron (RF-8(a)) and thermal deuterium (8(b)) power density for $k_\phi = 8\ \mathrm{m}^{-1}$ using the density and temperature profiles shown in Figures RF-6(a) and RF-6(b), respectively. The electron absorption is spread across a wide region between the magnetic axis and the last closed flux surface. On the other hand, from Figure RF-

8(b), one can see that the absorption of the thermal deuterium occurs at the location of the deuterium harmonic resonances in the plasma. The 2nd to 5th harmonic resonances of deuterium are within the last closed flux surface and the deuterium power density is mainly absorbed at the 5th deuterium

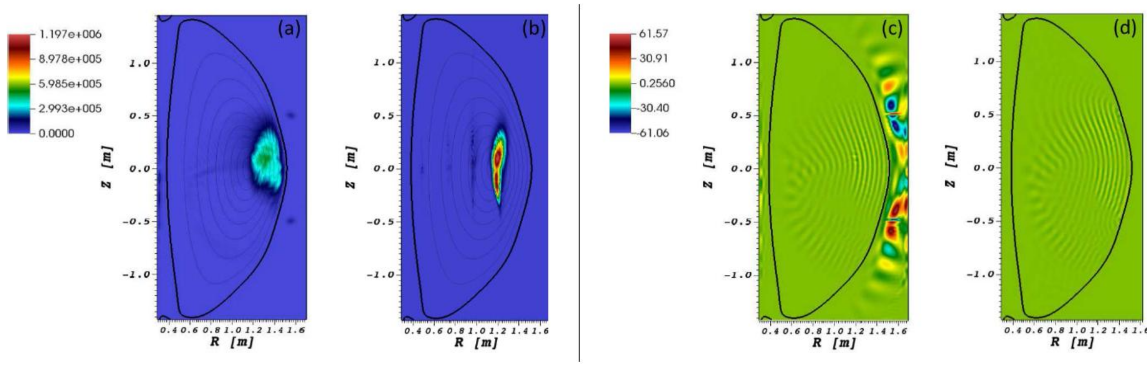

FIGURE RF-8. *Figures (a) and (b): contour plots of the power density (in W/m^3) absorbed by electrons (a) and thermal deuterium (b) for the NSTX-U case with $k_\phi = 8$ m^{-1}. Figures (c) and (d): two dimensional AORSA results of the real part of the parallel electric field (in V/m) with scrape-off layer (c) and without scrape-off layer (d) for the NSTX-U case with $k_\phi = 8$ m^{-1}. Figures (a) and (b) ((c) and (d)) are plotted with the same color scale.*

harmonic resonance, the closest to the magnetic axis. Figure RF-8(c) and RF-8(d) are the two dimensional AORSA results for the real part of the parallel electric field (in V/m) with (without) a scrape-off layer region, for $k_\phi = 8$ m^{-1}.. The main differences in these two figures is the strong electric field amplitude found in the scrape-off layer compared to the case without the scrape-off layer. One can also note that, inside of the last closed flux surface, no big differences appear in the parallel electric field for both cases, at this spatial resolution. In the initial simulations, no specific damping in the scrape-off region was been included, therefore no absorbed power has been found outside of the last closed flux surface, in contradiction to experimental studies of HHFW heating on the NSTX device, which have demonstrated that substantial HHFW power loss occurs along the open field lines in the scrape-off layer [RF-6: Perkins et al., 2012]. For this reason a collisional loss in the scrape-off layer of AORSA has recently been added to serve as a proxy for the damping processes there [RF-12: Bertelli et. al., 2013]]. Further detailed AORSA simulations for specific NSTX discharges and NSTX-U cases are now ongoing and results from the ongoing studies will be presented in an invited talk at the upcoming APS-DPP meeting in Denver in November 2013.

As part of these studies, comparisons of the predicted ion and electron power absorption partitioning from the AORSA, TORIC-HHFW and GENRAY codes were evaluated in both the HHFW and MHFW regimes. Significant differences between the three codes were found with higher ion temperatures or in the presence of an energetic beam ion species due to co-resonant NBI [RF-14: Phillips et al., 2012; RF-12: Bertelli et al, 2013], consistent with some earlier more limited studies [RF-18: Brecht et. al., 2009; RF-19: Phillips et. al. 2009]. In particular, higher ion absorption fractions are predicted by the TORIC-HHFW code compared to either AORSA or GENRAY. Several possible issues in the TORIC-HHFW code that could contribute to this discrepancy were identified in close collaboration with the PSFC-MIT. These include the neglect of toroidal broadening of the plasma dispersion function in the HHFW version of the code, and possible problems that could occur at high value of $k_\perp \rho_i$ in the evaluation of the Bessel functions in the plasma dielectric elements. Several studies are now underway to address these issues.

Parallel TORIC solver implementation in TRANSP

Implementation of a new parallel TORIC solver in TRANSP has now made it possible to perform transport analysis studies of HHFW heated plasmas in NSTX (and in NSTX-U in the future) using sufficient numerical resolution (N_m = 127 and N_R=480, whereas typical resolutions being used now are N_m = 31 and N_R=260. The new matrix solver [RF-20: Lee, 2013] developed by Dr. J. Wright and former graduate student Dr. J. P. Lee at MIT makes it possible to execute TORIC on a limited number of computing cores (~ 100) with excellent inverse scaling of wall clock time with processor number. This solver achieves parallelism not only in the poloidal block decomposition but also in the radial block dimension of the stiffness matrix. We recently carried out scaling tests with the parallel TORIC in TRANSP on the PPPL TRANSP server for cases of D-(H) minority heating in order to demonstrate the speed-up in time that can be expected for TORIC / TRANSP analysis of HHFW-heated discharges in NSTX and NSTX-U. The results are summarized in Table I. Since the TORIC solver is the primary source of CPU

Table RF-I: Parallel TORIC / TRANSP Timings for D(H) Minority Heating

Poloidal Mode Resolution (N_m) (Radial resolution of N_R = 320)	**Wall Clock Time (hours)**	**Processor Number**
31	7.29	1
31	4.22	16
31	2.09	32

usage in the TRANSP runs it can be seen that a significant decrease in wall clock time occurs for the entire analysis run with increasing processor number.

We have also carried out timing tests (see Table II) of parallel TORIC in TRANSP for analysis runs of combined D-(H) minority heating and D-(^{3}He) mode conversion in Alcator C-Mod, where large values of N_m are required to resolve the mode converted ICRF wave (either an ion Bernstein wave or an ion cyclotron wave). For the TRANSP analysis run shown in Table II it was found that ~127 poloidal modes was sufficient to resolve the mode converted ICRF waves. Although the work required to invert the TORIC matrix increases by a factor of about $(127/31)^3$ as the mode resolution is increased, the total time for the TRANSP analysis run only increases by about 25% by using 64 cores for the TORIC calculation.

Table RF-II: Parallel TORIC / TRANSP Timings for Combined D(H) Minority Heating and D-(^{3}He) Mode Conversion

Poloidal Mode Resolution (N_m) (Radial resolution of N_R = 320)	**Wall Clock Time (hours)**	**Processor Number**
31	9.54	1
127	11.87	64

The timing results shown in Table RF-I are important for TORIC in TRANSP simulations in NSTX and NSTX-U where multiple toroidal modes may be required in order to assess linear coupling physics in the scrape off layer (SOL) and thus it is important to reduce the wall clock time per toroidal mode simulation. The timing results in Table RF-II are directly relevant to the analysis of discharges in NSTX and NSTX-U where the injected HHFW may mode convert to a slow wave that can only be fully resolved with ultra-high poloidal mode number in the range of $N_m \geq 255$.

References

[RF-1] J.C. Hosea, et al., *Phys. Plasmas* **15**, 056104 (2008)
[RF-2] C.K. Phillips et al., *Nucl. Fusion* **49**, 075015 (2009)
[RF-3] J.C. Hosea et al., *AIP Conf Proceedings* **1187**, 105 (2009)
[RF-4] G. Taylor et al., *Physics of Plasmas* **17**, 056114 (2010)
[RF-5] J.C. Hosea, et al., AIP Conf. Proceedings 1406, 333 (2011)
[RF-6] R.J. Perkins et al., *Phys. Rev. Lett.* **109**, 045001 (2012)
[RF-7] R.J. Perkins, et al., *Proc. 39th EPS Conf. on Plasma Physics* **36F** (Stockholm 2012) paper P-1.011
[RF-8] R.J. Perkins, et al., IAEA Fusion Conference (San Diego 2012)
[RF-9] R.J. Perkins et al., *Nucl. Fusion* **53**, 083025 (2013)
[RF-10] R.J. Perkins et al., in appear in *AIP Conf. Proceedings*, 20th Topical Conference on Radio Frequency Power in Plasmas, June 25-28 2013, Sorrento, Italy
[RF-11] D.L. Green, et al., Phys. Rev. Lett. **107**, 145001 (2011)
[RF-12] N. Bertelli et al., in appear in *AIP Conf. Proceedings*, 20th Topical Conference on Radio Frequency Power in Plasmas, June 25-28 2013, Sorrento, Italy
[RF-13] N. Bertelli, et al., http://meetings.aps.org/link/BAPS.2011.DPP.NP9.64
[RF-14] C. K. Phillips, et al., http://meetings.aps.org/link/BAPS.2012.DPP.TP8.73
[RF-15] S. P. Gerhardt, R. Andre, and J.E. Menard, *Nucl. Fusion* **52**, 083020 (2012)
[RF-16] C. N. Lashmore-Davies, V. Fuchs, and R. A. Cairns, *Phys. Plasmas* **5**, 2284 (1998)
[RF-17] J. Menard, et al., *Phys. Plasmas* **6**, 2002 (1999)
[RF-18] T. Brecht et al., http://meetings.aps.org/link/BAPS.2009.DPP.JP8.67
[RF-19] C.K. Phillips et al., http://meetings.aps.org/link/BAPS.2009.DPP.PP8.75
[RF-20] J. P. Lee and J. C. Wright, "A versatile parallel block tri-diagonal solver for spectral codes", to be submitted to Computer Physic Communications (2013).

Solenoid Free Plasma Start-up

In FY2013 NSTX researcher initiated work on simulating CHI-only start-up plasmas in the NSTX-U geometry with the TSC code to develop plasma start-up scenarios for FY15 transient CHI experiments on NSTX-U. We are developing full discharge scenarios with the TSC code that involves, simulating a transient CHI discharge start-up and ramping it non-inductively using HHFW for heating and neutral beams for current drive. We initiated work on simulations using TRANSP to understand neutral beam absorption and current drive in low current plasmas, typical of those that would be produced by CHI, but with varying plasma parameters. The GENRAY code is being used to understand ECH absorption in CHI-like plasmas and is described in the Wave-particle section. Considerable progress was made in modeling the initial start-up phase of a transient CHI discharge with the NIMROD code. We converged on a CHI hardware design for the QUEST ST in Japan. Plasma start-up using point source helicity injection is being further developed at the Pegasus facility for implementation on NSTX-U during the later part of the NSTX-U 5YR plan.

NSTX-U will have numerous important upgrades for transient CHI that will significantly increase the CHI current start-up magnitude. These upgrades will be implemented over a period of three years. We formulated a detailed plan for implementing these systems in a systematic manner that would allow NSTX-U to demonstrate full non-inductive start-up and current ramp-up during the next five years. We conducted a study of the CHI systems and diagnostics required for CHI start-up on NSTX-U in FY2015, and identified additional CHI-related upgrades to diagnostics that are being installed on NSTX-U. We examined the needs for gas injectors and neutral pressure gauges to support all of NSTX-U plasma operations, as a result of which new ports are being installed on the NSTX-U vessel. These are described in detail in the NSTX-U 5yr plan document, so are not described here.

TSC/TRANSP Simulations

In support of the planned transient CHI studies on NSTX-U we have started to develop a model using the Tokamak Simulation Code (TSC) [SFSU-1,2,3] that uses the NSTX-U vessel geometry. TSC is a time-dependent, free-boundary, predictive equilibrium and transport code. It has previously been used for development of both discharge scenarios and plasma control systems.

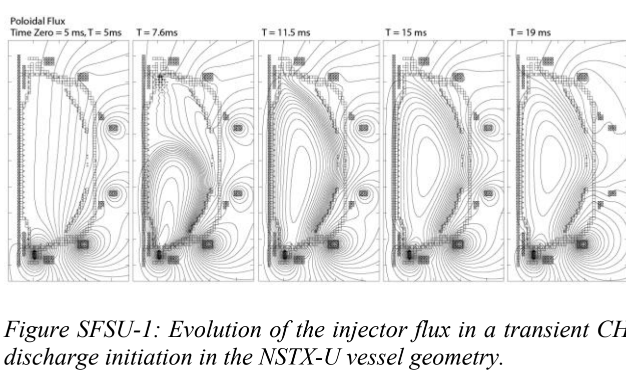

Figure SFSU-1: Evolution of the injector flux in a transient CHI discharge initiation in the NSTX-U vessel geometry.

For modeling CHI in NSTX, the vacuum vessel is specified as a conducting structure with poloidal breaks at the top and bottom across which an electric potential difference is applied from which TSC calculates the injector current using a model for the resistivity of the "halo" plasma. This circuit, however, contains a sheath resistance at each electrode, which is difficult to model. Since for transient CHI discharge initiation, it is the injector current and injector flux that are the governing parameters, we adopted the modeling strategy of adjusting the injector voltage in order to match the measured current rather than simply applying the measured injector voltage. This approach is adequate because this is also what is done experimentally. On the same machine, as the divertor surface conditions change, either due to increased gas loading on the electrodes or due to increased surface impurities, the voltage is adjusted to obtain the required injector current. Note that in the equation for the bubble burst current [SFSU-4], the injector current and not the voltage is the governing parameter for overcoming the magnetic field line tension of the injector flux.

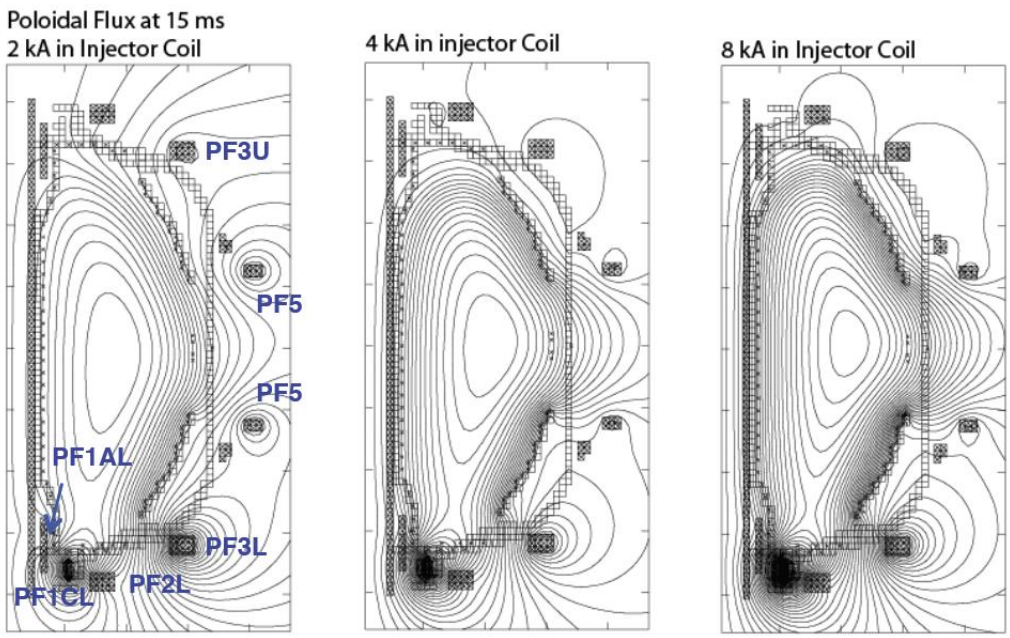

Figure SFSU-2: Flux surface plots at 15 ms as the current in the primary injector flux coil (PF1CL) is increased from 2 to 4 and then to 8 kA.

TSC simulations have been previously used to simulate transient CHI discharges from NSTX [SFSU-5]. These new studies in the NSTX-U vessel geometry, which are still in progress, examine the evolution of the injected poloidal flux as the magnitude of the injector flux is changed. The model has been simplified by using constant in time, coil currents and, thus far, no optimizations have been conducted, such as using the appropriate vertical field magnitude and shaping field required for the current in the CHI-produced plasma discharge or the appropriate voltage magnitude and pulse.

Figure SFSU-1 shows the evolution of the injected flux starting from t = 5 ms, at which time the discharge is initiated. For these initial cases a 5 ms voltage pulse is applied across the injection electrodes, which provides sufficient current to allow the discharge the fill the vessel. A relatively low current of 2 kA is used in the primary CHI injector coil (the PF1C coil). Relatively smaller

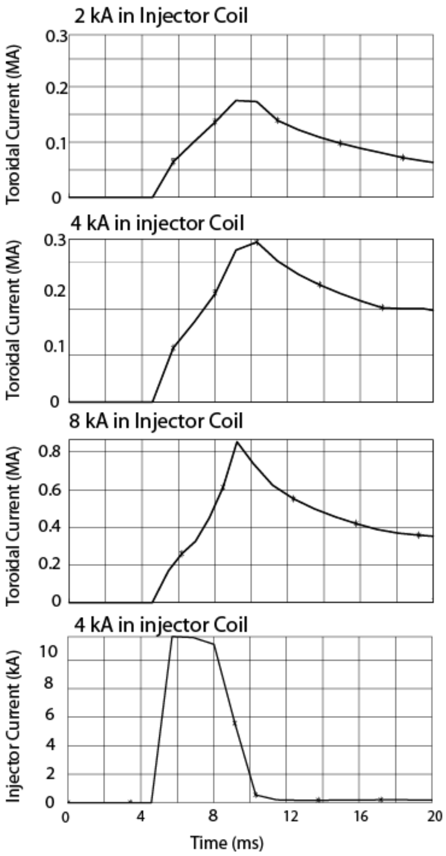

Figure SFSU-3: Toroidal and injector current for the cases in Figure SFSU-2

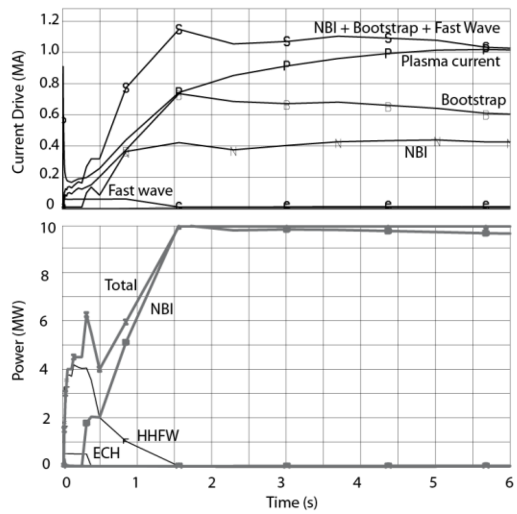

Figure SFSU-4: Time traces from a TSC current ramp-up simulation. The top frame shows the different current drive components. The lower traces show the injected power traces.

levels of currents are used in the other nearby coils as noted in the figure caption. All other coils have zero currents. This is typical of the way initial transient CHI-started discharges could be expected to be initiated on NSTX-U. Figure SFSU-2 shows the effect of increasing the current in the primary injector coil to 4 kA and then to 8 kA. The injector flux generated by this coil is directly proportional to the magnitude of the current driven in this coil. The primary injector flux coil (PF1CL) has a maximum rating of 318 kA.turns and it has 20 turns. Thus the maximum current rating for this coil is 16 kA, which is projected to generate a maximum of 250 mWb of injector flux. The corresponding CHI-generated toroidal current for these three cases is 150 kA, 300 kA and about 700 kA respectively, roughly reflecting the increased poloidal flux injection as the current in the injector coil is increased. Note from Figure SFSU-2 that the higher current discharges appear to bulge out from the mid-plane region suggesting that the currents in the PF5 and PF3 coils for these two cases are not adequate in this simulation. In addition, the toroidal current trace for the lowest current discharge shows the peak plasma current to saturate during the peak current phase. This is similar to the shape of experimentally generated toroidal currents in NSTX and results because the applied injector voltage magnitude and temporal shape is such that the CHI drive is gradually and correctly reduced as the CHI-produced plasma fills the vessel. In contrast, for the two higher current cases, and especially for the case with 8 kA in the PF1C coil, the toroidal current rises sharply;

suggesting that the applied voltage is still too high after the plasma has filled the vessel. These optimization studies will be the subject of continued work during FY2014.

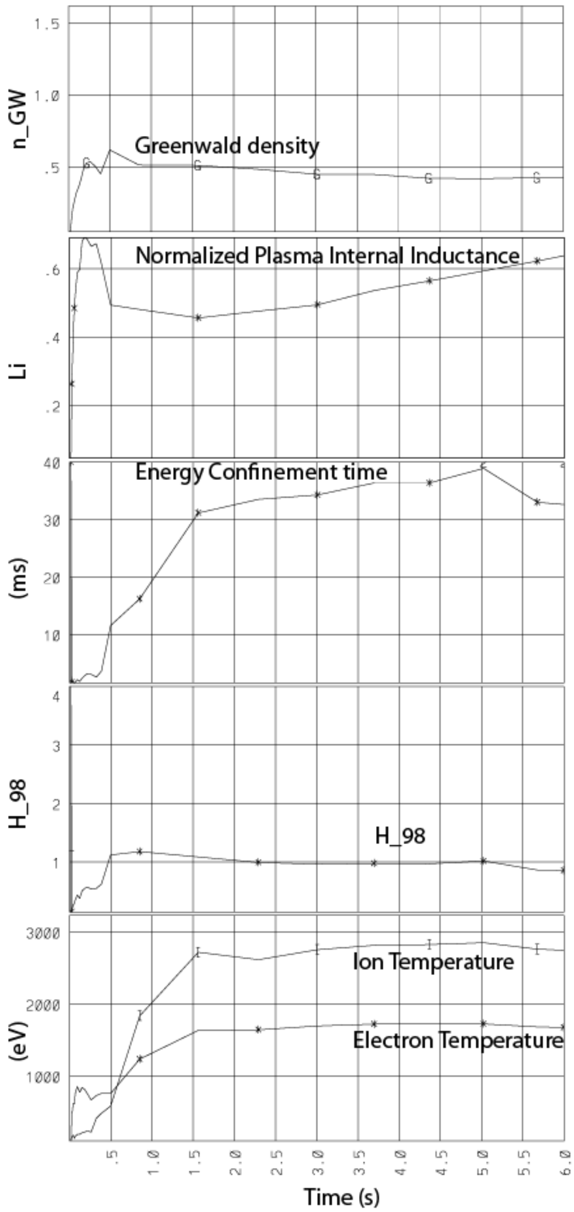

Figure SFSU-5: Time traces showing plasma parameters for the simulation shown in Fig. SFSU-4.

NSTX-U plans to use a 1 MW 28 GHz ECH system to boost the electron temperature of CHI started discharges to about 200-400 eV in about 20 ms. Simulations using the TSC code suggest that at 50% of the ITER L-mode confinement scaling, this temperature increase is possible [SFSU-6]. At the 300 eV electron temperatures, previous work on NSTX has shown that the electron temperature could be further increased above 1 keV in 20 ms using less than 1 MW of High Harmonic Fast Wave (HHFW) power [SFSU-7]. Discharges on NSTX have also demonstrated non-inductive current fractions of 0.7-1.1 in HHFW heated 300 kA plasmas [SFSU-7]. At the higher toroidal field in NSTX-U (1 T vs. 0.55 T in NSTX), HHFW coupling to the plasma is anticipated to improve [SFSU-7]. TRANSP simulations show that the new second neutral beam set on NSTX-U could provide 3-4 times higher current drive at low plasma current [SFSU-8]. This is due to a combination of 1.5 to 2 times higher current drive efficiency plus 2 times higher beam absorption. Initial TRANSP simulations for 300 kA plasmas suggest that the current drive efficiency at this lower current is also significant. The increased current drive requires the electron temperature of these plasmas to be in the 800 eV range or higher. Neutral beam coupling to these targets should then be possible to allow the combination of NBI current drive and bootstrap current overdrive to ramp the current to the sustained operation levels.

Figures SFSU-4 and 5 show results from an initial full discharge scenario TSC simulation that has all of the elements described above [SFSU-9]. The CHI discharge is initiated in TSC as described in Reference [SFSU-5], and a closed-flux target of >400 kA is established at 17 ms.

This is the seed current that is subsequently ramped-up using HHFW and neutral beams. The discharge is initially heated using 0.5 MW of absorbed ECH power. The HHFW power is ramped-up to 4 MW at 200 ms, maintained until 325 ms, then ramped down to zero. This is for the purpose of heating the plasma to increase the fraction of bootstrap current drive, as demonstrated with 300kA plasmas on NSTX [SFSU-7]. HHFW is assumed to generate 50 kA of fast wave current drive. Largely as a result of bootstrap current drive the current decay of the CHI plasma is first slowed down, and then it begins to ramp-up. During this phase, the neutral beam power is increased in steps so that the combination of NBI CD and bootstrap current drive provide current overdrive and they ramp the plasma current to 1 MA at about 4.5s. As shown in Figure 5, throughout the discharge, the Greenwald density is maintained at about 0.5, the normalized internal plasma inductance below 0.7, the energy confinement time below 40 ms, the H-98 factor close to 1. For the Copi-Tang transport model used in this simulation the electron and ion temperatures are about 1.7 and 2.8 keV respectively.

These studies with the TSC/TRANSP code, which will continue to be improved during FY2014, and after that using experimentally measured data, give confidence that NSTX-Upgrade appears well equipped to study non-inductive current formation and ramp-up as needed for an ST-FNSF.

CHI start-up modeling with NIMROD

Resistive MHD simulations using the NIMROD code are being used to model CHI start-up in NSTX; to improve understanding of the physics of injection, flux-surface closure, and current drive for CHI plasmas; and to extend these results to NSTX-U.

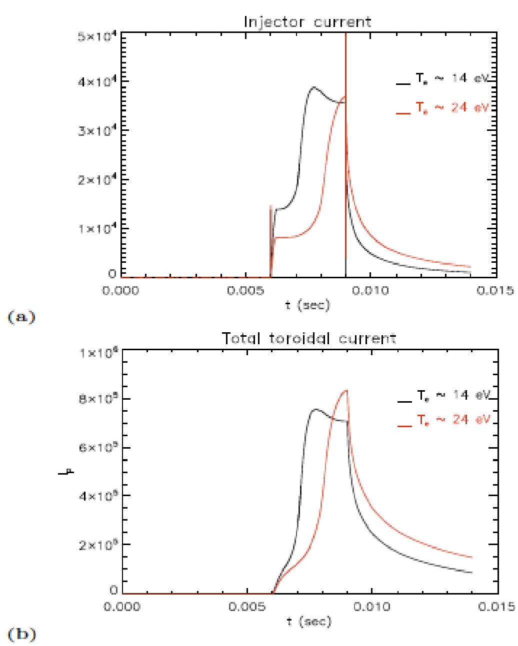

Figure SFSU-6: Time histories of (a) the injector current and (b) toroidal current for simulations at electron temperatures corresponding to 14 eV and 24 eV.

In the first set of studies, we use a simplified configuration. Constant poloidal field coil currents are used to generate the injector flux [SFSU-10]. Resistive MHD simulations with time-varying boundary conditions arising from poloidal-field coil changes as in the experiment have also been performed and also produce closed surfaces as in these simulations [SFSU-11]. However, this simplified model is more useful for understanding the key physics and the minimum conditions required for generating closed flux in a transient CHI discharge.

Under these conditions, the injector voltage is adjusted so that the J x B force sufficiently overcomes the field line tension [SFSU-4] and open field line plasma fills the vessel. Then, as in the experiment, the injector current is rapidly reduced, by turning off the

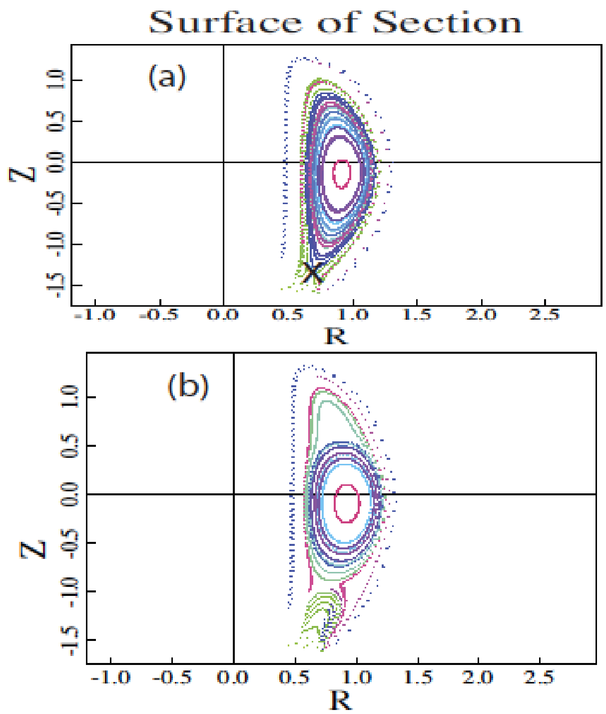

Figure SFSU-7: Pointcare plots soon after flux closure for (a) the 14 eV case at 9.4 ms and (b) the 24 eV case at 9.66 ms

applied voltage across the injector. Magnetic diffusivities similar to those in the experiment are used. Using simulations at zero pressure, we first investigate the effect of magnetic diffusivity (or Lundquist number) on the physics of flux closure. Simulations with large magnetic diffusivity ($\eta \sim 400$ m^2/s) (equivalent to T_e = 1eV) show no flux closure. A small volume of closed flux forms at magnetic diffusivities of about ($\eta \sim 40 - 20$ m^2/s). The volume of closed flux surfaces increases as the magnetic diffusivity is reduced to ($\eta \sim 8$ m^2/s) (equivalent to T_e = 14 eV). Time histories of injector current and total plasma current for two sets of simulations, ($\eta \sim 8$ m^2/s) and ($\eta \sim 3.5$ m^2/s) (equivalent to T_e = 24 eV) are shown in Figure SFSU-6. Both simulations reach similar values of injector current of about 36-37 kA at the time that the voltage is turned off. About 1 ms after the voltage is turned off, the injector currents drops sharply to about 10%-20% of their maximum values during the injection phase.

The formation of an X-point and closed flux surfaces is confirmed with the field line tracing of the Poincare plots shown in Figure SFSU-7(a). An X point starts to form at around t=9.005 ms and simultaneously closed flux surfaces begin to form. The physics of closed flux generation is described in detail in Reference [SFSU-10] and very briefly summarized here. As the injector voltage is turned off and the evolving toroidal magnetic field decreases in the injector region, the compression from the toroidal magnetic field exerts an effective bidirectional pinch force that brings the oppositely directed fields together to reconnect. Consistent with the bidirectional pinch force, as the injector voltage is turned off, a radial pinch $E \times B$ flow is generated, where the electric field (loop voltage) in the toroidal direction induces the poloidal-field evolution that leads to reconnection. An induced positive loop voltage during the decay phase of CHI has also been shown in TSC simulations [SFSU-5]. Here, our simulations show that oppositely directed magnetic flux (primarily the poloidal magnetic field, B_z) around the injector region collapses together through this oppositely directed flow $V_R \approx E_\phi B_Z$ and causes reconnection to occur.

Particularly interesting is the observation that closed flux surfaces during transient CHI can be explained through 2-D Sweet-Parker type reconnection [SFSU-12,13], and 3-D non-axisymmetric modes do not appear to play a dominant role. There are similarities between the transient Sweet-Parker reconnection found here and that reported in forced-reconnection laboratory plasmas [SFSU-14,15].

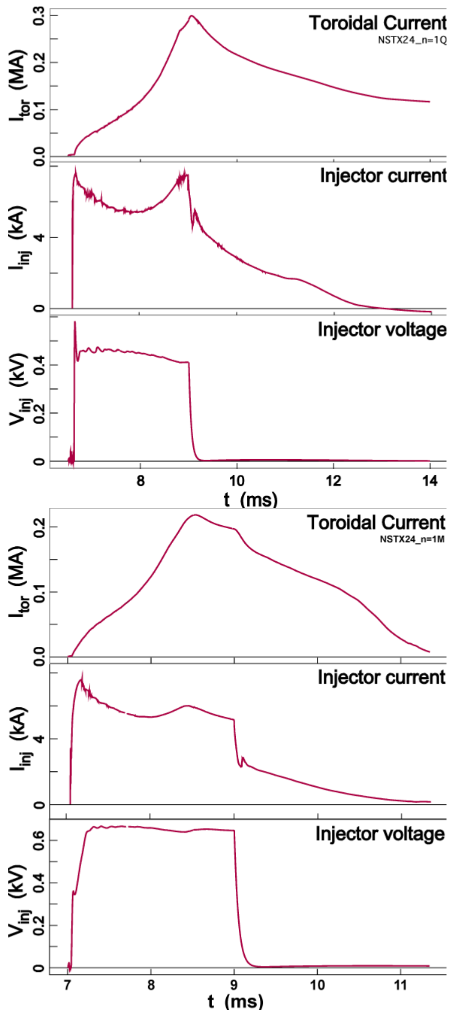

Figure SFSU-8. Discharge characteristics for (a) Case A – Top three frames, and (b) Case B – Lower three frames. Bottom to top: Injection gap voltage, injection current and toroidal current for simulation Case-A which includes the toroidal n = 0 and 1 modes. The power supply used a large capacitor to give a nearly flat voltage pulse and the currents are measured. Note the different time scales.

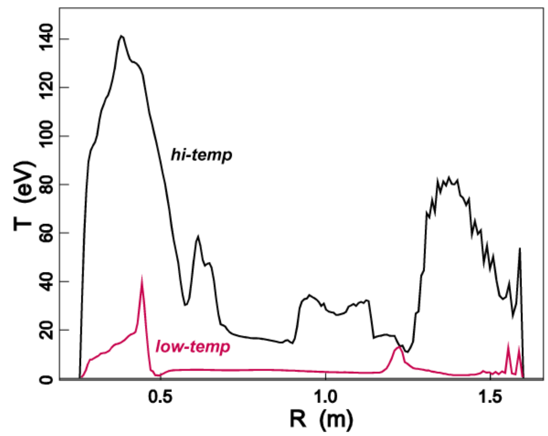

Figure SFSU-9. Temperature profiles at the midplane (Z=0) for the Case A (hi-temp) and Case B (low-temp) simulations at 9 ms.

In the second set of simulations, the vacuum perpendicular magnetic field line and flux on the computational boundary are used to develop models, the goal of which is to eventually simulate experimental discharges and to develop realistic models for transient CHI start-up. Currents and injection voltage for two simulated discharges are shown in Fig. SFSU-8. The simulation in Figure SFSU-8a (*case A*) was chosen because it is a better discharge in the sense that the toroidal current remains high to the end of the simulation at 14 ms, when the injector current has been reduced to zero, and represents a first step in a simulation discharge that is starting to reproduce some of the experimental observations. By 14 ms the toroidal current flows fully within the closed flux surfaces. This simulation had no impurities or radiated power which together with a low perpendicular thermal diffusion coefficient yielded electron temperatures of about 140 eV at z = 0 with a peak of 160 eV at higher z, greater than in the experiment where the measured electron temperatures during in CHI-only discharges (i.e., with no inductive drive from the transformer) are in the 20-30 eV range at z = 0.

Figure SFSU-8b (*Case B*) includes a generic radiation model that increases monotonically with temperature resulting in the temperature in the current layer dropping to a peak value of 50eV and to ~ 3eV in the core plasma. The peak temperature is still higher than measured in the experiment, but the result suggests that impurity radiation may be important for detailed comparisons with experiment. Both the injector and toroidal currents drop more rapidly than in

Case A, reaching zero soon after 11 ms. The temperature profiles are compared in Figure SFSU-9; the high-temperature peaks form in the channel at the surface where most of the injector current flows, and the profiles for both cases are similar to those seen by Thomson scattering measured electron temperatures in the experiment. In both simulations an X-point forms above the injector gap < 100 μs after 9 ms when the applied voltage is dropped. The "jogs" seen in the injector currents for both simulations occur when the X-point forms.

The injection voltage is dropped more rapidly than in the experiment to transition quickly (but smoothly) to the non-injection state. In the simulation the power supply is effectively short-circuited after the injector voltage reaches zero, ensuring no voltage across the injector gap. However, the rate of injector current drop is much slower than in the experiment, especially in *Case A*. This is due (at least in part) to the higher temperature therein as can be seen by comparing the injector-current decay rates in Fig. SFSU-8. Although these simulations did not have injection parameters identical to those of the experimental discharge, the plasma developed in a very similar way. Improving agreement with the experimental results, primarily by reducing the time required for reducing the injector current to zero while maintaining temperatures similar to those in *Case B* is the subject of on-going studies during 2014.

CHI Systems design for Quest:

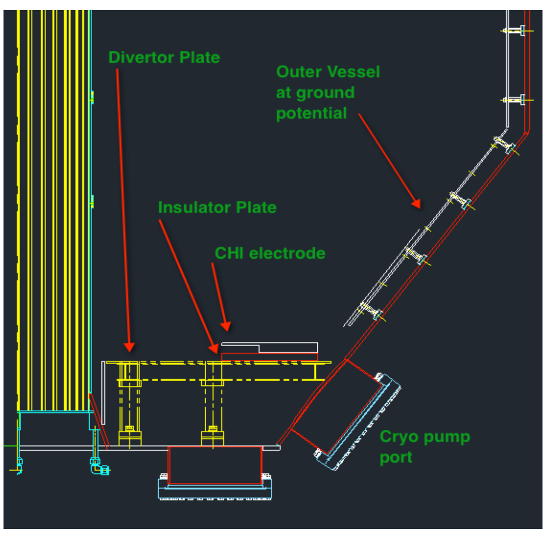

Figure SFSU-10: Proposed CHI electrode configuration on Quest. 1) The Quest divertor plate will be lowed by 16 cm, 2) An insulator plate and electrode plate would be mounted on the divertor plate, 3) The electrode would be biased with respect to the vessel, as on NSTX.

The QUEST is an ST located in Kyushu University in Japan. It has a major/minor radius of 0.68/0.4 m, the estimated plasma volume is about 4.5 m^3. Features present on QUEST, that are absent on HIT-II and NSTX are: 1) It is an all metal system, an aspect which is very desirable for the CHI method as low-Z impurities could be reduced to lower levels, 2) It is equipped with a high power Electron Cyclotron Resonance (ECH) heating system that will increase the electron temperature of CHI generated discharges, and thereby further improve their confinement properties, 3) Improvements to the CHI installation concept would allow QUEST to explore the method of steady-state or *driven* CHI to a level not possible in previous experiments.

Because it is an all-metal system, testing CHI capability on QUEST using metal electrodes would be particularly helpful to the NSTX-U CHI program as NSTX-U plans to install metal divertor plates during the present 5 YR period. We have now converged on the CHI electrode configuration design for QUEST. The design, shown in Figure SFSU-10, looks feasible and we plan to finish the final engineering design during 2014.

References

[SFSU-1] S.C. Jardin, C.E. Kessel, N. Pomphrey, Nucl. Fusion, **34** (1994) 8

[SFSU-2] S.C. Jardin, M.G. Bell, N. Pomphrey, Nucl. Fusion, **33** (1993) 371

[SFSU-3] S.C. Jardin, W. Park, Phys. Fluids, **24** (1981) 679

[SFSU-4] T.R. Jarboe, Nucl. Fusion, **52**, 083017 (2012)

[SFSU-5] R. Raman, S.C. Jardin, J.E. Menard, et al., Nucl. Fusion, **51** (2011) 113018

[SFSU-6] R. Raman, D. Mueller, S.C. Jardin, T.R. Jarboe, B.A. Nelson, M.G. Bell, J.E. Menard and M. Ono, Transient coaxial helicity injection plasma start-up in NSTX and CHI program plans on NSTX-U, IEEJ Transactions on Fundamentals and Materials, Vol. **132**, No. 7 pp 462-467 (2012)

[SFSU-7] G. Taylor et al., Phys. of Plasmas **19** (2012) 045001

[SFSU-8] J.E. Menard, et al. Nuclear Fusion **52**, (2012) 083051

[SFSU-9] R. Raman, T.R. Jarboe, S,C. Jardin, et al., "Non-inductive Plasma Current Start-up in NSTX using Transient CHI and subsequent Non-inductive Current Ramp-up Scenario in NSTX-U," O2.104, Proceedings of the 40th EPS Conference on Plasma Physics, Helsinki, Finland, July 1-5, 2013

[SFSU-10] F. Ebrahimi, et al., “Magnetic reconnection process in transient coaxial helicity injection,” – Accepted for publication as a Letter in Physics of Plasmas

[SFSU-11] E.B. Hooper, et al., “Resistive MHD simulations of helicity-injected start-up plasmas in NSTX,” – Accepted for publication in Physics of Plasmas

[SFSU-12] P. A. Sweet, in Electromagnetic Phenomena in Cosmical Physics, edited by B. Lehnert (1958), vol. 6 of IAU Symposium, p. 123.

[SFSU-13] E. N. Parker, J. Geophys. Res. 62, 509 (1957).

[SFSU-14] H. Ji, M. Yamada, S. Hsu, and R. Kulsrud, Physical Review Letters 80, 3256 (1998).

[SFSU-15] M. Yamada, H. Ji, S. Hsu, T. Carter, R. Kulsrud, and F. Trintchouk, Physics of Plasmas **7**, 1781 (2000).

Advanced Scenarios and Control

Plasma Control (General Atomics)

Inboard Midplane Gap Controllability Study

The effectiveness of the NSTX PF coil-set for gap control has been assessed using revalidated system and plasma response models. The assessment was done using a “decoupling” controller, produced by inverting the mapping matrix from coil currents to isoflux errors and plasma current. Figure PC-1 shows that this decoupling matrix controller produces poor decoupling of the inboard midplane gap (isoflux segment 7) error, and even this poor degree of decoupling requires unrealistically large coil current variation from the equilibrium values.

A key result of the recent model validation process is that the representation of experimental response appears accurate enough to enable reasonable calculation of high order matrix controllers produced using the decoupling approach or other model-based design method.

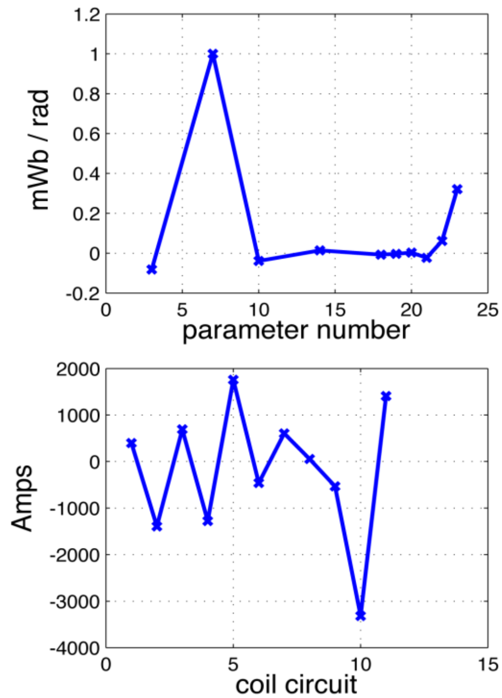

Fig. PC-1. Errors corresponding to best decoupling of isoflux segment 7 (inboard midplane gap) from other isoflux segments and corresponding coil current vector.

Steps Toward More Accurate Predictions of Vertical Growth Rates in NSTX

Studies of NSTX control have focused on understanding discrepancies between calculated and experimentally derived growth rates.

The growth rate of a VDE can be predicted by the plasma response codes rzrig and gspert (part of the GA TokSys computational environment for control design and analysis). For DIII-D these predictions have been in very good agreement with observed growth rates after triggered VDE’s for a range of growth rates. However, for VDE’s in NSTX the same codes predict values that are 3 times smaller than observed. One of the reasons for the observed discrepancy, and possibly the most significant, can be that the models make incorrect assumptions about how the current and pressure profiles are affected when the applied flux changes. Figure PC-2 is an example of predictions made by gspert. The example shows the flux at a point named “isoflux point 5”, which is an arbitrary point on the boundary.

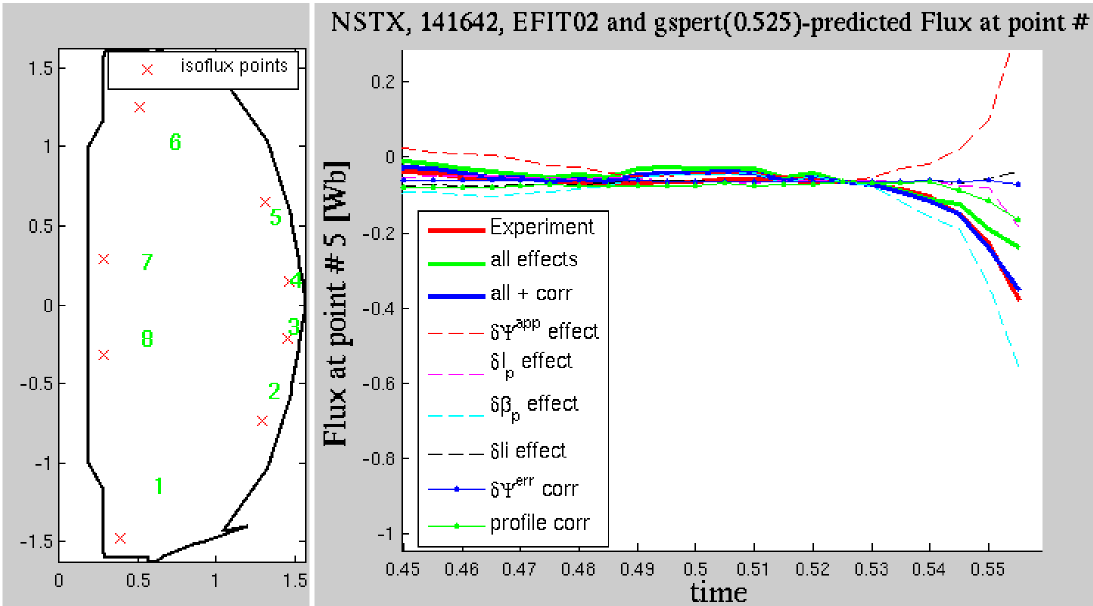

Fig. PC-2. Validation of isoflux response.

In this plot RED is the efits from the experiment, GREEN is gspert predictions, BLUE is gspert prediction with corrections for profile variation and convergence errors, dashed lines are individual effects from applied flux, ℓ_i, β_p, I_p, dashed lines with diamonds show effects from profile variations and convergence errors. The two remaining sources for discrepancies between gspert predictions and efits are due to the finite grid size and non-linearities in the plasma response. These are not shown.

The VDE occurs at 0.53 seconds in the shot. As can be seen, the gspert prediction in green is slower than the efits from the experiment in red. The blue line with gspert prediction corrected for details of the profile behavior is in good agreement with the efits. The gspert model is usually calculated with the assumption that li, betap, ip are unaltered by perturbations of the applied flux (with specific recipes for the details of the profiles). Any changes of these quantities are regarded as external influences, and responses corresponding to these constraints shown by the dashed lines in Fig. PC-2. If a model is developed that correctly includes the detailed response of the current and pressure profiles to changes in the applied flux then the prediction in blue would follow without the addition of any "external influences" and the growth rate should therefore be correctly predicted.

What is sought is therefore response objects such as: $\frac{\partial l_i}{\partial l_s}, \frac{\partial \beta_p}{\partial l_s}$.

The vertical growth rate is calculated by considering the circuit of conductors and plasma. The equations for voltages on conductors are:

$$V_j = R_j I_j + \left(M_{jk} + X_{jk}\right)\frac{dI_k}{dt} \quad ,$$

where M_{jk} is the regular mutual inductance and X_{jk} is an additional indirect coupling caused by the plasma response.

The equations are inverted to give an equation for the growth rate of currents,

$$\frac{dI_k}{dt} = -\left(M_{jk} + X_{jk}\right)^{-1} R_j I_j + \left(M_{jk} + X_{jk}\right)^{-1} V_j \quad .$$

The highest eigenvalue of $-\left(M_{jk} + X_{jk}\right)^{-1} R_j$ is the vertical growth rate.

In the above expression, the quantity X_{jk} should be corrected by adding:

$$\frac{\partial X_j}{\partial \beta_p}\frac{\partial \beta_p}{\partial \ell_k} + \frac{\partial X_j}{\partial \ell_i}\frac{\partial \ell_i}{\partial \ell_k} \quad .$$

The corrected vertical growth rate will be then be the highest eigenvalue of

$$\left(M_{jk} + X_{jk} + \frac{\partial X_j}{\partial \beta_p}\frac{\partial \beta_p}{\partial \ell_k} + \frac{\partial X_j}{\partial \ell_i}\frac{\partial \ell_i}{\partial \ell_k} \right)^{-1} R_j \quad .$$

It is expected that this form of the growth rate calculations will improve the match between model and experiment. A persistent mismatch will show that the b_p and ℓ_i response are not the source of the discrepancy.

NSTX-U TokSys Model Development

Recent studies for NSTX plasma control have been focused on developing a new TokSys model for the NSTX-U configuration, analyzing equilibria from the LRDFIT code, producing TokSys GSEQ equilibria for the new system, and analyzing the new configuration for relative vertical stability.

The initial TokSys model of NSTX-U is based on conductor specifications described in the LRDFIT code. IDL scripts were written to process LRDFIT files and write the conductor geometry into files with names *_lrdfit.dat, which are later processed by matlab routines in the TokSys /define directory. To allow for flexibility in later stages, the conductors were not grouped together at this point. Fig. PC-3 illustrates the TokSys conductor configuration, along with an equilibrium derived from LRDFIT.

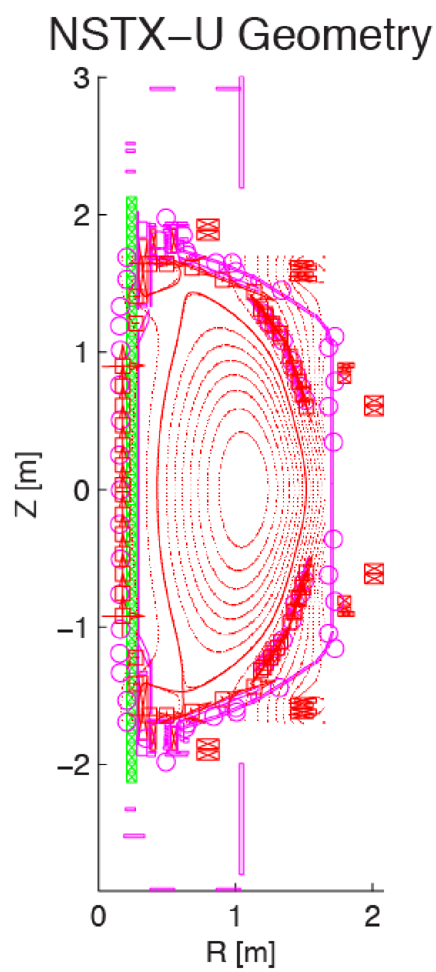

Fig. PC-3. NSTX-U geometry as specified in LRDFIT and implemented in TokSys.

New NSTX-U TokSys GSEQ Equilibrium and Vertical Stability Analysis

The TokSys designeq and convergeq codes were used to produce a well-converged lower single null equilibrium with the NSTX-U coilset for a 2 MA plasma current. Fig. PC-4 illustates this equilibrium along with the convergence quality for flux on the grid as well as coil currents.

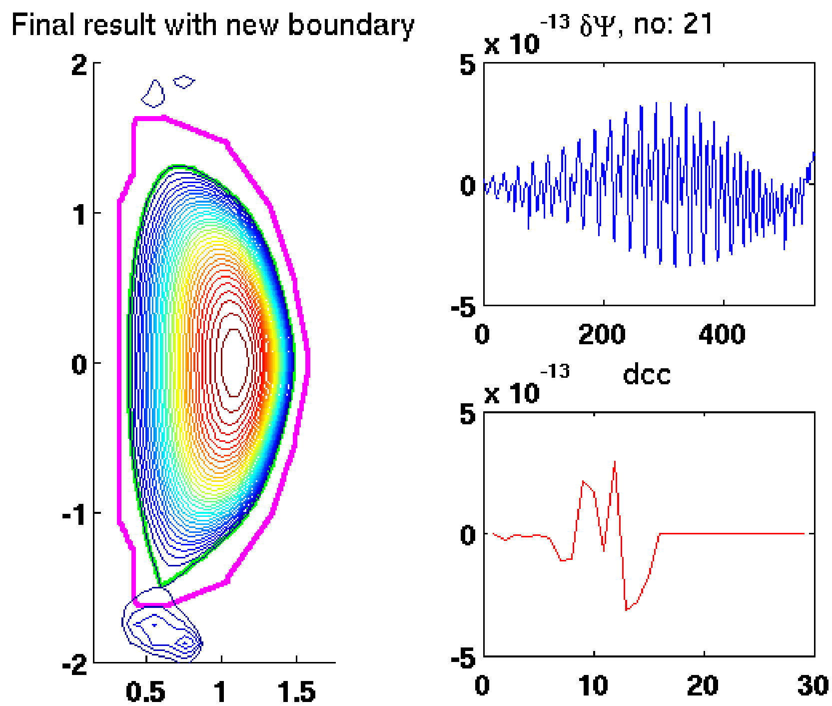

Fig. PC-4. NSTX-U equilibrium with 2.0 MA plasma current. Panels on right show corrections to flux and coil currents in the last iteration of the solution (Wb and A respectively) as a measure of convergence quality.

In the next step the code *gspert* was applied to this NSTX-U equilibrium. It gave a vertical growth rate of about 4 rad s^{-1} with the new TokSys conductor configuration. The unstable mode is shown in Fig. PC-5 below. In this model there is a simple assumption about how the current and pressure profiles would behave during a vertical displacement event. Let *W(V)* be the thermal energy contained within a flux surface where the volume is *V*. Let *I(A)* be the toroidal current contained within a flux surface with cross sectional area *A*.

In this case the simple assumption is that:
1. *W(V)* is unaltered by the vertical displacement
2. *I(A)* is changing in a way that preserves total *Ip* and *li*

The lower pane on the right side shows how *I(A)* is perturbed to maintain fixed *li*.
The pane on the right shows how the flux is perturbed at fixed points in space when the vertical displacement begins. The predicted mode in this case is not purely vertical. Although it is common for axisymmetric instabilities to have significant non-vertical, nonrigid components, it is possible that a better solution can be found by replacing the simple assumption for the behavior of

W(V) and *I(A)* by a more physically accurate model. Further studies will address the form of such modes in NSTX data, and produce calculations using appropriate constraints.

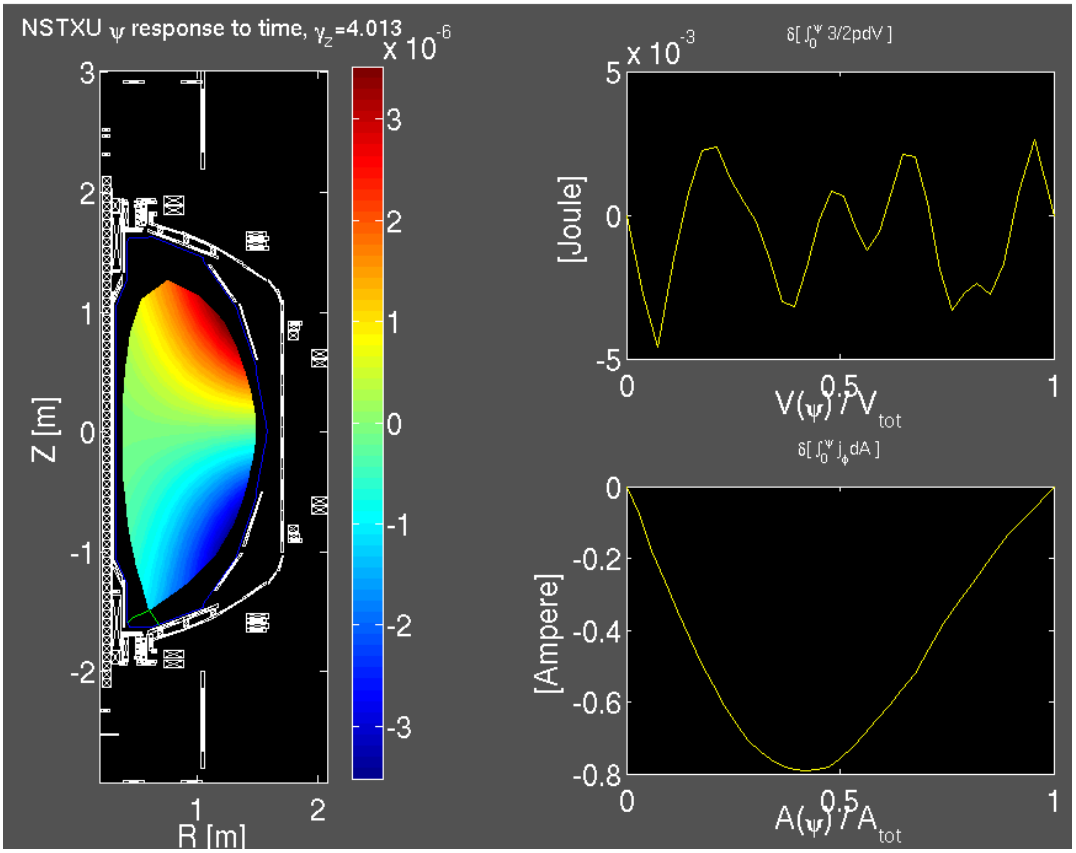

Fig. PC-5. Flux perturbation during vertical displacement event using simple assumptions for current and pressure profile responses. Panel at left shows flux perturbations on grid, while panels on right show changes in stored energy and current enclosed by flux surfaces as a function of normalized poloidal flux.

As a test of the GSEQ equilibrium code applied to the ST geometry, the equilibrium was evolved in free boundary mode as the plasma current was dropped with constant applied field. This evolution is a rough mockup of the dynamics observed in a major disruption current quench (though without self-consistent beta and li changes). Fig. PC-6 shows the results of this sequence, in which the plasma limits on the inboard surface with largely radial, minimally vertical motion. This is qualitatively consistent with typical observations in an ST major disruption with a highly balanced equilibrium such as the test case.

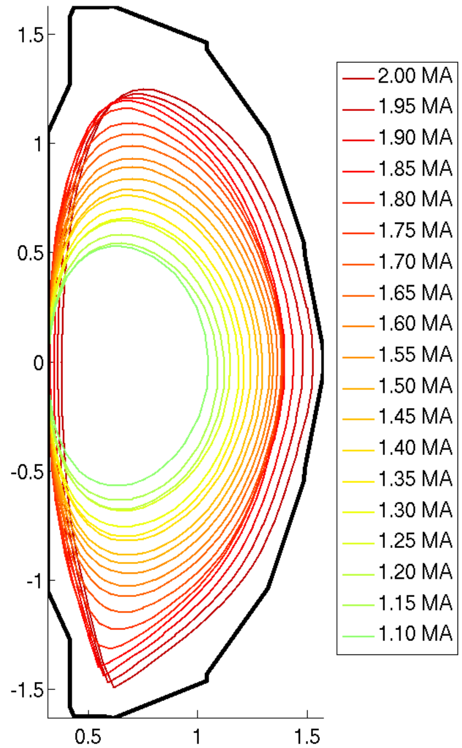

Fig. PC-6. Dropping plasma current without changing the applied vacuum field.

Note that fixing the externally applied vacuum field is similar to the result of inducing self-consistent vessel currents, which would tend to conserve flux at the vessel boundary. The computation time required for this free boundary equilibrium evolution sequence was a few seconds, indicating the usefulness of the tool for NSTX-U scenario study and equilibrium design.

Safety Factor (q) Profile Control Development (Lehigh University)

The need to optimize the tokamak concept, motivated by requirements of ITER, for the design of an economical, possibly steady-state, nuclear fusion power plant, has motivated extensive international research aimed at achieving the so-called Advanced Tokamak (AT) scenarios [QPC-1]. Such regimes are characterized by a high confinement state with enhanced magnetohydrodynamic stability, which yields a strong improvement in plasma performance that is quantified by increases in energy confinement time, plasma pressure, and fusion power density. Moreover, in AT scenarios a dominant fraction of the plasma current is self-generated by the neo-classical bootstrap mechanism, which alleviates the requirement on externally driven non-inductive current for steady-state operation.

The distributed-parameter nature of tokamaks makes the realization and sustainment of these advanced scenarios rely heavily on active control of the plasma spatial profiles, whose dynamics are governed by nonlinearly coupled partial differential equations (PDEs). In particular, it has been shown that the shape of the safety factor (q) profile plays a critical role in the achievement of AT scenarios characterized by the non-inductive sustainment of the plasma current. Therefore, while the control of scalar parameters associated with the safety factor q such as q_{min} has been proven critical to mitigate plasma instabilities and improve confinement, the shaping of the entire q profile (q at several points in space) will be necessary to stably maximize the fraction of bootstrap current in advanced scenarios such as those planned for ITER.

Motivated by this need, the Lehigh University (LU) Plasma Control Group led by Prof. Eugenio Schuster has recently started working in collaboration with PPPL on the development of control-oriented models for current-profile response in NSTX-U and on the design of active current-profile controllers based on these models. By making use of the new actuator and diagnostic capabilities in NSTX-U to their fullest, these new control algorithms will enhance the study and optimization of the Spherical Tokamak (ST) concept for future fusion reactors and will contribute to achieve NSTX-U scientific goals.

The nonlinearity and high dimensionality exhibited by the plasma demand a model-based control synthesis procedure that can accommodate this complexity through embedding the known physics within the design. By capturing the response of the plasma to the available actuators in a control-oriented model, model-based control design can achieve improved performance without the need for extensive trial-and-error tuning. The LU Plasma Control Group has advocated control-oriented modeling and model-based control for a wide spectrum of plasma control problems encompassing vertical position stabilization, shape control, MHD stabilization, burn control, and plasma (current, rotation, density, temperature) profile control. One of the major contributions of the on-going collaboration is the development of control-oriented, current-profile response models. It is important to emphasize that the plasma response models are developed only for control design and not for physical understanding, and consequently, they need to capture only the physics that is relevant for control design. The objective of the control-oriented plasma-response models to be developed within this collaboration is two-fold: control synthesis and control simulation. To be tractable from the point of view of existing control techniques, the complexity of models used for the synthesis of controllers usually needs to be lower than that of models used for the performance evaluation of controllers in closed-loop simulations. Therefore, the control-oriented models used for control simulation must be reduced further in complexity before being used for control synthesis. The control-oriented models used for control simulation need however to be much less sophisticated than those powering predictive codes such as PTRANSP, which is used for physics studies. This need is motivated by the fact that a control control-oriented predictive simulation code must be capable of running closed-loop simulations in a matter of minutes, at the most, to be an effective tool for iterative control design. The distinctive advantage of the modeling approach by the LU Plasma Control Group is the combination of widely accepted first-principles laws with empirical correlations obtained from physical observations, which leads to PDE models that capture the high dimensionality and the nonlinear magnetic-kinetic coupling of the system dynamics. This first-principles-driven (FPD) modeling approach has the potential of retaining the nonlinear dynamics of the plasma in the control-oriented model. Moreover, FPD modeling provides the freedom of arbitrarily handling the trade-off between the simplicity of the model and both its physics accuracy and its range of validity during the model reduction process prior to control synthesis (simulation-oriented model → synthesis-oriented model), does not require dedicated modeling (system identification) experiments although it relies on empirical correlations from experimental data, and is therefore more easily adaptable to different tokamaks and equilibrium configurations.

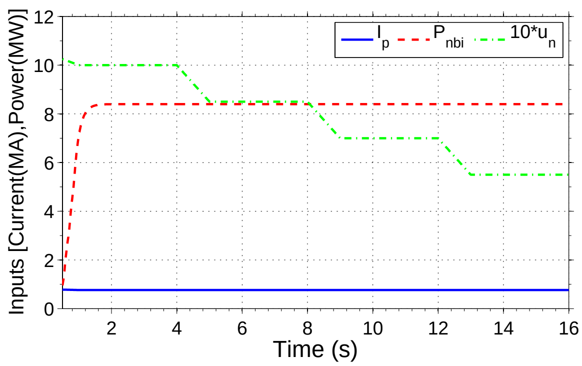

Fig. QPC-1: Control inputs applied during FPD-model and PTRANSP simulations (u_n is dimensionless)

The first-principles physics model of the poloidal magnetic flux profile evolution [QPC-2], which is related to the *q*-profile evolution, is converted into a form suitable for control design in NSTX-U by combining the poloidal flux evolution model with simplified control-oriented versions of physics-based models of the electron density and temperature profiles, the plasma resistivity, and the noninductive current-drives. The developed control-oriented model puts emphasis on high-confinement (H-mode) scenarios in NSTX-U, and extends previous models for low-confinement (L-mode) scenarios [QPC-3] by explicitly including the effects of the self-generated "bootstrap current" and by modeling each actuator (neutral beam injector) independently in order to utilize the full capabilities of the heating and current drive (H&CD) system. This model is developed with the goal of extending previous model-based feedforward [QPC-4, 5] and feedback [QPC6-11] control strategies to high-performance H-mode scenarios in NSTX-U. Preliminary prediction capabilities of the control-oriented FPD model are illustrated below by comparing them with PTRANSP simulations (142301M21). The inputs (total plasma current (I_{p}), total neutral beam injection power (P_{nbi}), and density regulation (u_{n})) applied during the simulation study are shown in Fig. QPC-1. The electron density and temperature profile evolutions are compared in Fig. QPC-2. The two main components of the noninductive current, neutral beam current and bootstrap current, are compared in Fig. QPC-3 and Fig. QPC-4, respectively. Time traces of the poloidal magnetic flux at various normalized effective minor radii are shown in Fig. QPC-5, and a comparison of FPD-model and PTRANSP predicted q profiles at various times is shown in Fig. QPC-6. As shown, the trends of the FPD model predicted plasma parameters show good agreement with those predicted by PTRANSP. Current efforts focus on improving the prediction capabilities by the FPD model and on designing model-based q-profile advanced controllers for NSTX-U. Closed-loop simulations of the developed controllers will help assess the true requirements for model accuracy before experimental testing.

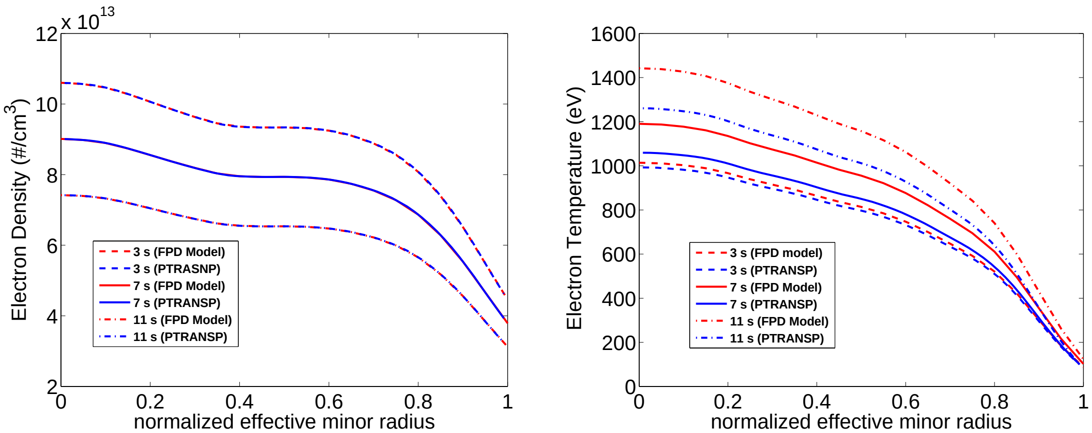

Fig. QPC-2: Electron density (left) and temperature (right) profiles: PTRANSP and PFD-Model simulations.

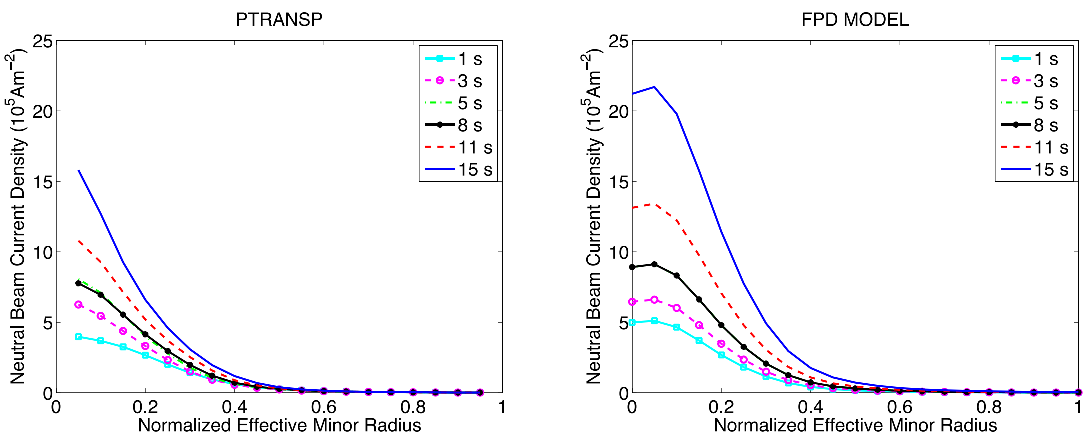

Fig. QPC-3: Noninductive neutral beam current density: PTRANSP and PFD-Model simulations.

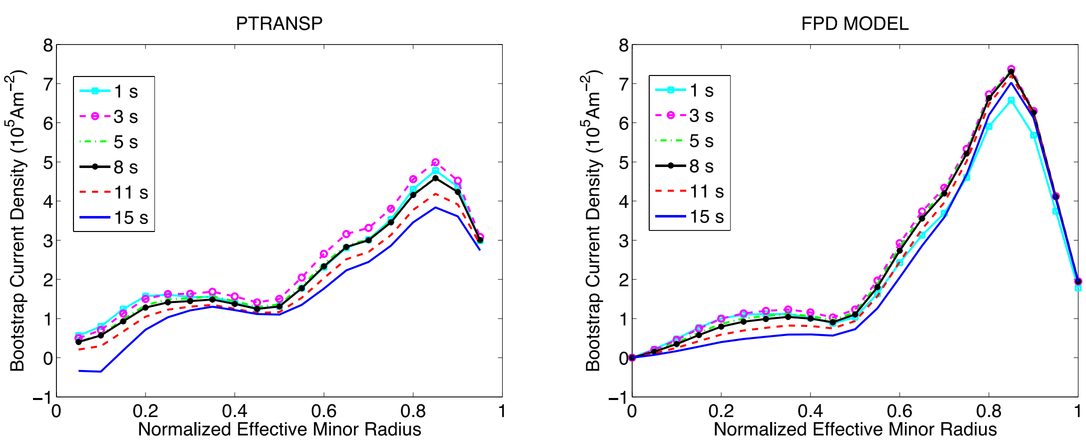

Fig. QPC-4: Non-inductive bootstrap current density: PTRANSP and PFD-Model simulations.

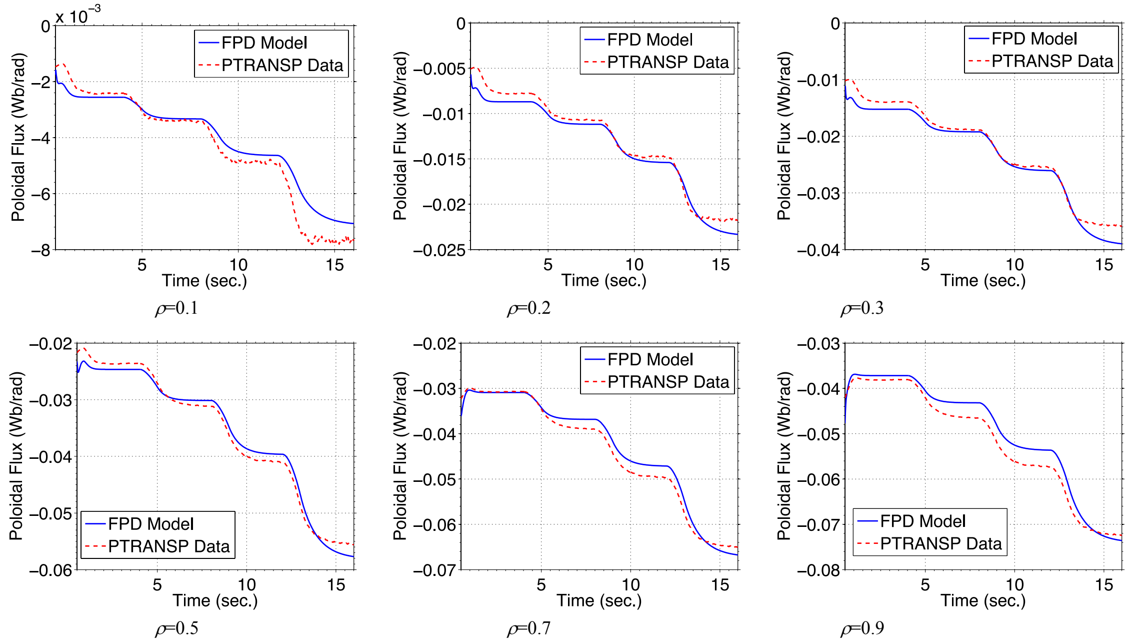

Fig. QPC-5: Time traces of poloidal magnetic flux at various locations: PTRANSP and PFD-Model simulations.

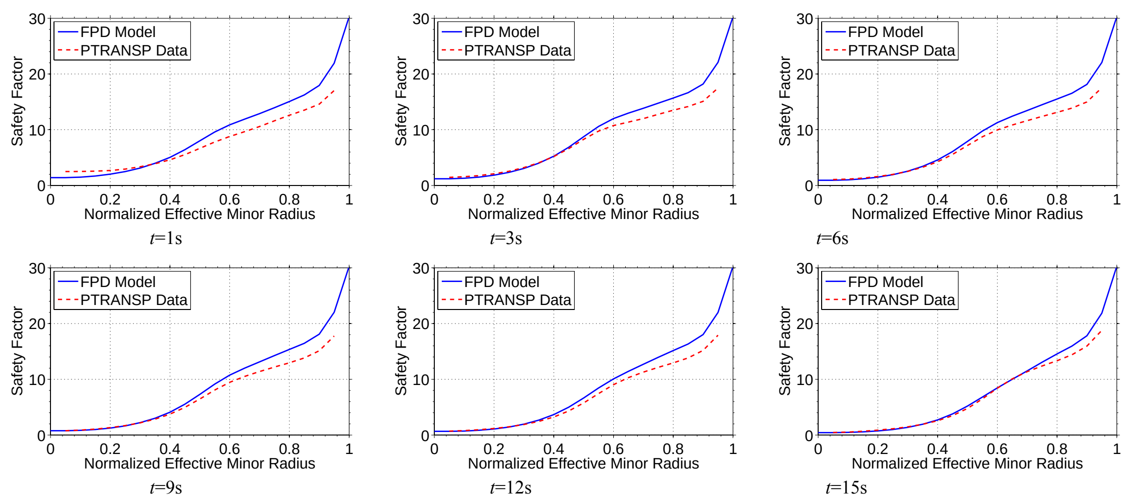

Fig. QPC-6: Safety factor (q) profile at various times: PTRANSP and PFD-Model simulations.

References

[QPC-1] T. Taylor, "Physics of advanced tokamaks," *Plasma Physics and Controlled Fusion*, vol.39, no. suppl. 12B, pp. B47–B73, 1997.

[QPC-2] F.L. Hinton and R.D. Hazeltine, "Theory of Plasma Transport in Toroidal Confinement Systems," *Reviews of Modern Physics*, vol. 48, no. 2, pp. 239–308, 1976.

[QPC-3] Y. Ou, T.C. Luce, E. Schuster, J.R. Ferron, M.L. Walker, C. Xu, and D.A. Humphreys, "Towards Model-based Current Profile Control at DIII-D," *Fusion Engineering and Design* 82 (2007) 1153–1160.

[QPC-4] Y. Ou, C. Xu, E. Schuster, T.C. Luce, J.R. Ferron, M.L. Walker and D.A. Humphreys, "Design and simulation of extremum-seeking open-loop optimal control of current profile in the DIII-D tokamak," *Plasma Physics and Controlled Fusion*, 50 (2008) 115001.

[QPC-5] C. Xu, Y. Ou, J. Dalessio, E. Schuster, T.C. Luce, J.R. Ferron, M.L. Walker and D.A. Humphreys, "Ramp-Up-Phase Current-Profile Control of Tokamak Plasmas via Nonlinear Programming," *IEEE Transactions on Plasma Science*, vol. 38, no 2, pp. 163-173, February 2010.

[QPC-6] Y. Ou, C. Xu and E. Schuster, "Robust Control Design for the Poloidal Magnetic Flux Profile Evo- lution in the Presence of Model Uncertainties," *IEEE Transactions on Plasma Science*, vol. 38, no. 3, pp. 375-382, March 2010.

[QPC-7] C. Xu, Y. Ou, E. Schuster, "Sequential Linear Quadratic Control of Bilinear Parabolic PDEs based on POD Model Reduction," *Automatica*, vol. 47, no. 2, pp. 418 – 426, February 2011.

[QPC-8] Y. Ou, C. Xu, E. Schuster, T. C. Luce, J. R. Ferron, M. L. Walker and D. A. Humphreys, "Receding-Horizon Optimal Control of the Current Profile Evolution During the Ramp-Up Phase of a Tokamak Discharge," *Control Engineering Practice*, 19 (2011) 2231.

[QPC-9] J. Barton, M.D. Boyer, W. Shi, E. Schuster, T.C. Luce, J.R. Ferron, M.L. Walker, D.A. Humphreys, B.G. Penaflor and R.D. Johnson, "Toroidal Current Profile Control During Low Confinement Mode Plasma Discharges in DIII-D via First-Principles-Driven Model-based Robust Control Synthesis," *Nuclear Fusion* 52 (2012) 123018 (24pp).

[QPC-10] M.D. Boyer, J. Barton, E. Schuster, T.C. Luce, J.R. Ferron, M.L. Walker, D.A. Humphreys, B.G. Penaflor and R.D. Johnson, "First-Principles-Driven Model-Based Current Profile Control for the DIII- D Tokamak via LQI Optimal Control," *Plasma Physics and Controlled Fusion* 55 (2013) 105007 (18pp).

[QPC-11] M.D. Boyer, J. Barton, E. Schuster, T.C. Luce, J.R. Ferron, M.L. Walker, D.A. Humphreys, B.G. Penaflor and R.D. Johnson, "Backstepping Control of the Toroidal Plasma Current Profile in the DIII-D Tokamak," *IEEE Transactions on Control Systems Technology*, under review.

NSTX-U Publications in FY2013 (October 2012-September 2013)

1) ZWEBEN SJ, Campanell MD, Lyons BC, et al.
Local effects of biased electrodes in the divertor of NSTX
Plasma Phys. Cont. Fusion 54 105012 (October 2012)

2) CLAYTON DJ, Tritz K, Stutman D, et al.
Multi-energy soft-x-ray technique for impurity transport measurements in the fusion plasma edge
Plasma Phys. Control. Fusion 54 105022 (October 2012)

3) ZHU YB, Bortolon A1 Heidbrink WW, et al.,
Compact solid-state neutral particle analyzer in current mode
Rev. Sci. Instrum. 83 10D304 (October 2012)

4) SMITH DR, Fonck RJ, McKee GR, et al.
Diagnostic performance of the beam emission spectroscopy system on the National Spherical Torus Experiment
Rev. Sci. Instrum. 83 10D502 (October 2012)

5) SKINNER CH, Gentile CA, and Doerner R
Simultaneous imaging/reflectivity measurements to assess diagnostic mirror cleaning
Rev. Sci. Instrum. 83 10D512 (October 2012)

6) CLAYTON DJ, Jaworski MA, Kumar D, et al.
Divertor electron temperature and impurity diffusion measurements with a spectrally resolved imaging radiometer
Rev. Sci. Instrum. 83 10D521 (October 2012)

7) LeBLANC BP, Diallo A, Labik G, et al.
Radial resolution enhancement of the NSTX Thomson scattering diagnostic
Rev. Sci. Instrum. 83 10D527 (October 2012)

8) DIALLO A, LeBlanc BP, Labik G, et al.
Prospects for the Thomson scattering system on NSTX-Upgrade
Rev. Sci. Instrum. 83 10D532 (October 2012)

9) TAYLOR CN, Heim B, Gonderman S, et al.
Materials analysis and particle probe: A compact diagnostic system for in situ analysis of plasma-facing components (Invited)
Rev. Sci. Instrum. 83 10D703 (October 2012)

10) SOUKHANOVSKII VA, Gerhardt SP, Kaita R, et al.
Diagnostic options for radiative divertor feedback control on NSTX-U
Rev. Sci. Instrum. 83 10D716 (October 2012)

11) HEIDBRINK WW, Bortolon A1 Muscatello CM, et al.,
http://rsi.aip.org/resource/1/rsinak/v83/i10/p10D903_s1
Rev. Sci. Instrum. 83 10D903 (October 2012)

12) ZHANG J, Peebles WA, Carter TA, et al.
Design of a millimeter-wave polarimeter for NSTX-Upgrade and initial test on DIII-D
Rev. Sci. Instrum. 83 10E321 (October 2012)

13) SCOTTI F, Roquemore AL and Soukhanovskii VA
Full toroidal imaging of non-axisymmetric plasma material interaction in the National Spherical Torus Experiment divertor
Rev. Sci. Instrum. 83 10E532 (October 2012)

14) JAWORSKI MA, Bell MG, Gray TK, et al.,
Modification of the electron energy distribution function during lithium experiments on the National Spherical Torus Experiment
Fusion Engineering and Design 87 1711 (October 2012)

15) KUGEL HW, Allain JP, Bell MG, et al.,
NSTX plasma operation with a Liquid Lithium Divertor
Fusion Engineering and Design 87 1724 (October 2012)

16) KRISTIC PS, Allain JP, Allouche A, et al.,
Dynamics of deuterium retention and sputtering of Li-C-O surfaces
Fusion Engineering and Design 87 1732 (October 2012)

17) BROOKS JN, Hassanein A, Sizyuk, et al.,
Modeling of plasma/lithium-surface interactions in NSTX: status and key issues
Fusion Engineering and Design 87 1737 (October 2012)

18) ONO M, Bell MG, Kaita R, et al.,
Recent progress of NSTX lithium program and opportunities for magnetic fusion research
Fusion Engineering and Design 87 1770 (October 2012)

19) SURLA V, Jaworski MA, Soukhanovskii V, et al.,
Characterization of transient particle loads during lithium experiments on the National Spherical Torus Experiment
Fusion Engineering and Design 87 1794 (October 2012)

20) AHN J-W, Kim H-S, Park Y-S, et al.,
Confinement and ELM characteristics of H-mode plasmas in KSTAR
Nucl. Fusion 52 114001 (November 2012)

21) KIM J, Jeon Y-M, Xiao W, et al.,
ELM control experiments in the KSTAR device
Nucl. Fusion 52 114011 (November 2012)

22) CAO B, Zweben SJ, Stotler DP, et al.,
Edge turbulence velocity changes with lithium coating in NSTX
Plasma Phys. and Controlled Fusion 54 112001 (November 2012)

23) YOSHIDA M, Kaye SM, Rice J, et al.,
Momentum transport studies from multi-machine comparisons
Nucl. Fusion 52 123005 (December 2012)

24) SECHREST Y, Munsat T, Battaglia DJ, et al.,
Two-dimensional characterization of ELM precursors in NSTX
Nucl. Fusion 52 123009 (December 2012)

25) DIALLO, A, Kramer GJ, Smith DR et al.,
Observation of ion scale fluctuations in the pedestal region during the edge-localized-mode cycle on the National Spherical Torus Experiment
Phys. Plasmas 20 012505 (January 2013)

26) FREDRICKSON ED, Crocker NA, Darrow DS, et al.
Fast-ion energy loss during TAE avalanches in the National Spherical Torus Experiment
Nucl. Fusion 53 13006 (January 2013)

27) DARROW DS, Crocker N, Fredrickson ED, et al.
Stochastic orbit loss of neutral beam ions from NSTX due to toroidal Alfven eigenmode avalanches
Nucl. Fusion 53 013009 (January 2013)

28) GERHARDT SP
Dynamics of the disruption halo current toroidal asymmetry in NSTX
Nucl. Fusion 53 023005 (February 2013)

29) GAN KF, Ahn J-W, Park J-K, et al.
2D divertor heat flux distribution using a 3D heat conduction solver in National Spherical Torus Experiment
Rev. Sci. Instrum. 84 023505 (February 2013)

30) KRAMER GJ, Budny RV, Bortolon A, et al.,
A description of the full-particle-orbit-following SPIRAL code for simulating fast-ion experiments in tokamaks
Plasma Phys. Controlled Fusion 55 025013 (February 2013)

31) KRSTIC PS, Allain JP, Taylor CN, et al.
Deuterium uptake in magnetic-fusion devices with lithium-conditioned carbon walls
Phys. Rev. Lett. 110 105001 (March 2013)

32) GOUMIRI IR, Rowley CW, Ma Z, et al.,
Reduced-order model based feedback control of the Modified Hasegawa-Wakatani model
Phys. Plasmas 20 042501 (April 2013)

33) GERHARDT SP, Bell RE, Diallo A, et al.
Disruptions, disruptivity and safer operating windows in the high-beta spherical torus NSTX
Nucl. Fusion 53 043020 (April 2013)

34) ZHANG J, Crocker NA, Peebles WA, et al.
A sensitivity assessment of millimeter-wave polarimetry for measurement of magnetic fluctuations associated with microtearing modes on NSTX-U
Plasma Phys. Controlled Fusion 55 045011 (April 2013)

35) FREDRICKSON ED, Gorelenkov NN, Podesta M, et al.,
Non-linear modulation of short wavelength compressional Alfvén eigenmodes
Phys. Plasmas 20, 042112 (April 2013)

36) CROCKER NA, Fredrickson ED, Gorelenkov NN, et al.,
Internal amplitude, structure and identification of compressional and global Alfvén eigenmodes in NSTX
Nucl. Fusion 53 043017 (April 2013)

37) KIM K, Park J-K, and Boozer AH,
Numerical verification of bounce-harmonic resonances in neoclassical toroidal viscosity for tokamaks
Phys. Rev. Lett. 110, 185004 (May 2013)

38) SMITH DR, Fonck RJ, McKee GR et al.,
Characterization and parametric dependencies of low wavenumber pedestal turbulence in the National Spherical Torus Experiment
Phys. Plasmas 20 055903 (May 2013)

39) MUELLER, DM
Physics of tokamak start-up
Phys. Plasmas 20, 058101 (May 2013)

40) KAYE SM, Gerhardt S, Guttenfelder W, et al,
The dependence of H-mode energy confinement and transport on collisionality in NSTX
Nucl. Fusion 53 063005 (June 2013)

41) MORADI S, PUSZTAI I, Guttenfelder W, et al.
Microtearing modes in spherical and conventional tokmamaks
Nucl. Fusion 53, 063025 (June 2013)

42) BORTOLON A, Heidbrink WW, Kramer GJ et al.,
Mitigation of Alfven activity in a tokamak by externally applied static 3D fields
Phys. Rev. Lett. 110, 265008 (June 2013)

43) PARK J-K, Bell RE, Kaye SM, et al.
Intrinsic rotation generation in NSTX ohmic H-mode Plasmas
Nucl. Fusion 53 063012 (June 2013)

44) SALEWSKI M. Geiger B, Nielsen SK, et al.,
Combination of fast-ion diagnostics in velocity-space tomographies
Nuclear Fusion 53 063019 (June 2013)

45) MYRA JM, Davis WM, D'Ippolito DA, et al.,
Edge sheared flows and the dynamics of blob filaments
Nucl. Fusion 53 073013 (July 2013)

46) RAMAN R, Mueller D, Jardin SJ, et al.,
Non-inductive plasma start-up on NSTX and projections to NSTX-U using transient CHI
Nucl. Fusion 53 073017 (July 2013)

47) EICH T, Sieglin B, Scarabosio A, et al.,
Empiricial scaling of inter-ELM power widths in ASDEX Upgrade and JET
Journal Nucl. Mater. 438 S72 (July 2013)

48) SOUKHANOVSKII VA, Bell RE, Diallo A, et al.,
Advanced divertor configurations with large flux expansion
Journal Nucl. Mater. 438 S96 (July 2013)

49) ABRAMS T., Jaworski MA, Kallman J, et al.,
Response of NSTX liquid lithium divertor to high heat loads
Journal Nucl. Mater. 438 S313 (July 2013)

50) AHN J-W, Gan KF, Scotti F, et al.,
Study of non-axisymmetric divertor footprints using 2-D IR and visible cameras and a 3-D heat conduction solver in NSTX
Journal Nucl. Mater. 438 S317 (July 2013)

51) GOLDSTON RJ
Scrape-off layer flows with pressure gradient scale length
Journal Nucl. Mater. 438 S372 (July 2013)

52) JAWORSKI MA, Bell MG, Gray TK, et al.,
Observation of non-Maxwellian electron distributions in the NSTX divertor
Journal Nucl. Mater. 438 S384 (July 2013)

53) LORE JD, Canik JM, Ahn J-W, et al.
Effect of n = 3 perturbation field amplitudes below the ELM triggering threshold on edge and SOL transport in NSTX
Journal Nucl. Mater. 438 S388 (July 2013)

54) McLEAN AG, Gan KF, Ahn J-W, et al.,
Measurement and modeling of surface temperature dynamics of the NSTX liquid lithium divertor
Journal Nucl. Mater. 438 S397 (July 2013)

55) KAITA R, Kugel HW, Abrams T, et al.,
Characterization of fueling NSTX H-mode plasmas diverted to a liquid lithium divertor
Journal Nucl. Mater. 438 S488 (July 2013)

56) SKINNER CH, Sullenberger R, Koel BE, et al.,
Plasma facing surface composition during NSTX Li experiments
Journal Nucl. Mater. 438 S647 (July 2013)

57) BOYLE DP, Canik JM, R. Maingi R, et al.,
Varying the pre-discharge lithium wall coatings to alter the characteristics of the ELM-free H-mode pedestal in NSTX
Journal Nucl. Mater. 438 S979 (July 2013)

58) CAO B, Stotler DP, Zweben SJ, et al.,
Comparison of gas puff imaging data in NSTX with DEGAS 2 simulations
Fusion Science and Technology 64 29 (July 2013)

59) WANG F, Fu GY, Breslua JA, et al.,
Simulation of non-resonant internal kink mode with toroidal rotation in the National Spherical Torus Experiment
Phys. Plasmas 20 072506 (July 2013)

60) REN Y, Guttenfelder W, Kaye SM, et al.,
Electron-scale turbulence spectra and plasma thermal transport responding to continuous ExB shear ramping-up in a spherical tokamak
Nucl. Fusion 53 083007 (August 2013)

62) SCOTTI F, Soukhanovskii VA, Bell RE, et al.,
Core transport of lithium and carbon in ELM-free discharges with lithium wall conditioning in NSTX
Nucl. Fusion 53 083001 (August 2013)

63) PERKINS RJ, Ahn J-W, Bell RE, et al.,
Fast-wave power flow along SOL field lines in NSTX and the associated power deposition profile across the SOL in front of the antenna
Nucl. Fusion 53 083025 (August 2013)

64) JAWORSKI MA, Abrams T, Allain JP, et al.,
Liquid lithium divertor characteristics and plasma–material interactions in NSTX high-performance plasmas
Nucl. Fusion 53 083082 (August 2013)

65) PODESTA M, Gorelenkov NN, White RB, et al.,
Properties of Alfven eigenmodes in the Toroidal Alfven Eigenmode range on the National Spherical Torus Experiment-Upgrade
Phys. Plasmas 20 085502 (August 2013)

66) CLAYTON DJ, Tritz K, Stutman D, et al.,
Electron temperature profile reconstructions from multi-energy SXR measurements using neural networks
Plasma Phys. Controlled Fusion 55 095015 (September 2013)

67) GUTTENFELDER, W, Peterson JL, Candy J et al.,
Progress in simulating turbulent electron thermal transport in NSTX
Nucl. Fusion 53 093022 (September 2013)

68) DIALLO A, Canik J, Goerler T, et al.,
Progress in characterization of the pedestal stability and turbulence during the edge-localized-mode cycle on National Spherical Torus Experiment
Nucl. Fusion 53 093026 (September 2013)

69) EICH T, Leonard AW, Pitts RA, et al.,
Scaling of the tokamak near the scrape-off layer H-mode power width and implications for ITER
Nucl. Fusion 53 093031 (September 2013)

70) PARK J-K, Jeon YM, Menard JE, et al.,
Rotational Resonance of Non-axisymmetric Magnetic Braking in the KSTAR Tokamak"
Phys. Rev. Lett. 111 095002 (September 2013)

71) MICHAEL, CA, Conway N, Crowley B, et al.,
Dual view FIDA measurements on MAST
Plasma Phys. Controlled Fusion 55 095007 (September 2013)

NSTX-U Presentations in FY2013 (October 2012-September 2013)

1) S. Gerhardt, “Disruptions in the High–β Spherical Torus NSTX", 2012 IAEA Fusion Energy Conference, San Diego, CA, October 2012

2) W. Guttenfelder, "Progress in simulating turbulent electron thermal transport in NSTX", 2012 IAEA Fusion Energy Conference, San Diego, CA, October 2012

3) S. Kaye, “The dependence of H-mode energy confinement and transport on collisionality in NSTX”, 2012 IAEA Fusion Energy Conference, San Diego, CA, October 2012

4) R. Maingi, “The nearly continuous improvement of discharge characteristics and edge stability with increasing lithium coatings in NSTX”, 2012 IAEA Fusion Energy Conference, San Diego, CA, October 2012

5) S. Sabbagh, “Overview of physics results from the National Spherical Torus Experiment”, 2012 IAEA Fusion Energy Conference, San Diego, CA, October 2012

6) J. Menard, “Progress on developing the spherical tokamak for fusion applications”, 2012 IAEA Fusion Energy Conference, San Diego, CA, October 2012

7) W. Guttenfelder, "Linear GYRO simulations of TC-15 shots in NSTX", ITPA-TC, San Diego, CA, October 2012

8) J. Menard, “Studies of ST-FNSF mission and performance dependence on device size”, 1st IAEA DEMO Programme Workshop, UCLA, October 2012

9) M. Jaworski, "NSTX liquid lithium divertor results and on-going research on liquid metal PFCs", 14th US/Japan High-Power Density Devices Workshop meeting, Del Mar, CA, October, 2012

10) C. Skinner, “First mirror and dust risk management”, 23rd ITPA Diagnostics Meeting, Gandhinagar, India November 2012

11) C. Skinner, “Progress in mirror Cleaning & dust detection”, 23rd ITPA Diagnostics Meeting, Gandhinagar, India November 2012

12) D. Mueller, “Physics of tokamak plasma start-up”, 54th Annual APS-DPP Meeting, Providence, RI, November 2012

13) J.R. Myra, “Edge sheared flows and blob dynamics”, Invited, 54th Annual APS-DPP Meeting, Providence, RI, November 2012

14) F. Scotti, " Modifications of impurity transport and divertor sources with lithium wall conditioning in NSTX", Invited, 54th Annual APS-DPP Meeting, Providence, RI, November 2012

15) D. Smith" Assessing low wavenumber pedestal turbulence in NSTX with measurements and simulations", Invited, 54th Annual APS-DPP Meeting, Providence, RI, November 2012

16) A. Bortolon, "Interplay between coexisting MHD instabilities mediated by energetic ions in NSTX H-mode plasmas", Invited, 54th Annual APS-DPP Meeting, Providence, RI, November 2012

17) J. Berkery, "Global mode control and stabilization for disruption avoidance in high-beta NSTX plasmas", at the 17th Workshop on MHD Stability Control, Columbia University, New York, November 2012

18) K.Kim, "NTV calculation with particle simulation and its validation in NSTX and DIII-D", 17th Workshop on MHD stability control, Columbia University, New York, November 2012

19) R. Raman, "Electromagnetic particle injector for NSTX-U," 17th MHD Control Workshop, Columbia University, New York, November 2012

20) R. Maingi, "How coating the walls with lithium improved plasma performance in the National Spherical Torus Experiment". Invited seminar at Pennsylvania State University, Dept. of Nuclear Engineering, November, 2012

21) R. Perkins, "Fast wave power flow along SOL field lines in NSTX," US-Japan RF Heating Physics Workshop, Nara, Japan, December 2012

22) N. Bertelli et al, "RF fields in the HHFW regime on NSTX-U and scattering in the LH regime on Alcator C-Mod", US-Japan Workshop on RF Heating Physics, Nara, Japan, December 2012

23) J. Menard, "Progress and plans for NSTX Upgrade", MIT Seminar, December 2012

24) M. Jaworski, "Possible technical solution for a liquid divertor in DEMO", 20th European Fusion Physics Workshop, Ericeira, Portugal, December, 2012

25) J. Menard, "Effect of rotation and drift-kinetic damping on NSTX kink stability with future application to tearing stability", Max-Planck-Princeton Center for Plasma Physics Workshop, IPP, Garching, Germany, January 2013

26) J. Menard, "NSTX Accomplishments and NSTX-U Research Plans in Support of Fusion Next-Steps", Invited, 25th IEEE Symposium on Fusion Engineering (SOFE), San Francisco, June 2013

27) K.Kim, "Delta-f particle simulation for calculating neoclassical transport and neoclassical

toroidal viscosity in perturbed tokamaks", Seminar, Seoul National University, Korea, January 2013

28) C.W. Domier, "A High-k Poloidal Scattering System for NSTX", U.S.-Japan Workshop on Millimeter Wave Technology and Fusion Plasma Fluctuation Diagnostics, Davis, CA, January 2013

29) R. Raman, "Overview of Physics Results from NSTX and the NSTX-U Program Goals", Kyushu University, Japan, January 2013

30) C.W. Domier, "A High-k Poloidal Scattering System for NSTX", U.S.-Japan Workshop on Millimeter Wave Technology and Fusion Plasma Fluctuation Diagnostics, Davis, CA, January 2013

31) A. Bortolon, "Interplay between coexisting MHD instabilities mediated by energetic ions in NSTX H-mode plasmas", ORNL Seminar, January 2013

32) R. Raman, "Overview of Physics Results from NSTX and the NSTX-U Program Goals", University of Hyogo, Japan, February 2013

33) R. Maingi, "The effect of lithium wall conditioning on discharges in the NSTX". Graduate student seminar at Princeton University, February 2013

34) W. Guttenfelder, "Microtearing modes: some physics and some unanswered questions", PPPL Graduate Student Seminar, March 2013

35) Ahn, J-W, "Divertor detachment studies in NSTX", ITPA DivSOL meeting Hefei, China, March 2013

36) Ahn, J-W, "ELM heat flux widths and toroidal asymmetry on NSTX", ITPA DivSOL meeting Hefei, China March 2013

37) R. Maingi, "The role of upstream edge transport and stability in the divertor power flux footprint", Invited plenary talk at the US-EU TTF Meeting, Santa Rosa, CA, April 2013

38) W. Guttenfelder, "Gyrokinetic predictions of momentum and impurity transport in NSTX", US-EU TTF, Santa Rosa, CA, April 2013

39) W. Guttenfelder, "Gyrokinetic predictions of momentum transport in NSTX", ITPA-TC, IPP-Garching, Garching, Germany, April 2013

40) C. Skinner, "Laser cleaning of candidate diagnostic mirrors for ITER", ITER workshop in First Mirror Surface Recovery, April 2013

41) C. Skinner, "First mirror and dust risk, ITER workshop in First Mirror Surface Recovery,

April 2013

42) R. Kaita, “Plasma-facing component research on NSTX-U: addressing the challenge of first wall materials for magnetic confinement fusion”, Department of Physics and Astronomy Seminar, Johns Hopkins University, Baltimore, MD, April 2013

43) C. Skinner, “Laser cleaning of candidate diagnostic mirrors for ITER”, 14th International Conference on Plasma-Facing Materials and Components for Fusion Applications, Julich, Germany, May 2013

44) A.L. Roqumore, “Upward facing lithium flash evaporator for NSTX-U”, 25th Symposium on Fusion Engineering San Francisco, CA, June 2013

45) R. Perkins, "Towards identifying the mechanisms underlying field-aligned edge-loss of HHFW power on NSTX," 20th Topical Conference on Radio Frequency Power in Plasmas, Sorrento, Italy, June 2013

46) R. Perkins, "Towards identifying the mechanisms underlying field-aligned edge-loss of HHFW power on NSTX," IPP Seminar, Garching, Germany, June 2013

47) M. Jaworski, "Liquid metal plasma-facing component research on the NSTX", 40th EPS in Espoo, Finland, July 2013

48) R. Raman, "Non-inductive plasma current start-up in NSTX using transient CHI and subsequent non-inductive current ramp-up scenario in NSTX-U," 40th EPS Conference on Plasma Physics, Helsinki, Finland, July 2013

49) C. Skinner, “Plasma-lithium interactions and dust detection” Invited, Gaseous Electronics Conference Workshop, Princeton, NJ, September/October 2013

50) N. Bertelli et al, "Fast wave edge power losses in NSTX and NSTX-U", SciDAC Project Workshop, PPPL, September 2013

51) N. Bertelli et al, "Full wave simulations for HHFW in NSTX and NSTX-U", US-Japan Workshop on Physics of RF Heating of Fusion Plasmas, MIT, Boston, MA, September 2013

52) B.A. Nelson, "Transient CHI plasma start-up and non-inductive current ramp-up in NSTX-U," International ST Workshop, University of York, Heslington, York, UK, September 2013

53) A. Bortolon, "Mitigation of Alfven activity in a tokamak by externally applied static 3D fields", ORNL Seminar, September 2013

54) A. Bortolon, "Mitigation of Alfven activity in a tokamak by externally applied static 3D fields", IAEA Technical Meeting on Energetic Particles, Beijing, China, September 2013

55) D. Liu, "M3D-K simulations of toroidicity-induced Alfven eigenmodes on NSTX", IAEA Technical Meeting on Energetic Particles, Beijing, China, September 2013

56) M. Jaworski, "Materials and plasma-facing component R&D for the NSTX-U 5-year plan", Plasma-Facing Components meeting, Oak Ridge, TN, September 2013

57) R. Maingi, “The dependence of discharge performance on pre-discharge lithium evaporation in high triangularity H-mode discharges in NSTX”, Plasma-Facing Components meeting, Oak Ridge, TN, September 2013